Doctoral theses at NTNU, 2018:230

Andres Belda Revert

Reinforcement corrosion in carbonated fly ash concrete

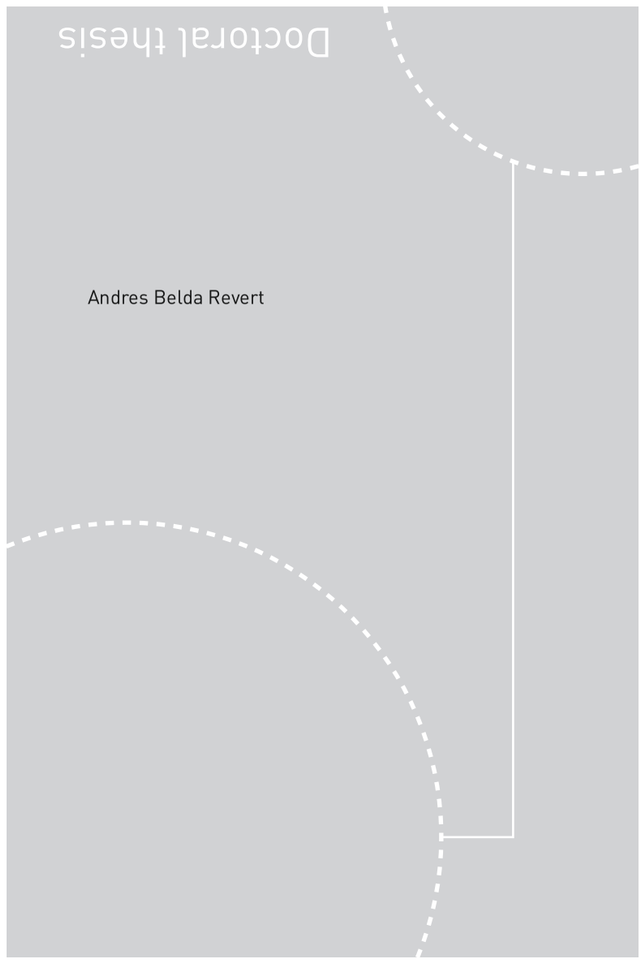

ISBN 978-82-326-3250-3 (printed ver.)
ISBN 978-82-326-3251-0 (electronic ver.)
ISSN 1503-8181

NTNU
Norwegian University of
Science and Technology

NTNU
Norwegian University of Science and Technology
Thesis for the Degree of
Philosophiae Doctor
Faculty of Engineering
Department of Structural Engineering

Doctoral theses at NTNU, 2018:230

NTNU
Norwegian University of
Science and Technology

Andres Belda Revert

Reinforcement corrosion in carbonated fly ash concrete

Thesis for the Degree of Philosophiae Doctor

Trondheim, September 2018

Norwegian University of Science and Technology
Faculty of Engineering
Department of Structural Engineering

NTNU
Norwegian University of
Science and Technology

NTNU
Norwegian University of Science and Technology

Thesis for the Degree of Philosophiae Doctor

Faculty of Engineering
Department of Structural Engineering

ISBN 978-82-326-3250-3 (printed ver.)
ISBN 978-82-326-3251-0 (electronic ver.)
ISSN 1503-8181

Doctoral theses at NTNU, 2018:230

Printed by NTNU Grafisk senter

Preface

The doctoral thesis is submitted to the Norwegian University of Science and Technology (NTNU) for the degree Philosophiae Doctor (PhD). The research was carried out at the Department of Structural Engineering, Faculty of Engineering Science and Technology at NTNU in Trondheim, Norway. The main supervisor was Professor Mette Rica Geiker (NTNU, Trondheim), and the co-supervisors were Associate Professor Klaartje De Weerdt (NTNU, Trondheim) and Senior Engineer Karla Hornbostel (Norwegian Public Roads Administration, Trondheim).

The PhD project started in January 2015 and the thesis was submitted in May 2018. During this period Andres Belda Revert worked for four months on a project sponsored by NORCEM AS.

The PhD study was part of NFR project no. 235211/O30: Development of low-carbon cement for concrete building structures with excellent durability "Lavkarbsem" (subproject 2B). The project manager of Lavkarbsem was Research Director Knut Ose Kjellsen, NORCEM AS. The project leaders of Lavkarbsem subproject 2B were Senior advisor Steinar Helland and Head of Concrete Technology Department Nina Plünneke Borvik, Skanska Norge, until 2017 when Professor Mette Rica Geiker (NTNU, Trondheim) took over the project leader position.

The doctoral thesis consists of the following parts:

Part I: extended summary

Part II: appended papers

Part III: appendices

In additions Part IV contains supplementary papers and reports which are used as supportive documentation for discussion.

Andres Belda Revert declares that the thesis and the work presented here are original. The material included in the thesis has not previously been submitted for a degree at this university or any other institution.

Andres Belda Revert

Trondheim, May 2018

Acknowledgements

I would like to acknowledge the financial support of the Norwegian Research Council and all the industrial partners (Mapei AS, Norbetong AS, Norcem AS, Skanska AS, and Rambøll Engineering AS) which made Lavkarsem project (NFR project no. 235211/O30) possible. The project manager, Knut Ose Kjellsen (NORCEM AS), is acknowledged for his genuine support in all matters. All my supervisors, Mette Rica Geiker (NTNU), Klaartje De Weerdt (NTNU) and Karla Hornbostel (NPRA), are warmly acknowledged for their support, valuable discussions, and patience during this long and intensive journey. I really appreciate the opportunity they gave me for undertaking the PhD study at NTNU.

I would like to thank all my colleagues from NTNU, Department of Structural Engineering, who have helped me during the PhD both technically and giving support when needed. Thanks to all the people in the administration and in the laboratory, especially to Bjørn Schjølberg, without his help many of the experiments would not have been performed. Thanks also to the students Helga Synnøve Kjos-Hanssen, Elisabeth Leite Skare, and Simon Langedal for their help in the laboratory. The support given by Tone Østnor, Ola Skjølsvold, Harald Justnes, and Marit Haugen from SINTEF Building and Infrastructure is highly appreciated. Ulla Hjorth Jakobsen (Danish Technological Institute) is acknowledge for her help with microstructural analyses.

I would like to acknowledge other PhD students working with similar projects in other countries which enriched my research and gave me different points of view by visiting NTNU or hosting me in their home university: Marco Messina from Politecnico di Milano and Matteo Stefanoni from ETH Zurich. Carlos Gil Berrocal from Chalmers University is warmly thanked for the time he stayed at NTNU.

All my colleagues from NTNU deserve a special thank for making daily life easier and keeping such a nice work atmosphere. Especial mention should be made to Andrei Shpak, Tobias Danner, Gilles Plusquellec, Cristian Torres Rodríguez, Jelena Zivkovic, and Daniel Cantero for their supportive talks over a cup of coffee.

Last but certainly not least, my family deserves the warmest acknowledgement, especially my wife Marta and our two daughters Salma and África, who made me forget about all thoughts related to work in our spare time and encourage me through the PhD. Also my parents, specially my mother Maria Josefa, and my siblings Marta, Sergio, and Jose were part of this trip as well. My parents-in-law, Jose and Carmen, and my brother-in-law, David, are warmly acknowledged.

Abstract

The cement industry contributes about 8% of the anthropogenic CO_2 emissions, partly due to large consumption of cement and the emissions associated with the production (for Portland cement (PC) approximately 800 kg/t). One approach to lower the CO_2 footprint is to substitute part of the Portland clinker by supplementary cementitious materials (SMCs), e.g. fly ash blends (PCFA). Blended cements may present advantages compared to PC. However, a main drawback is a lower carbonation resistance. This disadvantage is known and taken into account in the standards.

The objective of the PhD study was to improve the understanding of carbonation-induced corrosion in reinforced concrete structures containing fly ash blends.

For the tested materials and exposure conditions, the carbonation depth measured using thymolphthalein compared to carbonation depth determined using optical microscopy, calcium hydroxide to calcium carbonate profiles determined using thermogravimetric analysis, and free alkali metals (Na, K) in the pore solution determined using cold water extraction. Based on this, the pH indicator was used in the present study for detection of carbonation. Thymolphthalein solution sprayed on a freshly split surface allows to determine the spatial variation of the carbonation depth.

Based on investigations of the microstructure and solid phases, carbonation up to 5% CO_2 appears representative for natural carbonation. An increased degree of carbonation and an increased content of sulphate in the pore solution were observed in samples carbonated at 100% CO_2. However, the impact of the exposure condition was limited compared to the changes upon carbonation (from non-carbonated to carbonated condition).

Corrosion initiation is reported in the literature before the carbonation front compares to the concrete cover. We found that corrosion did not start until the concrete (mortar)-steel interface was carbonated as identified using pH indicator thymolphthalein. A relationship between the carbonated fraction of the mortar-steel interface (as identified using thymolphthalein) and the open circuit potential was observed. Carbonation causes a decrease in the hydroxyl concentration, variations into the carbon content, a reduction in the carbonate-to-bicarbonate ratio, and a release of detrimental ions such as sulphates and chlorides in the pore solution. This strongly increases the probability of corrosion compared to non-carbonated pore solution.

Microcell corrosion rates of reinforcement embedded in carbonated concrete were determined at different moisture conditions. The moisture content was found to have a large impact on the microcell corrosion current. High microcell current densities were observed for wet samples, whereas low microcell current densities were found over drying. The microcell current density was slightly higher in carbonated PCFA compared to PC. When reinforcement embedded in wet carbonated concrete was electrically connected to reinforcement in wet non-carbonated concrete, a macrocell corrosion rate of the same magnitude as the microcell corrosion rate was measured. The relative contribution of the partial processes in macrocell corrosion (cathodic polarization of passive steel, difference in potential between active and passive steel, and anodic polarization of active steel) depended on the cathode-to-anode ratio of the macrocouple.

Overall PCFA presented lower carbonation resistance and the embedded reinforcement corroded slightly faster than in PC. However, it appears that the corrosion rate in carbonated PC and PCFA concrete is only of importance at high moisture content. Reinforcement in carbonated PCFA concretes kept constantly at 90% RH corroded at low rate. In summary:

The total (microcell and macrocell) current density should be used for service life prediction of reinforced concrete structures exposed to CO_2 and periods of wetness (i.e. XC4)

The possible use of PCFA concrete exposed to CO_2 and periods of wetness (i.e. XC4) should be carefully considered

Table of contents

Part I- Extended summary

Part II- Appended papers

Part III- Appendices

Part IV- Supplementary papers

List of Appended papers (Part II)

The thesis includes the following appended papers, which are referred to by A-Roman number.

A-I. Carbonation Characterization of Mortar with Portland Cement and Fly Ash, Comparison of Techniques

Nordic Concrete Research, volume. 54, 50-72 (2016)

Revert, Andres Belda; De Weerdt, Klaartje; Hornbostel, Karla; Geiker, Mette Rica

A-II. Effect of carbonation on the pore solution of mortar

Submitted to Cement and Concrete Research

De Weerdt, Klaartje; Plusquellec, Gilles; Revert, Andres Belda; Geiker, Mette Rica; Lothenbach, Barbara

A-III. Carbonation-induced corrosion: investigation of the corrosion onset

Construction and Building Materials, vol 162, 847-856 (2018)

Revert, Andres Belda; De Weerdt, Klaartje; Hornbostel, Karla; Geiker, Mette Rica

A-IV. Macrocell corrosion in carbonated Portland and Portland-fly ash concrete - contribution and mechanism

Submitted to Cement and Concrete Research

Revert, Andres Belda; Hornbostel, Karla; De Weerdt, Klaartje; Geiker, Mette Rica

Declaration of authorship

Andres Belda Revert performed all work on which this thesis is based and contributed significantly to the writing, planning and running of the experiments in all the appended papers. The co-authors contributed in planning the experiments, discussing and evaluating the results, and by assisting in writing the papers.

In addition, in paper A-II, Andres Belda Revert and Gilles Plusquellec planned and ran the experiments. Klaartje De Weerdt wrote the main part of the manuscript and Andres Belda Revert contributed to the corrosion discussion.

List of Supplementary publications (Part IV)

The following supplementary publications are referred to by S-Roman number.

Enclosed publications in Part IV

Conference papers

S-I. Carbonation front characterization: pH colour indicators

Proceedings of the 35th Cement and Concrete Science Conference, Aberdeen, Scotland (2015)

Revert, Andres Belda; De Weerdt, Klaartje; Geiker, Mette Rica

S-II. Investigation of the effect of partial replacement of Portland Cement by Fly Ash on carbonation using TGA and SEM-EDS

Proceedings of the International RILEM Conference Materials, Systems and Structures in Civil Engineering, Lyngby, Denmark (2016)

Revert, Andres Belda; De Weerdt, Klaartje; Hornbostel, Karla; Geiker, Mette Rica

S-III. SEM-EDS of products formed at natural and accelerated carbonation of concrete from CEM I, CEM II/B-M and CEM II/B-V

XXIII Nordic Concrete Research Symposium, Aalborg, Denmark (2017)

Revert, Andres Belda; De Weerdt, Klaartje; Geiker, Mette Rica; Hjorth, Ulla Jakobsen

S-IV. Carbonation-induced corrosion, impact of sampling technique on predicted service life

Proceedings of the International RILEM 4th International Conference on Service Life Design for Infrastructure, Delft, Netherlands (2018)

Revert, Andres Belda; De Weerdt, Klaartje; Hornbostel, Karla; Geiker, Mette Rica

S-V. Impact of accelerated carbonation on microstructure and phase assemblage

Submitted to Nordic Concrete Research

Revert, Andres Belda; De Weerdt, Klaartje; Hjorth, Ulla Jakobsen; Geiker, Mette Rica

S-VI. Determination of the polarization resistance of steel in carbonated fly-ash concrete- effect of measurement technique

Proceedings EUROCORR 2017, Prague, Czech Republic (2017)

Revert, Andres Belda; Hornbostel, Karla; De Weerdt, Klaartje; Geiker, Mette Rica.

List of Supplementary publications (Part IV)

Popular science magazine papers

S-VII. Karbonatisering av miljøvennlig betong

Byggeindustrien 2016 (7) page 47

Revert, Andres Belda; De Weerdt, Klaartje; Hornbostel, Karla; Geiker, Mette Rica. (2016)

Draft Journal publications

S-VIII. Investigation of the relationship of the corrosion rate and concrete resistivity in Portland-fly ash carbonated concrete

To be submitted

Messina, Marco; Revert, Andres Belda; Hornbostel, Karla; Gastaldi, Matteo; Geiker, Mette Rica

Publications Andres Belda Revert has contributed but are not enclosed in Part IV

Draft Journal publications

S-IX. Effect of contact material between pre-existing material and post-embedded probe

To be submitted

Messina, Marco; Revert, Andres Belda; Gastaldi, Matteo; Geiker, Mette Rica

Reports

S-X. State-of-the-art report: Service life modelling: Carbonation of concrete and corrosion in carbonated concrete (main report included)

NTNU report, ISBN 82-7482-106-8, Trondheim (2017)

Revert, Andres Belda; De Weerdt, Klaartje; Hornbostel, Karla; Geiker, Mette Rica

https://brage.bibsys.no/xmlui/bitstream/handle/11250/2480580/2017_+RevertBelda_et_al.-STAR+I+Service+life+modelling%2C+carbonation+of+concrete+and+corrosion+in+carbonated+concrete.pdf?sequence=1

S-XI. Phenolphthalein and thymolphthalein for carbonation measurements

SINTEF akademisk forlag, 2016

Østnor, Tone Anita; Skjølsvold, Ola; Revert, Andres Belda

List of Supplementary publications (Part IV)

Declaration of authorship

Andres Belda Revert performed all work on which this thesis is based and contributed significantly to the writing, planning and running of the experiments in all the publications. The co-authors contributed in planning the experiments, discussing and evaluating the results, and by assisting in writing the papers.

In addition, in Paper S-V, a summary of the worked performed in the laboratory together with Gilles Plusquellec, results reported by Ulla Hjorth Jakobsen, results from Simon Langedal, NTNU master project, and additional investigations performed by Andres Belda Revert is given.

In addition, in paper S-VIII, Andres Belda Revert and Marco Messina planned and ran the experiments. Andres Belda Revert contributed in the writing.

In addition, in Paper S-IX, Andres Belda Revert and Marco Messina planned and ran the experiments. Marco Messina ran the numerical calculations and Andres Belda Revert contributed in the writing.

In addition, Paper S-XI, was mainly prepared by Tone Østnor and Ola Skjølsvold. Andres Belda Revert contributed in the writing.

List of symbols and abbreviations

AC-EIS: electrochemical impedance spectroscopy

BSE: back scatter electron mode

CH: calcium hydroxide (portlandite)

CSE: saturated calomel electrode

C-S-H: calcium silicate hydrates

CWE: cold water extraction

EDS: energy dispersive spectroscopy mode

GVP: galvanostatic pulse technique

i_{corr}: corrosion rate

ICP: inductively coupled plasma mass spectrometry

LPR: linear polarization resistance technique

OCP: open circuit potential

PC: Portland cement

PCFA: fly ash blend

RH: relative humidity

R_p: polarization resistance

SCM: supplementary cementitious material

SEM: scanning electron microscopy

TGA: thermogravimetric analysis

w/c: water-to-cement ratio (in mass)

XRD: X-ray diffraction

ρ: electrical resistivity of concrete

Part I- Extended Summary

1. Introduction

Reinforced concrete is one of the most common construction materials. Portland cement (PC) is made from low-cost raw materials, mainly limestone and clay, which are available all over the world. When concrete is in fresh state, it is fluid and can fill moulds of complex geometry. These advantages have promoted the use of concrete as construction material. Concrete is used from small buildings to civil engineering infrastructures, which have a huge variety of exposure conditions. Concrete has been conceived as a construction material with durable properties. However, some exposure conditions or inadequately selected raw materials can lead to early deterioration. The deterioration processes which are more economically relevant in reinforced concrete structures are related to the deterioration of the embedded reinforcement rather than the concrete. The two main causes of reinforcement corrosion are the carbonation of the concrete surrounding the reinforcement and chloride contamination.

The cement industry produces about 8% of the anthropogenic CO_2 emissions [1]. Portland cement mainly consists of Portland clinker, which has a CO_2 footprint of approximately 800 kg/t. Portland cements including supplementary cementitious materials (SMCs), have been developed among others to lower the CO_2 footprint including for example fly ash or other bi-products from the industry. Other SCMs included in the standards are ground granulated blast furnace slag, limestone and natural pozzolans [2]. An example of Portland-fly ash cement is the CEM II/B-V produced by NORCEM AS with a CO_2 footprint of 488 kg/t. Fly ash blends (PCFA) present some advantages compared to Portland cement such as lower heat hydration development and lower chloride diffusion coefficient [3]. A drawback is a lower carbonation resistance. This disadvantage is known and taken into account in the standards, e.g. in the NS-EN 206:2013+NA:2014 where the water-to-cement ratio (w/c) requirements for environmental class (bestandighetsklasse) M60 (M60 corresponds to exposure classes XC3 and XC4 in EN-1992-1 [4]) depends on the cement type. The higher the fly ash addition, the more restrictive the w/c allowed.

The service life of reinforced concrete structures is usually divided into the initiation period and the propagation period [5]. Reinforcement does not suffer from corrosion during the initiation period, where aggressive substances, e.g. CO_2 or Cl^-, penetrate through the concrete cover and gradually move towards the reinforcement. The initiation period ends when the reinforcement is depassivated, e.g. reinforcement in carbonated concrete. Today's regulations [4] define the end of the service life regarding carbonation-induced corrosion when the carbonation front reaches the reinforcement, accepting 10% probability of failure, which allows corrosion propagation to some extent.

The addition of fly ash leads to increase electrical resistivity compared to PC when the concrete is non-carbonated. Alonso et al. argued that a high electrical resistivity of the concrete could limit the corrosion rate in carbonated concrete [6]. Glass et al. pointed out that the resistance of the matrix limits the anodic reaction and overall controls the corrosion rate [7]. Gulikers claimed that the electrical resistivity in the vicinity of the corroding reinforcement together with the potentially restricted oxygen transport through the concrete cover determines the corrosion rate [8]. Stefanoni et al. proposed that the capillary condensation in the pore structure in contact with the steel is the parameter which controls corrosion in carbonated concrete [9].

This PhD study focuses on carbonation-induced reinforcement corrosion and the potential influence of fly ash on the corrosion development (microcell and macrocell).

1.1. Objectives

The objective of the PhD study was to improve the understanding of carbonation-induced corrosion in reinforced concrete structures containing fly ash blends. The following objectives were identified:

1. Initiation period and properties of carbonated concrete
   a) Select technique for the PhD study and service life prediction
   b) Quantify the impact of accelerated carbonation on microstructure and phase assemblage
2. Corrosion onset
   a) Identify the lack of knowledge in the current discussion on the relationship between the location of the carbonation front and the initiation of corrosion
3. Propagation period
   a) Study the role of fly ash on corrosion propagation in carbonated concrete covering both microcell and macrocell corrosion
4. Discus the implications for service life prediction.

1.2. Research approach and limitations

The study focuses on carbonation-induced reinforcement corrosion in reinforced/plain mortar and concrete. The performance of fly ash blends (CEM II/B-V and CEM II/B-M) was compared to the performance of Portland cement (CEM I) supplied by NORCEM AS (Norway).

The cements were compared using the same w/c. According to [10], different w/c limitations are given depending on the cement type for M60 durability class (XC3 and XC4 exposure class according to [4]).

The curing conditions used in this investigation (2 weeks at sealed condition and 20°C) may have limited the degree of reaction of the fly ash at the start of exposure.

Carbonation is a slow-developing reaction, accelerated conditions were used (increased CO_2 concentration compared to natural carbonation) to promote faster carbonation of the samples.

1.3. Organization of the thesis

The thesis consists of three parts:

- Part I: Extended summary and overview of the theoretical background
- Part II: Appended papers
  - A-I, A-II, A-III, A-IV
- Part III: Appendices including reports and experimental unpublished work
  - I, II, III, IV

As reference is made to several of the other publications prepared during the PhD study, they are included as supplementary papers in Part IV (S-I to S-VIII are enclosed).

  - S-I, S-II, S-III, S-IV, S-V, S-VI, S-VII, S-VIII, S-IX, S-X, S-XI

2. Theoretical background

In this section, carbonation and corrosion of steel embedded in carbonated concrete are briefly described.

Portland cement is mainly composed of CaO (60-70%), SiO_2 (18-22%), Al_2O_3 (4-6%), and Fe_2O_3 (2-4%) [11]. The addition of SCMs modifies the chemical composition of the cement and influences the phase assemblage upon hydration [12, 13]. Fly ash[1] is mainly composed of SiO_2 (50-60%) and Al_2O_3 (20-30%), thus when PC is blended with fly ash the amount of CaO is reduced. The main hydration phases in hardened PC are calcium silicate hydrates (C-S-H), portlandite (CH) and monosulphate (AFm). In hardened PC paste (w/c of 0.5) the approximate volume of each hydration phase is 50% for C-S-H, 12% for CH, and 3% for AFm [12]. The hardened PCFA paste presents less CH, more C-S-H (with a decreased Ca/Si ratio), and more AFm compared to PC, depending on the amount of replacement [13].

2.1. Carbonation

Carbonation is the spontaneous reaction of the CO_2 with the cement paste [14]. The phase assemblage, the solid phases [15] and the pore solution composition [16], is affected by carbonation. Carbonation leads, among others, to a drop in the pH of the pore solution from values in the range of 13 -14 [12] to 7-8 [16]. The phases carbonating include CH, C-S-H, AFt, AFm and unhydrated clinker particles [17].

The pore solution composition of non-carbonated concrete is rich in alkali metals, the addition of fly ash slightly reduces the alkali metal content in the pore solution [18]. The concentration of the alkali metals (Na and K) in the pore solution drops upon carbonation. Additionally, small amount of chlorides are released in the pore solution and the carbonation of AFt and AFm phases leads to an increased amount of sulphates in the pore solution [19, 20].

Natural carbonation is a slow process. For performance testing, carbonation is usually accelerated by keeping the relative humidity in a certain range (60-70%) [14] and using increased CO_2 concentration compared to natural carbonation [21]. Whether the reaction products formed upon accelerated carbonation are representative of natural carbonation is a subject under study. Paper S-V includes a discussion of the impact of the exposure conditions on the microstructure and phase assemblage upon carbonation.

2.2. Carbonation-induced corrosion

Corrosion is defined as the tendency of manufactured goods to convert back to the original state in which they are found in nature [22]. When reinforcement is embedded in sound concrete, the high pH promotes the formation of a dense oxide layer on the surface of the reinforcement. This layer, termed as passive layer, is composed of Fe_3O_4 and γ-Fe_2O_3 and limits the iron dissolution. [23] The pH of the pore solution decreases upon carbonation, which leads to the dissolution of the passive layer and active corrosion may occur depending on the exposure conditions (mainly water and oxygen) [24].

Once active corrosion can be sustained, the amount of electrons which are released on the anodic sites are consumed on the cathodic sites. The anodic reaction is the oxidation of iron and the cathodic reaction is the reduction of oxygen (for aerated structures). The corrosion process can be limited by different partial processes. If the dissolution of iron is limited, e.g. when a passive layer covers the reinforcement, the corrosion process is under anodic control. On the other hand, if the reduction of oxygen is limited, the

[1] The fly ash used in Norway (NORCEM), class F according to ASTM C618-17a

corrosion process is under cathodic control. Finally, the ions should move through the electrolyte (pore solution) during the corrosion process. If the electrical resistance limits the reaction rate the corrosion process is under resistance control. Different partial processes have been proposed to control the corrosion process in carbonated concrete [6-9].

Microcell (uniform) corrosion occurs when the anodic and cathodic sites are randomly distributed and continuously changing. The oxidation of the metal and the reduction of oxygen take place on neighbouring areas. Gulikers [8] explained the basis of uniform corrosion by the existence of heterogeneities, either on the steel or in the electrolyte, which are irregularly distributed on the steel surface and change their position randomly. When the anodes are located in fixed places, localized attack will develop (macrocell (galvanic) corrosion).

Macrocell corrosion occurs when two thermodynamically dissimilar metals are in electric contact. In the case of reinforced concrete, the metal is in principle the same (typically carbon steel) but the corrosion condition (open circuit potential) may vary due to differences in the thermodynamic condition, e.g. passive steel in contact with active steel [24]. Two kinds of macrocell corrosion can occur depending on the spatial location of the anode (active reinforcement) and the cathode (passive reinforcement) [25]. Face-to-face macrocell corrosion occurs in the case of carbonation-induced corrosion when a piece of reinforcement embedded in carbonated concrete is electrically connected to a piece of reinforcement embedded in non-carbonated concrete. Coplanar macrocell corrosion occurs in the case of carbonation-induced when a piece of reinforcement is partially embedded in carbonated and partially in non-carbonated concrete.

Thermodynamics of corrosion

Thermodynamics allows to determine whether a certain metal exposed to specific conditions may dissolve (corrode) or will not dissolve. Thermodynamics does not provide information about the rate of metal dissolution (corrosion). Corrosion in reinforced concrete structures is usually assumed to be composed of two half-cell reactions, the oxidation of a metal (iron) and the reduction of oxygen (or hydrogen). To determine the corrosion likelihood, Nernst equation, the potential analogue to Gibbs equation, is used, see Eq. 1.

$$E^{rev} = E^0 - \frac{R \cdot T}{n \cdot F} ln(Q) \qquad \text{Eq. 1}$$

Where

E^{rev}	reversible potential [mV]
E^0	standard half cell potential [mV]
R	ideal gas constant [8.314 J/(mol·Kelvin])
T	temperature [Kelvin]
n	number of electrons involved in the corrosion reaction [equi.]
F	Faraday's constant [96487 1/equi.]
Q	product of the activities of reactions products divided by the product of activities of the reactants

An equilibrium diagram, also named Pourbaix diagram, is a graphic representation of the Nernst equation. A Pourbaix diagram is used for distinguishing the different states in which a metal exposed to a certain electrolyte can be found [26]. Three states are possible in a Poubaix diagram. Active state means that stable corrosion products are soluble in the aqueous medium, passive state occurs when the stable species are solid products which deposit to a certain thickness over the metal surface, and immune state is the situation where the metal is not dissolved. It should be noted that a Pourbaix diagram gives information about the stability of different corrosion products of a metal submerged in an aqueous environment based on thermodynamic calculations assuming equilibrium. The Pourbaix diagram applied to reinforcement embedded in concrete is usually determined for pure iron in water [27]. However, the pore solution composition of concrete is a complex electrolyte [18] and could influence the equilibrium conditions. Other factor to be considered is the concentration of iron dissolved in the electrolyte [27].

The corrosion potential (or mixed potential) is determined by the rates of the oxidation and the reduction reactions. The open circuit potential (OCP) is the case when the oxidation and reduction reaction rates are equal (e.g. no external polarization). Steel embedded in sound aerated concrete presents OCP in the range of 100 to -200 mV vs. CSE, while once the concrete is carbonated the OCP range shifts to -200 to -500 mV vs. CSE [24]. The OCP of steel embedded in concrete is affected by the corrosion products formed, moisture content of concrete (concrete resistivity and oxygen content), presence of chloride or carbonation (reduced pH compared to sound concrete) among others [24]. It should be emphasised that OCP gives an indication of the corrosion likelihood, not the kinetics of the corrosion process.

Kinetics of corrosion

The current density (i_{corr}) of reinforcement embedded in concrete can be calculated using the Stern-Geary equation, as presented in Eq. 2. This equation was developed for uniform corrosion on which both anodic and cathodic reactions were activation-controlled [28]. The i_{corr} is calculated dividing a proportionality constant (B) by the polarization resistance (R_p). B depends on the slopes of the anodic and cathodic polarization curves. For steel embedded in concrete, tabulated B values are 56 mV for passive steel and 26 mV for active steel [29]. The R_p is the slope of the potential-current relationship of the reinforcement when polarizing the metal a small range around the OCP. Various methods can be applied to determine the R_p of steel embedded in concrete: linear polarization resistance technique (LPR), potentiodynamic polarization curves (PDP), galvanostatic pulse technique (GVP) or AC electrochemical impedance spectroscopy (EIS) among others. Paper S-VI discusses the influence of the measurement technique on the R_p.

$$i_{corr} = \frac{B}{R_p} = \frac{\frac{\beta_a \cdot \beta_c}{2.303 \cdot (\beta_a + \beta_c)}}{R_p} \qquad \text{Eq. 2}$$

Where:

i_{corr}: instantaneous current density [A/cm^2]

B: proportionality constant [V]

R_p: polarization resistance [Ω·cm^2]

β_a: slope of anodic polarization curve [V/decade]

β_c: slope of cathodic polarization curve [V/decade]

2.3. Concrete electrical resistivity

The electrical resistivity (ρ) of a material gives an indication of how much the material opposes to the flow of electric current. The electrical resistivity is calculated from the electrical resistance (R) applying a cell constant, as presented in Eq.3. The cell constant takes into account the electrical field distribution during the measurement. The cell constant can be determined analytically, numerically or empirically.

$$\rho = k \cdot R \qquad \text{Eq. 3}$$

Where:

ρ: electrical resistivity [Ω·m]

k: cell constant [m]

R: electrical resistance [Ω]

The electrical resistivity can be measured using direct current (DC) or alternating current methods (AC). The use of DC methods is not recommended in concrete due to the polarization of the electrolyte [30]. AC methods have been used in concrete and depending on the condition of the concrete different frequencies are recommended [30]. External or embedded electrodes can be used for the measurement. Embedded electrodes are recommended to avoid moisture changes in the samples when performing the measurement.

The addition of supplementary cementitious materials leads to higher ρ when concrete is non-carbonated. The ρ of carbonated concrete was reported to be higher compared to non-carbonated concrete [30]. It is not clear if carbonated concrete containing blended cements presents higher ρ compared to carbonated PC. Appendix II includes carbonated electrical resistivity of PC and PCFA exposed to 90% RH.

3. Overview of used experimental techniques

A summary of the experimental techniques used during the PhD study is presented. For further description of each technique the reader is referred to the Appended papers.

3.1. Detection of carbonation

Carbonation of concrete is usually detected spraying a pH indicator on a freshly split surface. The indicator shows a colour change depending on the pH threshold of the indicator, e.g. phenolphthalein becomes colourless below pH 8.5 and pinkish beyond 10. Phenolphthalein was classified as potentially carcinogenic [31], and alternative indicators have been introduced. Thymolphthalein was observed to give similar results [Paper A-I and S-I]. Thymolphthalein becomes blueish in the pH range 9-10.5 and colourless below it. Detecting carbonation with a pH indicator is simple, fast and economical. Once the sprayed indicator dries on a freshly split sample, carbonation depth is measured using a ruler according to EN-12390-10 [32]. However, this technique merely shows where the pH at a certain depth compares to the threshold of the indicator. It was argued that the pH threshold determined in a solution may differ when the indicator is applied to concrete, as the ions present in the concrete may interfere [33].

Carbonation can be investigated by thermogravimetric analysis (TGA) on homogenized profile ground samples [34]. TGA consists of monitoring the weight changes of the samples while heating up (e.g. from room temperature to 900°C). TGA allows to quantify compounds of known thermal reaction such as CH (due to dehydroxylation) or C$\underline{\text{C}}$ (due to decarbonation). CH shows usually a well-defined dehydroxilation peak in the range of 400 to 500°C. The decarbonation temperature of C$\underline{\text{C}}$ varies depending on the amount and polymorphs [35]. A TGA curve shows the weight changes during the heating and the derivative curve (DTG) the slope of the change in weight.

Crystalline phases such as CH and C$\underline{\text{C}}$ polymorphs can be investigated by X-ray diffraction (XRD) [36]. When using XRD, a crystalline material emits a characteristic pattern, which is related to the crystal structures and enables identification based on Bragg's law. Changes in CH and C$\underline{\text{C}}$ due to carbonation can be detected in homogenized profile ground samples. The C$\underline{\text{C}}$ polymorphs formed upon carbonation are aragonite, calcite and vaterite, which present different volume change compared to CH due to the crystal form.

Carbonation can be detected on thin sections impregnated with fluorescence dye using an optical microscope [37]. When using crossed polarized light, carbonated areas appear opaline and bright in colour while non-carbonated areas appear dark. When using fluorescent light changes in capillary porosity can be investigated based on the greenish tone of the cement paste.

The microstructure of cementitious materials can be investigated using Scanning electron microscopy (SEM) in the back scatter electron mode (BSE) on polished sections [38]. The denser the material the brighter the colour, e.g. air voids show a characteristic black colour. Differences in elemental composition can be investigated using SEM-EDS (energy dispersive spectroscopy mode) point analysis. The elements in a certain interaction volume are analysed, e.g. 1 μm^3. This volume comprises generally a mixture of cement phases. In order to be able to identify phases the results are expressed in ratios. Hence if a mixture of phases is analysed, the result should lie in between the ideal stoichiometry of these phases.

The pore solution composition can be determined using Inductively Coupled Plasma Mass Spectrometry (ICP-MS) [16]. First, the pore solution should be sampled, either by squeezing or cold leaching extraction methods [39]. The main elements which are found in the pore solution of concrete are Na, K, S, Ca, Al, Si, and Fe [18]. Carbonation lowers the pH of the pore solution and affects the composition [16].

Carbonation can be detected based on changes in the electrical resistivity of concrete using sensors embedded at different depths as reported by [40]. In this study, we determined the electrical resistivity of carbonated concrete using different electrode arrangements and non-conclusive results were found.

3.2. Detection of steel corrosion in concrete

Thermodynamics of corrosion

The open circuit potential is measured using a high-impedance voltmeter connected to a reference electrode (RE) and to the reinforcement (WE). The difference in potential between the WE and the RE is the OCP, which is related to the RE used. In this work different reference electrodes have been used: external saturated calomel reference electrode (SCE) supplied by Radiometer Analytical (France), embeddable ERE 20 reference electrode supplied by Force Technology (Denmark), and pseudo-reference electrodes made of activated titanium mesh.

Microcell corrosion, kinetics

A potentiodynamic polarization curve (PDP) is the response of a metal when is potentiostatically polarized in both anodic and cathodic directions. A PDP gives a comprehensive view of the corrosion process: anodic and cathodic polarization curves. Anodic and cathodic Tafel slopes can be determined and the corrosion current can be obtained by fitting tafel lines to the response (crossing point). The anodic slope in carbonated concrete is a straight line with a slope between 60 to 120 mV/decade, and the cathodic reaction in aerated concrete depends on the moisture content according to [14].

The polarization resistance methods allow to determine the instantaneous current density. The techniques used in this study are described:

- Linear polarization resistance technique (LPR). The R_p is determined by polarizing the steel potentiostatically in the range of 10-25 mV in both anodic and cathodic directions [41]. The R_p is defined as the slope of the response. If both anodic and cathodic reactions are activation-controlled, linear relationship between current density and potential should be observed. The R_p determination using LPR is highly dependent on the ohmic drop (R_Ω) between the WE and the RE, as both are included in the response.
- Galvanostatic pulse technique (GVP). The R_p is determined by polarizing the embedded steel galvanostatically, e.g. Glass et al. proposed 15 mV [42]. The transient while the steel goes back to the OCP is recorded and the R_p can be obtained by fitting an equivalent circuit [41].This technique allows to break down the recorded response into the polarization of the reinforcement and the concrete contribution (R_Ω).
- AC electrochemical impedance spectroscopy (EIS). The corrosion process of the concrete-reinforcement system is investigated by applying a sinusoidal alternating potential signal, e.g. ±10 mV, at varying frequencies. The bulk (concrete) properties are observed in the high frequency range while the electrode (concrete-reinforcement interface) properties in the low frequency range [43]. The R_p can be obtained from the low frequency response.

Macrocell corrosion, kinetics

The galvanic current flowing between the active and passive steel (electrodes) can be determined coupling the electrodes using a zero resistance ammeter (ZRA).

Total current density

The total current density or total corrosion rate of a system, is the oxidation rate of the metal related to the anodic area. In the case of microcell corrosion, the dissolution of the metal is related to the exposed area. In the case of macrocell corrosion, the galvanic current is related to the anodic (depassivated) area. If both microcell and macrocell corrosion take place on the same metal, they should be quantified separated as they affect different areas [44].

Gravimetric loss (GL) allows to investigate the average total corrosion rate in a destructive way. Only the average corrosion rate during the total exposure time can be estimated. The steel is weighted before embedding it in concrete and after the exposure. The accuracy of the measurement depends on the cleaning as well as on the initial measurement. Additionally, GL allows to investigate the corrosion morphology and the distribution. A similar approach is to determine the volume loss instead of gravimetric loss as presented in [45].

3.3. Concrete electrical resistivity

The electrical resistivity of concrete/mortar was determined using EIS. The resistance was attributed to the point with the lowest phase angle of the Nyquist plot. The resistivity was calculated applying a cell constant determined on electrolyte of known conductivity. Both external and internal electrodes were used in samples of different size and geometry.

4. Overview of the work

Table 1 presents a detailed description of the different setups related to the propagation of corrosion investigations.

Table 2 presents an overview of the PhD study. It is structured in three sections according to the corrosion condition of the embedded reinforcement: initiation period (carbonation propagation, no corrosion), corrosion onset (initiation of corrosion), and propagation period (active corrosion).

Table 1: Description of the corrosion propagation investigations

Geometry [mm]	Cover [mm]	Materials	Exposure		Topic	Paper/ Appendix
			Carbonation	Corrosion		
240x120x260[4]	20	Concrete (CEM II/B-V) Ribbed carbon steel, Ø 16 mm	20°C, 90% RH, 5% CO_2	20°C, 90% RH, 5% CO_2	Microcell and macrocell corrosion in carbonated PCFA	Appendix III
60x120x260	20	Concrete (CEM I, CEM II/B-M, CEM II/B-V) Ribbed carbon steel, Ø 16 mm	20-25°C, 60% RH, 100% CO_2	20-25°C, Wet-drying	Microcell corrosion in carbonated PCFA	Paper S-VIII Appendix IV
60x120x260 + 70x120x260	20 + 30	Concrete (CEM I, CEM II/B-M, CEM II/B-V) Ribbed carbon steel, Ø 16 mm	20°C, 60% RH, 100% CO_2	20-25°C, ≈100% RH	Microcell and macrocell corrosion in carbonated PCFA	Paper A-IV

[4] The samples were not fully conditioned by the end of the current study. Appendix III presents a description and preliminary data

Table 2: Summary of the PhD study

	Methods of characterization		Service life		Publications/ Papers	
	Literature	**Experimental**	**Input data**	**Models**		
Initiation period and properties of carbonated concrete	pH TGA FTIR XRD OM SEM-BSE/EDS MIP MAS-NMR ND CA	Mortar: *20°C, 60% RH, 1.5% CO_2* Concrete: *20°C, 60% RH, 1% CO_2* *20°C, 90% RH, 5% CO_2* *XC3* pH TGA XRD OM SEM-BSE/EDS	x_c distributions	x_c=f(t,…)	A-I, A-II S-I, S-II, S-III, S-V, S-X, S-XI Appendix I Appendix II	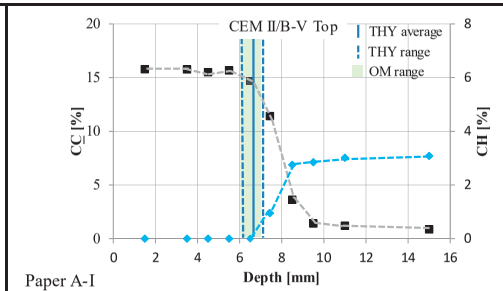 Paper A-I
Corrosion onset	pH OCP GL	Reinforced mortar: *20°C, 60% RH, 1.5% CO_2* Reinforced concrete: *20°C, 90% RH, 5% CO_2* pH OCP OM	OCP drop	-	A-III S-IV	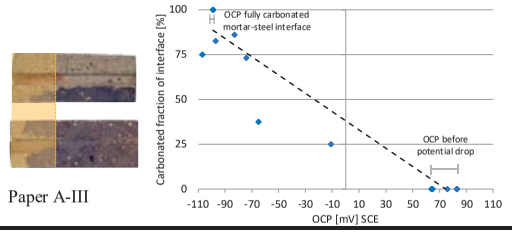 Paper A-III
Propagation period	LPR PDP GVP EIS I_g GL	Reinforced concrete: *20°C, 90% RH, 5% CO_2* *20°C, 100% CO_2, wetting-drying* Reinforced micro-mortar: *20°C, 90% RH, 5% CO_2* LPR PDP GVP EIS I_g	OCP i_{corr}: micro macro ρ_{carb}	i_{corr}=f(t,…)	A-II, A-IV S-VI, S-VIII, S-X Appendix III Appendix IV	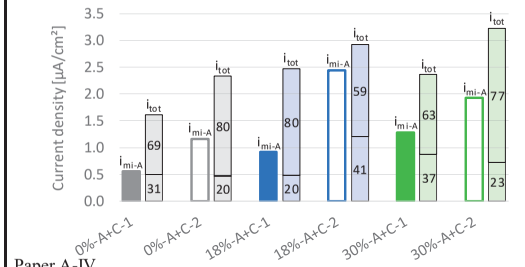 Paper A-IV

Carbonation depth (x_c), pH indicators (pH), Thermogravimetric analysis (TGA), Fourier-transform infrared spectroscopy (FTIR), X-ray diffraction (XRD), Optical microscopy (OM), Scanning electron microscopy (SEM-BSE/EDS), Mercury intrusion porosimetry (MIP), Magic-angle nuclear magnetic resonance spectroscopy (MAS-NMR), Neutron diffraction (ND), Chemical analysis (CA), Open circuit potential (OCP), Linear polarization resistance (LPR), Potentiodynamic polarization curve (PDP), Galvanostatic pulse (GVP), Galvanic current (I_g), Gravimetric loss (GL), Concrete electrical resistivity (ρ), current density (microcell, macrocell, and total (i))

5. Main findings

The main findings are discussed according to the objectives presented in Section 1.1 and repeated below.

The objective of the PhD study was to improve the understanding of carbonation-induced corrosion in reinforced concrete structures containing fly ash blends. The following objectives were identify:

1. Initiation period and properties of carbonated concrete
   a) Select technique for the PhD study and service life prediction
   b) Quantify the impact of accelerated carbonation on microstructure and phase assemblage
2. Corrosion onset
   a) Identify the lack of knowledge in the current discussion on the relationship between the location of the carbonation front and the initiation of corrosion
3. Propagation period
   a) Study the role of fly ash on corrosion propagation in carbonated concrete covering both microcell and macrocell corrosion
4. Discus the implications for service life prediction

5.1. Initiation period and properties of carbonated concrete

A literature review on carbonation characterization was prepared including experimental analysis of mortar samples exposed to 20°C, 60% RH and 1.5% CO_2 [Paper A-I]. The carbonation front was defined as the area/volume in which the measured property changes due to carbonation. The carbonation front is described by its width: a limited width leads to a sharp carbonation front. The carbonation depth spatial distribution can be defined by the average, standard deviation and range using a pH indicator. We observed that the carbonation depth detected using thymolphthalein compared to phenolphthalein in PC and PCFA [Papers A-I, S-I, S-XI]. Additionally, carbonation was detected using TGA and optical microscopy in the same materials. The methods yield to comparable carbonation depths considering the spatial variation [Paper A-I].

In contrast to expected, similar amount of carbonates were formed upon carbonation of PC and PCFA mortars exposed to 20°C, 60% RH and 1.5% CO_2 determined using TGA. A difference in the degree of hydration (lower for the PC) was found to be the reason [Paper S-II].

Mortars w/c of 0.55 containing PC and PCFA were prepared and exposed to 20°C, 60% RH and 1% CO_2 [Paper A-II]. The pore solution was analysed using CWE and ICP-MS, carbonation depths determined using pH indicators (phenolphthalein and thymolphthalein), and the solid phases were investigated using TGA in ground profiles. When the mortars were not carbonated, the PC samples presented higher amount of free alkali metals (Na and K) in the pore solution than the PCFA. Carbonation induced a decrease in the free alkali metal content and led to similar chemical composition in the two cements. The decrease in the free alkali metal content compared to the carbonation depths measured with pH indicator and CH-CC profiles determined using TGA when considering the spatial variation of the carbonation front. The decrease of the free alkali metal ions upon carbonation was attributed to their sorption by decalcified C-S-H.

The influence of carbonation on the electrical resistivity of concrete was investigated in [19, Appendix II]. The resistivity of non-carbonated PCFA concrete is higher compared to PC, and the higher the fly ash content the higher the difference in electrical resistivity when exposed to the same environment. The electrical resistivity of carbonated concrete was similar when comparing carbonated PC and PCFA exposed to 90% RH [Appendix II] or in capillary saturated condition [S-VIII].

The influence of the exposure condition on the microstructure and phase assemblage in carbonated concrete was investigated in [Paper S-V]. Concrete/mortar samples were prepared with w/c of 0.55 differing in fly ash content (0, 18 or 30%). The microstructure upon carbonation, investigated with optical microscopy, was similar for the concrete samples exposed to natural (XC3), 60% RH and 1% CO_2, or 90% RH and 5% CO_2. Local variations in the microstructure in the carbonated samples were attributed to inhomogeneities prior to carbonation. TGA indicated that the phase assemblage of samples carbonated at 1% and 100% CO_2 (60% RH, 20°C) presented comparable solid phases. However, the samples exposed to 100% CO_2 had a reduced peak(s) in the temperature range 100-200°C (corresponding to C-S-H, AFt, AFm and gypsum) and an increased peak in the carbonate range, indicating a higher degree of carbonation than the samples carbonated at 1% CO_2. SEM-EDS point analysis showed that the outer reaction products formed upon carbonation were independent of the exposure condition (XC3, 60% RH and 1% CO_2, or 90% RH and 5% CO_2) and cement type tested. The pore solution analysis of the carbonated samples showed that the free alkali metal content was reduced upon carbonation, while sulphur and chlorine were released into the pore solution. When comparing the influence of exposure condition, carbonation at 100% CO_2 led to a similar amount of free

alkali metals, and a higher amount of sulphates were found in the pore solution compared to the 1% CO_2 exposure. The impact of accelerated carbonation on the chloride content was non-conclusive. The increased sulphate content in the pore solution upon carbonation suggests further carbonation of the cement hydration phases containing sulphate (e.g. AFm and AFt), which is supported by TGA. According to the literature, carbonation up to 3% CO_2 (RH<75%) is representative for natural carbonation (no data on carbonation above 75% RH was found). Based on our data the range could be extended up to 5% CO_2. In agreement with literature reporting increased degree of carbonation at 10% and 100% CO_2,we found slightly increased degree of carbonation of samples carbonated at 100% compared to samples carbonated at 1% CO_2. Considering the impact of different exposure conditions, it should be noted that the influence of the exposure conditions was minor compared to the changes upon carbonation (from non-carbonated to carbonated condition).

Summary of the findings related to initiation period and properties of carbonated concrete

For the tested materials and exposure conditions the following conclusions were drawn:

- pH indicator thymolphthalein allows to determine the spatial variation of the carbonation depth
- Carbonation depth measured using thymolphthalein compared to carbonation depth determined using optical microscopy, calcium hydroxide to calcium carbonate profiles determined using thermogravimetric analysis and free alkali metals (Na, K) in the pore solution determined using cold water extraction
- Electrical resistivity of carbonated PC and PCFA concrete exposed to 90% RH or capillary saturated condition compared
- Carbonation up to 5% CO_2 appears representative for natural carbonation. An increased degree of carbonation determined using thermogravimetric analysis and an increased content of sulphate in the pore solution determined using cold water extraction were observed at 100% CO_2. However, it should be noted that the impact of the various exposure conditions was minor compared to the changes upon carbonation (from non-carbonated to carbonated condition)

5.2. Corrosion onset

A literature review of the carbonation-induced corrosion onset [Paper A-III] showed that there are discrepancies regarding the location of the carbonation front and the time when corrosion starts. There seems to be an agreement that corrosion starts before the carbonation depth compares to the concrete cover. Reinforced mortar samples containing PCFA were exposed to 20°C, 60% RH and 1.5% CO_2 until carbonation initiated corrosion. The open circuit potential (OCP) of the embedded steel was monitored and the carbonation development was followed by periodically spraying freshly split or dry-cut samples with thymolphthalein. The microstructure of the mortar around the rebars was investigated using optical microscopy on thin sections.

The carbonation development differed in plain and reinforced samples: higher carbonation depths were measured in the vicinity of the reinforcement. Based on optical microscopy, we concluded that the potential reason was a difference in the microstructure of the matrix in the vicinity of the reinforcement. The spatial variation of the carbonation depth considering the influence of the reinforcement could explain the apparent early onset of corrosion reported in the literature.

The carbonated fraction of the mortar-steel interface was determined and compared with the open circuit potential of the reinforcement right before examining the samples. A relationship between the OCP and the carbonated fraction of the concrete (mortar)-steel interface was observed. The higher the carbonated fraction of the interface the lower the OCP. This relationship illustrated that corrosion does not start until the concrete (mortar)-steel interface is carbonated. However the relationship it is not necessarily universal as depends on parameters such as moisture, concrete cover, cement composition or corrosion products among others.

The influence of carbonation on the pore solution was modelled and the influence of these changes on corrosion initiation and propagation was discussed [Paper A-II]. The predicted $[Cl^-]/[OH^-]$ compared to the suggested critical threshold given in literature for a pH as high as 12.5 due to the decrease in the hydroxyl concentration upon carbonation. Moreover, the $[Cl^-]/[OH^-]$ is in the range of 100 for the actual carbonation of the samples (exposed to 20°C, 60% RH, 1% CO_2). According to the literature, high corrosion rates (10 $\mu A/cm^2$) were measured on carbon steel exposed to simulated pore solution within this $[Cl^-]/[OH^-]$ [47]. It should be note that the $[Cl^-]/[OH^-]$ can become high either due to a reduction in the $[OH^-]$, e.g. carbonation, or due to increased amounts of $[Cl^-]$, e.g. chloride penetration. The two cases may differ in corrosion mechanism. Additionally sulphur is realised in the pore solution, which is detrimental for corrosion of carbon steel. However, investigations on the role of sulphates on corrosion are limited. In addition the potential impact of combining chlorides and sulphates in the pore solution could increase the probability of corrosion. The modelled amount of carbon in the pore solution varied upon carbonation. For the actual carbonation of the samples, the carbon concentration was lower compared to the original for both cements. According to the literature, reduced amount of carbon promote active corrosion. In addition, the modelled carbonate to bicarbonate ratio was below 1 indicating that bicarbonates started to be predominant for the actual carbonation of the samples. Higher amount of bicarbonates increases the corrosion rate of carbon steel.

Summary of the findings related to corrosion onset

- Corrosion did not start until the concrete (mortar)-steel interface was carbonated as identified using pH indicator thymolphthalein
- A relationship between the carbonated fraction of the mortar-steel interface (as identified using thymolphthalein) and the open circuit potential was observed
- The spatial variation of the carbonation depth when considering the influence of the reinforcement might explain the apparent early onset of corrosion reported in the literature
- Carbonation causes a decrease in the hydroxyl concentration, variations into the carbon content, a decrease in the carbonate-to-bicarbonate ratio, and a release of detrimental ions such as sulphates and chlorides in the pore solution. This strongly increases the probability of corrosion and the corrosion rate compared to non-carbonated pore solution

5.3. Propagation period

A literature review of the corrosion rate determination in carbonated concrete was prepared [Paper S-VI]. The polarization resistance of reinforcement embedded in carbonated concrete was determined using different techniques (LPR, GVP and EIS) and reference electrode locations (embedded or external). A three-cell corrosion arrangement probe was used which consisted of a working electrode (reinforcement), an external counter electrode (titanium mesh), and either an embedded pseudo-reference electrode or an external saturated calomel reference electrode. LPR without compensation requires knowledge on the ohmic drop (the automatic compensation feature for LPR measurement of the equipment used in this study was found not suitable). EIS resulted in slightly higher R_p compared to LPR which may be related to the fitting of the data. GVP was found the most suitable technique as it can be executed in a short time and gives separated information on the ohmic drop and the polarization resistance. However, GVP requires "trial-error" until the proper polarization range is obtained. The location of the reference electrode only influenced the ohmic drop. The determined polarization resistance for the three methods was comparable when the ohmic drop was taken into account.

A collaborative study with POLIMI [Paper S-VIII] was performed to investigate the relationship between current density and the electrical resistivity in carbonated concrete, and a supplementary discussion is presented in [Appendix IV]. An innovative approach was used to determine the electrical resistivity of concrete using post-embedded sensors [Paper S-IX]. This approach takes into account the influence of the contact material (grout). The corrosion activity (microcell) of reinforcement embedded in carbonated concrete samples exposed to wetting-drying cycles was investigated. Three different concretes differing in fly ash content (0, 18 or 30%) were prepared and carbonated at 100% CO_2. Once carbonated, the samples were immersed in water until capillary saturated condition and subsequently exposed to drying in the laboratory. Microcell current density, open circuit potential, mass change (due to water evaporation) and concrete electrical resistivity were monitored. The relationship between the microcell current density and the electrical resistivity in carbonated concrete was in agreement with data previously reported in the literature. The i_{corr}-ρ relationship appears to be binder independent within the scatter of the measurements. The relationship between the open circuit potential and the microcell current density depended on the cement. For low current densities, the OCP-i_{corr} trend of the PCFA samples compares to the trend of the PC samples, but shifted ca. 300 mV towards more positive values. In addition, there appears to be an impact of the sample position during the casting (bottom or top), especially for the PCFA samples. The OCP-i_{corr} relationship changes for high current densities, especially for the OPC samples towards a more horizontal trend. Glass et al. [7] observed similar behaviour but they did not discuss the observations. The potential parameters which could have influenced the OCP-i_{corr} relationship are the pore solution composition, the pore structure (pore water availability), the steel-concrete interface characteristics, and electrical resistivity of carbonated concrete. As mentioned by Glass al. [7], the OCP-i_{corr} data seems to mirror a cathodic polarization curve. From our understanding, this means that the anodic reaction is affected by the change in moisture in a much more pronounced way than the cathodic reaction. Overall, the corrosion process seemed to be under anodic resistance control regardless the cement type.

The influence of fly ash on macrocell corrosion in carbonated concrete was not previously reported in the literature. We investigated the corrosion activity of reinforcement embedded in carbonated concrete samples with and without electrical connection to reinforcement embedded in non-carbonated samples (microcell and macrocell (face-to-face) corrosion were measured) [Paper A-IV]. The cathode-to-anode ratio was either 1.6 or 5.0, and the samples were kept in a moist environment (≈100% RH). Three different concretes were

investigated differing in fly ash content (0, 18 or 30%). The microcell current density was slightly higher in the PCFA samples compared to PC when exposed to 100% RH. The macrocell current density was in all cases of the same magnitude as the microcell current density. Overall, the total current density was high independent of the cement. A simplified model based on the experimental observations was implemented and the governing partial processes (cathodic polarization of the passive steel, difference in potential between the passive and the active steel, and anodic polarization of the active steel.) depended on the cathode-to-anode ratio. This investigation included face-to-face macrocell corrosion which takes place between different reinforcement bars. When the same reinforcement bar is partially embedded in carbonated concrete (coplanar macrocell) similar consequences are expected. Further research is needed to understand how the microcell and macrocell corrosion develop over time in coplanar macrocell corrosion.

The setup described in Appendix III was prepared to investigate microcell and macrocell corrosion in carbonated concrete exposed to constant conditions (90% RH). Only data from the PCFA concretes (18% and 30% FA) is available and indicates low microcell corrosion rates.

Summary of the findings related to propagation period

- The microcell current density was found to be slightly higher in carbonated PCFA compared to PC (same w/c of 0.55) when exposed to the same environment
- The moisture content has large impact on the microcell corrosion current density
- Macrocell current density was not negligible in carbonated PC and PCFA reinforced concrete exposed to 100% RH, cathode-to-anode ratio 1.6 or 5.0, distance between reinforcement bars 50 mm. The higher the cathode-to-anode ratio the higher the galvanic current.
- The total current density (microcell and macrocell corrosion) was high in PC and PCFA exposed to 100% RH
- The governing partial process in macrocell corrosion depends on the cathode-to-anode ratio

5.4. Influence for service life prediction

A literature review describing carbonation models was prepared [Publication S-X]. The main parameters affecting carbonation resistance were summarized and some of the models were applied and compared to laboratory (mortars exposed to 20°C, 60% RH and 1.5% CO_2) and field measurements (Norwegian exposure, XC3 and XC4). The predictions ranged from 50% less to 50% more for the laboratory data. Three out of four predictions were in the same range as most the points for the field data (Norwegian field structures). Structures exposed to class XC4 presented considerable scatter, suggesting that a statistical approach is needed considering the spatial distribution of the carbonation depth.

A literature review on the propagation period (carbonation) models was prepared [Publication S-X]. The main parameters affecting corrosion were summarized. The review shown that most of the empirical models are based on limited experimental investigations and none of the reviewed models take into account the distribution of the corrosion products or the influence of the binder. Further research is required in order to understand if the binder plays a role in corrosion propagation both from the chemical point of view (pore solution) and the physical point of view (pore structure). We performed investigations in samples of different materials and geometry which were exposed to different conditions (see Table 1).

The influence of the sampling technique on the carbonation depth distribution and the predicted service life was studied in Portland cement concrete with and without fly ash exposed to 20°C, 90% RH and 5% CO_2 [Paper S-IV]. The manual approach described in the current standard (EN-12390-10 [32]) was compared to an image analysis approach which includes a detailed description of the statistics of the carbonation depth spatial variation. It was observed that the manual approach leads to measurements which could be operator dependent and the average of the determined distribution can be higher or lower compared to the “real carbonation distribution”. In addition, the manual approach leads to a lower standard deviation. However, only limited impact of the sampling technique on the predicted service life was observed. The carbonation depth determined manually according to the current standard is representative of the “real carbonation distribution”.

The total corrosion rate (microcell and macrocell) is the value which should be used for service life prediction, otherwise a non-conservative prediction may be done.

The PCFA has showed a shorter initiation period and slightly higher total (microcell and macrocell) current densities in the propagation period compared to PC (100% RH or water immersion). Thus the use of fly ash blends should be carefully assessed depending on the exposure conditions. It seems that fly ash should be avoided when carbonation is a treat and concrete is exposed to wetting-drying cycles (i.e. XC4). PCFA presents advantages compared to PC in other exposure conditions, e.g. marine environments, where PCFA has shown higher chloride penetration resistance compared to PC.

6. Conclusions

Carbonation-induced corrosion was experimentally investigated on mortars and concretes containing Portland cement and fly ash blends. The cements were compared using the same w/c of 0.55. The curing conditions used in this investigation (2 weeks in sealed condition at 20°C) may have limited the reaction of the fly ash. The following conclusions were drawn:

Initiation period (carbonation) and properties of carbonated concrete

- pH indicator thymolphthalein allows to determine the spatial variation of the carbonation depth
- Carbonation depth measured using thymolphthalein compared to carbonation depth determined using optical microscopy, calcium hydroxide to calcium carbonate profiles using thermogravimetric analysis and free alkali metals (Na, K) in the pore solution determined using cold water extraction
- Carbonation up to 5% CO_2 appears representative for natural carbonation. An increased degree of carbonation determined using thermogravimetric analysis and an increased content of sulphate in the pore solution determined using cold water extraction were observed at 100% CO_2. However, it should be noted that the impact of the various exposure conditions was minor compared to the changes upon carbonation (from non-carbonated to carbonated condition)

Corrosion onset

- A relationship between the carbonated fraction of the mortar-steel interface (as identified using thymolphthalein) and the open circuit potential was observed
- Corrosion did not start until the concrete (mortar)-steel interface was carbonated as identified using pH indicator thymolphthalein
- Carbonation causes a decrease in the hydroxyl concentration, variations into the carbon content, a decrease in the carbonate-to-bicarbonate ratio, and a release of detrimental ions such as sulphates and chlorides in the pore solution. This strongly increases the probability of corrosion and the corrosion rate compared to non-carbonated pore solution

Corrosion propagation

- Based on investigations performed on wet reinforced concrete (w/c=0.55), carbonated at high CO_2 concentration (100%), exposed to drying in the laboratory, the moisture content has large impact on the microcell corrosion current density. The microcell current density was slightly higher in carbonated PCFA compared to PC
- Based on investigations performed on wet reinforced concrete (w/c=0.55), carbonated at high CO_2 concentration (100%), electrically connected to non-carbonated reinforced samples (cathode-to-anode ratio 1.6 or 5.0), the following conclusions were drawn:
    - The macrocell current density was of the same magnitude as microcell corrosion
    - The total current density was high for all cements
    - The calculated relative contribution of the partial processes in macrocell corrosion depended on the cathode-to-anode ratio
- Based on preliminary data retrieved from reinforced concrete samples exposed to 20°C, 90% RH, and 5% CO_2 (no data for PC available) the following conclusions were drawn:
    - The microcell current density was low to negligible for PCFA
    - The microcell corrosion rate and the electrical resistivity determined in this set of samples was in line with the data determined in the samples carbonated at 100% CO_2

Service life prediction

- The total (microcell and macrocell) current density should be used for service life prediction
- Based on microcell current density measurements, the corrosion rate in carbonated PC and PCFA concrete is only relevant at high moisture content

7. Future research

Some of the samples were not fully conditioned during the PhD study. They will be kept and investigate when ready. The following aspects were not fully understood during the PhD study:

Electrical resistivity of carbonated concrete:

- The pore solution of carbonated concrete seems comparable regardless the fly ash addition. The pore structure of carbonated blended fly ash cement may not be that different either. For high moisture content the electrical resistivity could be comparable, and this moisture state is the one relevant for corrosion propagation. Further research is needed to understand this complex relation and give background for the use of electrical resistivity measurements as health monitoring tool.

Reinforced concrete wall elements 1200x1500x250 mm, concrete cover 20 mm, were prepared containing the same cements used in the PhD studies. The walls are exposed to natural carbonation (XC3 and XC4) and corrosion rates will be determined when the carbonation front compares to the concrete cover.

Microcell corrosion in carbonated concrete:

- The corrosion rates are slightly higher in the PCFA compared to PC when exposed to the same external environment, is it a question of a difference in the internal moisture in equilibrium due to a different pore structure?
  Additionally the kinetics of the water uptake and drying may pay a decisive role in the propagation period of field structures.
- Does the use of SCM influence the quality of the concrete-steel interface and thus the initiation and propagation of corrosion in carbonated concrete?

Macrocell corrosion in carbonated concrete:

- Is there a threshold in moisture which triggers galvanic corrosion?
- Coplanar macrocell corrosion in the same reinforcement bar partially embedded in carbonated concrete was not study in this PhD. Based on the observations for face-to-face macrocell corrosion similar effect is expected

Service life prediction.

- Probabilistic prediction coupling initiation and propagation periods

8. References

[1] J.G.J. Olivier, G. Janssens-Maenhout, M. Muntean, A.H.W.J. Peters, Trends in global CO_2 emissions: 2015, in, Netherlands Environmental Assessment Agency, 2016.
[2] EN-197-1, EN 197-1 Cement - Part 1: Composition, specifications and conformity criteria for common cements, 2011.
[3] R.K. Dhir, M.A.K. El-Mohr, T.D. Dyer, Developing chloride resisting concrete using PFA, Cement and Concrete Research, 27 (1997) 1633-1639.
[4] EN-1992-1, Design of concrete structures, 2004.
[5] K. Tuutti, Corrosion of steel in concrete, Swedish Cement and Concrete Research Institute, Stockholm, 1982.
[6] C. Alonso, C. Andrade, J. González, Relation between resistivity and corrosion rate of reinforcements in carbonated mortar made with several cement types, Cement and Concrete Research, 18 (1988) 687-698.
[7] G.K. Glass, C.L. Page, N.R. Short, Factors affecting the corrosion rate of steel in carbonated mortars, Corrosion Science, 32 (1991) 1283-1294.
[8] J. Gulikers, Theoretical considerations on the supposed linear relationship between concrete resistivity and corrosion rate of steel reinforcement, Materials and Corrosion, 56 (2005) 393-403.
[9] M. Stefanoni, U.M. Angst, B. Elsener, Electrochemistry and capillary condensation theory reveal the mechanism of corrosion in dense porous media, Scientific Reports, 8 (2018) .
[10] NS-EN 206:2013+NA:2014 Concrete, Specification, performance, production and conformity, Standard Norge, 2014.
[11] H. Pöllman, Chapter 2: Composition of cement phases, J. Bensted, P. Barnes (Eds.) Structure and performance of cements, Taylor & Francis, 2002, pp. 25-57.
[12] K. De Weerdt, M.B. Haha, G. Le Saout, K.O. Kjellsen, H. Justnes, B. Lothenbach, Hydration mechanisms of ternary Portland cements containing limestone powder and fly ash, Cement and Concrete Research, 41 (2011) 279-291.
[13] B. Lothenbach, K. Scrivener, R.D. Hooton, Supplementary cementitious materials, Cement and Concrete Research, 41 (2011) 1244-1256.
[14] L. Bertolini, B. Elsener, P. Pedeferri, E. Redaelli, R. Polder, Chapter 5: Carbonation-induced corrosion, Corrosion of Steel in Concrete, Wiley-VCH Verlag GmbH & Co, Weinheim, Germany, 2013, pp. 79-91.
[15] Z. Shi, B. Lothenbach, M.R. Geiker, J. Kaufmann, A. Leemann, S. Ferreiro, J. Skibsted, Experimental studies and thermodynamic modeling of the carbonation of Portland cement, metakaolin and limestone mortars, Cement and Concrete Research, 88 (2016) 60-72.
[16] D.J. Anstice, C.L. Page, M.M. Page, The pore solution phase of carbonated cement pastes, Cement and Concrete Research, 35 (2005) 377-383.
[17] V.G. Papadakis, M.N. Fardis, C.G. Vayenas, Fundamental modelling and experimental investigation of concrete carbonation, Materials Journal, 88 (1991) 363-373.
[18] A. Vollpracht, B. Lothenbach, R. Snellings, J. Haufe, The pore solution of blended cements: a review, Materials and Structures, (2015) 1-27.
[19] S.L. Langedal, Investigation of resistivity, porosity and pore solution composition in carbonated mortar prepared with ordinary Portland cement and Portland-fly ash cement, Norwegian University of Science and Technology, Trondheim, 2018.
[20] B. Huet, V. L'Hostis, L. Tricheux, H. Idrissi, Influence of alkali, silicate, and sulfate content of carbonated concrete pore solution on mild steel corrosion behavior, Materials and Corrosion, 61 (2010) 111-124.
[21] T.A. Harrison, M.R. Jones, M.D. Newlands, S. Kandasami, G. Khanna, Experience of using the prTS 12390-12 accelerated carbonation test to assess the relative performance of concrete, Magazine of Concrete Research, 64 (2012) 737-747.
[22] M.G. Fontana, N.D. Greene, Corrosion engineering, McGraw-Hill, New York, 1967.
[23] C. Andrade, P. Merino, X.R. Nóvoa, M.C. Pérez, L. Soler, Passivation of Reinforcing Steel in Concrete, Materials Science Forum, 1995, pp. 891-898.

[24] L. Bertolini, B. Elsener, P. Pedeferri, E. Redaelli, R. Polder, Corrosion of Steel in Concrete, Wiley-VCH Verlag GmbH & Co, Weinheim, Germany, 2013.
[25] C. Andrade, I.R. Maribona, S. Feliu, J.A. González, S. Feliu, The effect of macrocells between active and passive areas of steel reinforcements, Corrosion Science, 33 (1992) 237-249.
[26] M. Pourbaix, Atlas of Electrochemical Equilibria in Aqueous Solutions, NACE International, Houston, USA, 1974.
[27] A. Küter, Management of Reinforcement Corrosion A Thermodynamic Approach, in, Danish Technical University, Lyngby, Danmark, 2009.
[28] M. Stern, A.L. Geary, Theoretical Analysis of the Shape of Polarization Curves, Journal of the Electrochemical Society, 104 (1957) 7.
[29] C. Andrade, J.A. González, Quantitative measurements of corrosion rate of reinforcing steels embedded in concrete using polarization resistance measurements, Materials and Corrosion, 29 (1978) 515-519.
[30] R.B. Polder, Test methods for on site measurement of resistivity of concrete — a RILEM TC-154 technical recommendation, Construction and Building Materials, 15 (2001) 125-131.
[31] Norwegian Environment Agency, in, 2015.
[32] EN-12390-10, Testing hardened concrete - Part 10: Determination of the relative carbonation resistance of concrete, 2007.
[33] D.O. McPolin, P.A. Basheer, A.E. Long, Carbonation and pH in Mortars Manufactured with Supplementary Cementitious Materials, Journal of Materials in Civil Engineering, 21 (2009) 217-225.
[34] V.G. Papadakis, M.N. Fardis, C.G. Vayenas, Hydration and carbonation of pozzolanic cements, ACI Materials Journal, 89 (1992) 119-130.
[35] B. Lothenbach, P. Durdzinski, K. De Weerdt, Chapter 5: Thermogravimetric Analysis, in: K. Scrivener, R. Snellings, B. Lothenbach (Eds.) A Practical Guide to Microstructural Analysis of Cementitious Materials, CRC Press Boca Raton, United States, 2015.
[36] K. Scrivener, A. Bazzoni, B.M. Gassó, J.E. Rossen, Chapter 4: X-Ray Powder Diffraction. A Practical Guide to Microstructural Analysis of Cementitious Materials, CRC Press Boca Raton, United States, 2015.
[37] R.J. Detwiler, L.J. Powers, U.H. Jakobsen, W.U. Ahmed, K. Scrivener, K.O. Kjellsen, Preparing Specimens for Microscopy, Concrete International, (2001).
[38] K. Scrivener, A. Bazzoni, B.M. Gassó, J.E. Rossen, Chapter 8: Electron Microscopy. A Practical Guide to Microstructural Analysis of Cementitious Materials, CRC Press Boca Raton, United States, 2015.
[39] G. Plusquellec, M.R. Geiker, J. Lindgård, J. Duchesne, B. Fournier, K. De Weerdt, Determination of the pH and the free alkali metal content in the pore solution of concrete: Review and experimental comparison, Cement and Concrete Research, 96 (2017) 13-26.
[40] D. McPolin, P. Basheer, A. Long, K. Grattan, T. Sun, New Test Method to Obtain pH Profiles due to Carbonation of Concretes Containing Supplementary Cementitious Materials, Journal of Materials in Civil Engineering, 19 (2007) 936-946.
[41] C. Andrade, C. Alonso, Test methods for on-site corrosion rate measurement of steel reinforcement in concrete by means of the polarization resistance method, Materials and Structures, 37 (2004) 623-643.
[42] G.K. Glass, C.L. Page, N.R. Short, S.W. Yu, An investigation of galvanostatic transient methods used to monitor the corrosion rate of steel in concrete, Corrosion Science, 35 (1993) 1585-1592.
[43] L. Lemoine, F. Wenger, J. Galland, Study of the Corrosion of Concrete Reinforcement by Electrochemical Impedance Measurement, ASTM International, 1990.
[44] C. Andrade, I.R. Maribona, S. Feliu, J.A. González, Macrocell Versus Microcell Corrosion of Reinforcements Placed in Parallel, in: NACE International, 1992.
[45] K. Hornbostel, U.M. Angst, B. Elsener, C.K. Larsen, M.R. Geiker, Influence of mortar resistivity on the rate-limiting step of chloride-induced macro-cell corrosion of reinforcing steel, Corrosion Science, 110 (2016) 46-56.
[46] M. Castellote, L. Fernandez, C. Andrade, C. Alonso, Chemical changes and phase analysis of OPC pastes carbonated at different CO2 concentrations, Materials and Structures, 42 (2009) 515-525.

[47] P. Garcés, M.C. Andrade, A. Saez, M.C. Alonso, Corrosion of reinforcing steel in neutral and acid solutions simulating the electrolytic environments in the micropores of concrete in the propagation period, Corrosion Science, 47 (2005) 289-306.

Part II- Appended Papers

Paper A-I

Carbonation Characterization of Mortar with Portland Cement and Fly Ash, Comparison of Techniques

Revert, Andres Belda; De Weerdt, Klaartje; Hornbostel, Karla; Geiker, Mette Rica

Nordic Concrete Research, volume. 54, 50-72 (2016)

Carbonation Characterization of Mortar with Portland Cement and Fly Ash, Comparison of Techniques

Andres Belda Revert
M.Sc., PhD candidate
Norwegian University of Science and Technology (NTNU),
Department of Structural Engineering
Rich. Birkelandsvei 1 A, 7491. Trondheim
andres.b.revert@ntnu.no

Klaartje De Weerdt
PhD, Associate Professor
Norwegian University of Science and Technology (NTNU),
Department of Structural Engineering
Rich. Birkelandsvei 1 A, 7491. Trondheim
klaartje.d.weerdt@ntnu.no

Karla Hornbostel
PhD, Postdoctoral researcher
Norwegian University of Science and Technology (NTNU),
Department of Structural Engineering
Rich. Birkelandsvei 1 A, 7491. Trondheim
karla.hornbostel@ntnu.no

Mette Rica Geiker
PhD, Professor
Norwegian University of Science and Technology (NTNU),
Department of Structural Engineering
Rich. Birkelandsvei 1 A, 7491. Trondheim
mette.geiker@ntnu.no

Abstract
The aim of this paper is to investigate the applicability of selected techniques for the characterization of carbonation in mortar samples: pH indicators (phenolphthalein and thymolphthalein), thermogravimetric analysis, X-ray diffraction, analyses of thin sections and polished sections. The results obtained by the different techniques on two mortars (w/b= 0.55; Portland cement (CEM I) and Portland fly ash cement (CEM II/B-V)) exposed to accelerated carbonation (20ºC, 60% RH and 1.5% CO_2) were compared. Spraying with a pH indicator and treating the data by image analysis provides characterisation of the carbonation depth which is in agreement with the other investigated techniques and data on the spatial variation of the carbonation depth.

Key words: Carbonation, Portland fly ash cement, pH indicators, TGA, XRD, optical microscopy, SEM

1. INTRODUCTION

Carbonation-induced corrosion causes premature deterioration of reinforced concrete structures. Carbonation is the spontaneous reaction between the CO_2 present in the air and the cement paste. Carbonation causes, among others, a drop in the pH of the pore solution. Steel embedded in carbonated concrete is not passivated and may corrode [1].

Carbonation is a stepwise reaction which causes gradual changes in the cement paste. First CO_2 is dissolved in the pore solution and carbonic acid is formed. The carbonic acid reacts with the Ca ions from the different cement phases to form calcium carbonate (C$\underline{\text{C}}$). Portlandite (CH) is the first phase to react, followed by monosulphate and ettringite. Calcium silicate hydrate (C-S-H) starts to release calcium once CH is consumed [2]. Carbonation of C-S-H seems to follow two steps: first calcium from the interlayer and defect sites is consumed and once the Ca/Si ratio is 0.67, the calcium from the principal layers is consumed and amorphous silica gel is formed [3]. Additionally, unhydrated phases as alite and belite may carbonate [4].

Table 1 gives an overview of the techniques found in the literature to study carbonation in cementitious materials. The techniques are briefly described below.

The most common way to measure the carbonation depth in concrete is to spray a pH indicator on a freshly split surface and measure the depth at which a colour change takes place. Typically phenolphthalein (PHE) has been used (see e.g. EN 13295:2003 [5]). However, PHE was classified as potentially carcinogenic by the Norwegian Environment Agency in 2015 [6], and alternative indicators are being introduced. Thymolphthalein was observed to give similar results as PHE, see e.g. [7], or [8] where the same materials as used in the present paper were used.

Spraying with a pH indicator allows determination of the depth at which the pH of the pore solution changes in the range of the used pH indicator. If more detailed information is required the actual pH of the pore solution (PS) can be determined. The pH of the pore solution is usually measured on pressure extracted pore solution samples by the use of a pH electrode, see e.g. [9, 10]. McPolin et al. [11] measured the pH of the pore solution with a fibre optic sensor using based on sol-gel technology using either fluorescence life time measurements or absorbance measurements.

Carbonation can be characterized by thermogravimetric analysis (TGA) on homogenized profile ground samples. The monitoring of weight changes while heating up the samples allows the quantification of compounds with known thermal reaction such as the dehydroxilation of CH or the decarbonation of C$\underline{\text{C}}$. In the case of C$\underline{\text{C}}$ the decarbonation temperature varies depending on the polymorphs which are formed [12]. C$\underline{\text{C}}$ present in concrete arrives from different sources: the binder, the aggregates and carbonation.

Fourier-transform infrared spectroscopy (FTIR) allows detecting carbonation by studying the characteristic absorption frequencies of carbon-oxide bonds. Changes reflect the carbonation of CH to form C$\underline{\text{C}}$ [13, 14].

Table 1- Techniques used to detect changes due to carbonation in cementitious materials. Materials (Mat): C: Concrete, M: mortar, P: paste. Exposure: N: natural. Binder: Portland Cement (PC) or PC blends: FA: fly ash, MK: metakaolin, MS: microsilica, NP: natural pozzolan, S: slag. Abbreviations of the techniques are explained in the text. For overview, the techniques used in the present paper are also included (*).

First author and reference	Year	Mat	Binder		Exposure			pH in.	PS	TGA	FTIR	XRD	OM	SEM	TEM	MIP	ND	NMR MAS	γ–ρ	CA
			PC	Blend	T [%]	RH [%]	CO_2 [%]													
Schiessl [15]	1976	C	Not given		N (in- and outdoor)			x	x											
Tuutti [16]	1982	C, M	x	S	N (in- and outdoor)			x	x	x						x				
Litvan [17]	1986	C	x	S	N (in- and outdoor)			x		x						x				x
Parrott [18]	1989	C	Not given		N (in- and outdoor)			x		x										
Campbell [19]	1991	C	x	FA	23	50	0.03	x					x							
Papadakis [4, 20]	1991 1992	C, M	x	NP, FA	22, 30, 42	35-85	50	x		x						x				
Möller [21]	1994	C	Not given		20	30-60	0.03	x		x										x
Lo [13]	2002	C	x	-	21	-	2	x			x									
Chang [14]	2006	C	x	-	23	70	20	x	x	x	x	x								
Thiery [22]	2007	C	x	-	21	53	50	x		x									x	
Villain [23]	2007	C	x	-	20	53	45	x		x									x	x
Castellote [24, 25]	2008 2009	P	x	FA, MS	22	65	0.03, 10, 100	x		x		x				x	x	x		
Herrera [26]	2015	M	x	FA	28	60	50	x	x	x	x									
Herterich [27]	2015	P	x	FA, S	24	40, 55, 75	0.03			x	x	x			x			x		
Leemann [28]	2015	C, M	x	MS, S	20	57	4	x						x		x				
Sevelsted [3]	2015	P	Synthetic		-	100	0.03											x		
Wu [29]	2015	P	x	FA, S	20	75	3	x		x			x							
Shi [30]	2016	M	x	MK	20	57	1	x		x				x		x		x		
Belda (*)	2016	M	x	FA	20	60	1.5	x		x		x	x	x						

X-ray diffraction (XRD) allows the identification of crystalline phases such as CH and C$\underline{C}$ polymorphs. XRD applied to a crystalline material produces a pattern characterized by the peaks at varying intensities and diffraction angles, which are related to the crystal structures and enables its identification based on Bragg's law. When XRD is combined with Rietveld analysis the crystalline phases can be quantified [31]. Changes in crystalline phases due to carbonation can be detected.

Changes in the microstructure due to carbonation can be studied on thin sections by the use of optical microscopy (OM) with crossed polarized light. Carbonated areas appear opaline and brighter in colour, while non-carbonated areas appear in darker colours. [32] Additionally, changes in porosity can be observed by the use of fluorescent light in thin sections prepared with fluorescent dye [33].

Scanning electron microscopy with energy dispersive spectrometry (SEM-EDS) on polished sections can be applied to study carbonation of cementitious materials [34]. Differences in morphology and elemental composition can be investigated by studying the signals emitted by the electrons interacting with the atoms of the sample [30]. Changes in CH content and in the C-S-H composition due to carbonation can be investigated. However to observed changes in the C-S-H composition and morphology it is advised to use transmission electron microscopy (TEM) on ion-beam milled samples [27].

Mercury intrusion porosimetry (MIP) allows characterisation of the porosity. The connected pore volume and pore entry sizes can be characterized by MIP [35]. A non-wetting fluid (mercury) is intruded into the pore structure under increasing pressure. The intruded pore size is determined using the Washburn equation (assuming cylindrical pores) [36]. Changes in porosity due to carbonation can be investigated.

Magic-angle nuclear magnetic resonance spectroscopy (MAS-NMR) allows the identification of amorphous and crystalline phases. Depending on the nuclear-spin isotope studied, different phases can be quantified. If ^{29}Si is used, changes in the silicate chain structure of the C-S-H caused by carbonation can be investigated [37].

In addition to the above mentioned techniques, neutron diffraction (ND), see e.g. [24] or [38], and gammadensimetry (γ–ρ), see e.g. [23], have been used to study carbonation of cementitious materials. A discussion of the applicability of these methods is considered outside the scope of this paper.

Finally, chemical analysis (CA) has been applied to detect carbonation of cementitious materials: e.g. Litvan and Meyer [17] estimated the amount of C$\underline{C}$ by digestion in sulfuric acid and Möller [21] determined CH and bound CO_2 by acid digestion of ground powder dissolved in hydrochloric acid.

The aim of this paper is to investigate the applicability of selected techniques for the characterization of carbonation in mortar samples. Special emphasis is paid to the phase composition. The following techniques were investigated: pH indicators (phenolphthalein and thymolphthalein) were sprayed on freshly split samples, thermogravimetric analysis and X-ray diffraction were performed on homogenized profile ground samples, analyses of thin sections by optical microscopy and polished sections using scanning electron microscopy. The study is part of a larger project on the improvement of the carbonation resistance of low clinker blends and service life prediction, especially of fly ash blends.

2. EXPERIMENTAL

Figure 1 provides an overview of the applied experimental techniques and the sampling undertaken on the mortar prisms.

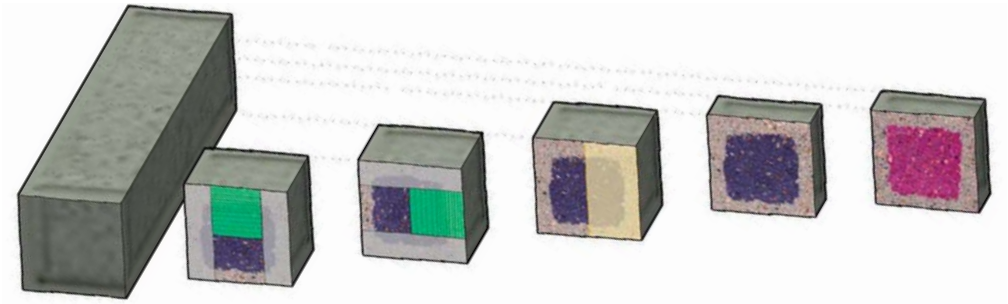

Figure 1- Overview of the used techniques and sampling on CEM I and CEM II/B-V mortar prism. The blue or pink area indicates the non-carbonated mortar identified by thymolphthalein or phenolphthalein.

2.1 *Material*

Mortar prisms 40 x 40 x 160 mm with two binders were investigated. The binders were: CEM I containing 4% limestone powder and CEM II/B-V containing 30% fly ash and 4% limestone powder. Table 2 presents the chemical composition of the binders determined by XRF. The mortar composition (water-to-binder ratio 0.55) was 450 g binder, 1350 g standard CEN sand (d_{max} 2 mm) and 247.5 g water per batch. The mortars were mixed and compacted according to EN 196 [39]. The prisms were stored in the moulds covered with a plastic wrap at 20°C for 24 hours after casting. After demoulding, the prisms were wrapped in plastic and stored at 20°C for 13 days in a sealed container.

Table 2- Chemical composition of the investigated binders determined by XRF [% by mass].

Compound	SiO_2	Al_2O_3	Fe_2O_3	CaO	MgO	SO_3	P_2O_5	K_2O	Na_2O
CEM I	20.4	4.8	3.4	61.7	2.2	3.5	0.2	0.9	0.5
CEM II/B-V	29.5	10.8	4.5	44.6	2	3.2	0.4	1.1	0.5

2.2 Exposure

Fourteen days after casting, the mortar prisms were exposed for four weeks to accelerated carbonation conditions: 20 ± 0.5ºC, 60 ± 1.5% RH and 1.5 ± 0.1% CO_2. Note that the short curing period only allows for a limited degree of reaction of the fly ash [27].

2.3 *Experimental techniques*

2.3.1 pH indicators

Freshly split mortar surfaces were sprayed with PHE 1% and THY 1% solution. The solutions were prepared by dissolving 1 g of each indicator in 30 ml of deionized water and 70 ml of ethanol. Pictures were taken with a reflex camera fixed on a frame with constant light conditions. Carbonation depth was measured by image analysis using a colour thresholding principle. The differentiation of the carbonated zone and the non-carbonated zone, pinkish for PHE (pH <9.5) and blueish for THY (pH <10.5), was determined using different threshold colour values

depending on the indicator. The image analysis treatment comprised the following steps: scaling of the image, determining sample area and non-carbonated area, and measuring the carbonation depth. Thirty points were taken per side avoiding the corner effect (due to the ingress from two directions).

Additionally THY 1% was sprayed on a freshly dry cut surface instead of a split surface to allow optical microscopy investigation.

2.3.2 Thermogravimetric analysis

TGA was performed on homogenized profile ground samples. To study carbonation as a one dimensional phenomenon, the lateral sides (10 mm on each) were removed by dry cutting before profile grinding, see Figure 1. The right (R) and top (T) side were studied. The outer 0-1 mm step was omitted as different paste content was expected. The grinding step was 1 mm for the first 10 mm and 2 mm-step for the rest of the sample. The TGA was performed with a Mettler Toledo TGA/DSC 3+, on samples of approximately 300 mg loaded in aluminum oxide crucibles. The samples were heated from 40 to 900ºC at a rate of 20ºC/min while the oven was purged with N_2 at 50 ml/min. The weight loss of the samples was monitored as a function of the temperature. The amounts of CH and C$\underline{C}$ were calculated following equation (1) and (2):

$$CH\ \% = \frac{W_{400\,^\circ C} - W_{550\,^\circ C}}{W_{850\,^\circ C}} \cdot \frac{74}{18} \cdot 100\% \quad (1)$$

$$C\underline{C}\ \% = \frac{W_{550\,^\circ C} - W_{850\,^\circ C}}{W_{850\,^\circ C}} \cdot \frac{100}{44} \cdot 100\% \quad (2)$$

2.3.3 X-ray diffraction

Ground mortar samples from the carbonated area (depth 1-2 mm) were investigated by XRD. The powder was sieved (300 μm) and front loaded for analysis with a D8 DaVinci diffractometer from Bruker. The following parameters were used: angle range 7-55 º2θ, step width 0.01 º2θ, time per step 0.5 s, axial soller 2.5º, rotation 30 min^{-1}, radiation 1.54 Å (Kα Cu) and generator 40/40 kV/mA.

2.3.4 Optical microscopy

Thin sections were studied by an optical microscope Nikon Eclipse LV 100 POL. CH and C$\underline{C}$ crystals were observed using crossed polarized light. Porosity changes due to carbonation were studied by comparing the intensity of the fluorescent light transmitted through the sample.

2.3.5 Scanning electron microscopy

Polished sections were investigated by a scanning electron microscope Quanta 400 ESEM from FEI, operated at high vacuum mode and accelerating voltage of 20 keV. Images were taken in back scatter electron (BSE) mode.

4. RESULTS

4.1 Terminology

Figure 2 introduces the used terminology and symbols applied in this paper:

- The carbonation depth ($x_{c,i}$) is the distance at location "i" from the outer surface inwards to which a colour change is observed on a freshly split sample sprayed with a pH indicator. The carbonation depth is described by the spatial variation:
  - Average ($\bar{x}_c$)
  - Median ($\tilde{x}_c$)
  - Range (δ_x)
- The carbonation front is the area/volume in which the measured property (e.g. pH, C$\underline{\text{C}}$ and CH content) changes due to carbonation. The carbonation front is described by its width (w_x)

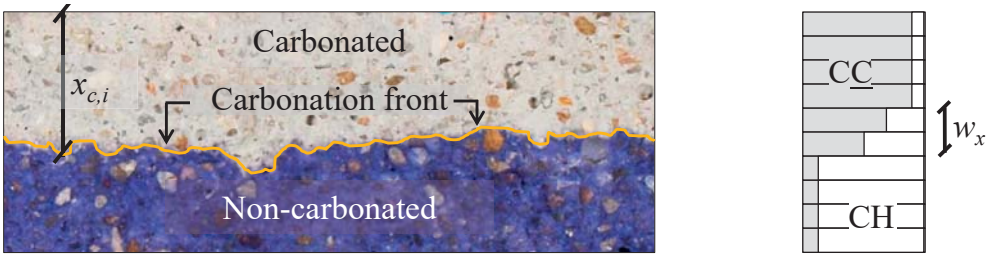

Figure 2- Used terminology to describe carbonation. Left: carbonated and non-carbonated mortar identified by pH indicator (THY); $x_{c,i}$: carbonation depth at location "i". Right: carbonation front characterized as change in CH and C$\underline{\text{C}}$ content determined using TGA; w_x: width of the carbonation front. Note that the width of the carbonation front depends on the measured property.

4.2 pH indicators

Carbonation depth estimated by the pH indicators show clear differences depending on the investigated side of the prisms: lateral and top sides showed similar carbonation depths, while the bottom side gave lower values. Similar observations were made on cut surfaces. Figure 3 illustrates the variation of carbonation depth across and along a mortar prism.

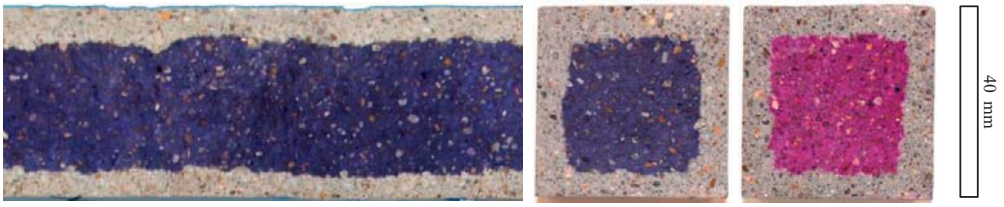

Figure 3- CEM II/B-V samples sprayed with pH indicators. Left: longitudinal section sprayed with TH. Middle: cross section sprayed with THY. Right: cross section sprayed with PHE.

Figure 4 presents the carbonation depth histograms for both mortars sprayed with THY. It can be observed that if the data is split into bottom side and the rest of the sides, then it tends to distribute as a normal distribution. In the case of the bottom side as the number of points is smaller the tendency is not as clearly observable as with the lateral and top side plot together. Data from the bottom sides are not included in this study for the comparison of the techniques.

Figure 5 illustrates the spatial variation of carbonation depth determined by the two pH indicators. Both PHE and THY showed clearly defined carbonation fronts and yielded similar carbonation

distributions. The range (δ_x) is comparable to the maximum grain size of the used aggregates (2 mm). As expected, the mortar with CEM II/B-V binder showed lower carbonation resistance compared to the mortar with CEM I. The values represent combined data from the lateral and top sides.

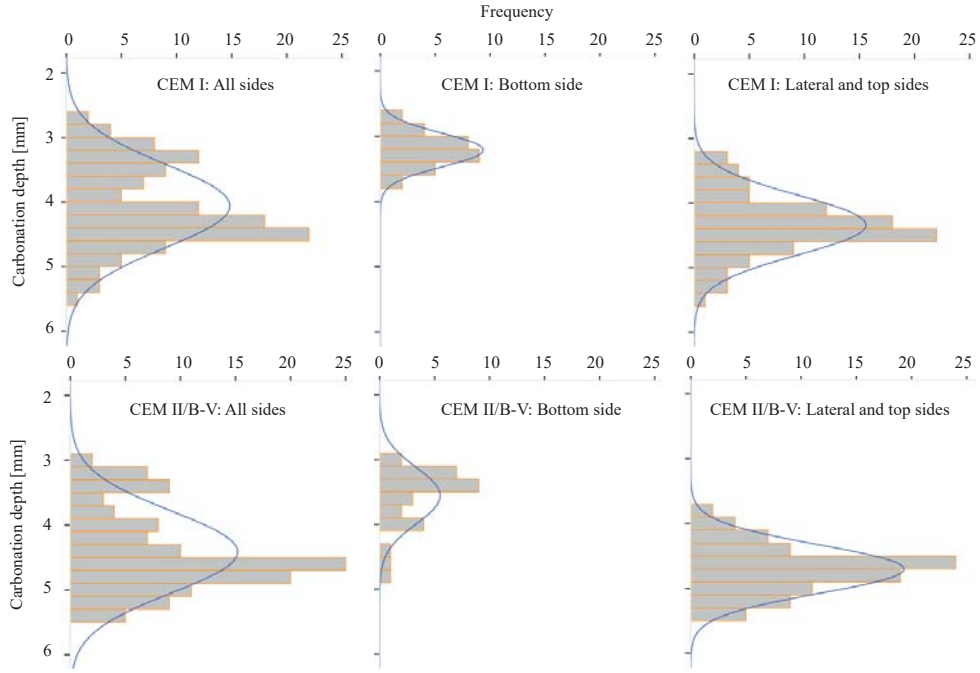

Figure 4- Histograms of CEM I and CEM II/B-V samples sprayed with THY. Left: all four sides. Middle: bottom side. Right: lateral and top sides.

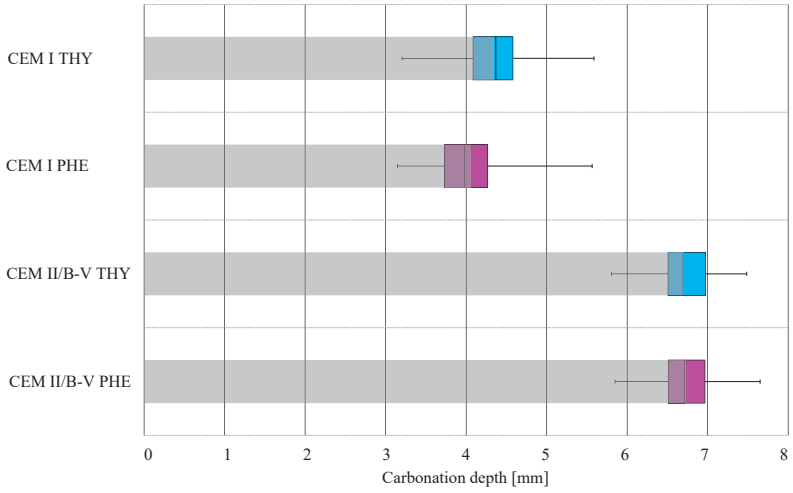

Figure 5- Spatial variation of carbonation depths: lateral and top sides of CEM I and CEM II/B-V mortar samples determined using THY and PHE. Boxes: values from the second to the third quartile and $\tilde{x}_c$, whiskers: δ_x, grey bars: $\bar{x}_c$.

4.3 Thermogravimetric analysis and X-ray diffraction

Figure 6 (left) presents an example of both mass loss and derivative curve for a non-carbonated sample (dark) and a carbonated sample (grey) determined by TGA. The carbonate peak for the carbonated sample (450-850 ºC) presented different shoulders. One of the possible explanations could be the presence of different C$\underline{C}$ polymorphs. However, only calcite was observed by XRD. The broad range of decomposition temperatures for the C$\underline{C}$ can be attributed to variations in crystallinity, differences in particple size, and a large amount C$\underline{C}$ present e.g. [23, 12, 40].

Ground powder taken from the carbonated area (depth 1-2 mm) of both mortars was analysed by XRD (see Figure 6 right), in order to identify potential C$\underline{C}$ polymorphs. Three different polymorphs can be found in concrete: calcite, vaterite and aragonite [41]. Due to the presence of the sand in the ground mortar samples, the spectrum was dominated by quartz peaks, complicating the identification of other crystalline phases. Nonetheless, for both mortars, calcite was the main C$\underline{C}$ polymorph which was observed, while the presence of vaterite and aragonite could not be confirmed. No distinct diffraction peaks related to CH could be observed in the carbonated sample.

Figure 7 gives the derivative curves for the investigated depths from the right side of CEM II/B-V. The amounts of CH and C$\underline{C}$ determined by TGA on the different profile ground sections are shown in Figure 10. The typical error for the C$\underline{C}$ estimation was not larger than 0.4% points and 0.3% points for the CH estimation. The error of position is considered the grinding step; 1 mm for the first 10 mm and 2 mm for the rest of the sample.

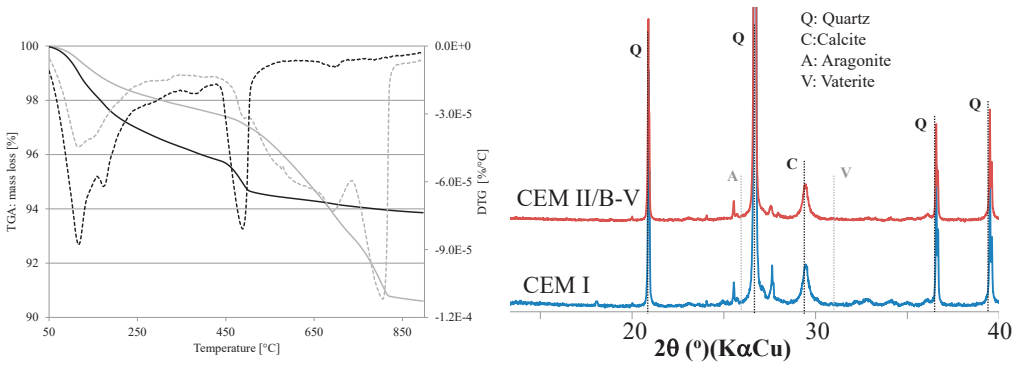

Figure 6- Left: weight loss in % of weight at 850 ºC (TGA, solid) and differential weight loss (DTG, dotted) of non-carbonated sample, depth 12-14 mm (black), and carbonated sample, depth 1-2 mm (grey) of CEM I. Right: XRD pattern of the carbonated samples, depth 1-2 mm.

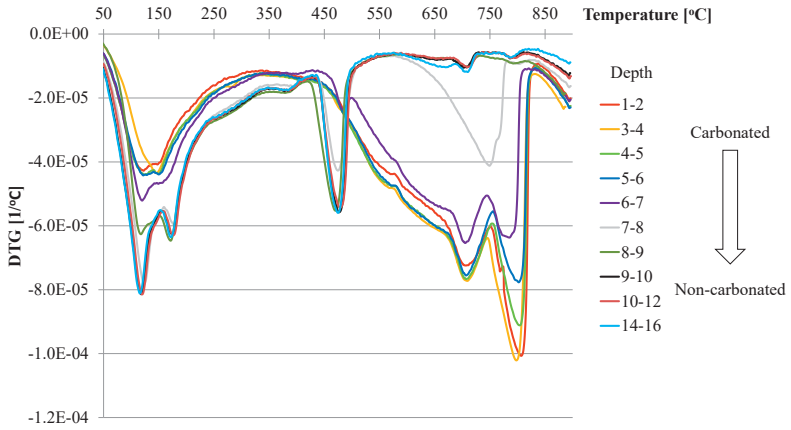

Figure 7- Differential weight loss (DTG) curves for sample CEM II/B-V right side at the different homogenized profile ground depths

4.4 Microscopy

Figure 8 presents the images taken by the optical microscope on cut sections (normal light) and thin sections (cross polarized light), and by SEM in BSE mode on polished sections. CO_2 penetrated from the top side inwards. Note that the images of the cut section give an overview of the carbonation front while the images of both the thin and the polished sections are focused on the transition from carbonated to non-carbonated mortar using higher magnification.

The normal light pictures demonstrate the sharpness of the front assessed by THY. In addition, the pictures show the spatial variation of the carbonation depth over the width of the samples and how the carbonation depth is affected by the presence of air voids and sand grains.

Under cross polarized light in the optical microscope, CC crystals were observed in the carbonated zone, rendering the paste opaline and brighter in colour. In the non-carbonated area, CH crystals were observed as bright and colourful spots in the darker surrounding sound paste. A relatively sharp transition from carbonated to non-carbonated paste was observed. In addition, the spatial variation of the carbonation front and the impact of aggregates are once more demonstrated. The range of the carbonation front determined by optical microscopy using cross polarized light is presented in Table 3.

Table 3- Carbonation depth range (δ_x) determined by optical microscopy.

	CEM I Top	CEM I Right	CEM II/B-V Top	CEM II/B-V Right
δ_x [mm]	4-5.5	3.5-4.5	6-7	6-7

Changes in the microstructure caused by carbonation were difficult to observe by the use of SEM. The absence or presence of CH indicates the position of the carbonation front. However, neither clear difference in grey tone nor morphology of hydrates could be observed between carbonated and non-carbonated paste. This is further discussed in [40]. However, Shi et al. [30] observed clear differences in the microstructure between carbonated and non-carbonated paste using SEM-BSE.

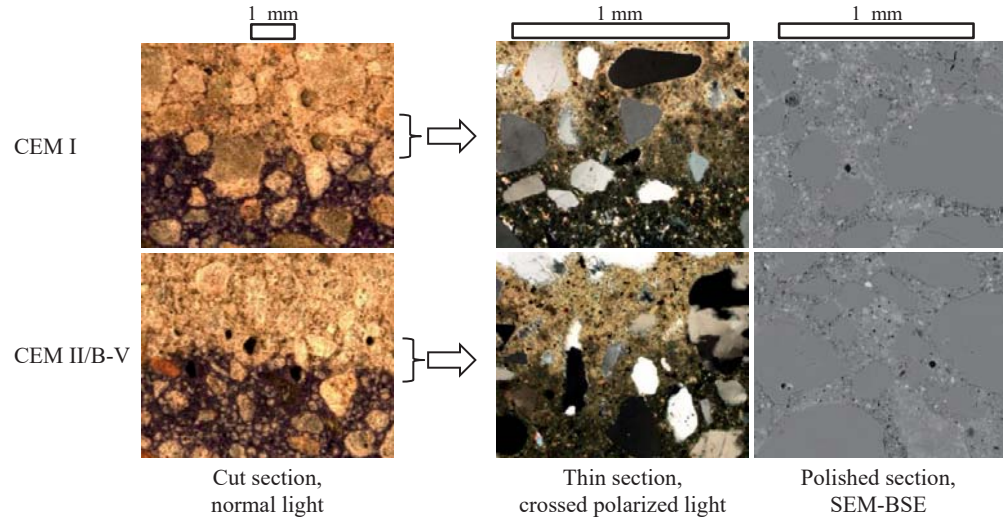

Figure 8 - Pictures taken by optical and scanning electron microscopy. Carbonation from the top side. Images of thin sections taken by Marit Haugen and images of polished sections taken by Ulla H. Jakobsen.

Figure 9 presents the images taken on the thin sections by the optical microscope using fluorescence light. The porosity, investigated using UV light transmitted through the fluorescent impregnated thin sections did not seem to be affected by carbonation for any of the mortars. The images indicated no major changes in porosity due to carbonation in any of the mortars. The darker spots observed in the thin section were due to the penetration of form oil and should not be mistaken for densifications. This is in disagreement with the expected change in porosity [1]. The w/b at 0.55 is considered at the limit to estimate changes porosity by the eye, for high w/b more sophisticated methods should be used [32, 33].

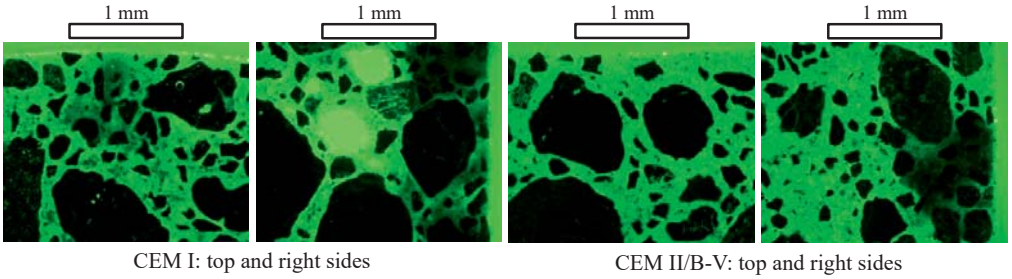

Figure 9- Pictures of carbonated mortar taken by optical microscopy with fluorescence light on the thin section. Images taken by Marit Haugen.

5. DISCUSSION

The carbonation characterization obtained by THY, TGA and optical microscopy are compared in Figure 10. For TGA, carbonation was characterized by a decrease in the CH content and an increase in the C$\underline{C}$ content. When comparing the results of the different techniques, the sampling process should be kept in mind. When profile grinding (as in the case of TGA), the content of the different phases is homogenized over the depth of the step (1 or 2 mm), thereby averaging the spatial variations. A split section (THY) or thin section, on the other hand, shows the spatial variation, but only represents a limited section of the mortar sample. Additionally, the comparison is also influenced by the spatial variation of carbonation in the longitudinal axes of the prism: each technique was applied to the same mortar sample, but on different sections (see Figure 1). From Figure 10, it can be seen that the carbonation depth determined by THY and the depth of CH depletion determined by TGA are in relatively good agreement when considering the impact of sampling. Using TGA an apparent gradual change of phases can be observed. For the CEM I mortar the width of the carbonation front determined by TGA can be explained by the spatial variation of the carbonation depth observed by THY, but could also be due to kinetics. For the CEM II/B-V mortar C$\underline{C}$ are formed at deeper depths. From Figure 10, it can also be seen that the carbonation depth determined by THY and optical microscopy are in relatively good agreement.

Chang and Chen [14] investigated concrete samples made with Portland cement with w/b=0.65 exposed to accelerated carbonation for 8 and 16 weeks (23ºC, 70% RH and 20% CO_2). They assumed that the carbonation depth determined by TGA was the depth where the C$\underline{C}$ content approached the bulk content of the non-carbonated material (which is deeper than the depth of CH depletion considered above). Using their definition the carbonation depth by TGA was for the investigated material and exposure found to be twice as deep compared to the one obtained with PHE. Shi et al. [30] compared PHE and TGA for mortars prepared with binders with calcined clay and limestone exposed to accelerated carbonation (20ºC, 57% RH and 1% CO_2). They also observed that C$\underline{C}$ were found deeper compared to the carbonation depth obtained by PHE, e.g. Portland cement mortar with limestone addition (30%) cured for 90 days showed after 90 days of exposure a carbonation depth of 8 mm determined by PHE while the plateau of the C$\underline{C}$ was found at a depth of 10 mm. Litvan and Meyer [17] observed that the C$\underline{C}$ approached the bulk content up to 15 mm inwards while the PHE colour changed was close to 5 mm in a Portland cement concrete exposed to natural carbonation for 20 years.

Comparing the TGA data for the two cements it can be observed that CH is contributing to carbonation to a larger extent in the CEM I mortar than in the CEM II/B-V mortar. The CO_2 binding capacity of the two cement types is discussed in a separate paper [40].

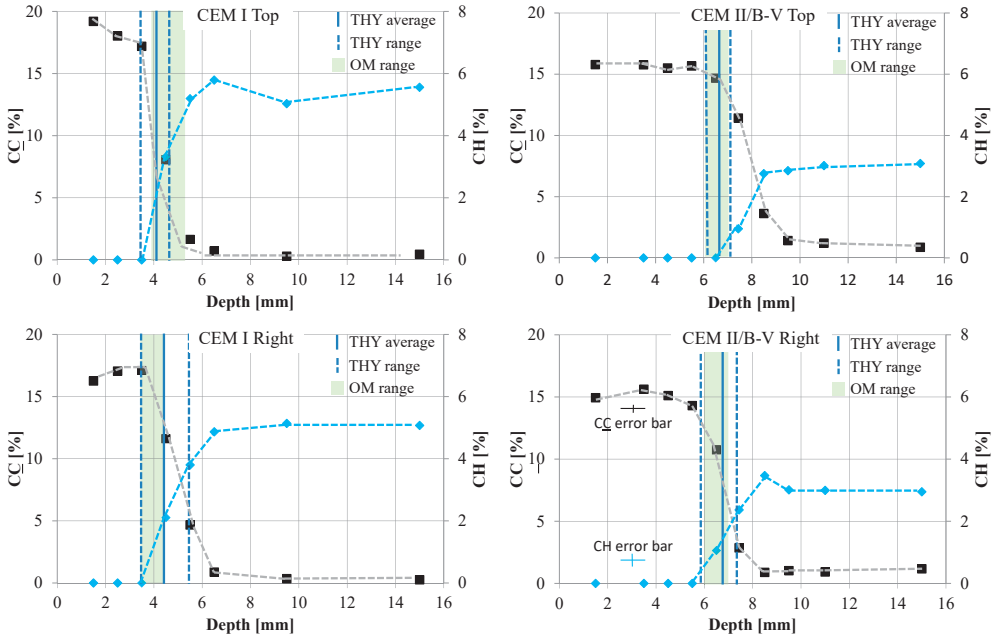

Figure 10- Carbonation characterization by the use of THY (continuous line: $\bar{x}_c$, dotted lines:δ_x), TGA (C$\underline{C}$: squares, CH: diamonds) and optical microscopy (shady area:δ_x). The horizontal axis represents the depth (0 outer surface and positive inwards) while the vertical axis presents the C$\underline{C}$ content to the left and CH content to the right in each graph. Note the difference between the scales for C$\underline{C}$ and CH. The typical error for the C$\underline{C}$ estimation was not larger than 0.4% points and 0.3% points for the CH estimation. The error of position is considered the grinding step; 1 mm for the first 10 mm and 2 mm for the rest of the sample.

Table 4 presents a summary of the applicability of the techniques and sampling used to investigate carbonation in this study. The carbonation front seems to be steep for the examined mortars and exposure. Carbonation characterization using THY sprayed on a freshly broken surface was found to be well in agreement with the optical microscopy and thermogravimetric analysis. THY was found to be the most economic and simple technique to apply, which together with the image analysis gives statistical information for service life design.

Table 4 - Comparison of the investigated techniques. Brackets: limited information.

Technique	Measured property	Spatial variation of carbonation depth	Width of the carbonation front	Cost - Complexity
pH indicator	pH (threshold)	Yes	[Yes]	Low
TGA	CH, C$\underline{C}$	No	Yes	Med
XRD	CH, C$\underline{C}$ polymorphs	Not investigated		Med
OM	Porosity, phases	Yes	Yes	High
SEM	Porosity, phases	[Yes]	[Yes]	High

When using carbonation data for probabilistic modelling of service life, statistical data are required. Maage and Smeplass [42] proposed to use a normal distribution for carbonation depth in connection with service life prediction. The statistical treatment of the carbonation depths determined by THY (see, Figure 4) suggests that carbonation depths are distributed in two groups for the tested materials and exposure. It was found that if lateral plus top side were plot together and the bottom side separated, each of the groups presented a normal distribution. Greve-Dierfeld and Gehlen [43] also suggested a normal distribution to be used for the carbonation depths, but including all four sides of the sample.

6. CONCLUSIONS

The following conclusions were found:

- The carbonation depth determined by the pH indicator and optical microscopy and the depth of CH depletion determined by TGA are in relatively good agreement when considering the impact of sampling.
- TGA results showed gradual changes in CH and CC. The wider width of the carbonation front detected with TGA compared with the narrower width found using the other techniques can be explained by the observed spatial variation of the carbonation depth averaged in ground samples, but could also be due to kinetics. For the CEM II/B-V mortar, a broader width of the carbonation front is observed compared to CEM I mortar.
- SEM did not allow clear identification of the carbonation depth for the examined material and exposure.
- Using a pH indicator coupled with image analysis provides statistical information on the spatial variation of the carbonation depth
- Carbonation depths in the same sample formed two normally distributed groups of data. Lateral and top sides presented higher values than bottom side.

7. FURTHER RESEARCH

In the continuation of this project, the propagation period will be studied by the use of electrochemistry measurements on embedded steel using the same binders for both accelerated and natural carbonation.

8. ACKNOWLEDGEMENTS

The authors acknowledge the Norwegian Research Council for facilitating the research (NFR project no. 235211/O30: LAVKARBSEM) and the financial support provided by the partners of the LAVKARBSEM project: Heidelberg Technology Center GmbH, Mapei AS, Norbetong AS, Norcem AS, NTNU, Rambøll Engineering AS, SINTEF Byggforsk avd Trondheim, Skanska Norge AS, Spenncon AS. Also, the authors would like to acknowledge Marit Haugen (SINTEF) and Ulla Hjorth Jakobsen (DTI) for their assistance with microscopy, and Tone Østnor (SINTEF) for the assistance with TGA.

9. REFERENCES

[1] Bertolini, L., Elsener, B., Pedeferri, P., Redaelli, E. and Polder, R., "Chapter 5: Carbonation-induced corrosion," in *Corrosion of Steel in Concrete*, Wiley-VCH Verlag GmbH & Co, Weinheim, Germany, 2013, pp. 79-91.

[2] Lagerblad, B., "Carbon dioxide uptake during concrete life cycle – State of the art," Report, Swedish Cement and Concrete Research Institute, Stockholm, 2006.

[3] Sevelsted, T. F. and Skibsted, J., "Carbonation of C–S–H and C–A–S–H samples studied by ^{13}C, ^{27}Al and ^{29}Si MAS NMR spectroscopy," Cement and Concrete Research, Vol. 71, 2015, pp. 56-65.

[4] Papadakis, V. G., Vayenas, C. G. and Fardis, M. N., "Fundamental modelling and experimental investigation of concrete carbonation," Materials Journal, Vol. 88, No. 4, 1991, pp. 363-373.

[5] EN 13295:2003: Products and systems for the protection and repair of concrete structures. Test methods. Determination of resistance to carbonation, 2003.

[6] Norwegian Environment Agency, 2015, http://www.miljodirektoratet.no/no/

[7] Yu, M.-Y., Lee, J.-Y. and Chung, C.-W., "The application of various indicators for the estimation of carbonation and pH of cement based materials," Journal of testing and evaluation, Vol. 38, No. 5, 2010.

[8] Belda, A., De Weerdt, K. and Geiker, M., "Carbonation front characterization pH color indicators," 35th Cement and Concrete Science Conference, Aberdeen, Scotland, 2015.

[9] Vollpracht, A., Lothenbach, B., Snellings, R. and Haufe, J., "The pore solution of blended cements: a review," Materials and Structures, 2015, pp. 1-27.

[10] Plusquellec, G., Geiker, M., Lindgård, J., Duchesne, J., Fournier, B. and De Weerdt, K., "Determination of the pH and the free alkali metals content in the pore solution of concrete: review and experimental comparison," To be submitted to: Cement and Concrete Research, In preparation.

[11] McPolin, D., Basheer, P., Long, A., Grattan, K. and Sun, T., "New Test Method to Obtain pH Profiles due to Carbonation of Concretes Containing Supplementary Cementitious Materials," Journal of Materials in Civil Engineering, Vol. 19, No. 11, 2007, pp. 936-946.

[12] Lothenbach, B., Durdzinski, P. and De Weerdt, K., "Chapter 5: Thermogravimetric Analysis," in *A Practical Guide to Microstructural Analysis of Cementitious Materials*, Ed(s) K. Scrivener, R. Snellings and B. Lothenbach, CRC Press, Boca Raton, United States, 2015.

[13] Lo, Y. and Lee, H. M., "Curing effects on carbonation of concrete using a phenolphthalein indicator and Fourier-transform infrared spectroscopy," Building and Environment, Vol. 37, No. 5, 2002, pp. 507-514.

[14] Chang, C.-F. and Chen, J.-W., "The experimental investigation of concrete carbonation depth," Cement and Concrete Research, Vol. 36, No. 9, 2006, pp. 1760-1767.

[15] Schiessl, P., "Zur Frage de zulässigen rissbreite und der erforder lichen betondeckung im stahlbetonbau- unter besonderer berücksichtigung der karbonatisierung des betongs," PhD thesis, Technical University of Munich, Berlin, 1976.

[16] Tuutti, K., "Corrosion of steel in concrete," PhD thesis, Swedish Cement and Concrete Research Institute, Stockholm, 1982.

[17] Litvan, G. G. and Meyer, A., "Carbonation of Granulated Blast Furnace Slag Cement Concrete During Twenty Years of Field Exposure," American Concrete institue, special publication, Vol. 91, 1986.

[18] Parrott, L. J. and Killoh, D. C., "Carbonation in a 36 year old, in-situ concrete," Cement and Concrete Research, Vol. 19, No. 4, 1989, pp. 649-656.

[19] Campbell, D. H., Sturm, R. D. and Kosmatka, S. H., "Detecting Carbonation," Concrete Technology Today, Vol. 12, No. 1, 1991.
[20] Papadakis, V. G., Fardis, M. N. and Vayenas, C. G., "Hydration and carbonation of pozzolanic cements," ACI Materials Journal, Vol. 89, No. 89, 1992, pp. 119-130.
[21] Möller, J. S., "Measurement of carbonation in cement-based materials," PhD thesis, Chalmers University of Technology, Göteborg, 1994.
[22] Thiery, M., Villain, G., Dangla, P. and Platret, G., "Investigation of the carbonation front shape on cementitious materials: Effects of the chemical kinetics," Cement and Concrete Research, Vol. 37, 2007, pp. 1047-1058.
[23] Villain, G., Thiery, M. and Platret, G., "Measurement methods of carbonation profiles in concrete: Thermogravimetry, chemical analysis and gammadensimetry," Cement and Concrete Research, Vol. 37, No. 8, 2007, pp. 1182-1192.
[24] Castellote, M., Andrade, C., Turrillas, X., Campo, J. and Cuello, G. J., "Accelerated carbonation of cement pastes in situ monitored by neutron diffraction," Cement and Concrete Research, Vol. 38, No. 12, 2008, pp. 1365-1373.
[25] Castellote, M., Fernandez, L., Andrade, C. and Alonso, C., "Chemical changes and phase analysis of OPC pastes carbonated at different CO2 concentrations," Materials and Structures, Vol. 42, 2009, pp. 515-525.
[26] Herrera, R., Kinrade, S. D. and Catalan, L. J. J., "A Comparison of Methods for Determining Carbonation Depth in Fly Ash-Blended Cement Mortars," Materials Journal, Vol. 112, No. 2, 2015, pp. 287-294.
[27] Herterich, J., Black, L. and Richardson, I., "Microstructure and phase assemblage of low-clinker cements during early stages of carbonation," 14th International Congress on the Chemistry of Cement Beijing, 2015.
[28] Leemann, A., Nygaard, P., Kaufmann, J. and Loser, R., "Relation between carbonation resistance, mix design and exposure of mortar and concrete," Cement and Concrete Composites, Vol. 62, 2015, pp. 33-43.
[29] Wu, B. and Ye, G., "Comparative studies of carbonation fronts of cement paste blend with SCMs," 3rd International conference of service life design for infrastructures, Zhuhai, China, 2016.
[30] Shi, Z., Lothenbach, B., Geiker, M. R., Kaufmann, J., Leemann, A., Ferreiro, S. and Skibsted, J., "Experimental and thermodynamic modeling studies on carbonation of Portland cement - metakaolin - limestone mortars," To be submitted to: Cement and Concrete Research, In preparation.
[31] Snellings, R., "Chapter 4: X-Ray Powder Diffraction," in *A Practical Guide to Microstructural Analysis of Cementitious Materials*, Ed(s) K. Scrivener, R. Snellings and B. Lothenbach, CRC Press, Boca Raton, United States, 2015.
[32] Jakobsen, U. H., Personal comunication: "Carbonation characterization by optical microscopy," 2016.
[33] Jakobsen, U. H., Laugesen, P. and Thaulow, N., "Determination of Water-Cement Ratio in Hardened Concrete by Optical Fluorescence Microscopy," American Concrete institue, special publication, Vol. 191, 1999.
[34] Scrivener, K., Bazzoni, A., Gassó, B. M. and Rossen, J. E., "Chapter 8: Electron Microscopy," in *A Practical Guide to Microstructural Analysis of Cementitious Materials*, Ed(s) K. Scrivener, R. Snellings and B. Lothenbach, CRC Press, Boca Raton, United States, 2015.
[35] Berodier, E., Bizzozero, J. and Muller, A. C. A., "Chapter 9: Mercury Intrusion Porosimetry," in *A Practical Guide to Microstructural Analysis of Cementitious Materials*, Ed(s) K. Scrivener, R. Snellings and B. Lothenbach, CRC Press, Boca Raton, United States, 2015, pp. 419-444.

[36] Washburn, E. W., "Note on a method of determining the distribution of pore sizes in a porous material," the National Academy of Sciences of the USA, 1921, pp. 115-116.
[37] Skibsted, J., "Chapter 6: High-Resolution Solid-State Nuclear Magnetic Resonance Spectroscopy of Portland Cement-Based Systems," in *A Practical Guide to Microstructural Analysis of Cementitious Materials*, Ed(s) K. Scrivener, R. Snellings and B. Lothenbach, CRC Press, Boca Raton, United States, 2015.
[38] Galan, I., Andrade, C., Castellote, M., Rebolledo, N., Sanchez, J., Toro, L., Puente, I., Campo, J. and Fabelo, O., "Neutron diffraction for studying the influence of the relative humidity on the carbonation process of cement pastes," Journal of Physics: Conference Series, Vol. 325, 2011.
[39] EN 196-1:2005: Methods of testing cement – Part 1: Determination of strength, 2005.
[40] Belda, A., De Weerdt, K., Hornbostel, K. and Geiker, M., "Investigation of the effect of partial replacement of Portland cement by fly ash on carbonation using TGA and SEM-EDS," International RILEM Conference on Materials, Systems and Structures in Civil Engineering, Lyngby, Denmark, 2016.
[41] Matala, S., "Effects of carbonation on the pore structure of granulated blast furnace slag concrete," PhD thesis, Helsinki University of Technology, Espoo, 1995.
[42] Maage, M. and Smeplass, S., "Third Workshop: Service Life Design of Concrete Structures From Theory to Standardisation," DuraNet, Tromsø, 2001.
[43] Greve-Dierfeld, S. and Gehlen, C., "Performance based deemed-to-satisfy rules," The Fourth International fib-Congress 2014, Mumbai, 2014.

Paper A-II

Effect of carbonation on the pore solution

De Weerdt, Klaartje; Plusquellec, Gilles; Revert, Andres Belda; Geiker, Mette Rica; Lothenbach, Barbara

Submitted to Cement and Concrete Research

Effect of carbonation on the pore solution of mortar

De Weerdt K.[1], Plusquellec G.[1], Belda Revert A.[1], Geiker M.R.[1], Lothenbach B.[1,2]

[1]*Department of Structural Engineering, Norwegian University of Science and Technology (NTNU), 7491 Trondheim, Norway*

[2]*EMPA, Dübendorf, Switzerland*

Email: klaartje.d.weerdt@ntnu.no

Abstract

Understanding the changes in the pore solution upon carbonation is crucial with respect to comprehending the mechanisms of reinforcement corrosion in carbonated mortar or concrete.

In this paper we used Cold Water Extraction (CWE), a rapid leaching method, on profile ground powder from partially carbonated Portland cement and Portland-fly ash cement mortars to study changes in the pore solution composition.

Carbonation decreased the free alkali metal content measured with CWE, which matched with the portlandite profiles determined by thermogravimetry and the carbonation depth detected with pH indicator.

The alkali metal uptake by carbonation products was confirmed by SEM-EDS and thermodynamic modelling. Besides the decrease in the alkali metal concentration in the pore solution upon carbonation, we observed for both binders a considerable increase in chlorine and sulphur concentrations. This can further accelerate corrosion in carbonated concrete.

Keywords

B. pore solution, B. thermodynamic calculations, C. corrosion, C. carbonation, D. blended cement

1 Introduction

Carbonation induced corrosion is one of the major deterioration mechanisms of reinforced concrete. The passive layer formed on the reinforcement in sound concrete turns unstable due to the decrease in pH of the pore solution upon carbonation. During the carbonation process, CO_2 is dissolved in the pore solution as CO_3^{2-} at pH ≥ 9 and HCO_3^- at 6 ≤ pH ≤ 9 [1]. The pH of the pore solution of a standard Portland cement is generally between 12.5 and 14 [2], but decreases in presence of CO_3^{2-}. As a result, hydrates like portlandite ($Ca(OH)_2$) are destabilised while calcium carbonate ($CaCO_3$) precipitates due to its low solubility [3, 4]. Similarly, ettringite is destabilised while gypsum, calcium carbonate and Al hydroxide precipitates [5-7]. Also decalcification of calcium silicate hydrate (C-S-H) occurs [8]; the decrease of its calcium-to-silicon ratio (Ca/Si) leads to an elongation of its silica chains length and increases at the same time its ability to sorb alkali metal ions (Na^+ and K^+). For example, L'Hôpital et al. [9] showed that for a synthetic C-S-H in equilibrium with a 0.1 mol/l KOH solution, an alkali-to-silicon ratio of approx. 0.02 was measured at Ca/Si of 1.5, whereas the alkali-to-silicon ratio increased to 0.26 at Ca/Si of 0.67.

The changes in the solids upon carbonation are accompanied by changes in the pore solution. The concentration of alkali metal ions in the pore solution is expected to decrease with carbonation as more alkalis are sorbed by the decalcified C-S-H compared to non-decalcified C-S-H. The carbonation of ettringite is expected to increase the concentration of sulphates in the solution while the decomposition of C-S-H and potentially Friedel's salt could increase the chloride concentration.

The pore solution composition in carbonated concrete is of particular interest for the corrosion process of the steel reinforcement, both with regard to corrosion initiation and corrosion rate. Even though the pore solution composition might play a major role in understanding corrosion in carbonated concrete, very little data is available [10]. One of the main reasons is that carbonated concrete is generally also exposed to drying resulting in low amounts of free water, which makes it difficult to extract pore solution.

Different methods have been used to analyse the pore solution of paste, mortar or concrete [11]. The most common method is pore water expression (PWE), where a mechanical press is used to squeeze out the pore solution. PWE may not be applicable on samples containing too little free water as e.g. old, dense or dried samples. In these cases, cold water extraction (CWE) can be used as an alternative. CWE is a leaching method during which a powdered sample in mixed

with deionized water [12]. It is however not clear if CWE can be used to determine the free alkali metal content in carbonated concrete. The question remains whether alkali metal ions sorbed on C-S-H are released during CWE.

Mortars with two different types of cement (CEM I and CEM II/B-V) exposed to accelerated carbonation conditions were investigated in this study. To follow the progress of carbonation, the samples were split and sprayed with a pH indicator. Free alkali metal profiles were determined using CWE on profile ground powder. The changes in the phase assemblage were determined using thermogravimetric analysis and SEM-EDS. The experimental findings were compared with a thermodynamic model. The model was further used to predict changes in the pore solution composition upon carbonation.

2 Materials and methods

2.1 Mortars

Mortars were prepared with two cement types, Portland cement (CEM I) and Portland-fly ash cement (CEM II/B-V, 30% fly ash). CEN-standard sand according to EN 196-1 was used. The compositions of the cements and the sand determined by X-ray fluorescence (XRF) are given in Table 1. The mortars were prepared with a water-to-binder (w/b) ratio of 0.55 or 0.40 and apaste-to-sand volume ratio of approx. 0.7. Table 2 shows the mix composition of the mortars.

A mixing procedure based on EN 196-1 was followed. First, the water and the cement were placed in the mixing bowl. The mixer was then immediately started and, after 30 seconds of mixing, the sand was added steadily during the next 30 seconds. Then, the mortar was mixed for 30 seconds and the mixing was stopped for 90 seconds while the mortar was manually homogenized using a spatula. Finally, the mixing continued for 60 additional seconds. Two types of samples were cast:

1) mortar blocks (140x40x160 mm) for carbonation exposure, and

2) cylinders, with 50 mm in diameter and 60 mm in height, which were later cut into disks.

The blocks were casted in steel moulds and the compaction was done using a vibration table. Two 20-mm layers were compacted by applying 5 seconds of vibration for w/b 0.55 and 10 seconds for w/b=0.40 on each layer. The vibration table applied a fixed frequency of 50 Hz and a vertical amplitude 0.65 mm. The moulds were firmly held against the vibrating table during the compaction.

The cylinders were cast in bottles, which were filled in three layers of 20 mm and jolted compacted (30 jolts per layer). After casting, the blocks were covered with plastic and the bottles were sealed. After one day, the blocks were demoulded, sealed in plastic and all the samples were stored at 20 °C for 13 days. Prior to carbonation, each bottle was cut in three disks of 15 mm in thickness to allow complete carbonation of the disks during the exposure period.

After this, the mortar samples were exposed to different exposure conditions, see Table 3. The samples exposed to carbonation were stored for 9 weeks in a climate chamber at 20 °C, 60% RH and 1% CO_2. The reference samples were stored sealed in plastic at 20 °C for 9 weeks. The different curing conditions might have affected the degree of reaction of the cements.

Table 1: Chemical compositions measured by XRF (%wt) and physical characteristics of the two cements, fly ash (provided by the manufacturer) and the sand.

	Sand	FA	CEM I	CEM II/B-V
SiO_2	95.8	56.8	20.4	29.5
Al_2O_3	1.6	24.3	4.77	10.8
Fe_2O_3	0.67	6.90	3.43	4.51
CaO	0.1	4.89	61.71	44.6
MgO	0.07	1.74	2.19	2.01
K_2O	0.66	1.68	0.92	1.06
Na_2O	0.01	0.58	0.51	0.47
SO_3	0	0.64	3.48	3.16
P_2O_5	-	0.80	0.17	0.39
Na_2O Eq.	-	1.68	1.12	1.17
CaO_{free}	-	-	1.59	1.37
Chlorine	-	-	0.04	0.03
LOI*	0.3	-	2.14	2.74
Fly ash	-	-	0	30.3
Blaine [m^2/kg]	-	301	420	501
Density [g/cm^3]	2.66		3.13	2.91

*based on LOI we estimated the CO_2 = 1.14% for CEM I

Table 2: Mix composition of the mortars

w/b	Binder	Sample	Binder (g)	Water (g)	Sand (g)	Paste/sand (volume)
0.55	CEM I	block	2124	1169	6743	0.71
0.55	CEM II/B-V	block	2974	1636	9447	0.73
0.55	CEM I	cylinder (disk)	425	234	1350	0.71
0.55	CEM II/B-V	cylinder (disk)	425	234	1350	0.73
0.40	CEM II/B-V	block	2042	818	5399	0.73

Table 3: Overview of the investigated samples and their exposure conditions

Cement type	CEM I		CEM II/B-V		
w/b	0.55	0.55	0.55	0.55	0.40
Exposure	20 °C 100% RH Wrapped	20 °C 60% RH 1% CO_2	20 °C 100% RH Wrapped	20 °C 60% RH 1% CO_2	20 °C 60% RH 1% CO_2
Type of sample	block & disk	block & disk	block & disk	block & disk	block
Label	CEM I_{ref}	CEM $I_{0.55}$	CEM II_{ref}	CEM $II_{0.55}$	CEM $II_{0.40}$

The “moisture content” of the mortar samples was determined by oven-drying. Pieces of approx. 70 g were retrieved by splitting the carbonated and non-carbonated mortars based on the carbonation detection using a pH indicator. The pieces obtained this way may include fractions of carbonated/non-carbonated mortar due to the spatial variation of the carbonation depth. For each mortar three parallel pieces were analysed, except for the reference mortars were only one piece was used. The pieces were dried for 7 days at 105 °C (the mass loss was lower than 0.025% within 24 hours after 7 days). The amount of pore solution or free water content in the mortar samples ($m_{ps,mortar}$), was calculated with Equation (1):

$$\%m_{ps,mortar} = \frac{m_o - m_{105C}}{m_{105C}} \cdot 100 \quad (1)$$

where m_o is the mass of the piece prior to oven drying (g) and m_{105C} is the mass after drying at 105 °C (g). It should be noted that this method will overestimate the actual amount of free-water, as at 105 °C hydrates such as ettringite and C-S-H are partially decomposed releasing water. On the other hand, a lower temperature would have increased the drying time and might therefore allow further hydration [11].

Table 4 presents the moisture content determined by oven-drying at 105 °C measured 11 weeks after casting. The sealed cured reference samples have a higher moisture content than the non-carbonated zone of the samples exposed to 1% CO_2 and 60% RH. For all three mortars, the carbonated zone has a lower moisture content than the carbonated zone.

Table 4: Amount of pore solution or free water in the mortar samples 11 weeks after casting, $m_{ps,mortar}$, in (%wt) measured by oven-drying (average ± standard deviation).

$\%m_{ps,mortar}$	CEM $I_{0.55}$	CEM $II_{0.55}$	CEM $II_{0.40}$
Sealed (ref)	8.3	8.9	n.d.
Non-carbonated zone	6.1 ± 0.1	6.3 ± 0.2	6.3 ± 0.2
Carbonated zone	4.5 ± 0.4	3.6 ± 0.1	4.6 ± 0.3

n.d.: not determined

2.2 Analytical techniques

Each mortar block was split in five pieces (Fig. 1). The pieces were investigated with different techniques. The pieces (1) and (5) were used to determine the carbonation depth by spraying a freshly split surface with thymolphthalein and phenolphathalein pH indicators. The sides from pieces (2)-(4) were removed (approx. 15 mm) to eliminate the impact from carbonation from the sides. Piece (2) was profile ground and the obtained powder was investigated by thermogravimetric analysis (TGA) and cold water extraction (CWE). A sawn surface of piece (3) was scanned by micro-XRF to determine the elemental maps. On piece (4) the moisture content was determined by oven drying.

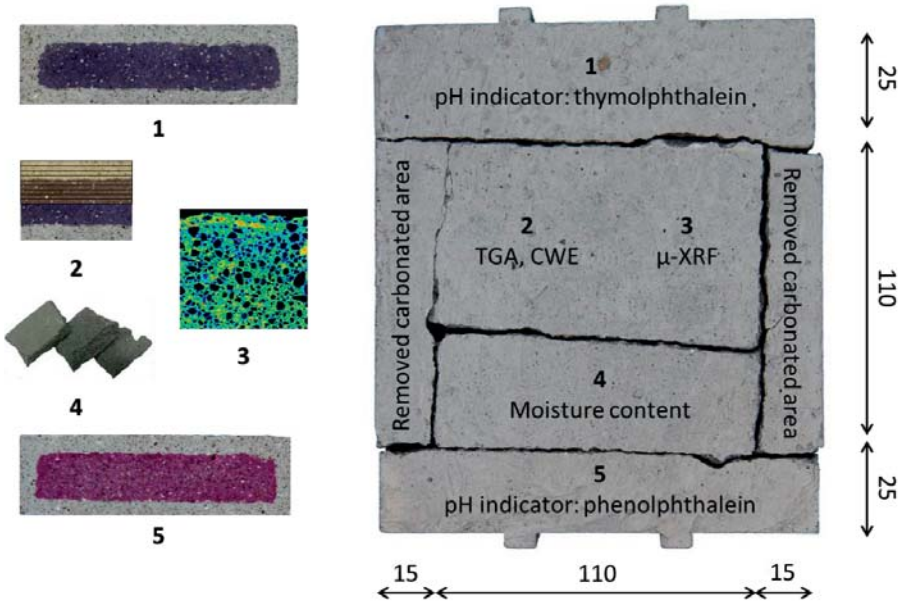

Fig. 1: Investigation program carried out for each mortar block. Methods applied on the different pieces: pH indicator: thymolphthalein (1) and phenolphthalein (5), profile grinding for CWE (also performed on the disks) and TGA (2), micro-XRF (3) and moisture content (4). Dimensions are given in mm.

2.2.1 pH indicator

The carbonation depth was determined by spraying freshly split surfaces with thymolphthalein or by phenolphthalein (1% solution). The solutions were prepared by dissolving 1 gram of each indicator (powder, grade "ACS, Reag. Ph Eur" (VWR)) in a mix of 30 ml of deionized water and 70 ml of ethanol. Thymolphthalein changes from colourless to blue in the pH range of 9 to 10.5, and phenolphthalein changes in the pH range of 8.2 to 9.8. The distribution of the carbonation depth was determined by image analysis as described in [13]. First, pictures of the freshly split samples sprayed with the pH indicators were taken using a Reflex camera fixed to a frame with constant light conditions. Then, the pictures were treated using the freeware Image J as follows: the picture was scaled, the colour threshold was adjusted to differentiate between carbonated and non-carbonated areas, and the carbonated depth distribution was obtained on the top side of the samples over a length of 100 mm and avoiding the corners (sixty measuring points per sample). The carbonation depth measurements obtained using thymolphthalein are presented in Box-and-whisker plots. The solid line in the box indicates the median value, the box indicates the first and third quartile and the whiskers show the lowest and highest

carbonation depth measurements. The average carbonation depth value is indicated by the grey columns.

2.2.2 Thermogravimetric analysis

Profile grinding was performed with different step sizes depending on the carbonation depth determined with the pH indicators. 1-mm steps were used in the carbonated zone and broader steps, up to 4-mm, in the non-carbonated zone. For the reference samples grinding steps of 3 mm were used. After grinding, the particles size was checked using an 80 µm sieve. If needed, the powder was ground one more time with a mortar by hand until all the material passed through the sieve. This was carried out as quick as possible to limit additional carbonation.

The powder was analysed by TGA with a TGA/DSC 3+ from Mettler Toledo to identify changes in the phase assemblage and to quantify changes in the amount of portlandite (CH) and calcium carbonate (C$\underline{\text{C}}$) upon carbonation. Approx. 300 mg of powder was placed in a 600 µl alumina crucible. The weight was monitored while the powder was heated from 40 °C to 900 °C at 10 °C/min and the sample chamber was purged with N_2 at 50 ml/min in accordance with the guidelines from [14].

Phase changes upon carbonation were identified by comparing the DTG-curves (first derivative of the thermogravimetric curves) of the profile ground sections. The amount of portlandite and calcium carbonate in the sections are presented as a percentage of the dry mass (i.e. the mass of the dry and decarbonated sample at 800 °C) and calculated according to Equations (2) and (3). The temperatures indicated here are only informative – the exact boundaries were determined based on the derivative curves.

$$\text{CH} = \frac{m_{450} - m_{550}}{m_{800}} \cdot \frac{74}{18} \tag{2}$$

$$\text{C}\underline{\text{C}} = \frac{m_{550} - m_{800}}{m_{800}} \cdot \frac{100}{44} \tag{3}$$

where m is the weight loss at the indicated temperature, 74 g/mol is the molar mass of $Ca(OH)_2$, 18 g/mol is the molar mass of H_2O, 44 g/mol is the molar mass of CO_2, and 100 g/mol is the molar mass of $CaCO_3$.

2.2.3 Cold water extraction

The remaining powder was used to measure the free alkali metal content by CWE. 5, 10 or 20 g of powder (depending on the amount of powder left) were mixed with 5, 10 or 20 g of deionized water (resistivity of 18.2 MΩ.cm) and stirred for 5 min. The suspension was then

filtrated for approx. 1 minute using a water pump and a Grade 40, 8 µm particle retention Whatman cellulose filter. Preliminary investigations showed no significant uptake of ions by the filter and no release/adsorption of alkali metals from the sand used [11]. Finally, each solution was diluted 10 times with deionized water and acidified with HNO_3 in order to obtain a final HNO_3 concentration of 0.1 mol/l. The solutions were analysed for Na and K using Inductively Coupled Plasma Mass Spectrometry (ICP-MS).

Based on the ICP-MS results, the free alkali metal content was calculated using Equation (4) :

$$X = [X]_{ps+extr} \cdot \frac{V_{ps} + V_{extr}}{m_{sample}} \quad (4)$$

where X is either the free Na or K content in the sample (mmol/kg), $[X]_{ps + extr}$ is the concentration of the element in the filtrate obtained after CWE (mmol/L), V_{ps} the volume of pore solution in the sample in L (considered equal to m_{ps} see Table 4), V_{extr} the volume of deionized water that is added during CWE (L) (considered equal to m_{extr}), and m_{sample} is the mass of the sample (kg).

The concentration of the alkali metals in the pore solution was calculated with Equation (5):

$$[X]_{ps} = [X]_{ps+extr} \cdot \frac{m_{ps} + m_{extr}}{m_{ps}} \quad (5)$$

where $[X]_{ps}$ is the alkali metal concentration in the pore solution in (mmol/L).

2.2.4 SEM-EDS

Polished sections were prepared according to [15] and carbon coated. SEM-EDS point analysis was performed using a JEOL JXA – 8500F Electron Probe Micro analyzer and a Hitachi S-3400N equipped with an Oxford EDS at an accelerating voltage of 15 kV. EDS point analysis were performed to investigated the composition of the reaction products as described in [16]. The points were manually selected on the outer hydration products in carbonate and non-carbonated mortar avoiding unreacted fly ash, clinker grains and sand. During SEM-EDS point analysis a volume of approx. 1 μm^3 comprising a combination of different phases is analysed. In order to identify phases, the results are expressed as molar ratios. In a dot plot, the data point will be found in between the ideal stoichiometry of the phases it comprises.

2.2.5 µXRF

Sawn mortar samples were investigated by µXRF analysis using a M4 Tornado from Bruker equipped with an Ag X-ray tube and two SDD detectors. Each sample was mapped with a pixel size of 40 µm and an analysis time of 2 ms/pixel. Contrary to CWE which only measures the free alkali metals present in the pore solution, the elemental analysis by µXRF considers the entire sample, i.e. pore solution and solid phase. First, the samples were mapped. We needed to differentiate between paste and sand as the sand contained K rich particles. We did so using a phase recognition tool of the µXRF based on the calcium map. Areas of approx. 200 μm^2 were selected for elemental analysis in the paste phase at different depths from the exposed surface. The results are presented as molar ratio profiles, in this case K/Ca ratio, due to the lack of calibration on a similar matrix. The results concerning sodium content are not presented here because it is a too light element to be measured with a good accuracy, using the applied settings.

2.2.6 Thermodynamic modelling

Thermodynamic calculations were carried out using the Gibbs free energy minimization software GEMS 3.5 [17, 18], which is a geochemical modelling code that computes equilibrium phase assemblages and speciation in complex chemical systems. The general thermodynamic database [19, 20] was expanded with the Cemdata18 database [21], which contains solubility products of solids relevant for cementitious systems. The data-set includes thermodynamic data for common cement minerals such as ettringite (AFt) and calcium aluminate ferrite hydrate monophases (AFm), hydrotalcite, hydrogarnet, zeolites and C–S–H phases. The C–S–H phases were modelled using the CSHQ model developed by Kulik [22], which is based on a continuous solid solution between four C-S-H end-members with different Ca/Si ratios resulting in C-S-H phases with Ca/Si ratios between 0.67 to 1.6. The formation of an ideal solid solution between Friedel's salt and monocarbonate was considered as detailed in [23]. Data for Na- and Ca-containing zeolites were taken from Lothenbach et al. [24], and completed with data for K-containing zeolites (Phillipsite(K), Clinoptilolite(K) and Merlinoite(K)) and Phillipsite(Na) using the solubility products provided by [25]. The formation of magnesite, dolomite, quartz, and thaumasite was suppressed in the modelling due to their slow formation kinetics at ambient temperature.

The activity coefficients of the aqueous species y_i were computed with the built-in extended Debye-Hückel equation with common ion-size parameter a_i of 3.67 Å for KOH solutions and common third parameter b_y according to Equation (6)

$$\log \gamma_i = \frac{-A_y z_i^2 \sqrt{I}}{1 + B_y a_i \sqrt{I}} + b_y I \quad (6)$$

where z_i denotes the charge of species *i*, I the effective molal ionic strength, b_y is a semi-empirical parameter (~0.123 for KOH electrolyte at 25°C), and A_y and B_y are P,T-dependent coefficients. This activity correction is applicable up to approx. 1 M ionic strength [26].

For the modelling, mortar recipes normalised to 100 g of cement were used, the masses are summarised as m_{cem}, m_{water} and m_{sand} in Table 5. For the mortars exposed to 100% relative humidity (RH), the total amount of water added to the mix was used for the calculations, i.e. 55 or 40 g water per 100 g cement. For the samples exposed to 1% CO_2 and a relative humidity of 60%, part of the moisture was lost due to drying. Thus the total mass of water (bound and free) in the non-carbonated mortar samples exposed to 60%RH, $m_{water,60\%RH}$, was calculated as follows:

$$m_{water,60\%RH} = m_{o,60\%RH} - m_{tot,dry} \quad (7)$$

where $m_{o,60\%RH}$ is the mass of the mortar after exposure to 60% RH and $m_{tot,dry}$, the dry mass of the mortar both relative to 100 g of cement.

In order to determine $m_{o,60\%RH}$, using the measured $\%m_{ps,mortar,60\%RH}$ in Equation (8) (rearranged Equation (1)), we need to know the amount of bound water, which was calculated from the mass of the mortar at 105 °C relative to 100 g cement.

$$m_{o,60\%RH} = \frac{m_{105C}}{1 - \%m_{ps,mortar,60\%RH}} \quad (8)$$

Assuming that the sealed and exposed samples have the same amount of bound water, the m_{105C} per 100 g of cement can be calculated based on the amount of pore solution measured in the sealed samples, $\%m_{ps,mortar,sealed}$, using Equation (9).

$$m_{105C} = \frac{m_{tot}}{1 + \%m_{ps,mortar,sealed}} \quad (9)$$

where m_{tot} is the total mass of the sealed mortar sample relative to 100 g of cement (g) and $\%m_{ps,mortar,sealed}$ is the mass percentage of pore solution in the sealed mortar samples determined by drying (%) see Table 4.

Table 5: Calculations for the input of water in the GEMS files.

	CEM $I_{0.55}$	CEM $II_{0.55}$	CEM $II_{0.40}$
m_{cem} (g)	100	100	100
m_{water} (g)	55	55	40
m_{sand} (g)	317	318	264
m_{tot} (g)	473	473	404
$m_{tot,dry}$ (g)	417	418	364
$\%m_{ps,mortar,sealed}$	8.3%	8.9%	8.9%
m_{105C} (g)	436	434	371
$\%m_{ps,mortar,60\%RH}$	6.1%	6.3%	6.3%
$m_{o,60\%RH}$ (g)	465	463	396
$m_{water,60\%RH}$ (g)	47	46	32

The $m_{o,60\%RH}$ obtained with the above described calculations are given in Table 5. Thus upon exposure to 60% RH the amount of water in the system was reduced from 55 to 47 g for CEM $I_{0.55}$, from 55 to 46 g for CEM $II_{0.55}$, and from 40 to 32 g for CEM $II_{0.40}$.

When modelling the carbonation of the CEM I mortars, complete hydration was assumed for the Portland cement, while for the 30% fly ash in the CEM II mortar, a reaction degree of 20% of the fly ash was used after 1 month [27], and complete hydration of the Portland clinker.

To simulate the effects of accelerated carbonation on the hydrate assemblage, the hydrated CEM I and CEM II were virtually titrated with varying volumes of dry synthetic air containing 1% CO_2, as described in detail in [28, 29]. The modelling was performed at 20°C and a pressure of 1 atm. The amounts of CO_2 were varied from 0 g to 40 g per 100 g cement in the calculations, which is equivalent to a variation from 0 L to 2222 L of CO_2 containing air per 100 g of cement. This allows predicting the progressive changes in solid and solution composition and porosity and is used to mimic the ingress of CO_2 assuming that the surface of the mortar is fully carbonated and centre of the mortar is not carbonated. The uptake of alkali metals by the C-S-H phase was taken into account by employing distribution ratios, R_d in (ml/g), to describe the

partitioning of alkali metals between C-S-H and solution as a function of the alkali metal concentration in the solution according to Equation (10):

$$R_d = \frac{c_s \cdot w}{c_d \cdot s} \quad (10)$$

where c_s corresponds to the alkali metal concentration in the solid phase (mol/l), c_d to the alkali concentration in the solution (mol/l) and w/s is the water/solid ratio in ml/g as described in more detail in [30]. The same R_d values were used for both Na and K and a continuous increase of the R_d value from 0.45 ml/g at Ca/Si = 1.62 to R_d = 6.7 ml/g at Ca/Si = 0.67 was considered based on the experimental data published by Hong and Glasser [31]. This simplified approach has been observed to predict alkali metal concentration in the pore solution satisfactorily [30, 32, 33], although it might somewhat over predict alkali metal binding to C-S-H.

3 Results

3.1 Carbonation depth by pH indicators

Fig. 2 presents the carbonation depth distribution measured on the thymolphthalein sprayed samples (colour change between pH 9.3 – 10.5). Similar carbonation depths were measured with phenolphthalein (colour change between pH 8.2 – 10). This is in line with observations in [34] where the similar materials and exposure conditions were used. The mortar containing CEM I presented a higher carbonation resistance compared to the CEM II with the same w/b ratio (0.55). The CEM II with w/b 0.40 presented the highest carbonation resistance.

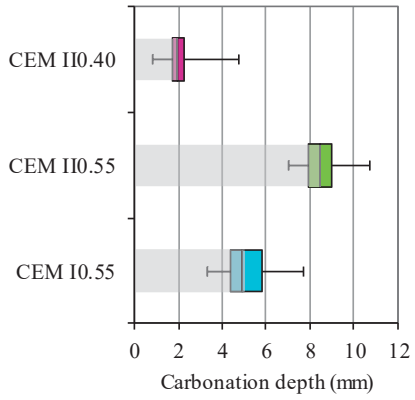

Fig. 2: Box-and-whisker plot for the carbonation depth distribution for the investigated mortars using thymolphtalein pH indicator.

3.2 Measured changes in the hydrated assemblage upon carbonation

Fig. 3 shows the first derivative of the thermogravimetric (DTG) curves as a function of the temperature for the different profile ground sections of the carbonated CEM $I_{0.55}$, CEM $II_{0.55}$ and CEM $II_{0.40}$ mortars.

For CEM $I_{0.55}$, the DTG curves of the non-carbonated sections, such as 10-14 mm or 14-16 mm, show decomposition peaks of portlandite, C-S-H, ettringite and monocarbonate. Upon carbonation, i.e. moving towards the outermost sections, there is a clear gradual increase in the weight loss peak associated with carbonates as well as changes in the hydration products. When comparing the outermost sections such as 0-3 mm and 3-4 mm with the non-carbonated sections, a decrease in the peaks associated with portlandite, C-S-H and ettringite is observed. The remaining weight loss peaks in the temperature range from 100 to 400 °C in the carbonated sections might indicate the presence of hemi-hydrate or gypsum (typical weight loss 100-130 °C), strätlingite (around 200 °C), or zeolite-like phases such as phillipsite (100-200 °C) or natrolite (300 - 350 °C) [14, 24].

The phase changes observed for the CEM $II_{0.55}$ and CEM $II_{0.40}$ samples are similar to the changes described above for the CEM $I_{0.55}$ sample. The main difference is the presence of less portlandite in the non-carbonated sections and slightly higher monocarbonate content in the CEM II samples compared to the CEM I sample. The presence of fly ash diluted the clinker and the pozzolanic reaction of the fly ash consumed portlandite and provided additional aluminates to form monocarbonate [2, 11, 27]. The carbonated sections of all investigated mortars have very similar DTG curves, besides that a little shoulder of remaining portlandite in the outermost section of the CEM I sample whereas no remaining portlandite was observed for the CEM II samples.

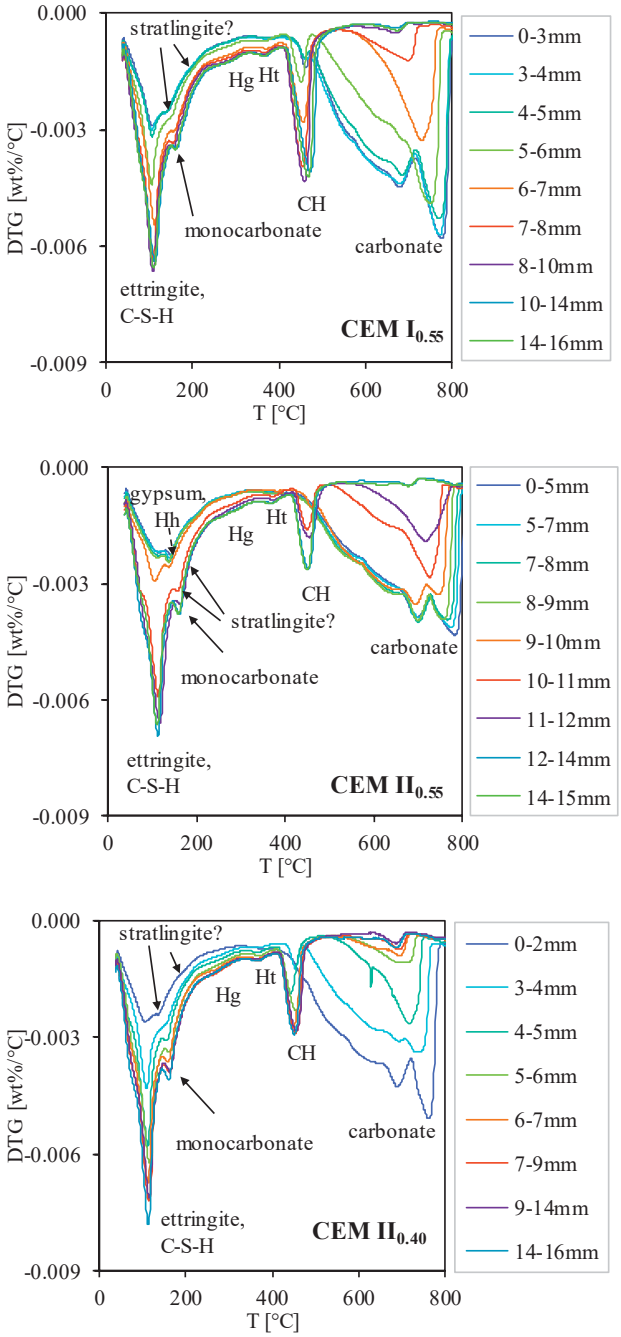

Fig. 3: The DTG curves for the profile ground sections of the CEM $I_{0.55}$, CEM $II_{0.55}$ and CEM $II_{0.40}$ mortars exposed to carbonation. The decomposition peaks of the following phases are indicated: ettringite, C-S-H, gypsum, hemihydrate (Hh), monocarbonate, strätlingite, hydrogarnet (Hg), hydrotalcite (Ht), portlandite (CH) and carbonates.

Fig. 4 presents the amount of calcium carbonate (C$\underline{C}$) and portlandite (CH) obtained by TGA on the profile ground sections of the mortar samples as a function of the depth.

Some CH and small amounts of C$\underline{C}$ (approx. 4%) were detected in the reference samples (CEM I_{ref} and CEM II_{ref} - indicated by the not filled symbols). This is due to the presence of limestone in the cement as indicated by the high loss on ignition reported in Table 1. The amount of CH and C$\underline{C}$ in the reference samples were found to be approx. constant over the entire depth in the reference samples.

In the samples exposed to carbonation, the CH and C$\underline{C}$ content varied as a function of depth. A clear increase in the amount of C$\underline{C}$ was found in the carbonated surface zone while no or very little CH was detected. In Fig. 4 the carbonation depth determined by pH indicator (Fig. 2 from first to the third quartile) is represented by the dashed lines. This pH decrease coincides more or less with the zone in which the C$\underline{C}$ content drops and CH content increases in agreement with the observations reported in [34]. There are some differences, however, in the depth determined by the pH indicator and the CH and C$\underline{C}$ profiles in samples CEM $II_{0.55}$ and CEM $II_{0.40}$, which could be due to the spatial variation of the carbonation front in the individual samples and to the sampling techniques. The non-carbonated zones have in all cases similar amounts of CH and C$\underline{C}$ compared to the reference samples.

For the CEM I mortar, the exposure conditions (sealed (Ref) or accelerated carbonation (0.55)) do not seem to influence considerably the degree of clinker reaction as the CH content is similar. However, for the CEM II mortar, sealed curing (Ref CH) resulted in a lower CH content compared to the mortars exposed to accelerated carbonation (0.55 – CH), indicating that fly ash has reacted slightly more and consumed more CH under the sealed curing conditions.

As mentioned above the non-carbonated CEM II mortars contain less CH than the CEM I mortar due to the clinker dilution by fly ash and the pozzolanic reaction of the fly ash [2, 11, 27]. The lower CaO content in CEM II (see Table 1) could also explain the lower C$\underline{C}$ content upon carbonation for the CEM II mortars, although differences in the degree of clinker reaction also affect the amount of calcium carbonate formed as shown in [34].

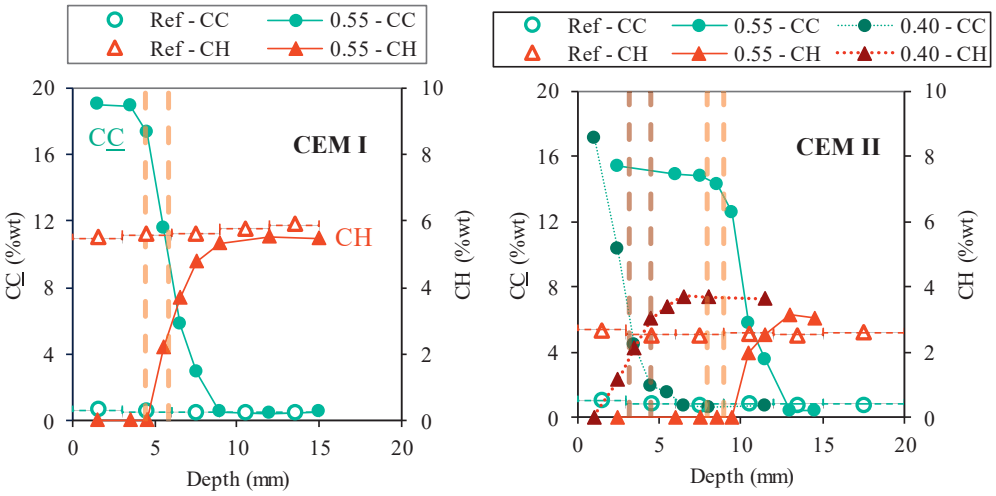

Fig. 4: The portlandite (CH) and calcium carbonate (C$\underline{C}$) profiles for a) the CEM I mortars and b) the CEM II mortar. The marked area corresponds to the carbonation depth measured with thymolphthalein (first and third quartiles of the box-and-whisker plot (Fig. 2)).

3.3 SEM/EDS data

Fig. 5 shows the SEM-EDS dot plots for carbonated and non-carbonated CEM $I_{0.55}$ mortar. Fig. 5 a) is the conventional SEM-EDS plot showing the Al/Ca molar ratio versus the Si/Ca ratio. The data confirms the presence of C-S-H, CH and AFm phases in non-carbonated CEM I mortar as data points can be found in between the ideal stoichiometry of these phases. The major part of the EDS points of carbonation products collect around lower Si/Ca ratios compared to the non-carbonated C-S-H. This seems odd as carbonation causes decalcification of the C-S-H resulting in an increasing the Si/Ca ratio. The observed lowering of the Si/Ca ratio has observed previously by [16] and has been attributed to the fine intermixing of the decalcified C-S-H and the precipitated calcium carbonate.

For the other graphs in Fig. 5, the horizontal axis is kept the same as in Fig. 5 a), while different molar ratios are shown on the vertical axes. This allows us to compare the effect of carbonation on C-S-H. In Fig. 5 b) and c) the vertical axes are replaced by K/Si and Na/Si molar ratios, which allows the comparison of the alkali metal uptake by the reaction products. The data points of reaction products upon carbonation shift upwards relative to the points related with C-S-H in the non-carbonated mortar, indicating a higher K and Na uptake by the carbonation products. Fig. 5 d) shows that the Al uptake in the carbonation products is similar or slightly higher compared to the Al-uptake in the C-S-H. Sulfur uptake in C-S-H is similar in the

carbonated as in the non-carbonated mortar as shown in Fig. 5 e), while Fig. 5 f) shows a lower Cl uptake by the carbonation products compared to C-S-H in the not-carbonated mortar.

Fig. 6 shows the SEM-EDS dot plots for carbonated and non-carbonated CEM $II_{0.55}$ mortar. It should be noted that fewer points were analyzed compared to the CEM I mortar. Both the Si/Ca and Al/Ca ratio of the C-S-H in the CEM II mortar and its alkali metal uptake are higher compared to the C-S-H in the CEM I mortar, as reported previously [27]. The composition after carbonation, however, is similar in both mortars.

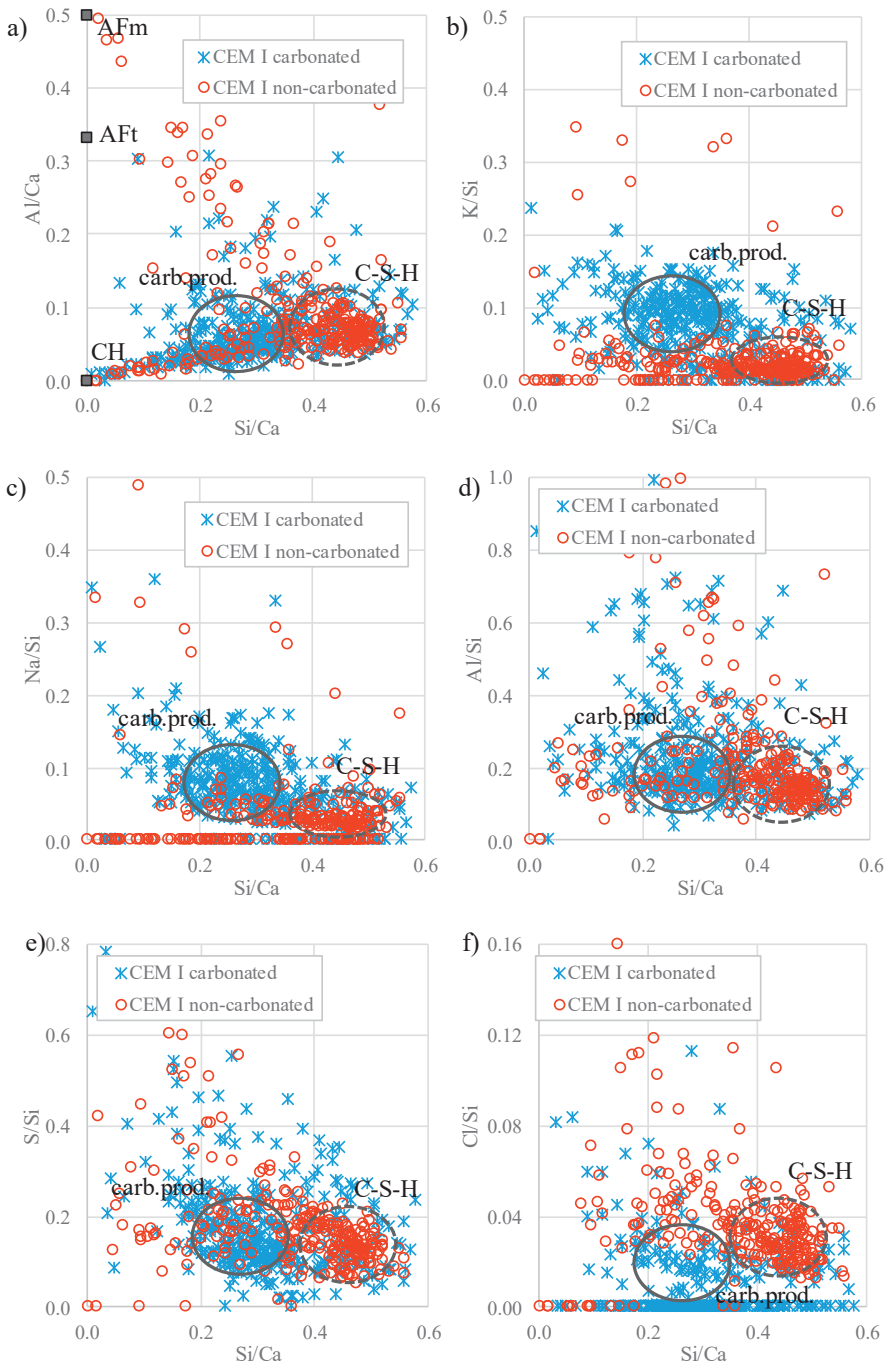

Fig. 5: SEM-EDS dot plots for carbonated and non-carbonated CEM $I_{0.55}$ mortar, showing the molar ratio of a) Al/Ca, b) K/Si, c) Na/Si, d) Al/Si, e) S/Si and f) Cl/Si in function of the Si/Ca molar ratio. C-S-H (dotted circle) and carbonation products (full circle) are indicated as a guide for the eye.

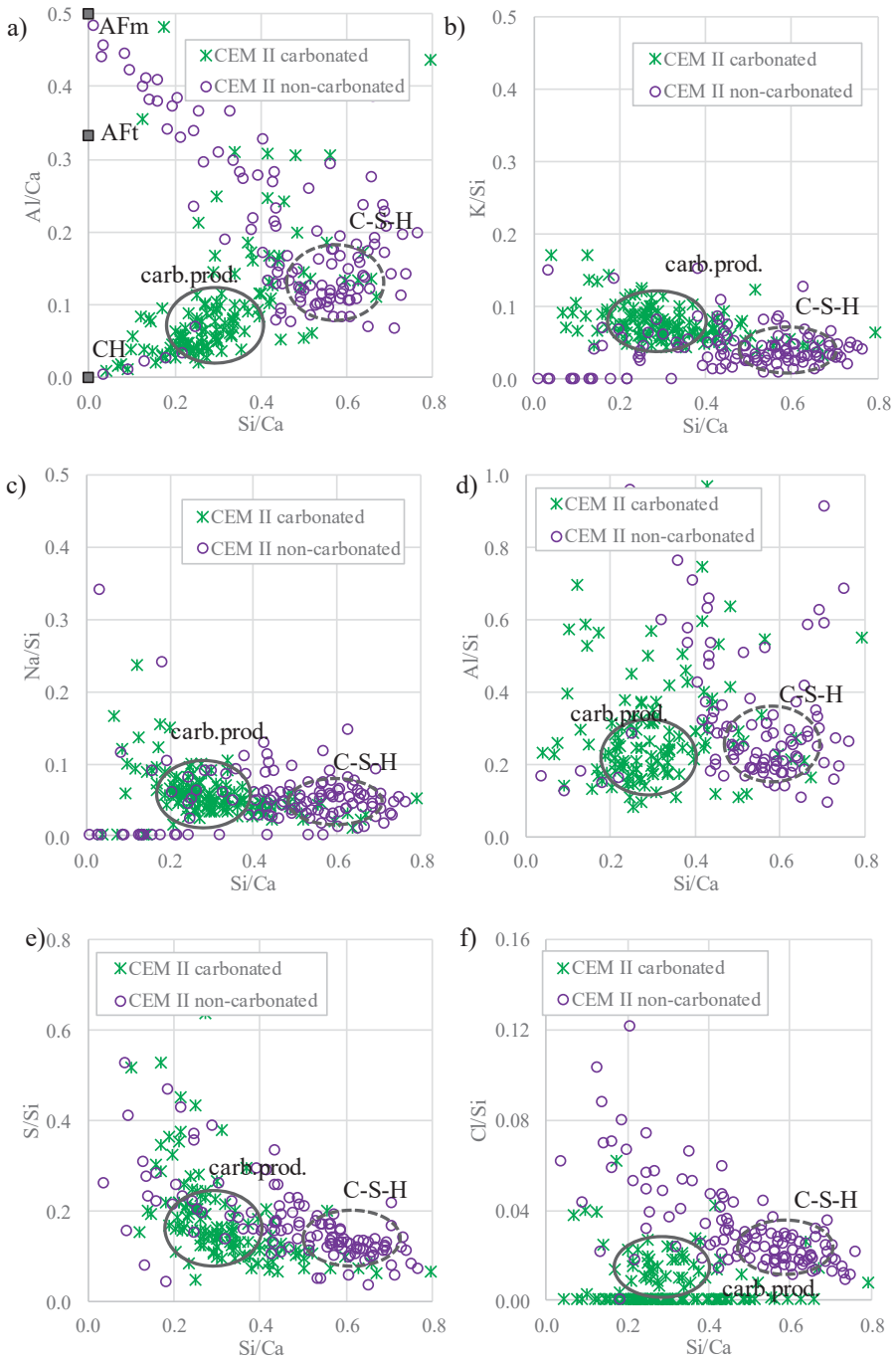

Fig. 6: SEM-EDS dot plots for carbonated and non-carbonated CEM $II_{0.55}$ mortar, showing the molar ratio of a) Al/Ca, b) K/Si, c) Na/Si, d) Al/Si, e) S/Si and f) Cl/Si in function of the Si/Ca molar ratio. C-S-H (dotted circle) and carbonation products (full circle) are indicated as a guide for the eye.

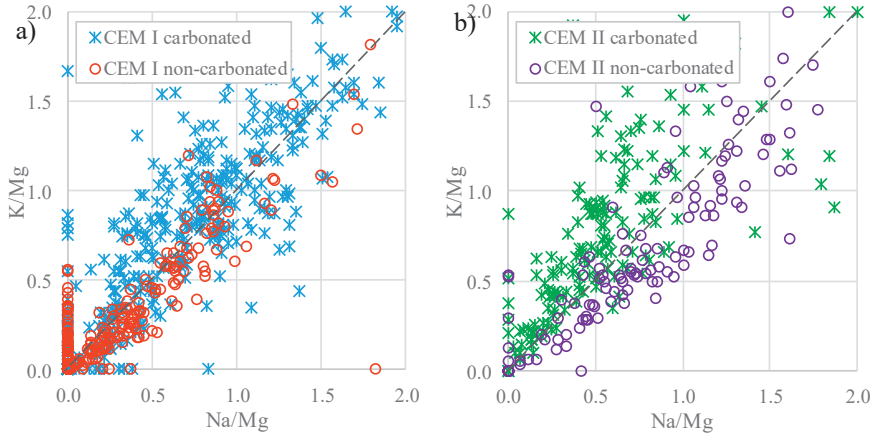

Fig. 7: SEM-EDS dot plots of K/Mg molar ratio in function of Na/Mg molar ratio for carbonated and non-carbonated CEM $I_{0.55}$ and CEM $II_{0.55}$ mortar.

In Fig. 7, the effect of carbonation on potassium and sodium uptake by the solid phases is investigated. Potassium and sodium are plotted against Magnesium to assess whether there is a correlation between the potassium and sodium and whether preferences change upon carbonation. The element magnesium was chosen as denominator as it is present in the cement only (see Table 1) in contrast to for example silicon, which is present both in the cement and the aggregates. Magnesium is finely dispersed such that it is found in low levels in most point analyses. In addition, magnesium is predominantly present as unreacted MgO or as hydrotalcite, both phases are not expected to interact with alkalis such that magnesium can be considered as an independent element.

From Fig. 7 it can be seen for both CEM I and CEM II, that similar amounts of sodium and potassium are present in the solids of the non-carbonated mortar even though the cement contains 15 molar-% more potassium than sodium (Table 1). In the carbonated mortars, a shift towards higher levels of potassium is observed, in particular for the CEM II, which indicates the presence of somewhat more potassium in the solids.

3.4 Measured total potassium profiles

Fig. 8 shows the K/Ca profiles obtained in the paste phase of the mortars by µXRF on cut samples. For the reference mortars, the K distribution is more or less homogeneous within the paste. The level of the K/Ca molar ratios are in the range of what would be expected based on the XRF compositions of the cements (Table 1), 0.02 for CEM I and 0.03 for CEM II. After exposure to carbonation, a redistribution of K can be observed: the carbonated surfaces present a higher K/Ca ratio than the inner part of the samples. For the CEM I mortar a clear drop in the

K/Ca ratio is observed at approx. 5 mm inwards from the surface, which coincides with the carbonation depth determined by the pH indicator. Similarly, a drop in the K/Ca ratio is observed at around 10 mm for the CEM $II_{0.55}$ mortar, which is also in line with the depth given by the pH indicator. For CEM $II_{0.40}$ the carbonation depth is limited and therefore only in the outermost section an increase in the K/Ca ratio is observed.

The increase in K content towards the exposed surface in the carbonated samples is most likely caused by drying, leading to transport of moisture and thereby also ions from the core of the sample towards the surface. Near the surface the relative humidity will drop below a certain level causing the ions to precipitate and leading to an accumulation of ions near the surface. This phenomena is known as wick action [35]. As the increase in K at the carbonated surface is not observed by CWE as discussed below, the accumulated K near the surface indicates an increase of K in the solid phases.

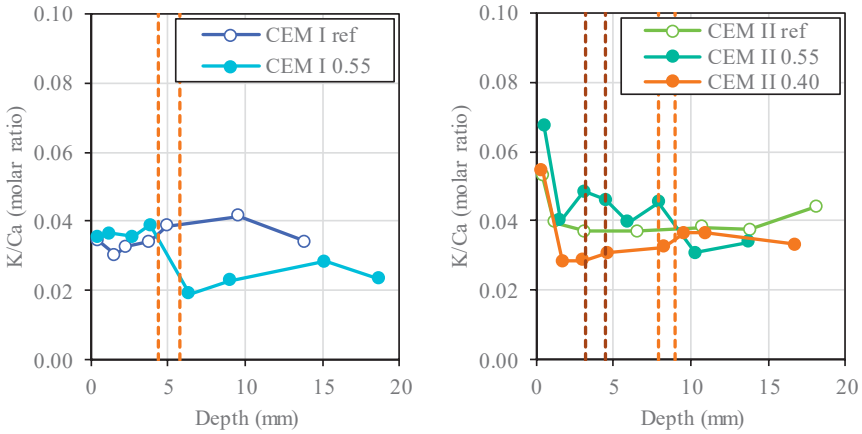

Fig. 8: K/Ca profiles obtained by µXRF a) on the CEM I mortars exposed to carbonation (CEM I 0.55) or sealed cured (CEM I ref), and b) on the CEM II mortars exposed to carbonation (CEM II 0.55 and CEM II 0.40) or sealed cured (CEM II ref). The dotted lines indicate the carbonation depth determined by the pH indicator.

3.5 Measured free alkali metal profiles

Fig. 9 presents the free alkali metal profiles obtained by CWE, i.e. the alkalis present in solution and easily extractable, for the CEM I and CEM II mortars. The carbonation depths measured with the pH indicator are also marked.

For both reference samples, CEM I_{ref} and CEM II_{ref}, the free alkali metal content does not vary with the depth. The free K content determined by CWE is higher than the free Na content for both samples in agreement with the higher K than Na content in the cements (Table 1).

It should be noted that even deepest points in the non-carbonated zone exhibit lower free alkali metal contents than the reference samples. The concentrations of free Na and K in the pore solution in (mmol/L) are compiled in Appendix 1. As the concentrations have been calculated based on the results obtained by CWE in mmol/kg using Equation (5) the values presented in Appendix 1 strongly depend on the measurement of the free water content as given in Table 4.

For the samples exposed to accelerated carbonation, CEM $I_{0.55}$, CEM $II_{0.55}$ and CEM $II_{0.40}$, we can observe a decrease of the free alkali metal content towards the surface indicating an increased binding of alkalis by the solid phases. The lower end of the CWE profiles systematically coincide with the carbonation depths measured with the pH indicators and gives thus the same ranking regarding carbonation resistance: CEM $II_{0.55}$ < CEM $I_{0.55}$ < CEM $II_{0.40}$. In contrast to the not-carbonated areas, less free K is observed in the carbonated zone indicating an increased uptake of K in the solid phase in agreement with SEM-EDS and μXRF data.

Fig. 10 compares the free alkali metal content obtained by CWE on the outer- and innermost sections of the carbonated blocks (CEM $I_{0.55}$ and CEM $II_{0.55}$ blocks) and non-carbonated (CEM I_{ref} and CEM $II_{ref,}$ blocks) with results obtained on sealed non-carbonated disks and fully carbonated mortar disks of both CEM I and CEM II mortar (for details see Table 3). Comparable free alkali metal contents were obtained for the selected area of the block samples and the disks as expected, only a slightly higher alkali metal content was found in the non-carbonated CEM II/B-V disks compared to the blocks. On the disks samples, in addition the free sulphate and chloride content was determined by CWE. The results, shown in Fig. 11 indicate the release of sulphates and chlorides into the pore solution upon carbonation, which is consistent with the observed destabilisation of ettringite and AFm-phases during carbonation. Appendix II summarises the free Na, K, S and Cl concentrations retrieved on the mortar disks.

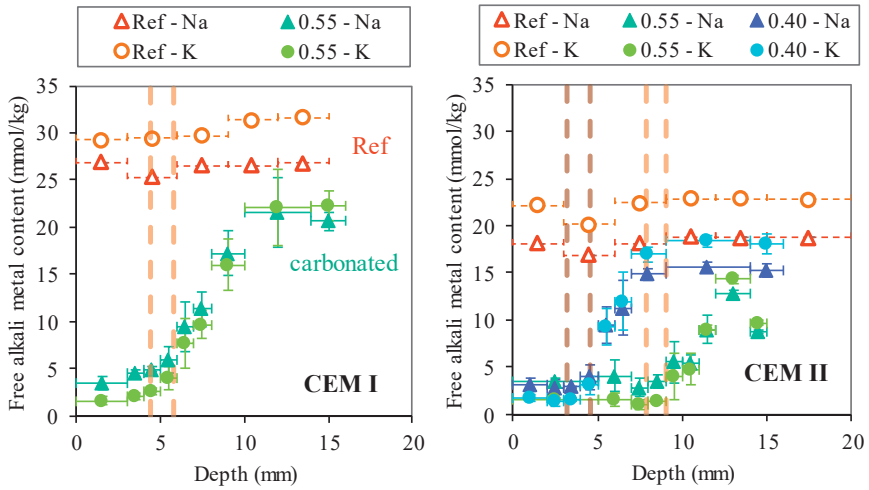

Fig. 9: Free alkali metal profiles obtained by CWE for a) the CEM I mortar exposed to carbonation (0.55–Na and K for CEM $I_{0.55}$) and the sealed cured reference mortar (Ref-Na and K for CEM I_{ref}), and b) the CEM II mortars (w/c 0.40 and 0.55) exposed to carbonation (0.55 and 0.40-Na and K for CEM $II_{0.55}$ and CEM $II_{0.40}$) and the sealed cured reference mortar (Ref-Na and K for CEM II_{ref}). The horizontal bars represent the grinding step and the vertical error-bars the standard deviation based on three measurements. The marked area corresponds to the carbonation depth measured with thymolphthalein (first and third quartiles of the box-and-whisker plot (Fig. 2)).

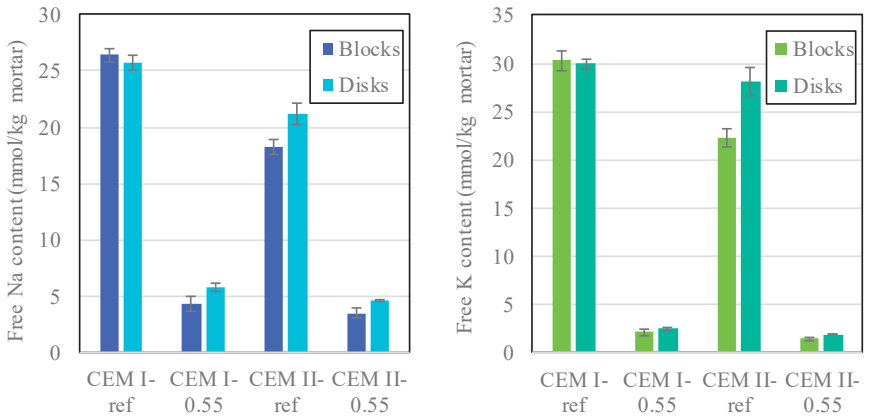

Fig. 10: Free alkali metal obtained by CWE from blocks and disk samples: CEM I mortar exposed to carbonation (CEM $I_{0.55}$) and the sealed cured reference mortar (CEM I_{ref}), and the CEM II mortars exposed to carbonation (CEM $II_{0.55}$) and the sealed cured reference mortar (CEM II_{ref}). Error bars represent standard deviation

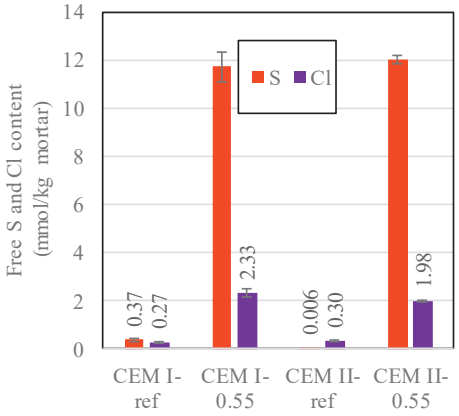

Fig. 11: Free sulphate and chloride content obtained by CWE from disk samples: the sealed cured reference mortar (CEM I_{ref}), CEM I mortar exposed to carbonation (CEM $I_{0.55}$), the sealed cured reference mortar (CEM II_{ref}) and the CEM II mortars exposed to carbonation (CEM $II_{0.55}$). Error bars represent standard deviation.

3.6 Modelling of changes in phase assemblage due to carbonation

3.6.1 Predicted phase changes

Fig. 12 shows the calculated changes in the phase assemblage as carbonation progresses in the cement paste of the CEM I and CEM II mortar in an environment containing 1% CO_2.

The top graphs of Fig. 12 shows the volume of the solids phases in the cement paste in (cm^3/kg dry mortar). In the non-carbonated paste of the CEM I mortar (displayed on the right hand side of the graph), the presence of C-S-H, portlandite, and ettringite is predicted plus minor quantities of monocarbonate, hydrotalcite and siliceous hydrogarnet. This is in agreement with the SEM-EDS (Fig. 5) and TGA data (Fig. 3). The predicted solid phases in the non-carbonated CEM II mortar contain similar phases as the CEM I mortar except for the unreacted fly ash. In addition, less portlandite and ettringite is predicted and more monocarbonate and C-S-H which is in agreement with the TGA data (Fig. 3).

The changes in the solid phases for CEM I and CEM II mortar upon carbonation are similar. In the presence of CO_2, portlandite is calculated to be the first phase to carbonate and convert to calcite, followed by C-S-H, which progressively decalcifies. This has also been observed experimentally by ^{29}Si-NMR of C-S-H phases exposed to carbonation [8]. The initial decalcification of C-S-H is accompanied by a decrease of the calculated pH to approximately 13. As carbonation continuous monocarbonate and siliceous hydrogarnet react with CO_2 (in the equations shown as H_2CO_3 = H$\underline{C}$) and C-S-H to strätlingite and calcite according to

Equation (11) (for siliceous hydrogarnet and C-S-H simplified formulas, C_3ASH_4 and CSH, have been used). After the monocarbonate and siliceous hydrogarnet are depleted, C-S-H is further decalcified while the pH drops to <11. Finally, at around pH 10.5, strätlingite and C-S-H are calculated to be destabilised to calcite and to zeolitic phases such as natrolite (NAS_3H_2) and K-phillipsite (KAS_6H_6) consuming Na and K from the pore solution as indicated by Equation (12). Also, ettringite is calculated to be destabilised to calcite, gypsum and zeolitic phases at pH 10.3 (Equation (13)).

$$C_4A\underline{C}H_{11} + C_3ASH_4 + CSH + 3H\underline{C} \rightarrow 2C_2ASH_8 + 4C\underline{C} \quad (11)$$

$$C_2ASH_8 + 2CSH + 4H\underline{C} + N \rightarrow 4C\underline{C} + NAS_3H_2 + 12H \quad (12)$$

$$C_6A\underline{S}_3H_{32} + 3CSH + 6H\underline{C} + N \rightarrow 6C\underline{C} + 3C\underline{S}H_2 + NAS_3H_2 + 35H \quad (13)$$

Even though the above described carbonation reactions are valid for both CEM I and CEM II, the total amount of CO_2 needed for complete carbonation of C-S-H in CEM I (> 40 g CO_2) is considerably more than for CEM II (32 g CO_2). It looks like the CEM II figure is shifted by about 10-15 g CO_2 to the right. This underlines that the amount of CO_2 bound depends to a large extent on the availability of CaO as previously discussed by [29, 36].

As the crystallisation of well-ordered zeolites can be very slow in a cementitious environment [24], it can be expected that rather zeolitic precursors might be present, similar as in alkali activated systems [37] or that they only form after long reaction times. For comparison, the calculations were repeated while the zeolite formation was prevented (see Fig. 13). The major differences in the phase assemblage occur at progressed carbonation (20-40 g CO_2). Instead of zeolites, amorphous silica and aluminium hydroxide ($Al(OH)_3$) are predicted to form. The gypsum content also reduces almost to half.

Carbonation is calculated to increase the binding of alkalis in the solids as shown in the middle graphs of Fig. 12 and Fig. 13. At intermediate carbonation level this is related to the decrease of the Ca/Si in the C-S-H allowing for increased alkali binding. If the possible formation of zeolites is considered (Fig. 12), the alkali metals are calculated to be bound also in the most carbonated zones, while if the formation of zeolites is supressed, the alkali binding is expected to decrease once C-S-H is destabilised (Fig. 13).

During the carbonation reactions, carbonates are bound in the solids and water is released as can be seen from Equation (11) to (13). This leads to an increase in the predicted amount of pore solution (see middle graphs of Fig. 12 and Fig. 13). In reality, part of the produced

moisture will be transported towards the drying surface of the mortar. However, in the current model such transport is not accounted for.

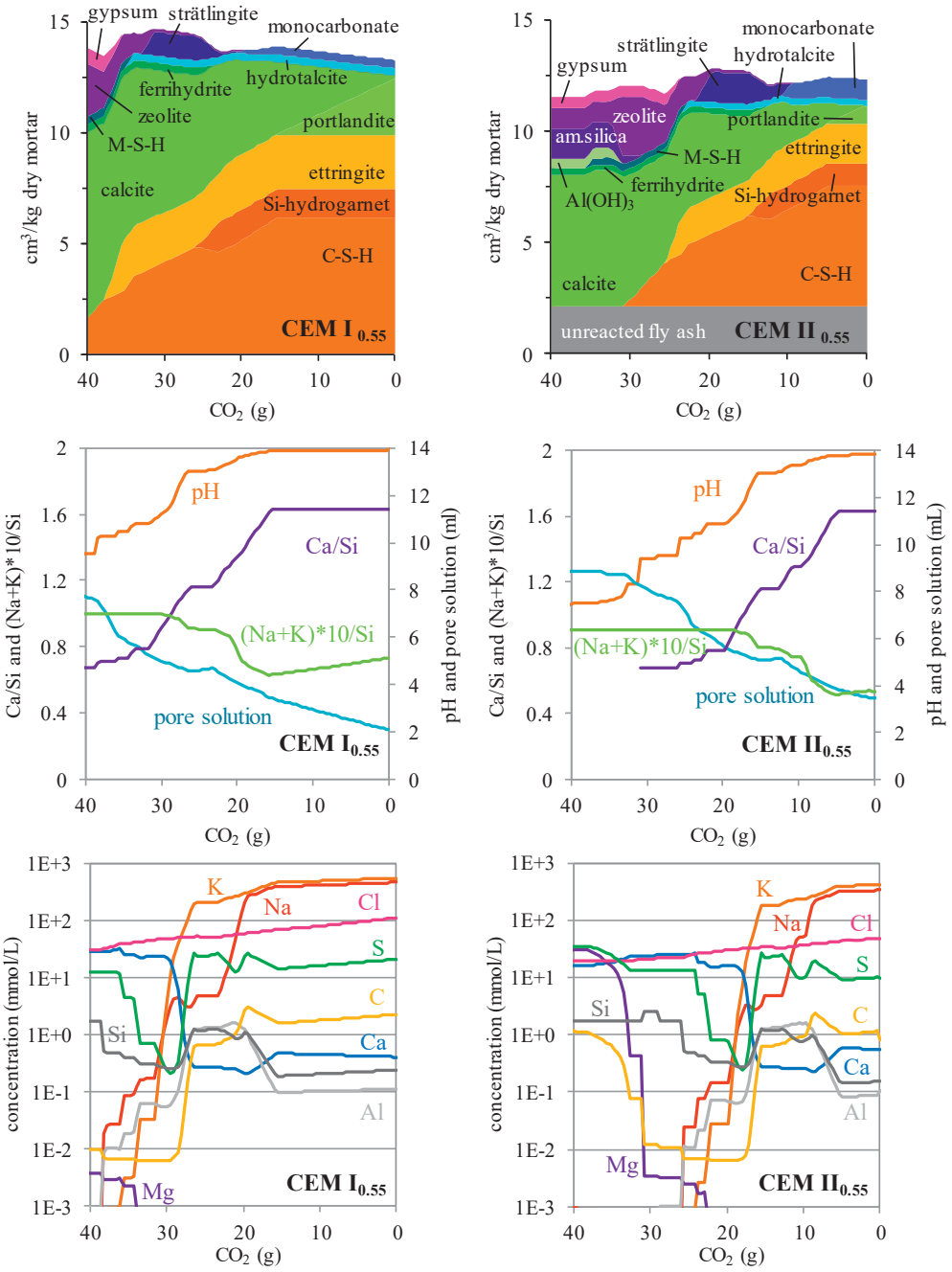

Fig. 12: Modelled changes in the phase assemblage (cm^3/ kg mortar), the amount of pore solution (mL), the pH, the molar Ca/Si ratio of C-S-H, the (Na+K)*10/Si molar ratio in the solids, and the pore solution composition

(mmol/L) upon carbonation of a) CEM $I_{0.55}$ mortar (317 g sand, 100 g of fully hydrated cement and 47 g of water), and b) CEM $II_{0.55}$ mortar (317 g sand, 70 g fully hydrated PC, 30 g FA 20% reacted and 46 g of water) both exposed to accelerated carbonation, 1% CO_2 and 60%RH.

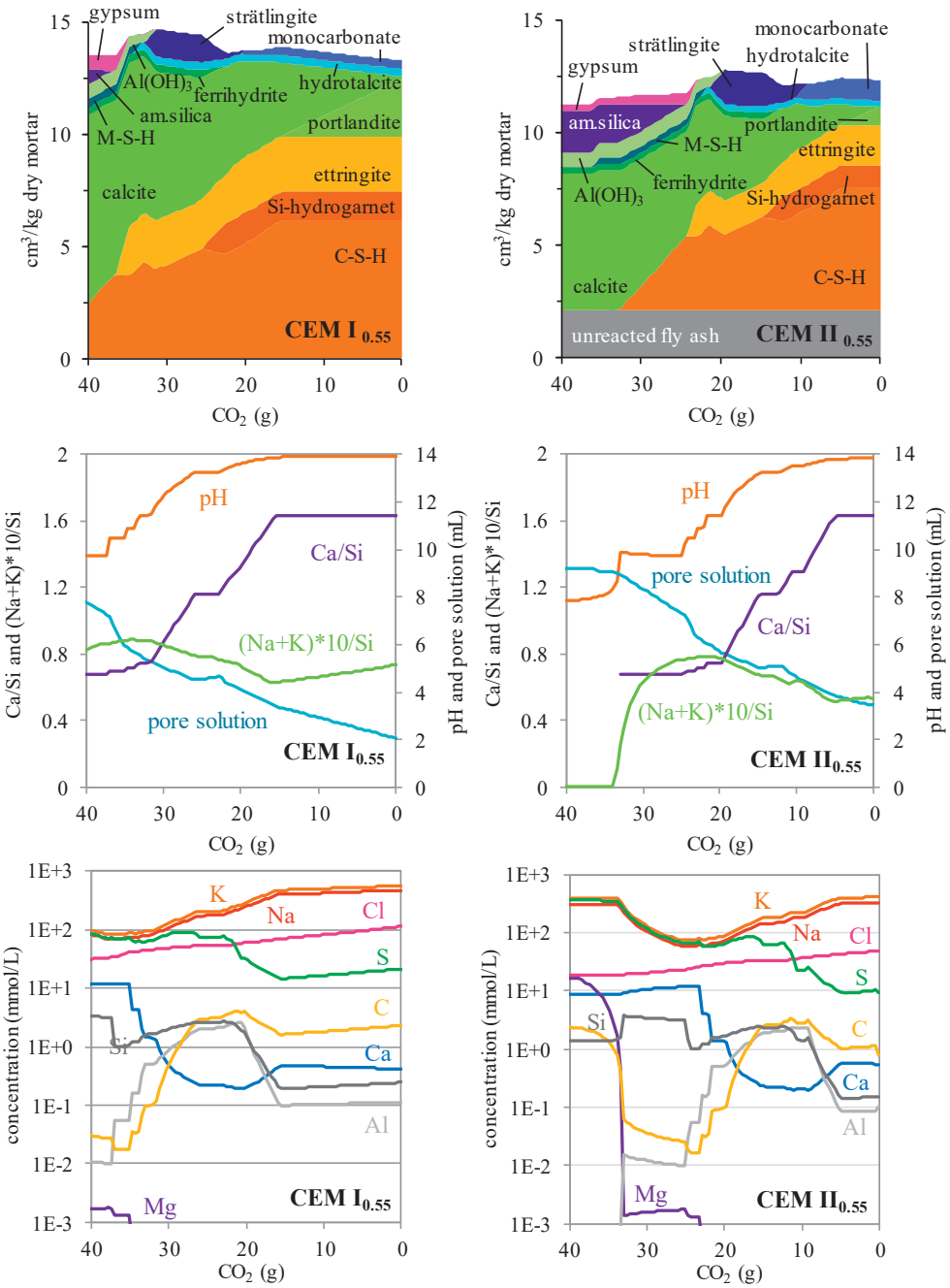

Fig. 13: Modelled changes in the phase assemblage (cm^3/ kg mortar), the amount of pore solution (mL), the pH, the molar Ca/Si ratio of C-S-H, the (Na+K)*10/Si molar ratio in the solids, and the pore solution composition

(mmol/L) upon carbonation of a) CEM $I_{0.55}$ mortar (100 g of fully hydrated cement and 47 g of water), and b) CEM $II_{0.55}$ mortar (70 g fully hydrated PC, 30 g FA 20% reacted and 46 g of water) both exposed to accelerated carbonation, 1% CO_2 and 60%RH. **Zeolite formation supressed**.

The bottom graphs in Fig. 12 and Fig. 13 show the predicted changes in pore solution composition in equilibrium with the solids for the CEM I and CEM II mortars upon carbonation in (mmol/L) respectively with and without zeolite formation. The predicted changes in the pore solution upon carbonation for CEM $II_{0.55}$ compared to CEM $II_{0.55}$ in Fig. 12 showed besides a shift in the CO_2 additions comparable trends.

The Si and Al concentration are in general low (<5 mmol/L) and fluctuate depending on the predicted silicon and aluminium contain solid phases. The Ca and Mg concentrations are also rather low but they increase as the pH of the pore solution decreases upon carbonation, as expected. Contrary to what one might expect, the predicted carbon concentration does not increase upon exposure to CO_2 gas and remains below (1 mmol/L).

The changes in the major elements in the pore solution such as Na, K, S and Cl upon carbonation are discussed using Fig. 15 in which the concentrations are converted to mmol/kg mortar, which enables comparison with the experimental results.

3.6.2 Predicted free alkali metal profiles

The free OH^-, K, Na, S, and Cl content[1] in (mmol/kg mortar), shown in Fig. 14, was calculated using their modelled concentration in the pore solution multiplied with the modelled amount of pore solution (per 100 g cement see Fig. 12 and Fig. 13) and divided by the mass of the mortar (containing 317 g sand, 100 g cement and 47 or 46 mL of water for the CEM $I_{0.55}$ and CEM $II_{0.55}$ mortar, as detailed in Table 4). The predicted contents in mmol/kg mortar are therefore very sensitive to the predicted amount of pore solution. One should also keep in mind that the model does not account for moisture and ion movement in the mortar. The predictions are plotted both for allowing (solid lines) and preventing (dashed lines) zeolite formation.

Upon complete carbonation of the portlandite (<15 g CO_2 for CEM I and <5 g CO_2 for CEM II), a modest increase of the free alkali metal content is predicted. This is due to the formation of additional water during the carbonation reaction, which leads to an increase in the amount of predicted pore solution and thereby to an increase in the amount of free alkali metals. This

[1] The free C concentration is not added in Fig. 14 as the values remain below 1 mmol/kg mortar for all investigated CO_2 levels (see also the low concentrations in Fig. 12 and Fig. 13).

increase in volume of pore solution is probably overestimated in the calculations in comparison to the experiments, where additional water and ions will be transported towards the drying surface of the sample. Similarly an increase in free chlorine and sulphur content upon moderate carbonation is predicted due to the increase in the predicted amount of pore solution. It is however less visible in Fig. 14 due to their relatively low contents.

At a higher degree of carbonation (>16 g CO_2 for CEM I and >6 g CO_2 for CEM II), a decrease of the free alkali metal content is predicted as decalcified C-S-H is able to bind significantly more alkali metals than C-S-H with a high calcium content [9, 31, 38]. Up to 10 g and 20 g of CO_2 for CEM $II_{0.55}$ and CEM $I_{0.55}$ mortar the predictions with and without zeolites are similar.

However, at higher levels of carbonation (>30 g CO_2 for CEM I and >20 g CO_2 for CEM II), the zeolite formation resulted in a drastic decrease of the free alkali metal content as the zeolites are predicted to take up nearly all alkali metals present in the system. When zeolite formation is blocked the following phases are predicted to form: calcite, magnesite, ferrihydrite, alumium hydroxide and amorphous silica, and the amount of gypsum predicted is about halved (Fig. 12 and Fig. 13). The predicted higher levels of alkali metals, when zeolite formation is blocked, are thus explained by the inability to take up alkali metals by the predicted phases, and the high free sulphur contents are explained by the partial decomposition of the gypsum. The predicted chlorine content in Fig. 14 does not show any distinct changes upon carbonation.

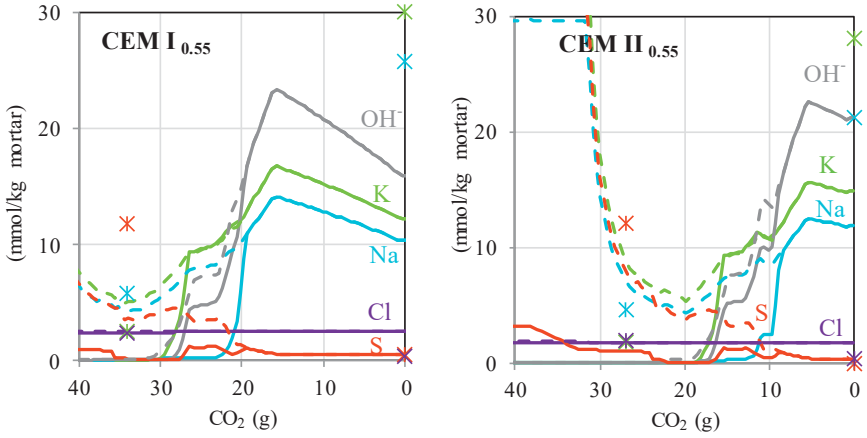

Fig. 14: Modelled changes in the free alkali metals, hydroxyl, sulphur and chlorine profiles (mmol / kg mortar) due to carbonation in a) fully hydrated CEM $I_{0.55}$ and b) hydrated CEM $II_{0.55}$ and CEM $II_{0.40}$ mortars (20% reaction of FA) exposed to accelerated carbonation (1% CO_2 and 60% RH). The solid lines represent the predictions including the formation of zeolites and the dashed lines indicate the predictions if the formation of zeolites is

supressed. The symbols give the measured concentrations in the carbonated (34 g and 27g CO_2 for the CEM $I_{0.55}$ and CEM $II_{0.55}$ samples respectively), and the non-carbonated disc samples (0 g CO_2).

It should be noted that the hydroxide and pH levels with or without zeolites are similar (Fig. 12 and Fig. 13) even though the alkali metal levels peak when zeolites are blocked. This is due to the increase in sulphur concentration in the pore solution, reducing the hydroxyl levels necessary to charge compensate for the high alkali metal concentration in the pore solution, as illustrated in Fig. 14.

The experimentally determined free alkali metals, sulphur and chlorine contents in carbonated and non-carbonated discs are also indicated in Fig. 14 with stars at respectively 34 g and 27 g of CO_2 for the fully carbonated CEM I and CEM II samples, and 0 g CO_2 for the non-carbonated samples. The predicted and measured results are compared in the discussion section of the paper.

4 Discussion

Understanding the changes in the pore solution upon carbonation is crucial with respect to understanding the mechanisms of reinforcement corrosion in carbonated mortar or concrete. As carbonated mortar or concrete is generally dry, we are not able to obtain pore solution by pressing it out with a mechanical press. In this paper Cold Water Extraction (CWE), a rapid leaching method, was used to provide further insights into the composition of pore solution in carbonated mortar. The experimental findings are compared with the predictions of a thermodynamic equilibrium model.

4.1 Comparison of the free alkali metal profiles from CWE with portlandite profiles from TGA and carbonation depth determined by the pH indicator

In Fig. 15 the sodium and potassium profiles determined by CWE are compared to the portlandite profiles determined by TGA and the carbonation depth determined by the pH indicator (data from Fig. 2). It should be noted that the TGA and CWE analysis were performed on samples taken from the same homogenised ground section of mortar, whereas the carbonation depth is determined in one split surface, which can lead to variation in carbonation depth due to spatial inhomogenities.

Within the experimental uncertainty the carbonation depth determined by the pH indicator coincides with the depth at which the alkali metal levels start to increase considerable when moving further inwards into the mortar for all investigated mortars. For the CEM $I_{0.55}$ and CEM $II_{0.55}$ this is also the depth after which the portlandite content starts to be detected and its amount

starts to increase. For the CEM $II_{0.40}$ mortar some portlandite is already present at this depth indicating that the mortar is not fully carbonated at the depth.

The increase of the free alkalis tends to occur at somewhat higher depths compared to the increase of the portlandite content. The reason for this is unclear but it might indicate that either alkali metal ions start to be taken up by the solids before the portlandite starts to carbonate, which is unlikely, or that free alkali metals have been transported together with water towards the exposure surface due to drying.

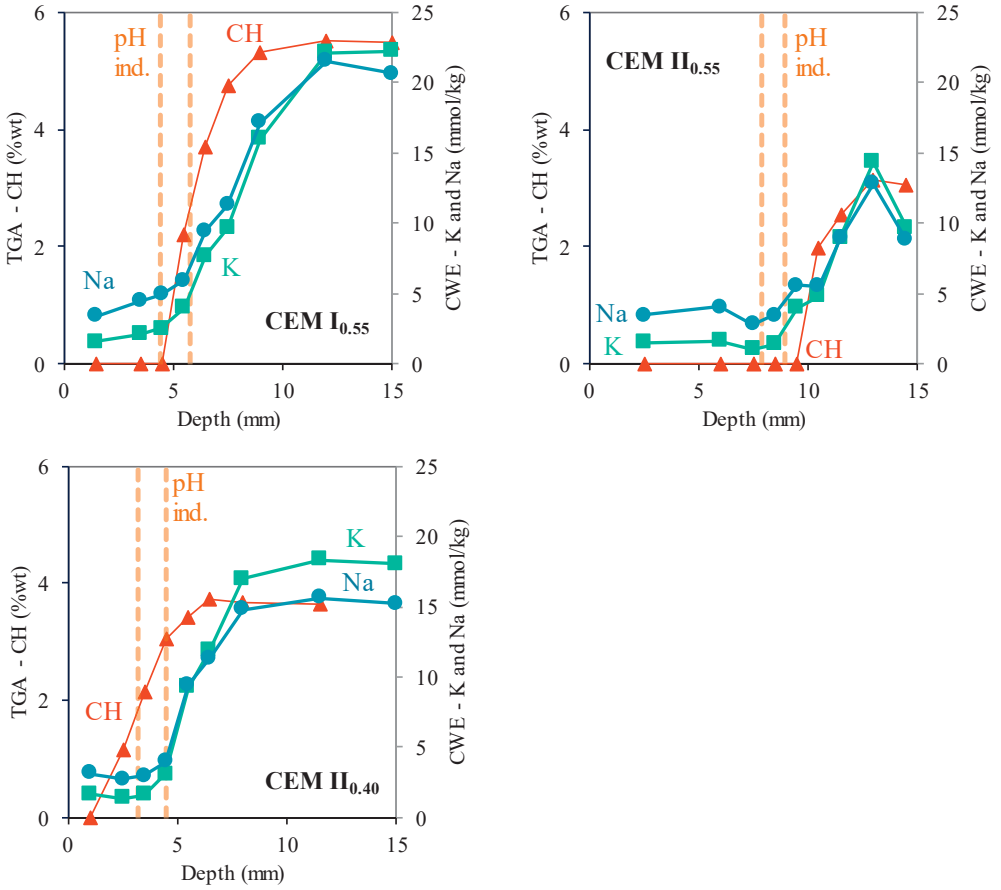

Fig. 15: Comparison of the portlandite profiles (TGA – CH), the sodium and potassium profiles (CWE – K and Na) and the carbonation depth obtained with pH indicators (dashed vertical lines) for the CEM $I_{0.55}$, CEM $II_{0.40}$ and CEM $II_{0.55}$ mortars.

4.2 Changes in the solid phases upon carbonation

4.2.1 Solids that sorb alkali metals

With CWE, a decrease of the free alkali metal content of mortar is measured upon carbonation. This indicates that more alkali metals are taken up by the solids upon carbonation. This was confirmed with the SEM-EDS point analysis of both CEM I and CEM II mortar shown in Fig. 5 and Fig. 6. The carbonation products contain considerably more sodium and potassium than in the C-S-H in the non-carbonated samples.

The exact composition of the reaction products which incorporated the alkali metals upon carbonation could however not be identified with SEM-EDS as the analysed volume for each EDS point analysis was too large. The carbonation leads to an intimate intermixing of the reaction products and the analysed volume does not contain a single phase but always a mixture of different phases. This is amongst others demonstrated by the apparent lowering of the Si/Ca ratio of the carbonation products in the SEM-EDS dot-plots (Fig. 5 and Fig. 6), indicating a fine intermixing of the precipitated calcium carbonated and the decalcified C-S-H in almost all analysed points [16].

Also the thermodynamic model predicts an increase of alkalis in the solid phase in the carbonated zones, in particular when the formation of zeolites was considered (Fig. 12 and Fig. 13). However, it should be noted that the thermodynamic model used is an equilibrium model and thus transport is not taken into account. As indicated by the total potassium profiles obtained with the μXRF (Fig. 8), there is transport of ions towards the exposed surface as carbonation in conditions of 1% CO_2 and 60%RH goes along with drying, and thereby transport of water and ions. In addition, alkali uptake was considered by a simple uptake coefficient approach, which introduces further inaccuracy in the predictions of the alkali concentrations.

Upon initial carbonation (<20 g CO_2 for CEM I and <8 g CO_2 for CEM II in Fig. 12 and Fig. 13), the model predicts a reduction of alkali metals in the pore solution mainly due to the increased alkali metal sorption by low Ca/Si C-S-H. C-S-H is the main hydrate and is able to sorb Na and K [9, 39, 40] due to its negative surface charge. C-S-H with high Ca/Si binds only little alkalis, while the ability to bind alkalis is dramatically increased at lower calcium-to-silicon ratio (Ca/Si) [39-41]. The Ca/Si of the C-S-H prior to carbonation is predicted to be about 1.6 (Fig. 12 and Fig. 13), comparable to the Ca/Si ratio of CEM I (Fig. 5) and CEM II (Fig. 6) of about 1.8 and 1.4 determined by SEM-EDS point analysis. Thus, only little alkali metal ions are sorbed on C-S-H before carbonation. The carbonation process induces a

decalcification of the C-S-H, i.e. a decrease of Ca/Si resulting in an increase of the alkali uptake in agreement with the higher alkali to silicon ratios experimentally determined (Fig. 5 and Fig. 6) for the samples after carbonation.

Upon progressed carbonation (>20 g CO_2 for CEM I and >8 g CO_2 for CEM II), the formation of zeolitic phases is predicted by the model (Fig. 12). Zeolites are aluminosilicates capable of incorporating relatively large amounts of cations such alkali metals and their formation is predicted to cause a drastic decrease in the alkali metal concentration in the pore solution, in particular for K where the formation of K-phillipsite ($KAlSi_3O_8 \cdot 3H_2O$) is predicted. However, the formation of zeolitic phases is generally very slow [24] and the formation of crystalline products seems unlikely to occur during such a short period of time, i.e. 3 months, although amorphous, more soluble zeolitic precursors might have formed as in the case of alkali activated systems [37]. We therefore also predicted the phase assemblage supressing the zeolite formation (Fig. 13), where the predicted reduction in the alkali metal concentration in the pore solution is much more modest compared to the system with zeolite formation. When C-S-H starts to decompose to amorphous silica, which in the model does not have ability to sorb alkali metals (>37 g CO_2 for CEM I and >25 g CO_2 for CEM II in Fig. 13), the alkali metal concentration in the pore solution are calculated to even start to increase again. The EDS results presented in Fig. 7 point towards a preferential uptake of K in the carbonated mortar.

4.2.2 Portlandite (CH) and calcium carbonate (C$\underline{C}$)

Besides the decalcification of the C-S-H and the increase of its alkali metal uptake, carbonation also causes the decomposition of series of phases such as portlandite, monocarbonate and ettringite. Most of the calcium in the solid phase of the system ends up as calcium carbonate upon carbonation, and a small part as gypsum. Fig. 16 shows the changes in the predicted amounts of calcium carbonate and portlandite upon carbonation. The experimental data for the non-carbonated and carbonated mortar (inner- and outermost section in Fig. 4) are shown with square symbols at 0 and 40 g CO_2 respectively. There is a relatively good correspondence between the initial amount of portlandite and calcite of the CEM $I_{0.55}$ mortar. For the CEM $II_{0.55}$ mortar, the amount of portlandite is slightly underestimated which might be due to some deviation in the degree of reaction of the fly ash or the predicted Ca/Si ratio of the C-S-H. When comparing the experimentally determined amount of calcite with the predicted one, we can estimate the CO_2 level in the model, which corresponds to carbonation in the outmost

sections of the investigated mortars. For CEM $I_{0.55}$, the CO_2 level is approx. 34 g and for the CEM $II_{0.55}$ it is approx. 27 g. These are the CO_2 levels corresponding to the following phase assemblage when zeolites formation is supressed (Fig. 13) resulting in C-S-H with a Ca/Si ratio of approx. 0.7, decomposition of almost all ettringite and the formation of calcite, ferrihydrite, aluminium hydroxide, M-S-H and gypsum.

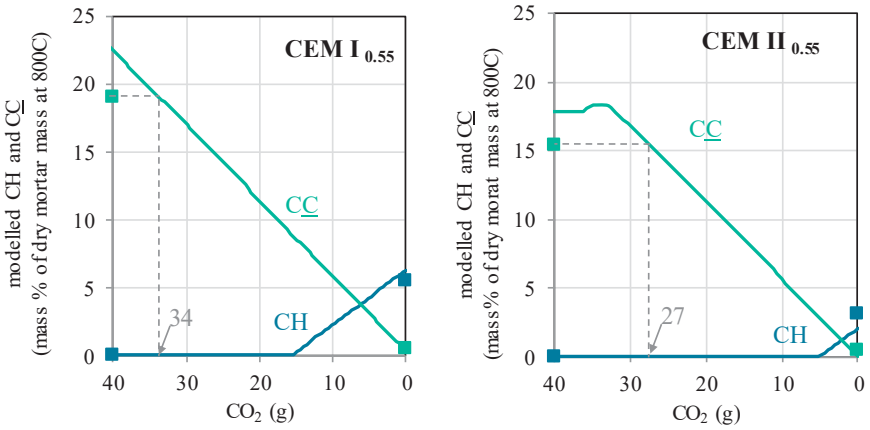

Fig. 16: Modelled (line) and measured (square symbol) changes in calcium carbonate (CC) and calcium hydroxide (CH) content upon carbonation in a) CEM $I_{0.55}$ mortar (100 g of fully hydrated cement and 47 g of water), and b) CEM $II_{0.55}$ mortar (70 g fully hydrated PC, 30 g FA 20% reacted and 46 g of water) both exposed to accelerated carbonation, 1% CO_2 and 60%RH. The modelled amounts only change marginally dependent on whether or not zeolite formation is blocked. The measured CC and CH values are taken from the outermost section and innermost section of the carbonated CEM I and CEM II mortars shown in Fig. 4

4.3 Changes in the pore solution upon carbonation

The CWE method gives the free element content in mortar in mmol/kg mortar. The model on the other hand predicts the concentration of the elements in the pore solution in equilibrium with the predicted solids in mmol/L. In order to compare the experimental with the modelled results we need to make an assumption with regard to the amount of pore solution in the mortar. We do not have accurate moisture profiles in the samples neither experimentally nor through modelling (as drying was not considered in the modelling) so the assumption of the measured moisture content is a considerable source of error.

In Fig. 14 the modelled results are converted to mmol/kg mortar, and are compared to the CWE results in carbonated and non-carbonated mortar. Fig. 17 gives a direct comparison of the predicted free Na, K, S and Cl content for 34 g CO_2 for CEM I and 27 g CO_2 at CEM II, with the measured pore solution composition. The predicted carbonate content was rather low (<1 mmol/L see Fig. 13) and is therefore not presented in Fig. 17.

For non-carbonated mortar (CEM I_{ref} and CEM II_{ref}), the free Na and K content is underestimated by the model compared to the measured amount (CEM $I_{0.55}$ and CEM $II_{0.55}$). This is either due to a discrepancy in the assumptions of alkali metal sorption by the C-S-H in the simple sorption model used, and/or due to the release of some of the loosely sorbed alkali metals during CWE. The free Cl and S content in the non-carbonated mortar are on the other hand overestimated by the model. In the case of Cl, this can be due to the fact that the model does not take into account the presence of Cl in the diffuse layer of the C-S-H [42] which might not be released during CWE [43].

The overestimation of S by the model cannot be explained, but it does indicate that ettringite does not decompose during CWE.

Upon carbonation the free alkali metal content drops considerably, however, not to the same extent as predicted when allowing zeolite formation (see Fig. 14). This points towards the absence of crystalline zeolites although some zeolitic precursor might have formed during carbonation. When preventing zeolite formation a more moderate reduction in the free alkali metal content is observed as well as an increase in the free sulphur content, which agrees somewhat better with experimental observation. The model predicts no change in the chlorine concentration upon carbonation whereas the experimental data shows an increase upon carbonation. The experimentally observed increase in the free chlorine content upon carbonation is caused by the release of the chlorine originally sorbed onto the non-carbonated C-S-H and present as a minor element in monocarbonate upon their decomposition. Both the model and the experimental results show and increase in the free sulphur content upon carbonation, which can be related to the decomposition of ettringite and gypsum.

It should be noted that the carbonated mortars have very similar measured free Na, K, S and Cl contents independent of the binder used. This is in accordance with a previous investigation [16], in which the carbonation of Portland cement and fly ash blends leads to similar chemical composition of the reaction products. The slight differences in the predicted free contents should not be over-interpreted as they depend strongly on the CO_2 level chosen for the comparison.

Based on the pore solution composition in the carbonated concrete, the pH can be calculated. The model predicts a pH of 10.9 for the CEM I mortar exposed to 34 g CO_2 and a pH of 9.7 for CEM II mortar exposed to 27 g CO_2. These values are considerably lower than the roughly estimated pH solely based on the free alkali metals which ends up around 13 as

described in[2]. The pore solution composition and its pH in carbonated concrete is strongly influenced by the free S content besides the Na and K content.

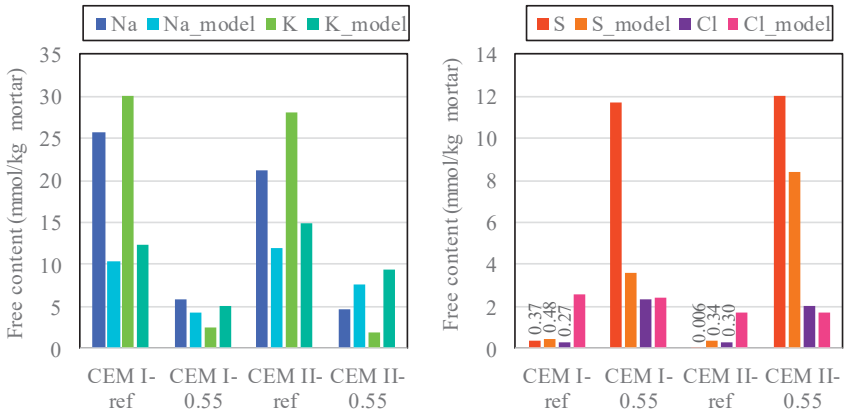

Fig. 17: Comparison of measured and modelled pore solution composition for the non-carbonated (ref) and carbonated (0.55) mortar in (mmol/kg mortar). For the modelled results 34 g CO_2 was used for CEM I and 27 g CO_2 for CEM II, and zeolite formation was supressed.

4.4 Effect of carbonation on corrosion

The pore solution composition plays a decisive role in the corrosion process of the steel reinforcement, both for corrosion initiation and corrosion propagation. The interaction between the components in the pore solution of carbonated concrete and carbon steel is complex; see e.g. [44]. For the discussion here, we choose to focus on changes in the molar ratios of chlorine to hydroxyl ($[Cl^-]/[OH^-]$), sulphate to hydroxyl ($[SO_4^{-2}]/[OH^-]$), and carbonate to bicarbonate ($[CO_3^{2-}]/[HCO_3^-]$) in the pore solution, as well as the total concentration of carbonate and bicarbonate ($[CO_3^{2-}] + [HCO_3^-]$).

Fig. 18 and Fig. 19 present the modelled changes in $[Cl^-]/[OH^-]$, $[SO_4^{-2}]/[OH^-]$, and $[CO_3^{2-}]/[HCO_3^-]$ molar ratios upon carbonation in the pore solution with and without zeolite formation for CEM $I_{0.55}$ and CEM $II_{0.55}$ mortar, respectively. In addition we include the total carbon

[2] The pH could be roughly estimated assuming that the alkali metal concentration equals the hydroxyl concentration: $pH=14+\log([OH^-])=14+\log([Na^+]+[K^+])$. If this is done using the alkali metal concentrations of the outermost carbonated sections of the exposed mortar blocks (see Appendix) a pH of in the range of 13 is achieved.

content in the pore solution as a measure of the total concentration of carbonate and bicarbonate ($[CO_3^{2-}] + [HCO_3^-]$).

Higher concentrations of chlorides and sulphates relative to the hydroxyl concentration [45, 46], and lower carbonate relative to bicarbonate concentrations in the pore solution can increase the corrosion rate of carbon steel [44]. Selected thresholds for corrosion initiation for $[Cl^-]/[OH^-]$, $[SO_4^{-2}]/[OH^-]$, and $[CO_3^{2-}]/[HCO_3^-]$ suggested in the literature are included in Fig. 18 and Fig. 19 ($[Cl^-]/[OH^-]>0.6$ [45], $[SO_4^{-2}]/[OH^-]>1.5$ based on [46], $[CO_3^{2-}]/[HCO_3^-]<0.1$ to 0.01 based on [44]). It should be mentioned that the use of thresholds is a simplification as corrosion depends on many factors.

When the zeolite formation is suppressed, the modelled $[Cl^-]/[OH^-]$ decreases, the $[SO_4^{-2}]/[OH^-]$ increases, and the $[CO_3^{2-}]/[HCO_3^-]$ increases somewhat compared to the predicted ratios when zeolite formation is allowed (see Fig. 18 and Fig. 19). However, the trends are similar independent of whether the zeolite is considered or not.

When the materials are not carbonated (0 g CO_2 on the horizontal axes in Fig. 18 and Fig. 19), the $[Cl^-]/[OH^-]$ and $[SO_4^{-2}]/[OH^-]$ are slightly higher in the CEM $I_{0.55}$ mortar compared to the CEM $II_{0.55}$ mortar due to the dilution effect of fly ash (less clinker) and differences in the phase assemblage. The $[Cl^-]/[OH^-]$ and $[SO_4^{-2}]/[OH^-]$ thresholds are reached for the CEM $I_{0.55}$ mortar in the range of 25-30 g CO_2 compared to 15-20 g CO_2 for the CEM $II_{0.55}$ mortar. These CO_2 levels are below the actual carbonation level of the samples (34 g CO_2 for the CEM $I_{0.55}$ and 27 g for the CEM $II_{0.55}$), i.e. the thresholds will be reached before complete carbonation. The threshold for the chloride is reached at slightly lower CO_2 levels than the sulphate threshold. The predicted pH in the pore solution, at the CO_2 levels corresponding to the critical chloride and sulphate content, is 12 or higher (Fig. 12 and Fig. 13). At the actual carbonation level of the samples (34 g CO_2 for the CEM $I_{0.55}$ and 27 g for the CEM $II_{0.55}$), the $[Cl^-]/[OH^-]$ and $[SO_4^{-2}]/[OH^-]$ are in the range of 100 for the CEM $I_{0.55}$ mortar and in the range of 1000 for the CEM $II_{0.55}$ mortar. This $[Cl^-]/[OH^-]$ range indicates the potential for high corrosion rates (10 $\mu A/cm^2$), as measured in [47] on carbon steel exposed to simulated pore solution within this $[Cl^-]/[OH^-]$ range.

The carbonate-to-bicarbonate ratio, $[CO_3^{2-}]/[HCO_3^-]$, is very high (in the range of 10 000) in both non-carbonated samples (0 g CO_2 on the horizontal axes) as mainly carbonates are found in the pore solution, while $[CO_3^{2-}]/[HCO_3^-]$ becomes lower upon carbonation as the bicarbonate concentration increases. At the actual carbonation levels, the modelled carbonate-to-

bicarbonate ratio was around 10 for the CEM $I_{0.55}$ mortar and around 1 for the CEM $II_{0.55}$ mortar, indicating that bicarbonates are becoming more predominant in the pore solution. This range is getting closer to the suggested threshold $[CO_3^{2-}]/[HCO_3^-]$ below which corrosion is expected to be promoted, 0.1 to 0.01 based on [44].

Carbonate and bicarbonate have been found to act as depassivators at low concentrations, but as inhibitors at high concentrations [44, 48-50]. Critical concentrations at 0.1 M for HCO_3^- and 0.01 M for CO_3^{2-} were suggested in [48]. The modelled amount of total carbonates in the pore solution varied upon carbonation. At the actual level of carbonation of the samples, the carbonate concentration was lower (0.02 mmol/L for the CEM I and 0.001 mmol/L for the CEM II) compared to the non-carbonated mortar for both cements (2 mmol/L for the CEM I and 0.8 mmol/L for the CEM II).

In summary, there are several reasons for reinforcement corrosion to be promoted in such systems. The modelled $[Cl^-]/[OH^-]$ and $[SO_4^{-2}]/[OH^-]$ in the pore solution of the carbonated mortar are beyond the applied thresholds and are expected to promote reinforcement corrosion. The predicted $[CO_3^{2-}]/[HCO_3^-]$ in the pore solution approaches a critical level and the total carbon concentration in the pore solution is low. However, it should be noted that the applied thresholds and concentrations are derived for simplified systems and not necessarily generally applicable.

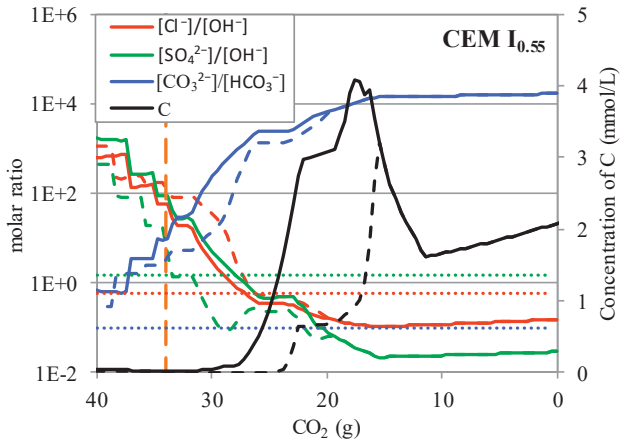

Fig. 18: Modelled changes in the $[Cl^-]/[OH^-]$, $[SO_4^{-2}]/[OH^-]$, and $[CO_3^{2-}]/[HCO_3^-]$ molar ratios and the carbon (C) concentration in the pore solution upon carbonation of CEM $I_{0.55}$ mortar (fully hydrated CEM I exposed to accelerated carbonation, 1% CO_2 and 60% RH (47 g of water). Dashed lines are used for the modelled results including zeolite formation, solid lines for the model where zeolite formation is suppressed and dotted lines for the corrosion threshold from literature $(Cl^-)/[OH^-]>0.6$ [45], $[SO_4^{-2}]/[OH^-]>1.5$ based on [46], $[CO_3^{2-}]/[HCO_3^-]>0.1$ based on [44]).

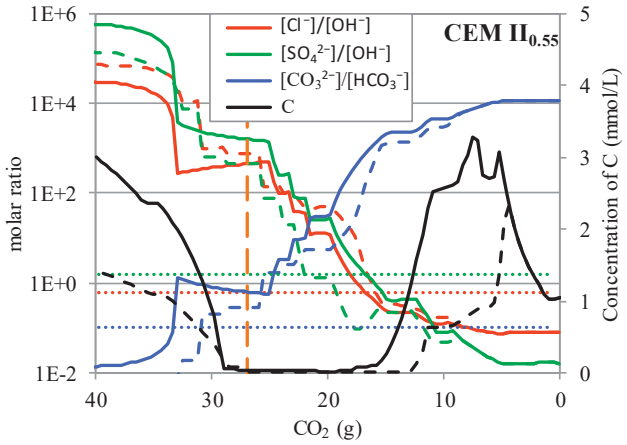

Fig. 19: Modelled changes in the $[Cl^-]/[OH^-]$, $[SO_4^{-2}]/[OH^-]$, and $[CO_3^{2-}]/[HCO_3^-]$ molar ratios and the carbon (C) concentration in the pore solution upon carbonation of CEM $II_{0.55}$ mortar (70 g fully hydrated CEM I and 30 g FA 20% reacted) exposed to accelerated carbonation, 1% CO_2 and 60% RH (46 g of water). Dashed lines are used for the modelled results including zeolite formation, solid lines for the model where zeolite formation is suppressed and dotted lines for the corrosion threshold from literature $[Cl^-]/[OH^-]>0.6$ [45], $[SO_4^{-2}]/[OH^-]>1.5$ based on [46], $[CO_3^{2-}]/[HCO_3^-]>0.1$ based on [44]).

5 Conclusion

Understanding the changes in the pore solution upon carbonation is crucial with respect to understanding the mechanisms of reinforcement corrosion in carbonated mortar or concrete. As carbonated mortar or concrete is generally dry, we are not able to obtain pore solution by pressing out pore solution with a mechanical press. In this paper we used Cold Water Extraction (CWE), a rapid leaching method, to provide further inside into the composition of pore solution in carbonated mortar. We applied CWE to obtain the free alkali metal profiles in carbonated mortar with Portland cement (CEM I) and mortar with fly ash Portland cement containing 30 mass% fly ash (CEM II).

We succeeded in obtaining decreasing alkali metal profiles in the carbonated mortar, indicating uptake of alkali metals by the solids upon carbonation. The depth where the changes in the free alkali metal profiles were observed agree well with the decreasing portlandite profiles obtained on the same sections of the mortar using TGA and with the carbonation depth determined by a pH indicator.

The alkali metal uptake by the carbonation products was confirmed by SEM-EDS. A thermodynamic model of the system predicted the increased uptake of alkalis in the decalcified C-S-H formed during carbonation and hinted towards the possible formation of zeolites or

zeolitic precursors, i.e. aluminosilicate minerals able to take up alkali in the cementitious system under strongly carbonated conditions. However, the observation of measureable free alkali metals in the CWE and the relatively high sulphate concentrations indicates that no or very little zeolites have formed; such that the carbonated cements were rather a combination of calcite, decalcified C-S-H, amorphous silica, aluminium hydroxide and gypsum.

The experimentally obtained pore solution composition and the predicted one indicate that upon carbonation the chlorine and sulphur concentrations increase while the pH decreases. The pore solution plays a decisive role in the corrosion process of the steel reinforcement, both for corrosion initiation and corrosion propagation. Carbonation causes a decrease in the hydroxyl concentration, variations in the carbon content, a reduction of the carbonate-to-bicarbonate ratio, and a release of detrimental ions such as chlorides and sulphates. This strongly increases the probability of corrosion and the corrosion rate.

Finally, we could also conclude that the phase assemblage and pore solution chemistry for the two tested binders was rather similar upon carbonation.

6 Acknowledgment

The authors acknowledge the financial support for the project 'Lavkarbsem' (NFR project no. 235211/O30) and for the project 236661/O30 “ASR – alkali silica reaction in concrete – reliable concept for performance testing” supported by the Norwegian Research Council and industrial partners: Norcem, NorStone, Norsk Stein, Hydro Energy, Axion and the Norwegian Road administration.

Simon Langedal, Johannes Osorio Mydland, Niklas Amundsen, Øyvind Lindgård, Kristine Nøttveit and Syverin Lierhagen (NTNU) and Roger Leistad (SINTEF) are warmly acknowledge for their help during the experimental study.

7 References

1. Zeebe, R.E. and D. Wolf-Gladrow, *CO2 in Seawater : Equilibrium, Kinetics, Isotopes*. Elsevier Oceanography Series. 2001, Burlington: Elsevier Science.
2. Vollpracht, A., et al., *The pore solution of blended cements: a review.* Materials and Structures, 2015. **49**: p. 3341-3367.
3. Papadakis, V.G., C.G. Vayenas, and M.N. Fardis, *Experimental investigation and mathematical modeling of the concrete carbonation problem.* Chemical Engineering Science, 1991. **46**(5): p. 1333-1338.
4. Ekolu, S.O., *A review on effects of curing, sheltering, and CO2 concentration upon natural carbonation of concrete.* Construction and Building Materials, 2016. **127**: p. 306-320.

5. Nishikawa, T., et al., *Decomposition of synthesized ettringite by carbonation.* Cement and Concrete Research, 1992. **22**(1): p. 6-14.
6. Shi, Z., et al., *Experimental studies and thermodynamic modeling of the carbonation of Portland cement, metakaolin and limestone mortars.* Cement and Concrete Research, 2016. **88**: p. 60-72.
7. Robl, T., U. Graham, and D. Taulbee, *The effect of carbonation reactions on the long term stability of products made from dry FGD materials.* Preprints of Papers, American Chemical Society, Division of Fuel Chemistry, 1996. **41**(CONF-960376--).
8. Sevelsted, T.F. and J. Skibsted, *Carbonation of C–S–H and C–A–S–H samples studied by 13 C, 27 Al and 29 Si MAS NMR spectroscopy.* Cement and Concrete Research, 2015. **71**: p. 56-65.
9. L'Hôpital, E., et al., *Alkali uptake in calcium alumina silicate hydrate (C-A-S-H).* Cement and Concrete Research, 2016. **85**: p. 122-136.
10. Anstice, D.J., C.L. Page, and M.M. Page, *The pore solution phase of carbonated cement pastes.* Cement and Concrete Research, 2005. **35**(2): p. 377-383.
11. Plusquellec, G., et al., *Determination of the pH and the free alkali content in the pore solution of concrete: review and experimental comparison.* Cement and Concrete Research, 2017. **96**: p. 13.
12. Plusquellec, G., et al., *Determination of the pH and the free alkali metal content in the pore solution of concrete: Review and experimental comparison.* Cement and Concrete Research, 2017. **96**: p. 13-26.
13. Belda Revert, A., et al., *Carbonation-induced corrosion: Investigation of the corrosion onset.* Construction and Building Materials, 2018. **162**: p. 847-856.
14. Lothenbach, B., P. Durdzinski, and K. De Weerdt, *Thermogravimetric analysis*, in *A practical guide to microstructural analysis of cementitious materials*, K. Scrivener, R. Snellings, and B. Lothenbach, Editors. 2016, CRC Press: Boca Raton. p. 177-212.
15. Detwiler, R.J., et al., *Preparing Specimens for Microscopy.* Concrete International, 2001. **23**(11): p. 50-58.
16. Belda Revert, A., et al. *SEM-EDS analysis of products formed under natural and accelerated carbonation of concrete with CEM I, CEM II/B-M and CEM II/B-V* in *XXIIIth Symposium on Nordic Concrete Research & Developement*. 2017. Aalborg, Denmark.
17. Kulik, D., et al., *GEM-Selektor geochemical modeling package: revised algorithm and GEMS3K numerical kernel for coupled simulation codes.* Computational Geosciences, 2013. **17**(1): p. 1-24.
18. Wagner, T., et al., *GEM-Selektor geochemical modeling package: TSolMod library and data interface for multicomponent phase models.* Canadian Mineralogist, 2012. **50**: p. 1173-1195.
19. Thoenen, T., et al., *The PSI/Nagra Chemical Thermodynamic Data Base 12/07*. 2014, Villigen PSI, Switzerland: PSI report 14-04. 416.
20. Thoenen, T. and D.A. Kulik, *Nagra/PSI Chemical Thermodynamic Data Base 01/01 for the GEM-Selektor (V.2- PSI) Geochemical Modeling Code: Release 28-02-03. Internal Report TM-44-03-04.* available from: http://gems.web.psi.ch/GEMS3/doc/pdf, 2003.
21. Lothenbach, B., et al., *Cemdata18: A thermodynamic database for hydrated Portland cements and alkali-activated materials.* Cement and Concrete Research, 2018: p. Accepted.
22. Kulik, D.A., *Improving the structural consistency of C-S-H solid solution thermodynamic models.* Cement and Concrete Research, 2011. **41**(5): p. 477-495.

23. Balonis, M., et al., *Impact of chloride on the mineralogy of hydrated Portland cement systems.* Cement and Concrete Research, 2010. **40**(7): p. 1009-1022.
24. Lothenbach, B., E. Bernard, and U. Mäder, *Zeolite formation in the presence of cement hydrates and albite.* Journal of Physics and Chemistry of the Earth, 2017. **99**: p. 77-94.
25. Blanc, P., et al., *ThermoChimie database developments in the framework of cement/clay interactions.* Applied Geochemistry, 2015. **55**: p. 95-107.
26. Merkel, B.J. and B. Planer-Friederich, *Groundwater Geochemistry. A Practical Guide to Modeling of Natural and Contaminated Aquatic Systems*, ed. D.K. Nordstrom. 2008: Springer Berlin.
27. De Weerdt, K., et al., *Hydration mechanisms of ternary Portland cements containing limestone powder and fly ash.* Cement and Concrete Research, 2011. **41**(3): p. 279-291.
28. Hargis, C.W., et al., *Carbonation of calcium sulfoaluminate mortars.* Cement and Concrete Composites, 2017. **80**: p. 123-134.
29. Shi, Z., et al., *Experimental studies and thermodynamic modeling of the carbonation of Portland cement - metakaolin - limestone mortars.* Cement and Concrete Research, 2016. **88**: p. 60-72.
30. Lothenbach, B. and F. Winnefeld, *Thermodynamic modelling of the hydration of Portland cement.* Cement and Concrete Research, 2006. **36**(2): p. 209-226.
31. Hong, S.-Y. and F.P. Glasser, *Alkali binding in cement pastes. Part I. The C-S-H phase.* Cement and Concrete Research, 1999. **29**: p. 1893-1903.
32. Lothenbach, B., *Thermodynamic equilibrium calculations in cementitious systems.* Materials and Structures, 2010. **43**: p. 1413-1433.
33. Lothenbach, B. and E. Wieland, *A thermodynamic approach to the hydration of sulphate-resisting Portland cement.* Waste Management, 2006. **26**(7): p. 706-719.
34. Belda Revert, A., et al., *Carbonation Characterization of Mortar with Portland Cement and Fly Ash, Comparison of Techniques* Nordic Concrete Research, 2016: p. 60-76.
35. Åhs, M., *Redistribution of moisture and ions in cement based materials*. 2011: Lund University.
36. Leemann, A., et al., *Relation between carbonation resistance, mix design and exposure of mortar and concrete.* Cement and Concrete Composites, 2015. **62**(Supplement C): p. 33-43.
37. Bernal, S.A., et al., *Role of carbonates in the chemical evolution of sodium carbonate-activated slag binders.* Materials and Structures, 2015. **48**(3): p. 517-529.
38. Lothenbach, B. and A. Nonat, *Calcium silicate hydrates: solid and liquid phase composition.* Cement and Concrete Research, 2015. **78**: p. 57-70.
39. Bach, T.T.H., et al., *Retention of alkali ions by hydrated low-pH cements: Mechanism and Na+/K+ selectivity.* Cement and Concrete Research, 2013. **51**: p. 14-21.
40. Plusquellec, G., *Analyse in situ de suspensions de silicate de calcium hydraté: application aux interactions ioniques à la surface des particules*. 2014, Université de Bourgogne.
41. Haas, J., *Etude expérimentale et modélisation thermodynamique du système CaO-SiO2-(Al2O3)-H2O*. 2013, Université de Bourgogne.
42. De Weerdt, K., et al., *Impact of the associated cation on chloride binding of Portland cement paste.* Cement and Concrete Research, 2015. **68**: p. 196-202.
43. Plusquellec, G. and A. Nonat, *Interactions between calcium silicate hydrate (CSH) and calcium chloride, bromide and nitrate.* Cement and Concrete Research, 2016. **90**: p. 89-96.
44. Huet, B., et al., *Influence of alkali, silicate, and sulfate content of carbonated concrete pore solution on mild steel corrosion behavior.* Materials and Corrosion, 2010. **61**(2): p. 111-124.

45. Hausmann, D.A., Steel corrosion in concrete. How does it occur?, 1967: p. 19-23.
46. Liu, G., et al., *Corrosion behavior of steel submitted to chloride and sulphate ions in simulated concrete pore solution.* Construction and Building Materials, 2016. **115**(Supplement C): p. 1-5.
47. Garcés, P., et al., *Corrosion of reinforcing steel in neutral and acid solutions simulating the electrolytic environments in the micropores of concrete in the propagation period.* Corrosion Science, 2005. **47**(2): p. 289-306.
48. Alonso, M.C. and M.C. Andrade, *The electrochemical behaviour of steel reinforcements in Na2CO3 and NaHCO3 solutions in relation to stress corrosion cracking.* Corrosion Science, 1989. **29**(9): p. 1129-1139.
49. Huet, B., et al., *Electrochemical behavior of mild steel in concrete: Influence of pH and carbonate content of concrete pore solution.* Electrochimica Acta, 2005. **51**(1): p. 172-180.
50. Moreno, M., et al., *Corrosion of reinforcing steel in simulated concrete pore solutions: Effect of carbonation and chloride content.* Corrosion Science, 2004. **46**(11): p. 2681-2699.

8 Appendix

Appendix 1: The calculated Na and K concentration in in the pore solution as a function of the depth. The volume of pore solution used for the calculation is also indicated.

Sample	Depth (mm)	Na (mmol/l)		K (mmol/l)		Moisture content (wt. %)
		Average	*Std dev.*	Average	*Std dev.*	
CEM I_{ref}	0-3	350	-	380	-	8.3
	3-6	329	-	383	-	8.3
	6-9	345	-	387	-	8.3
	9-12	346	-	408	-	8.3
	12-15	348	-	412	-	8.3
CEM $I_{0.55}$	0-3	79	*16*	37	*10*	4.5
	3-4	103	*8*	48	*9*	4.5
	4-5	113	*6*	59	*8*	4.5
	5-6	137	*34*	92	*30*	4.5
	6-7	164	*46*	133	*45*	6.1
	7-8	196	*31*	168	*25*	6.1
	8-10	299	*40*	277	*47*	6.1
	10-14	374	*64*	385	*70*	6.1
	14-16	359	*17*	386	*26*	6.1
CEM II_{ref}	0-3	221	-	270	-	8.9
	3-6	206	-	246	-	8.9
	6-9	221	-	273	-	8.9
	9-12	230	-	278	-	8.9
	12-15	229	-	279	-	8.9
	15-20	228	-	278	-	8.9
CEM $II_{0.55}$	0-5	99	*9*	42	*4*	3.6
	5-7	116	*47*	46	*21*	3.6
	7-8	81	*28*	30	*14*	3.6
	8-9	99	*21*	40	*6*	3.6
	9-10	93	*37*	67	*42*	6.3
	10-11	92	*13*	81	*29*	6.3
	11-12	151	*25*	151	*9*	6.3
	12-14	216	*6*	241	*8*	6.3
	14-15	148	*3*	163	*4*	6.3
CEM $II_{0.40}$	0-2	70	*16*	38	*8*	4.6
	2-3	61	*20*	30	*10*	4.6
	3-4	67	*2*	36	*3*	4.6
	4-5	89	*29*	70	*21*	4.6
	5-6	159	*33*	156	*33*	6.3
	6-7	190	*50*	201	*52*	6.3
	7-9	250	*10*	286	*14*	6.3
	9-14	263	*8*	309	*10*	6.3
	14-16	256	*12*	303	*17*	6.3

Appendix 2: The determined free Na, K, S and Cl content in carbonated and non-carbonated mortar disks.

Sample	Na (mmol/kg)	K (mmol/kg)	S (mmol/kg)	Cl (mmol/kg)
CEM I_{ref}	25.9	30.4	0.3	0.2
	26.4	30.3	0.4	0.3
	24.9	29.3	0.4	0.3
CEM $I_{0.55}$	5.3	2.3	11.0	2.2
	6.2	2.5	12.5	2.6
	5.8	2.4	11.6	2.2
CEM II_{ref}	19.9	25.9	0.1	0.3
	22.0	29.4	0.1	0.3
	21.6	29.0	0.1	0.3
CEM $II_{0.55}$	4.7	1.9	12.2	2.0
	4.5	1.8	11.8	2.0
	4.6	1.8	12.1	1.9

Paper A-III

Carbonation-induced corrosion: investigation of the corrosion onset

Revert, Andres Belda; De Weerdt, Klaartje; Hornbostel, Karla; Geiker, Mette Rica

Construction and Building Materials

https://doi.org/10.1016/j.conbuildmat.2017.12.066

Construction and Building Materials 162 (2018) 847–856

Contents lists available at ScienceDirect

Construction and Building Materials

journal homepage: www.elsevier.com/locate/conbuildmat

Carbonation-induced corrosion: Investigation of the corrosion onset

Andres Belda Revert [a,*], Klaartje De Weerdt [a], Karla Hornbostel [b], Mette Rica Geiker [a]

[a] Norwegian University of Science and Technology, Department of Structural Engineering, Norway
[b] Norwegian Public Roads Administration (Statens vegvesen), Trondheim, Norway

HIGHLIGHTS

- Apparent early carbonation-induced corrosion onset is reported in the literature.
- Conditions for corrosion are met once the mortar-steel interface is carbonated.
- The spatial variation of the carbonation depth is influenced by the reinforcement.
- The apparent early corrosion onset was due to the influence of reinforcement.
- The influence of reinforcement should be considered in service life prediction.

ARTICLE INFO

Article history:
Received 13 September 2017
Received in revised form 5 December 2017
Accepted 8 December 2017

Keywords:
Carbonation
Corrosion onset
pH indicator
Corrosion potential
Petrographic analysis

ABSTRACT

There are different views in the literature on the relationship between the location of the carbonation front and the onset of reinforcement corrosion. Theoretically, corrosion starts when the carbonation front reaches the reinforcement, but some authors have observed an apparent earlier start of corrosion. In the present study, mortar samples with and without reinforcement were exposed for up to 22 weeks to 20 °C, 60% RH and 1.5% CO_2. The state of the reinforcement was monitored by potential measurements. The carbonation of the bulk and the mortar-steel interface was detected by spraying a pH indicator on a freshly split or cut surface. Good agreement was found between low potential values (compared to reinforcement in the passive state) and the carbonation of the mortar-steel interface. A difference in the spatial variation of the carbonation depth was observed between plain and reinforced samples. The differences found in the literature between the location of the carbonation front and the corrosion onset can probably be explained by the spatial variation of the carbonation depth in the vicinity of the reinforcement.

1. Introduction

Corrosion is one of the major causes of deterioration in reinforced concrete structures [1]. Chloride ingress and carbonation are the most common causes of initiation of reinforcement corrosion. Reinforcement embedded in concrete is prevented from corrosion by a thin layer of iron oxides, which is stable in the high-alkaline environment of sound concrete [2]. Upon carbonation, the pH of the pore solution is reduced to values below 7 [3]. The oxide layer is no longer stable in such a low pH and reinforcement embedded in carbonated concrete can corrode depending on the exposure. Differences are found in the literature on the location of the carbonation front and the onset of the reinforcement corrosion. Some authors have observed that reinforcement corrosion can start before the carbonation depth compares to the concrete cover. Table 1 presents a summary of published experimental investigations on carbonation-induced corrosion onset.

Parrott detected corrosion when the difference between the average carbonation depth in plain concrete and the concrete cover (in reinforced samples), the "unneutralized remainder", was 10–15 mm, i.e. he observed corrosion before the apparent carbonation front reached the reinforcement [4,5]. He determined ongoing corrosion by gravimetric analysis of the reinforcement, and the unneutralized remainder from the carbonation depth measurements in plain samples. For further description of materials and exposure conditions, see Table 1. Carbonation development in

Abbreviations: CO_2, carbon dioxide concentration in the air (volume); D_{max}, maximum aggregate size; FA, fly ash; GGBFS, ground-granulated blast-furnace slag; L, limestone; OCP, open circuit potential; pH, pH indicator; RH, relative humidity; SCE, saturated calomel reference electrode; t, time; T, temperature; w/b, water-to-binder ratio; w_x, width of the carbonation front; $x_{c,i}$, carbonation depth measurement "i"; δ_x, spatial variation of the carbonation depth; Ø, reinforcement diameter.

* Corresponding author.
E-mail address: andres.b.revert@ntnu.no (A. Belda Revert).

https://doi.org/10.1016/j.conbuildmat.2017.12.066
0950-0618/

Table 1
Summary of the experimental investigations on carbonation-induced corrosion onset.

Authors		Parrot [4,5]	Yoon et al. [6]	Hussain et al. [7,8]
Materials	Type	Concrete	Concrete	Concrete
	SCMs	FA, GGBFS, L	–	–
	w/b	0.35, 0.47, 0.59, 0.71, 0.83	0.45, 0.5, 0.55	0.45
Geometry	Samples [mm]	Cubes, 100	Prims, length 200	Prims, 200 × 100 × 100
	Cover [mm]	4, 8, 12 and 20	12	13
	D_{max} [mm]	10	25	20
	Ø [mm]	6.4	8	13
Curing	T [°C]	not reported	20	20
	Moisture conditions	Wet cured	Wet cured	Sealed
	t [days]	1, 3, 28	28	28
Exposure	T [°C]	Indoors	20	20
	RH [%]	45–58% outdoors sheltered or exposed	65	55
	CO_2 [%]	0.04%	3, 5, 10	10
Characterization	Carbonation	pH in plain samples	pH in plain samples	pH in plain samples
	Corrosion onset	Gravimetric analysis	Gravimetric analysis, LPR	Corrosion potential
	Criteria for corrosion onset	Weight loss [not reported]	Weight loss 0.2–0.5 g	Potential drop ≈200 mV

FA: fly ash, GGBFS: ground granulated-blast furnace slag, L: limestone, D_{max}: maximum aggregate size, Ø: reinforcement diameter, pH: pH indicator.

the plain samples and corrosion in the reinforced samples were measured after 6, 18 and 48 months of exposure.

Yoon et al. also compared the corrosion onset in reinforced samples with carbonation depth measurements in plain samples. They found that corrosion started before the apparent carbonation front reached the reinforcement, but as long as the unneutralized remainder was more than 5–10 mm in thickness the risk of carbonation-induced corrosion was low [6]. This is in agreement with the findings by Parrott [4,5], although the unneutralized remainder determined is lower. For further description of materials and exposure conditions, see Table 1. Carbonation development was monitored in the plain samples and the corrosion rate in the reinforced samples using linear polarization resistance and gravimetric analysis at the end of the exposure.

In agreement with the above observations, Hussain et al. found that corrosion started when the carbonation depth in plain samples was 80% of the concrete cover [8]. For further description of materials and exposure conditions, see Table 1. The corrosion potential was monitored during the exposure and the corrosion rate was estimated from gravimetric analysis of the reinforcement after exposure. Corrosion onset was identified by a potential drop of 200 mV.

The above observations are also reflected in JSCE Guidelines, which state that corrosion starts before the carbonation front reaches the reinforcement: *"It has been learned from laboratory tests and investigations on actual structures that the corrosion of steel may begin before the carbonation depth actually exceed(s) the cover thickness"* [9]. According to the JSCE, to avoid corrosion onset the unneutralized remainder should be at least 10 mm, and as much as 25 mm if chlorides are present. No references are given to support these statements.

In this study, we investigated three possible hypotheses that could explain the apparent early onset of carbonation-induced reinforcement corrosion:

1. Width of carbonation front (w_x). When detecting carbonation, there will be a volume where the investigated property changes from sound to carbonated concrete. The detected width of this carbonation front depends on the characterisation method used [10]. A large carbonation front width could lead to conditions for corrosion onset before carbonation can be detected at the level of the reinforcement.
2. Spatial variation of carbonation depth:
   2.1. Spatial variation in plain samples (δ_x). The spatial variation in the carbonation depth measured in plain samples could induce corrosion on parts of the reinforcement before the average carbonation depth reaches the level of the reinforcement.
   2.2. Spatial variation in reinforced samples (δ_x). Differences in microstructure between plain and reinforced samples could induce differences in the spatial variation of the carbonation depth and faster carbonation in the vicinity of the reinforcement.

Fig. 1 illustrates the nomenclature used. Moreover, when we refer to the data from the literature, all the authors detected the carbonation in plain samples, so the term "apparent" carbonation front is used.

Mortar samples varying in size and reinforcement position were prepared using 3 different compaction methods. The samples were sealed, cured for 2 weeks, and exposed to accelerated carbonation for up to 22 weeks. The state of the embedded steel was monitored by potential measurements. The carbonation of the bulk and the mortar-steel interface was studied by spraying a pH indicator on a freshly split or cut surface. In addition, thin sections were investigated using optical microscopy. We found that the embedded steel affects the spatial variation of the carbonation depth, possibly due to differences in microstructure between plain and reinforced samples. These differences cannot be attributed to the specific materials or the exposure; similar observations were reported in a field assessment [11]. Based on these observations, monitoring carbonation development in plain samples and assuming similar carbonation development in reinforced samples might give non-conservative prediction of the corrosion onset.

2. Experimental

A set of plain and reinforced mortar samples with different geometries were prepared using various compaction methods:

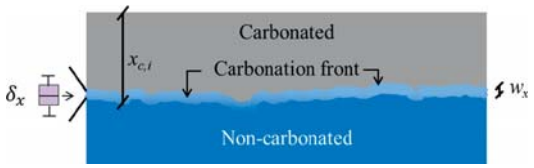

Fig. 1. Nomenclature used: δ_x: spatial variation of the carbonation depth, $x_{c,i}$: carbonation depth measurement "i", w_x: width of the carbonation front. The sketch illustrates carbonation detected using a pH indicator, adapted from previous work [10].

jolted (J), vibrated (V) and tapped (T). Table 2 summarizes the experimental matrix.

2.1. Geometry

Reinforced (A, B and C) and plain (A′ and C′) mortar samples were prepared. The reinforced samples contained ribbed carbon steel bars (Ø 6 mm) embedded in different positions, but always with a 10 mm cover, see Fig. 2. Type A samples contained only one reinforcement bar, type B three bars, and type C eight bars (for labelling of the bars, cf. Fig. 2). In addition, one stainless steel bar was embedded in the middle of the C samples, cf. Fig. 2. In the following sections, the samples are labelled as follows: <sample type>-<compaction method>-<bar position>, e.g. 120 × 80 × 160 mm tapped samples with reinforcement in position 1 are labelled: C-T-1.

2.2. Mortar composition and reinforcement

The mortar samples contained Portland-fly ash cement (CEM II/B-V in accordance with EN-197-1 [12]) supplied by NORCEM AS and standard sand in accordance with EN 196-1 [13] (D_{max} 2 mm). Filtered tap water was used for the mixing. The XRF analysis of the cement given by NORCEM AS is: 29.5% SiO_2, 10.8% Al_2O_3, 4.5% Fe_2O_3, 44.6% CaO, 2% MgO, 3.2% SO_3, 0.4% P_2O_5, 1.1% K_2O, 0.5% Na_2O, and 0.03 chlorine.

The recipe was based on EN 196-1 [13], but the cement and water content was adjusted to obtain w/b 0.55, keeping the volumetric paste-sand ratio constant. Two batches (each approximately 12 Ls) were required to cast all the samples. The following amount of each component was required per batch: 4355 g of cement, 2395 g of water and 13,500 g of sand. The mixing steps were as defined in EN 196-1 [13], except that the mixer was used with a constant mixing speed. Water and binder were placed in the mixing bowl and the mixer was immediately started. After 30 s of mixing, sand was added steadily over the next 30 s, and the mortar was mixed for 30 more seconds once all the sand had been added. The mixing was stopped for 90 s while the mortar adhering to the wall and bottom of the bowl was detached and moved to the middle of the bowl. Finally, the mixing was continued for another 60 s. Ribbed carbon steel bars 6 mm in diameter (B500NC in accordance with NS 3576 [14]) were used as reinforcement, and an additional AISI 2205 6 mm bar was embedded in the middle of the type C samples for use as a pseudo-reference electrode. The reinforcement was cut into 160 mm pieces and both ends were polished. The steel was cleaned in HCl containing urotropine (HCl 1:1 + 3 g/l urotropine), placed in an ultrasonic bath for 5 min, rinsed with distilled water, and dried using a hairdryer. Finally, 30 mm of both ends of each bar were coated with beeswax by dipping the reinforcement into the melted wax twice. The reinforcement pieces were kept in a desiccator including a drying agent (silica gel), until they were embedded in mortar.

2.3. Preparation of the samples

Three compaction methods were used to prepare the samples: jolting, vibrating table, and tapping. Jolting is the standard compaction method for mortar samples according to EN 196-1 [13], in which the moulds are filled in two layers, applying sixty jolts per layer. For the vibrating table compaction, 20 mm layers were compacted by applying 5 s of vibration, frequency 50 Hz and vertical amplitude 0.65 mm, to each layer. The mould was firmly held against the vibrating table during compaction. The vibration time was selected on the basis of the cessation of air bubbles and limited bleeding. For the tapping compaction, a 6 mm diameter, smooth, straight, stainless steel rod with rounded ends was used. 20 mm layers were tapped compact by applying 30 strokes per layer uniformly distributed over the cross section of the mould. The first layer was compacted without tapping the bottom of the mould and the subsequent layers were compacted avoiding penetration of the previous layers. At the end, the sides of the mould were gently tapped with the steel rod until large air bubbles ceased to appear.

The samples were kept in the moulds covered with plastic for one day after casting at room temperature (approx. 20 °C). Then they were demoulded, wrapped in plastic, and stored at 20 °C for 13 days.

2.4. Exposure

After the 14 curing days, the samples were exposed to 20 °C, 60 ± 2% RH, and 1.5 ± 0.1% CO_2 for up to 22 weeks in climate cabinets with forced ventilation, which were set up to ensure homogeneous exposure conditions for the samples.

2.5. Methods

2.5.1. Open circuit potential (OCP)

The open circuit potential (OCP) of the embedded steel was monitored using an external saturated calomel reference electrode (SCE) and a high impedance voltmeter (Fluke 76, input impedance 10 MΩ). Ultrasound gel was applied on the mortar surface to provide electrical contact. The OCP was monitored twice a week.

Table 2
Summary of samples and measurements. Reinforced (A, B and C) and plain (A′ and C′).

Samples				Property investigated				
				OCP		Carbonation		Micro-structure
Id.	Size [mm]	Compaction method	No.	Bars	Duration [weeks]	Bulk	Mortar-steel interface	
A	40 × 40 × 160	Jolted (J)	2	1	20	x	–	–
		Vibrated (V)	1	1	20	x	–	–
		Tapped (T)	1	1	20	x	–	–
A′	40 × 40 × 160	Jolted (J)	1	–	–	x	–	–
		Vibrated (V)	1	–	–	x	–	–
		Tapped (T)	1	–	–	x	–	–
B	120 × 40 × 160	Vibrated (V)	1	3	20	–	–	–
		Tapped (T)	1	3	20	–	–	–
C	120 × 80 × 160	Vibrated (V)	1	8	10	x	x	–
		Tapped (T)	1	8	10	x	x	x
C′	120 × 80 × 160	Vibrated (V)	1	–	–	x	–	–
		Tapped (T)	1	–	–	x	–	–

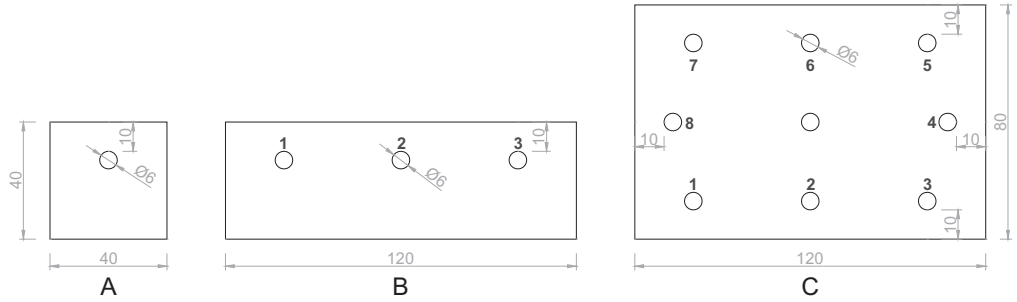

Fig. 2. Reinforced mortar samples [mm]. A′ and C′ plain mortar samples have the same geometry as A and C. Numbers refer to the position of steel bars. The mortar was poured from the top.

2.5.2. Carbonation characterization

Carbonation was detected by spraying a thymolphthalein solution on either a freshly split or a freshly dry-cut sample. Pictures were taken using an Olympus E-630 camera attached to a set-up with fixed lighting conditions. The thymolphthalein solution was prepared by dissolving 1 g of the indicator (powder, grade "ACS, Reag. Ph Eur" (VWR)) in a mix of 30 ml of deionized water and 70 ml of ethanol. The colour change of thymolphthalein occurs in the pH range of 9 to 10.5. Above this range, an intense bluish colour is observed while, below it, thymolphthalein becomes colourless. Phenolphthalein is the pH indicator recommended for detecting carbonation according to EN 13295 [15], but it has been classified as carcinogenic [16]. We have previously tested thymolphthalein on the same materials and exposure, and observed similar carbonation depths to those found with phenolphthalein [10].

The distribution of the carbonation depth was determined by image analysis using a colour threshold principle. First, the pictures were scaled, then the sample area and the non-carbonated area were determined, and finally the carbonation depths were measured. When taking measurements, we avoided the corners (due to the ingress from two directions).

The carbonation of the mortar-steel interface was investigated by splitting reinforced samples longitudinally and spraying the imprint of the reinforcement bar (the mortar-steel interface) with thymolphthalein. To quantify the carbonated fraction of the mortar-steel interface, the colour threshold of the pictures was manually adjusted to differentiate more clearly between the carbonated and non-carbonated areas. Next, the interface was discretized in a 1×1 mm grid and the state of each cell was assessed (carbonated or non-carbonated). A geometric factor was applied to take into account the circular shape of the reinforcement. The mortar-steel interface of the reinforcement bars in some of the vibrated samples could not be investigated, because the samples broke into small pieces when split longitudinally.

2.5.3. Petrographic analysis of thin sections

Thin sections were prepared at the Danish Technological Institute in accordance with Nordtest [17] for a general investigation of the microstructure. The samples were impregnated with an epoxy resin containing fluorescent dye, mounted on a glass plate, ground to a thickness of 20 μm, and then covered with a second glass plate. The thin sections prepared included reinforcement located in three different positions (bottom, middle and top) from sample C-T. The thin sections were prepared after 22 weeks of exposure (after corrosion onset). The thin sections were investigated with an optical microscope Nikon Eclipse LV 100 POL using transmitted, crossed polarized and fluorescent light.

3. Results

3.1. Open circuit potential (OCP)

Fig. 3 presents the OCP measurements in the A and B samples over 20 weeks. Fig. 4 presents a summary of the OCP measurements in the C samples over the first 10 weeks of exposure. The mortar-steel interface of the C samples was investigated after 10 weeks of exposure.

3.2. Carbonation depth

Fig. 5 presents the carbonation investigation of the A′ samples. The carbonation front presented a trapezoidal shape in the jolted samples, indicating separation in these samples. The other two compaction methods seem to have caused less segregation, leaving the top and lateral sides comparable. The impact of an air bubble is observed in the tapped sample (Fig. 5, right). Fig. 6 shows the carbonation front in the C′-T and C-T samples after 10 and 22 weeks of exposure. Similar trends were observed in the vibrated samples, which are not shown here. Fig. 7 presents the histograms of the carbonation depth measurements taken in the plain C′-T after 10 and 22 weeks of exposure. The data set includes the measurements from the top and lateral sides. Figs. 8 and 9 present the carbonation of the mortar-steel interface for the reinforced C-T and C-V samples after 10 weeks of exposure. Note that the data from the vibrated samples is limited due to problems with the sampling.

3.3. Petrographic analysis of thin sections

Fig. 10 presents micrographs taken by Ulla Hjorth Jakobsen (DTI) and sketches of microcracking observed. Photographs using fluorescent lighting were taken close to the reinforcement in the top, middle and bottom positions. A radial crack pattern was observed in the vicinity of the reinforcement in the top and middle positions, while fewer cracks and a different pattern were observed in the vicinity of the bottom reinforcement. According to Ulla Hjorth Jakobsen, all the cracks observed were formed during the plastic stage and were smaller than 10 μm. If we compare the greenish colours of the micrographs, a small difference in porosity can be observed between the thin sections from the bottom and the top and middle positions. However, it was not possible to quantify this difference.

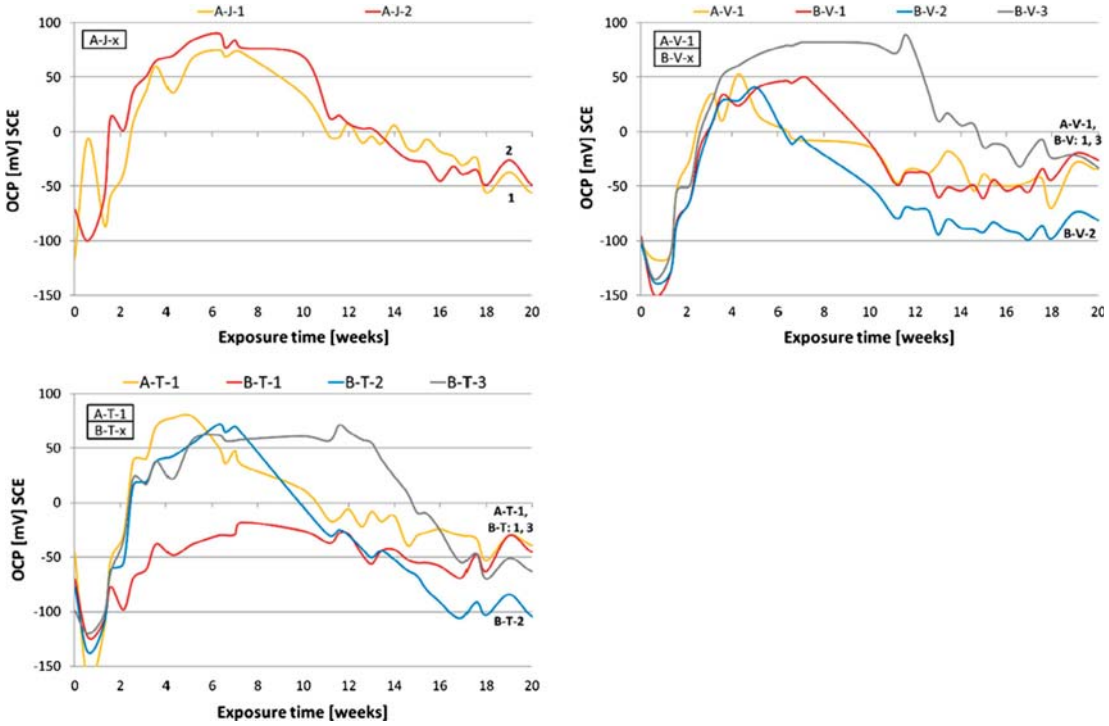

Fig. 3. OCP of jolted (J), vibrated (V) and tapped (T) 40 × 40 × 160 (A) and 120 × 40 × 160 mm (B) samples over the first 20 weeks of exposure at 20 °C, 60% RH, and 1.5% CO_2.

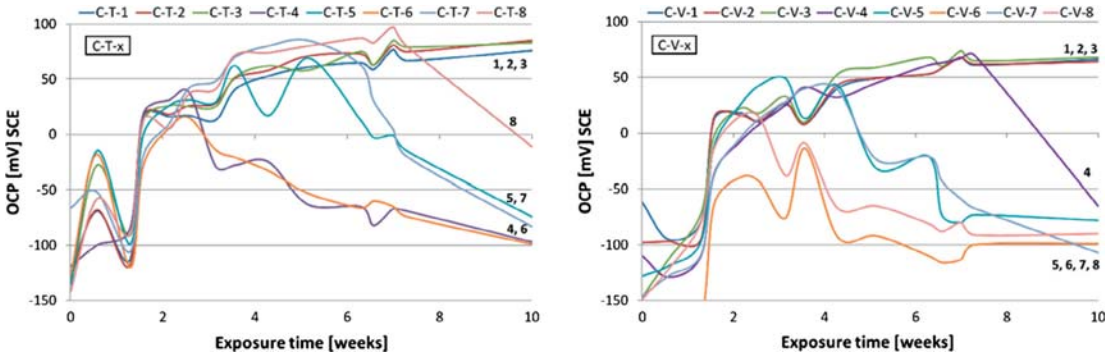

Fig. 4. OCP of tapped (T) and vibrated (V) 120 × 80 × 160 mm (C) samples over 10 weeks of exposure at 20 °C, 60% RH, and 1.5% CO_2.

4. Discussion

4.1. Relationship between carbonation of the mortar-steel interface and the OCP

The pictures shown in Figs. 8 and 9 were used to quantify the carbonated fraction of the mortar-steel interface. In Fig. 11, the carbonated fraction of the interface is plotted against the OCP for each reinforcement bar at the time the samples were split (after 10 weeks of exposure). During the carbonation of the mortar-steel interface, there seems to be a gradual change towards more negative OCP values. Similar OCP trends were observed during carbonation in all the samples regardless the compaction method. Although the data is limited, we found that the carbonated fraction of the mortar-steel interface correlates with the OCP measured. For steel embedded in non-carbonated mortar, OCP in the range of +60 to +90 mV vs. SCE was measured, whereas when the carbonated fraction of the mortar-steel interface exceeded 75% the values gathered around −70 to −110 mV vs. SCE. Overall, we observed that a drop of approx. 140–200 mV in the OCP indicated the complete carbonation of the mortar-steel interface. The OCP remained within the same range after the onset of corrosion, see Fig. 3. On this basis, we conclude that the OCP drop was due to the carbonation of the mortar-steel interface rather than other factors, e.g. moisture changes.

RILEM TC-235 CTC defines the onset of chloride-induced corrosion as follows: "*significant drop of the measured potential, and the*

Fig. 5. Carbonation detection in the plain A′ (40 × 40 × 160 mm) mortar samples. From left to right: cross sections of A′-J, A′-V and A′-T. The samples were sprayed with thymolphthalein after 8 weeks of exposure.

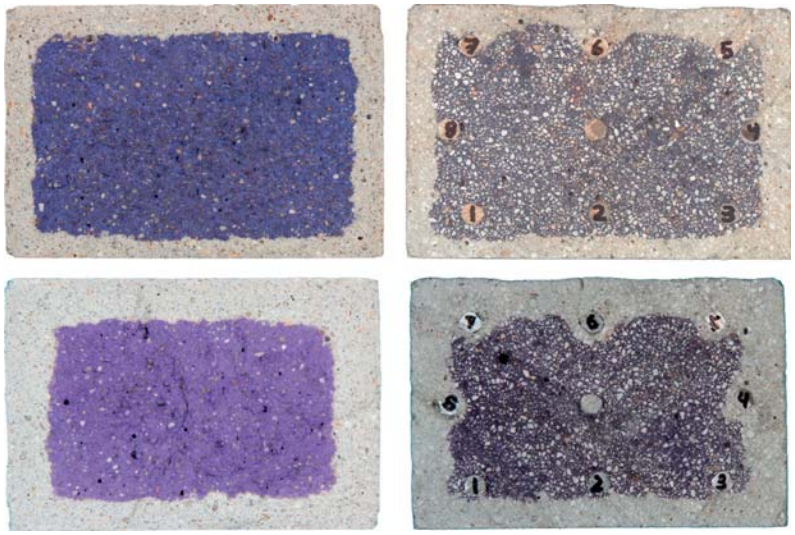

Fig. 6. Carbonation detection in C′-T and C-T samples (120 × 80 × 160 mm). Cross sections sprayed with thymolphthalein after 10 weeks (top) and 22 weeks (bottom) of exposure.

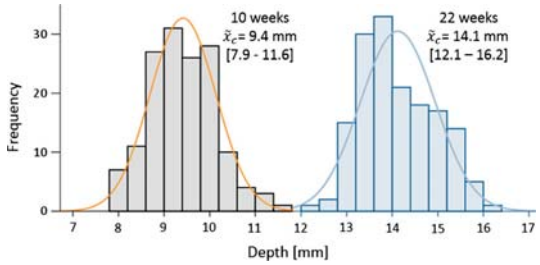

Fig. 7. Carbonation depth histograms of the plain C′-T mortar sample after 10 and 22 weeks of exposure, giving average and range. The line shows the normal distribution curve.

corrosion activity is defined as being stable when the potential has dropped and remained at a potential at least 150 mV lower than the passive level for more than 7 days" [18]. The literature reports a similar potential drop for carbonation-induced corrosion [7,8], which is in agreement with the present study. However, for carbonation-induced corrosion, the time required for stable OCP indicating corrosion seems to be longer. In the present study, a gradual change in OCP towards more negative values was observed. The change in potential took from 4 to 10 weeks depending on the sample, see Fig. 3. We attribute the gradual change in OCP to the steady carbonation of the mortar-steel interface, as shown in Fig. 11. In contrast to what is typically seen for chloride-induced corrosion, there was no indication of re-passivation of the steel embedded in the carbonated mortar within the test period.

4.2. Width of the carbonation front

When detecting carbonation using a pH indicator, the pH threshold of the indicator should be taken into account. In a previous investigation, we compared a set of pH indicators, including phenolphthalein (pH 8.2–9.8) and thymolphthalein (pH 9–10.5) among other indicators [19]. Comparable carbonation depths were measured and all the indicators illustrated a sharp drop in pH and a narrow carbonation front width for the tested materials and exposure conditions. According to the Pourbaix diagram [20] for Fe-H_2O (10^{-6} mol/L), active corrosion starts at approx. pH 7 [21] for the OCP range measured. For this simplified system, therefore, active corrosion is not expected before thymolphthalein becomes colourless. The observations indicate that the width of the carbonation front may not have caused the early corrosion onset reported in

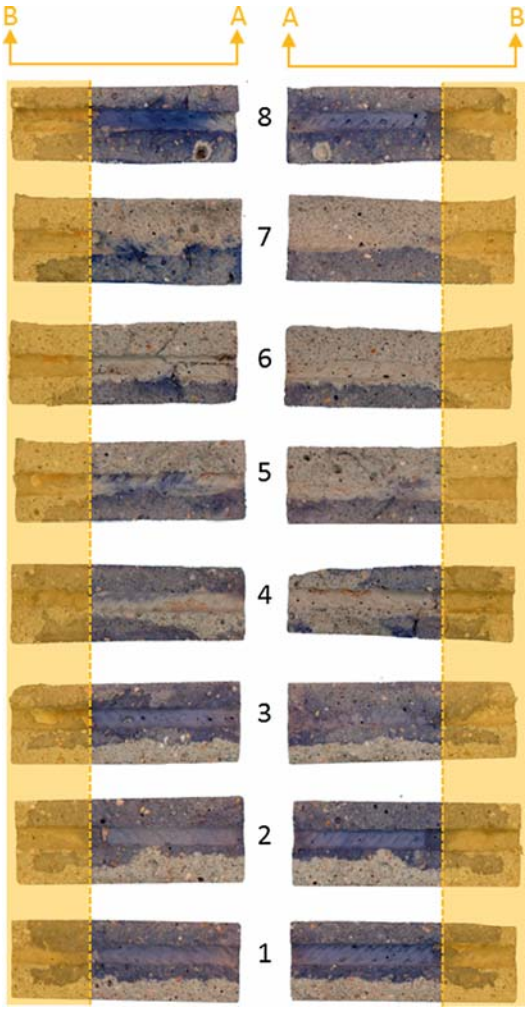

Fig. 8. Carbonation investigation of the mortar-steel interface of the C-T sample after 10 weeks of exposure. The shaded areas represent the length of the reinforcement which was coated with beeswax.

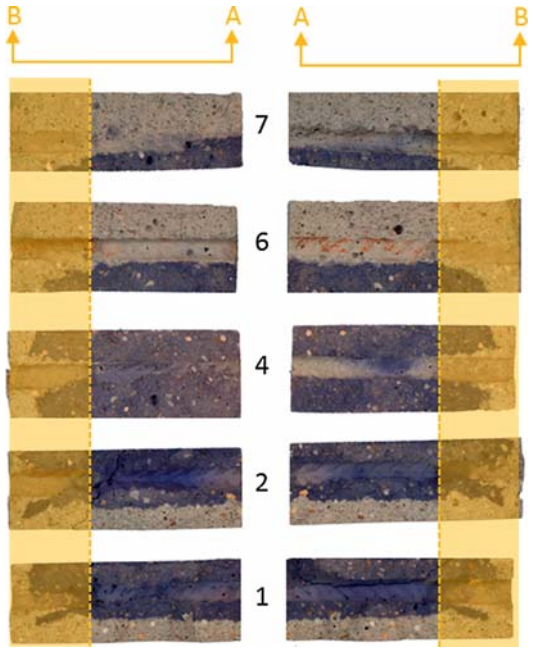

Fig. 9. Carbonation investigation of the mortar-steel interface of the C-V sample after 10 weeks of exposure. The shaded areas represent the length of the reinforcement which was coated with beeswax.

the literature. However, cementitious materials do contain some chloride, and during carbonation the pH drops, which might increase the $[Cl^-]/[OH^-]$ ratio in the pore solution and thus the probability of corrosion.

4.3. Spatial variation of the carbonation depths in plain samples

For the plain tapped samples (C′), the carbonation depth on the top and lateral sides merged together is normally distributed (Fig. 7). After 10 weeks of exposure, the average carbonation depth was 9.4 mm and the standard deviation of 0.7 mm. Assuming a cover depth of 10 mm and a reinforcement diameter of 6 mm, as used in the reinforced samples, the carbonation of the mortar embedding the steel would have been complete when the carbonation front had penetrated up to 16 mm. In Fig. 12, the carbonation depth distribution in the plain mortar samples after 10 weeks of exposure is compared with the position of the reinforcement in the reinforced samples. After 10 weeks of exposure, 20% of the carbonation depth population in the plain mortar samples was higher than the cover (10 mm). Part of the steel was therefore embedded in carbonated mortar when the average value of the carbonation front was 9.4 mm. If we assume that the mortar is uniformly carbonated to a depth of 11.6 mm (worst-case scenario), 20% of the steel surface would be embedded in carbonated mortar. Considering the relationship between the carbonated fraction of mortar-steel interface and the OCP presented in Fig. 11, positive OCP values are expected at this stage. Nevertheless, corrosion onset indicated by low potential values was observed for several of the rebars after 10 weeks (see Figs. 3 and 4), which cannot be explained by the spatial distribution of the carbonation depth in the plain samples.

4.4. Spatial variation of the carbonation depth in reinforced samples

The observations made by Parrott [4,5], Hussain et al. [6], and Yoon et al. [7,8] were based on carbonation depth measured in plain samples. In the present investigation, we found that the presence of reinforcement has an impact on the spatial variation of the carbonation depth (cf. Fig. 6). Fig. 13 shows the carbonation depth distribution of the reinforced tapped (C-T) sample after 22 weeks of exposure. The carbonation depth was measured in areas without reinforcement (“M”) and in the vicinity of the reinforcement (“R”). The data set includes the measurements from the top and lateral sides. The measurements are grouped in two populations: population “M”, which is similar to the carbonation depth measured in the plain tapped (C-T) sample (Fig. 7), and population “R”, which presented higher carbonation depths. This shows that the reinforcement influenced the spatial variation of the carbonation depth distribution. The impact of embedded steel on carbonation development has also been observed by Köliö et al. [11], who

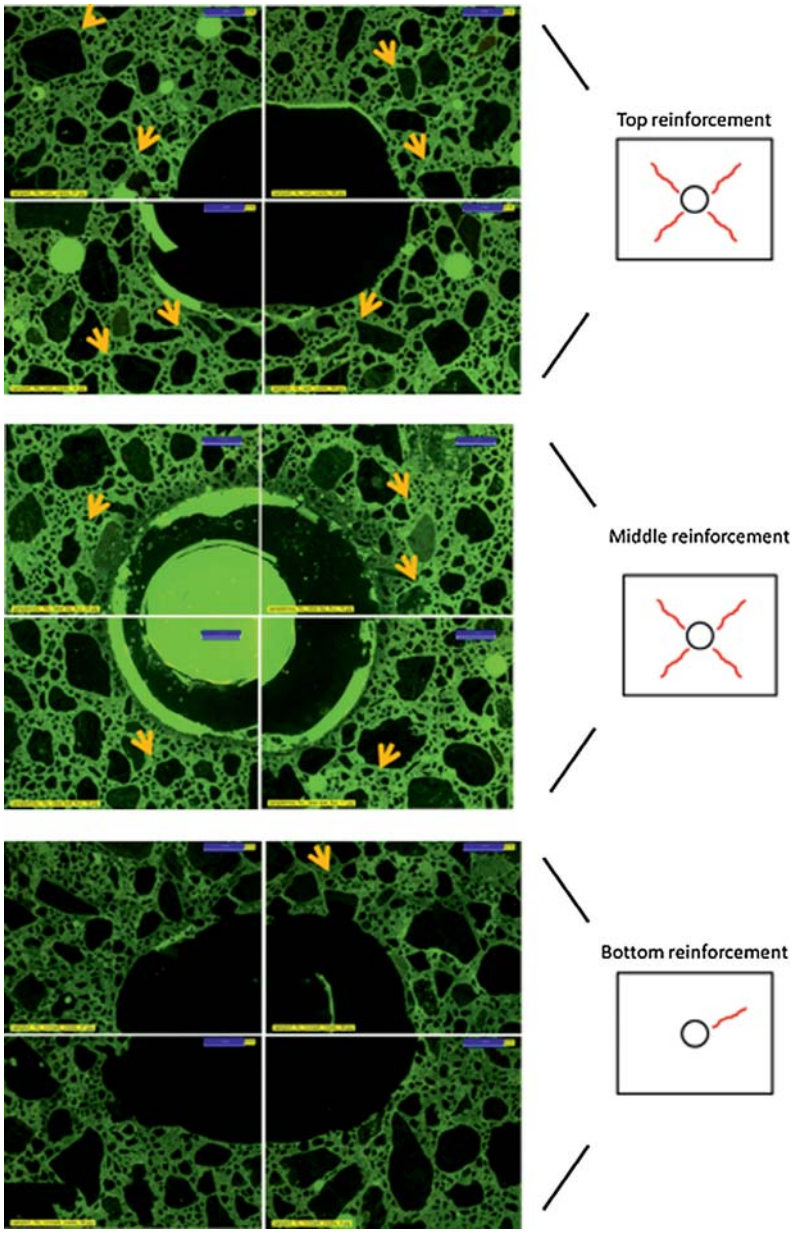

Fig. 10. Micrographs taken in fluorescent light using an optical microscope with magnification ×16 (width of each micrograph 6.5 mm) on the C–T sample after 22 weeks of exposure. Arrows indicate the cracks observed. Crack patterns observed in the top, middle and bottom reinforced samples are included in the sketches on the right.(For interpretation of the references to colour in this figure legend, the reader is referred to the web version of this article.)

report deeper carbonation depths in the vicinity of the reinforcement in cores extracted from façades exposed to natural carbonation.

A recent publication presented an overview of the characteristics of the concrete-steel interface [22]. One of the characteristics is the so-called "top-bar effect", which is defined as void formation under the horizontal rebars located mainly in the upper parts of the structural members as a result of segregation, settlement, and bleeding of fresh concrete [23]. This top-bar effect is observed to increase the higher in a cast section the position of the reinforcement is. Based on the shape of the carbonation front, which is evenly distributed around the top and middle reinforcements and the observation of micro-cracks radiating in all directions from the top and middle reinforcements (see Fig. 10), we attribute the deeper carbonation depth in the vicinity of the reinforcement to these microstructural defects rather than to the top-bar effect. The assessment of the mortar-steel interface (see Figs. 8 and 9) indicated no bleeding underneath any of the rebars.

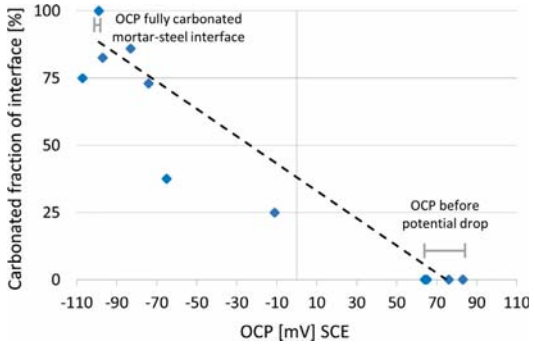

Fig. 11. Relationship between the carbonated fraction of the mortar-steel interface and the OCP measured in the C samples. 100% means complete carbonation of the mortar-steel interface and 0% means no carbonation.

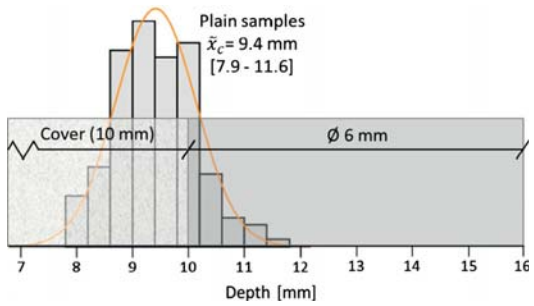

Fig. 12. Comparison of the measured carbonation depth distribution in plain samples (type C′) after 10 weeks (the lateral and top sides merged together) with the position of reinforcement in the reinforced samples. Note that the horizontal axis starts at 7 mm.

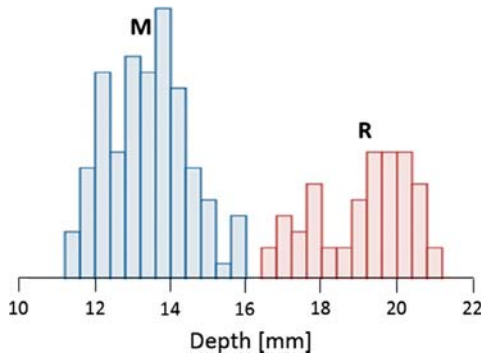

Fig. 13. Carbonation depth distribution in C-T sample after 22 weeks of exposure. M: bulk mortar and R: vicinity of the reinforcement. Note that the horizontal axis starts at 10 mm.

5. Conclusions

The aim of the present study was to investigate the conditions for carbonation-induced corrosion onset. In the literature, it has been observed that corrosion can initiate before the apparent carbonation depth (measured in parallel plain samples) compares to the depth of the reinforcement. Plain and reinforced mortar samples were prepared. The samples were exposed to 20 °C, 60% RH and 1.5% CO_2 for up to 22 weeks. The open circuit potential (OCP) of the embedded steel was monitored and the carbonation development was followed by periodically spraying freshly split or dry-cut samples with thymolphthalein. The microstructure of the mortar around the rebars was investigated by optical microscopy on thin sections. The following conclusions can be drawn:

1. When plain and reinforced mortar samples are compared, corrosion onset is observed before the carbonation depth in the plain mortar samples compares to the cover depth of the reinforced samples. This apparent early corrosion onset is in agreement with the literature.
2. Neither the width of the carbonation front nor the spatial distribution of the carbonation depth in the plain samples can explain this apparent early corrosion onset.
3. However, the spatial variation of the carbonation depth was different in the reinforced and the plain mortar samples. Increased carbonation depth in the vicinity of the reinforcement was observed in the reinforced samples, which can explain the apparent early onset of corrosion reported in the literature.
4. Good agreement was observed between the carbonation of the mortar-steel interface and the corrosion potential drop. Corrosion does not start until the mortar-steel interface is (partially) carbonated.
5. When predicting carbonation-induced corrosion onset in field structures, the potential influence of reinforcement in carbonation development should be taken into account to avoid a non-conservative prediction.

Acknowledgements

The current paper is part of a larger research project, 'Lavkarbsem' (NFR project no. 235211/O30). The project is supported by the Norwegian Research Council and the following companies: Mapei AS, Norbetong AS, Norcem AS, Skanska AS, and Rambøll Engineering AS. The authors would also like to thank Marit Haugen (SINTEF) and Ulla Hjorth Jakobsen (DTI) for their assistance with the optical microscopy and Helga Synnøve Kjos-Hanssen and Elisabeth Leite Skare (NTNU) for their assistance in the laboratory.

References

[1] P. Bamforth, Enhancing reinforced concrete durability: Guidance on selecting measures for minimising the risk of corrosion of reinforcement in concrete. Concrete Society Technical Report No. 61, Camberley, United Kingdom, 2004.
[2] L. Bertolini, B. Elsener, P. Pedeferri, E. Redaelli, R. Polder, Chapter 5: carbonation-induced corrosion, in: Corrosion of Steel in Concrete: Prevention, Diagnosis, Repair, second ed., Wiley-VCH Verlag GmbH & Co, Weinheim, Germany, 2013, pp. 79–92.
[3] D.J. Anstice, C.L. Page, M.M. Page, The pore solution phase of carbonated cement pastes, Cem. Concr. Res. 35 (2) (2005) 377–383, https://doi.org/10.1016/j.cemconres.2004.06.041.
[4] L.J. Parrott, A study of carbonation-induced corrosion, Mag. Concr. Res. 46 (166) (1994) 23–28, https://doi.org/10.1680/macr.1994.46.166.23.
[5] L.J. Parrott, Some effects of cement and curing upon carbonation and reinforcement corrosion in concrete, Mater. Struct. 29 (3) (1996) 164–173, https://doi.org/10.1007/bf02486162.
[6] I.-S. Yoon, O. Çopuroğlu, K.-B. Park, Effect of global climatic change on carbonation progress of concrete, Atmos. Environ. 41 (34) (2007) 7274–7285, https://doi.org/10.1016/j.atmosenv.2007.05.028.
[7] R. Hussain, T. Ishida, Critical carbonation depth for initiation of steel corrosion in fully carbonated concrete and development of electrochemical carbonation induced corrosion model, Int. J. Electrochem. Sci. 4 (8) (2009) 1178–1195.
[8] R.R. Hussain, T. Ishida, M. Wasim, Experimental investigation of time dependent non-linear 3D relationship between critical carbonation depth and corrosion of steel in carbonated concrete, Corr. Eng. Sci. Technol. 46 (5) (2011) 657–660, https://doi.org/10.1179/147842210X12659647007086.
[9] Japan Society of Civil Engineers, Standard specifications for concrete structures: design, JSCE Guidelines for Concrete No. 15, 2007.

[10] A. Belda Revert, K. De Weerdt, K. Hornbostel, M.R. Geiker, Carbonation characterization of mortar with portland cement and fly ash, Comp. Tech. Nordic Concr. Res. 54 (1) (2016) 60–76.
[11] A. Köliö, M. Honkanen, J. Lahdensivu, M. Vippola, M. Pentti, Corrosion products of carbonation induced corrosion in existing reinforced concrete facades, Cem. Concr. Res. 78 (Part B) (2015) 200–207, https://doi.org/10.1016/j.cemconres.2015.07.009.
[12] EN-197-1, EN 197-1 Cement – Part 1: composition, specifications and conformity criteria for common cements, 2011.
[13] EN-196, EN 196-1:2005: Methods of testing cement – Part 1: determination of strength, 2005.
[14] NS-3576-3, NS-3576-3:2012. Armeringsståal. Mål og egenskaper. Del 3: Kamstål B500NC. (Steel for the reinforcement of concrete. Dimensions and properties. Part 3: Ribbed carbon steel B500NC), 2012.
[15] EN-13295, EN 13295:2003: Products and systems for the protection and repair of concrete structures. Test methods. Determination of resistance to carbonation, 2003.
[16] Norwegian Environment Agency, 2015.
[17] Nordtest, Concrete, Hardened: Water-Cement Ratio – NT Build 361, 1999.
[18] RILEM TC 235-CTC Final test report on DTI's participation in round robin test, 2014.
[19] A. Belda Revert, K. De Weerdt, M.R. Geiker, Carbonation front characterization pH colour indicators, in: 35th Cement and Concrete Science Conference, Aberdeen, Scotland, 2015.
[20] M. Pourbaix, Atlas of Electrochemical Equilibria in Aqueous Solutions, NACE International, Houston, USA, 1974.
[21] A. Küter, Management of Reinforcement Corrosion – A Thermodynamic Approach, Technical University of Denmark, 2009.
[22] U.M. Angst, M.R. Geiker, A. Michel, C. Gehlen, H. Wong, O.B. Isgor, B. Elsener, C. M. Hansson, R. François, K. Hornbostel, R. Polder, M.C. Alonso, M. Sanchez, M.J. Correia, M. Criado, A. Sagüés, N. Buenfeld, The steel–concrete interface, Mater. Struct. 50 (2) (2017) 143.
[23] R. Zhang, A. Castel, R. François, Influence of steel–concrete interface defects owing to the top-bar effect on the chloride-induced corrosion of reinforcement, Mag. Concr. Res. 63 (10) (2011) 773–781.

Paper A-IV

Macrocell corrosion in carbonated Portland and Portland-fly ash concrete - contribution and mechanism

Revert, Andres Belda; Hornbostel, Karla; De Weerdt, Klaartje; Geiker, Mette Rica

Submitted to Cement and Concrete Research

Macrocell corrosion in carbonated Portland and Portland-fly ash concrete - contribution and mechanism

Andres Belda Revert[1], Karla Hornbostel[2], Klaartje De Weerdt[1], Mette Rica Geiker[1]

[1]*Norwegian University of Science and Technology. Department of Structural Engineering.*
andres.b.revert@ntnu.no

[2]*Norwegian Public Road Administration (Statens vegvesen), Trondheim, Norway*

Abstract

The corrosion of reinforcement in moist carbonated concrete was measured with and without electrical connection to reinforcement in non-carbonated concrete. The impact of the fly ash content, casting position (microstructure), and cathode-to-anode ratio was studied. A model was applied to quantify the contribution of the anodic, cathodic and ohmic partial processes to the macrocell corrosion.

The total current density was high in all cases regardless the cement type. The governing partial process depends on the cathode-to-anode ratio.

Keywords:

C. Carbonation

C. Corrosion

D. Blended cement

D. Fly ash

E. Concrete

Nomenclature/definitions:

Microcell (uniform) corrosion: the corrosion process in which the anodic and cathodic sites are randomly distributed and continuously alternating. The oxidation of the metal and reduction of oxygen (or hydrogen) take place in adjacent places on the same metal part.

Macrocell (galvanic) corrosion: the corrosion process in which the oxidation of the metal and reduction of oxygen (or hydrogen) take place in defined and spatially separated places that can be either on the same metal part or on two different metal parts that are electrically connected.

AC-EIS (EIS): alternating electrochemical impedance spectroscopy

C/A: cathode-to-anode area ratio [-]

CE: counter electrode

i: current density [$\mu A/cm^2$]

i_{mi-A}: microcell current density when there is no macrocouple [$\mu A/cm^2$]

i_{mi-A+C}: microcell current density in the active electrode of the macrocouple [$\mu A/cm^2$]

i_g: macrocell (galvanic) current density in the active electrode of the macrocouple [$\mu A/cm^2$]

I_g: galvanic current intensity [μA]

LPR: linear polarization resistance

m_{A-an}: activation control slope for active reinforcement [mV/Dec]

m_{A-cath}: activation control slope for passive reinforcement [mV/Dec]

m_{C-an}: activation control slope for sample C anodic reaction [mV/Dec]

m_{C-cath}: activation control slope for sample C cathodic reaction [mV/Dec]

OCP: open circuit potential [mV]

PC: Portland cement

PCFA: Portland-fly ash cement

PDP: potentiodynamic polarization curve

$R_{A\text{-}C}$: electrical resistance between reinforcement in carbonated concrete and non-carbonated concrete [Ω]

RE: reference electrode

RH: relative humidity [%]

R_P: polarization resistance [Ω]

SCE: external saturated calomel reference electrode

w/c: water-to-cement ratio [-]

WE: working electrode

ZRA: zero resistance ammeter

ΔE_A: anodic polarization of active steel (anode) when coupled with passive steel [mV]

$\Delta E_{A\text{-}C}$: difference in potential between active and passive steel when coupled [mV]

ΔE_C: cathodic polarization of passive steel when coupled with active steel [mV]

ρ: electrical resistivity of concrete [Ω·m]

1. Introduction

1.1. Corrosion of reinforcement in carbonated concrete

Carbonation is the spontaneous reaction of the CO_2 present in the atmosphere with hydrated cement. Reinforcement embedded in sound concrete is covered with a thin oxide layer which protects the reinforcement from further corrosion [1]. Once the carbonation front reaches the reinforcement and the concrete-steel interface is carbonated, active corrosion can develop, mainly depending on the moisture content [2].

The corrosion process of steel embedded in carbonated concrete comprises four complementary processes: the oxidation of the iron at the anodic site, the reduction of oxygen or hydrogen at the cathodic site, the transport of electrons through the reinforcement, and the transport of ions through the concrete. At any given time, the most restrictive process controls the overall corrosion process. [1] Microcell corrosion (uniform) occurs when both the anodic and cathodic reactions take place randomly at neighbouring sites on the same metal part [3]. Macrocell corrosion takes place when the anodic sites are spatially separated from the cathodic sites. Two kinds of macrocell corrosion can occur [4]: face-to-face (e.g. a reinforcement bar fully embedded in carbonated concrete electrically connected with a bar embedded in non-carbonated concrete) or coplanar (e.g. a reinforcement bar which is partially embedded in carbonated and partially embedded in non-carbonated concrete).

Carbonation is usually assumed to lead to microcell (uniform) corrosion in the depassivated fraction of the reinforcement. However, carbonation is a process over time and space, so parts of the reinforcement will remain passive due to either the progress and spatial variation of the carbonation front [2], or the reinforcement layout. This leads to macrocell corrosion in carbonated concrete.

In the current investigation, we studied the extent to which the face-to-face macrocell contribution to the total corrosion rate is relevant, and the potential influence of selected parameters: fly-ash addition, microstructure (casting position), and the cathode-to-anode ratio (C/A)). Reinforcement embedded in carbonated concrete with different amounts of fly ash was electrically connected to reinforcement embedded in non-carbonated concrete (C/A=1.6 or C/A=5.0) and kept in a moist environment (≈100% RH). The concrete resistivity of every sample was measured individually, and the electrical resistance between the reinforcement embedded in carbonated and non-carbonated concrete was measured. The microcell current density and open circuit potential were measured for the reinforcement in the carbonated samples. Once the reinforcement in the non-carbonated samples was connected with the reinforcement in the carbonated samples, the galvanic current and corrosion potential of the macrocouples were monitored. The total current density (microcell and macrocell) was high for all the binder compositions investigated. We found that the governing partial process of macrocell corrosion in carbonated concrete depends on the cathode-to-anode ratio. It should be noted that the performance of fly ash blends is compared to Portland cement concretes using the same water-to-cement ratio (w/c). According to the NS-EN 206 [5], the w/c is limited to maximum 0.60 for CEM I and 0.50 for CEM II/B-V, while CEM II/B-M cannot be used for concretes in the M60 durability class (M60 corresponds to exposure classes XC3 and XC4 in EN-1992-1-1 [6]).

1.2. Microcell corrosion in carbonated Portland and Portland-fly ash concrete

Results in the literature indicate slightly higher microcell current density for steel embedded in carbonated Portland-fly ash (PCFA) concrete/mortar than in Portland (PC) concrete/mortar when exposed to the same environment [7-11]. Figure 1 summarizes our literature review of documented current densities in various exposure conditions, including the average, maximum and minimum values reported in each investigation reviewed. The following paragraphs give a summary of the investigations.

Alonso et al. [7] investigated mortar samples (w/c 0.50) containing PC and PCFA (30% FA) among other cements. They prepared 20x55x80 mm mortar samples and cured them for 28 days at 100% RH. The samples were carbonated at 50-70% RH in a high CO_2 concentration (not specified). The carbonated samples were exposed to cycles of 100% RH, 50% RH, and partial immersion. The microcell current density was determined using Linear Polarization Resistance (LPR) with positive feedback for the ohmic drop compensation. Their measurements were non-conclusive.

Dhir et al. [8] prepared a series of concretes varying in w/c (0.35-0.66) and fly ash replacement (26%-36% by mass). They prepared 100 mm reinforced concrete cubes with embedded steel (ribbed carbon steel with diameter 10 mm and concrete cover 25 mm). The cubes were cured for 28 days either immersed in water or exposed to air at 55% RH. Then the cubes were exposed to accelerated carbonation (55% RH, 4% CO_2) until the carbonation front reached 35 mm. Carbonation development was monitored in complementary plain samples. The carbonated cubes were exposed for 20 weeks to various exposure conditions: 55%, 75% or 95% RH or 55-95% RH cycles. The corrosion rate was determined using LPR (Sycopel potentiostat) with automatic ohmic drop compensation. The microcell current density in the PCFA samples was slightly higher than in the PC samples.

Arachchige [9] prepared 100 mm reinforced concrete cubes containing PC and PCFA (30% FA) and varying amounts of cement and of fine and coarse aggregates, aiming at a w/c of 0.55. Embedded steel (ribbed carbon steel with diameter 10 mm and concrete cover 25 mm) was used. The cubes were cured for 28 days at 55% RH and subsequently exposed to carbonation (55% RH, 4% CO_2) until the carbonation front was 35 mm. Finally, the cubes were exposed to 95% RH for 24 weeks. The corrosion rate was determined using LPR with automatic ohmic drop compensation. The microcell current density measured at 95% RH was higher in the PCFA samples than in PC samples.

Zornoza et al. [10] prepared 20x60x80 mm mortar samples (w/c 0.40) containing PC and PCFA (30% FA) including two 8 mm reinforcement bars with 6 mm of cover. The samples were cured for 80 days at 100% RH and then exposed to carbonation at 65% RH and 100% CO_2. Once carbonated, they were kept at 100% RH. The corrosion rate was determined by LPR using a potentiostat-galvanostat (EG&G PAR Model 362). No information is given on how the ohmic drop was compensated. The microcell current density measured in the PCFA samples was similar to the current density in the PC samples, but lower values were reported than in other investigations.

Messina et al. [11] prepared reinforced concrete samples (w/c 0.55) containing PC and PCFA (18% or 30% FA). They used ribbed carbon steel diameter 16 mm, and the concrete cover was 20 mm. The samples were sealed cured for two weeks and then exposed to high CO_2 concentration (5% for 10 months and ≈100% until fully carbonated (detected using pH indicator thymolphthalein)). The samples were exposed to wetting–drying cycles while monitoring the current density. The current density was determined using non-compensated LPR, and the ohmic drop was determined using EIS. The microcell current density measured in the PCFA samples was slightly higher than in PC samples.

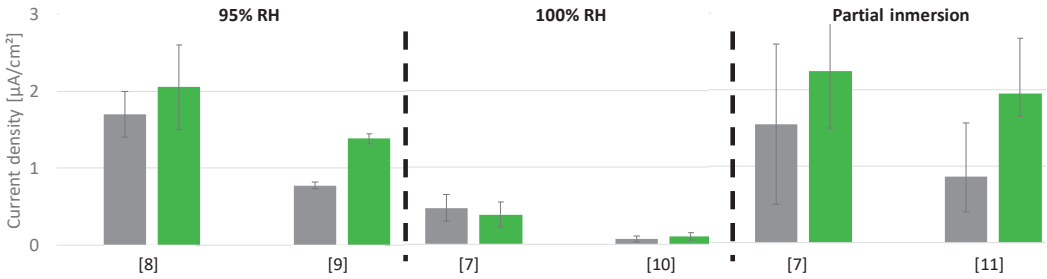

Figure 1: Microcell current density of carbon steel embedded in carbonated cementitious materials containing PC (grey bars) and PCFA (green bars) in three different exposure conditions (RH 95%, 100%, or partial immersion). Average (bars) and range (error bars). The number in brackets indicates the reference. After [7-11]

1.3. Macrocell corrosion in carbonated concrete

The literature provides no results on the influence of fly ash on macrocell corrosion in carbonated concrete, so the literature review given here focuses on macrocell corrosion in carbonated concrete prepared with plain Portland cement.

Castel et al. [12-14] investigated galvanic corrosion in reinforcement embedded in carbonated PC concrete coupled with reinforcement embedded in non-carbonated PC concrete. They prepared reinforced concrete samples (w/c 0.45) containing reinforcement bars (diameter 12 mm) either as-received or cleaned (the mill scale was removed), and with or without casting defects in the concrete-steel interface (owing to so-called top-bar effect [15]). The carbonated samples were coupled with the non-carbonated samples with half of their height immersed in water using a zero-resistance ammeter (ZRA). The distance between the reinforcement bars was 60 mm, and both C/A=2.0 and C/A=5.0 were tested. The microcell activity was determined in complementary fully carbonated samples using LPR, compensating for ohmic drop using EIS. Castel et al. found that the macrocell current density was higher than the microcell current density in the materials and conditions tested. They investigated the influence of casting defects in the concrete-steel interface, the so-called the top-bar effect, and concluded that microcell corrosion was not affected, while macrocell corrosion depended on the defects. Figure 2 presents a summary of the current density in samples with reinforcement as-received, with and without casting defects on the concrete-steel interface (C/A=2).

Sohail et al. [16] investigated macrocell corrosion between reinforcement embedded in carbonated PC concrete and reinforcement embedded in non-carbonated PC concrete. First, they carbonated a concrete cylinder (diameter 65 mm) containing a carbon steel bar diameter 20 mm. The carbonated sample was cast in new concrete, in the middle of a cylindrical mould with four concentric carbon steel bars (diameter 20 mm) with 65 mm between reinforcement bars. The samples were kept with half their height immersed in water for the measurements. Sohail et al. measured galvanic currents, using a ZRA when coupling 1, 2, 3 or all 4 bars and determined macrocell current densities from 0.7 to 4.0 µA/cm² depending on the C/A. Microcell activity was not determined in this investigation, but the results show that the macrocell contribution may not be negligible.

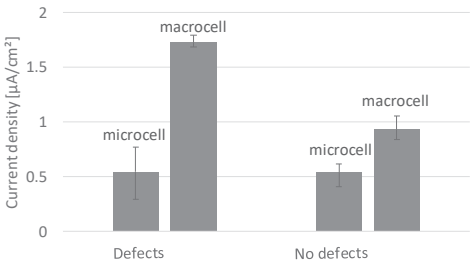

Figure 2: Microcell and macrocell current density of as-received reinforcement embedded in PC concrete (w/c 0.45, C/A=2.0). Half of the sample height immersed in water. Samples with casting defects in the concrete-reinforcement interface (top bar during casting) or no defects (bottom bar during casting). Bars (average) and error bars (range). After [14]

2. Experimental

Reinforced concrete samples were prepared and fully carbonated in a previous investigation [11]. In the following, these samples are referred to as "A samples", indicating active corrosion. In addition, reinforced concrete samples with three reinforcing bars were prepared. These samples are referred to as "C samples", i.e. samples that offer additional cathode when coupled with A samples. Similar cement, aggregates and reinforcement were used in both types of sample.

Figure 3 presents an overview of the samples, methods and coupling conditions together with a legend. Samples were prepared with three different cements, which are indicated with different colours: grey is used for the PC (0% FA), blue for the 18% FA, and green for the 30% FA. There is an additional parameter which is the position of reinforcement in the A samples during the casting: top (open symbol) or bottom (solid symbol)). When the samples were coupled (A+C), two cathode-to-anode ratios were investigated: 1.6 (circle symbols) and 5.0 (square symbols).

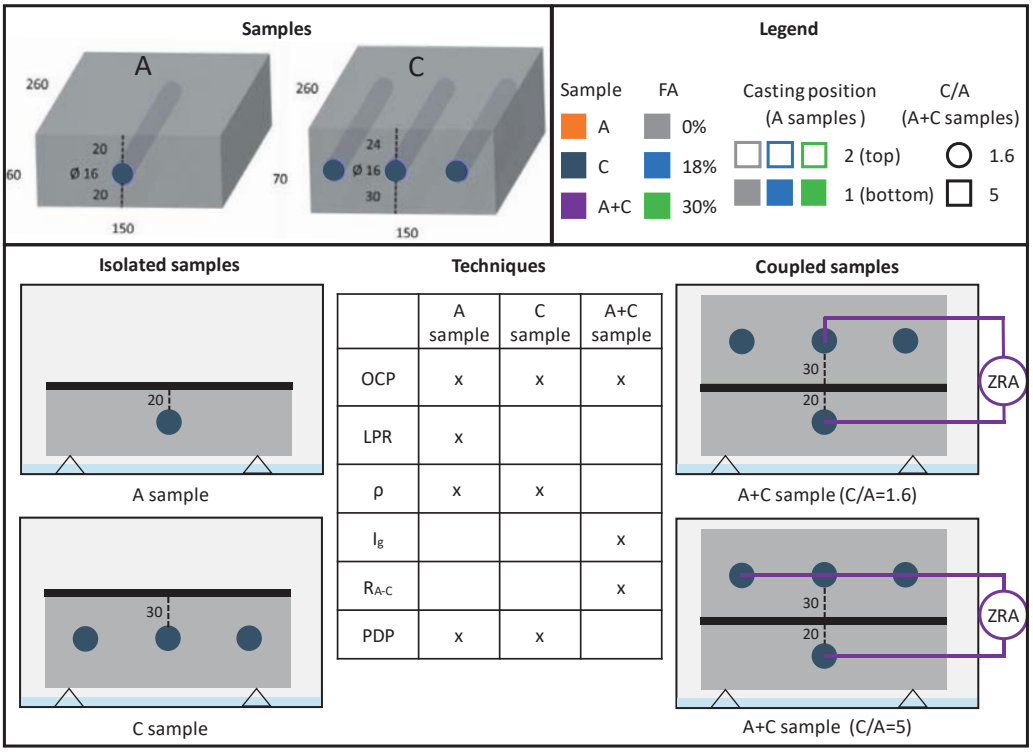

Figure 3: Overview of the reinforced concrete samples and methods: sample dimensions [mm] (carbonated (A) and non-carbonated (C)); legend (sample type, amount of fly ash (FA), casting position, and coupling condition (A and C samples isolated or coupled with C/A=1.6 or C/A=5.0)); and experimental techniques. The experimental techniques are described in the text

2.1. Concrete composition

Table 1 gives the chemical composition of the three cements investigated, as determined by XRF.

Table 1: Chemical composition of the cements investigated, as determined by XRF facilitated by NORCEM AS [% by mass]

Cement	% FA	SiO_2	Al_2O_3	Fe_2O_3	CaO	MgO	SO_3	P_2O_5	K_2O	Na_2O
CEM I	0%	19.6	4.9	3.1	60.8	2.3	3.7	0.1	0.9	0.5
CEM II/B-M	18%	25.5	7.6	4.2	50.7	2.1	3.3	0.2	1.1	0.6
CEM II/B-V	30%	28.4	8.8	4.4	46.9	2.2	2.7	0.2	1.2	0.6

Concretes were prepared aiming at water-to-cement (w/c) ratio 0.55. Table 2 presents the concrete composition of the type A samples, which were cast in a precast plant in Norway, with a batch volume of 1 m^3, and the concrete composition of the type C samples, which were cast in the laboratory, with a batch volume of 7 litres.

Table 2: Concrete compositions of A and C samples [kg/m³]. Weight of the aggregates given in saturated-surface dry condition

Constituent	A samples [kg/m^3]			C samples [kg/m^3]		
	CEM I	CEM II/B-M	CEM II/B-V	CEM I	CEM II/B-M	CEM II/B-V
Cement	371.4	369.8	369.5	376.6	376.6	376.6
Sand 0/8 mm	1173.2	1166.9	1160.3	923.2	923.2	923.2
Gravel 5/16 mm	624.2	628.5	629.6	769.2	769.2	769.2
Free Water	206.9	202.9	200.9	207.2	207.2	207.2
Superplasticiser (Dyn. XTend)	3.78	3.69	3.68	-	-	-
w/c	0.56	0.55	0.54	0.55	0.55	0.55

2.2. Preparation and conditioning of A samples

The A samples were cast with two reinforcement bars 260 mm in length. Both ends of the bars were coated with beeswax to a length of 50 mm. The concrete was poured into the moulds and gentle compaction was applied by tapping on the sides with a rod until no air bubbles appeared on the surface. The samples were sealed cured for 14 days. Initially, they were 150x120x260 mm in size, but they were longitudinally cut into two samples differing only in casting position (casting position 1 (bottom and 2 (top)). The samples were carbonated using a high CO_2 concentration (5% for 10 months and ≈100% until fully carbonated (detected using pH indicator thymolphthalein)). Probes were embedded in one of the longitudinal sides on each sample and a pseudo-reference electrode (a piece of activated titanium 25 mm in length and 1 mm in diameter) was embedded close to the reinforcement. The samples were exposed to one wetting-drying cycle and kept in the laboratory until the current investigation.

For the current investigation, the samples were immersed in water for 4 weeks and then kept over water in a sealed plastic box while coupled with C samples. At this time, the samples were approximately two years old.

2.3. Preparation and conditioning of samples C

The C samples were cast in the laboratory. Three reinforcement bars 16 mm in diameter, 260 mm in length, were embedded in each C sample. An electrical connection was prepared for each bar. The reinforcement bars were separated from each other by 50 mm and by 25 mm from the edges of the sample. The concrete was poured into the moulds and gentle compaction was applied by tapping on the sides with a rod until no air bubbles appeared on the surface. The samples were sealed cured for 5 weeks at 20°C and 4 weeks at 38°C to promote the hydration of the cement and enhance differences in the electrical resistivity of the concretes. After the curing, the samples were kept over water for 3 days in a sealed plastic box before they were coupled with A samples.

2.4. Exposure

During the experimental period, the samples (both A and C) were kept over water in sealed boxes. To ensure electrical contact between them, a piece of wet cloth was placed as illustrated in Figure 3 (thick black line). The temperature varied between 18 and 22 °C, and the RH in the boxes was close to 100%. The distance between the reinforcement bars embedded in the A and C samples was approximately 50 (±5) mm. Two cathode-to-anode configurations were investigated: 1) the middle bar from the C samples connected to the bar from the A samples (C/A=1.6), and 2) all the three bars from the C samples connected to the bar from the A samples (C/A=5.0).

2.5. Methods

A diagrammatic summary of the experimental techniques used on each sample is presented in Figure 3. A description of each technique is given in the following text.

The open circuit potential (OCP) was measured on A and C samples before they were coupled, and at regular intervals after coupling. The OCP of the reinforcement was measured using an external saturated calomel reference electrode (SCE) applied on the concrete surface and a high impedance voltmeter (Fluke 76, input impedance 10 MΩ). The measurement was taken every day for C/A=5.0 and occasionally for C/A=1.6.

The microcell corrosion in the A samples was determined using linear polarization resistance (LPR) before the coupling. The polarization resistance of the reinforcement was determined using LPR without compensating for the ohmic drop. The current density was calculated from the Stern-Geary equation [17] assuming B=52 mV [18]. We used a three-probe corrosion cell consisting of an embedded pseudo-reference electrode (RE), a titanium mesh applied to the concrete surface (CE), and the reinforcement (WE). The reinforcement was polarized ±10 mV from the OCP at a rate of 0.167 mV/min. The ohmic drop between the RE and WE was determined using AC electrochemical impedance spectroscopy (EIS) applying an alternating sinusoidal voltage of 10 mV in the range of 500 kHz to 1 Hz. The ohmic drop was attributed to the lowest phase angle of the Bodo plot.

The electrical resistivity of the concrete (ρ) in the A samples was determined from the ohmic drop between the WE and RE (same setup as used for LPR). The cell factor of this corrosion cell was empirically determined from the data retrieved in a previous investigation [11]. The electrical resistivity of the concrete in the C samples was determined using EIS with each of the two neighbouring reinforcement bars as electrodes. An alternating sinusoidal voltage of 10 mV in the range of 500 kHz to 1 Hz was applied and the resistance associated with the lowest phase angle of the Bodo plot was attributed to the electrical resistance of the concrete. The cell factor of each sample was empirically determined using an electrolyte of known conductivity before the concrete was cast.

The electrical resistance ($R_{A\text{-}C}$) between the reinforcement bars embedded in the A and C samples was determined using EIS. An alternating sinusoidal voltage of 10 mV in the range of 500 kHz to 1 Hz was applied and the resistance associated with the lowest phase angle of the Bodo plot was attributed to the electrical resistance of the concrete. The resistance between the reinforcement in the C and A samples was determined before the macrocoupling and after disconnecting them.

The macrocell (galvanic) current (I_g) flowing between the reinforcement embedded in carbonated and non-carbonated concrete was measured using a ZRA.

Potentiodynamic polarization curves (PDPs) were performed on A and C samples. An SCE applied on the concrete surface was used as RE, a titanium mesh applied on the opposite concrete surface as CE, and the reinforcement as WE. The reinforcement was polarized at a rate of 1 mV/s, step height 1 mV (ohmic drop non-compensated), first cathodically, and once back to the OCP, anodically. The C samples (with 3 reinforcement bars electrically connected) were polarized from -500 mV to + 250 mV vs. the OCP, while

the A samples were polarized from -400 mV to + 200 mV vs. the OCP. The ohmic drop was determined using the same procedure as for LPR.

3. Results

3.1. Electrical resistivity of concrete and electrical resistance between electrodes

The electrical resistivity (ρ) of the carbonated and non-carbonated concrete was determined before the macrocoupling, see Figure 4.

The electrical resistance between the reinforcement embedded in sample A and sample C ($R_{A\text{-}C}$) was determined before and after the macrocoupling (C/A=5.0 and C/A=1.6), see Figure 5.

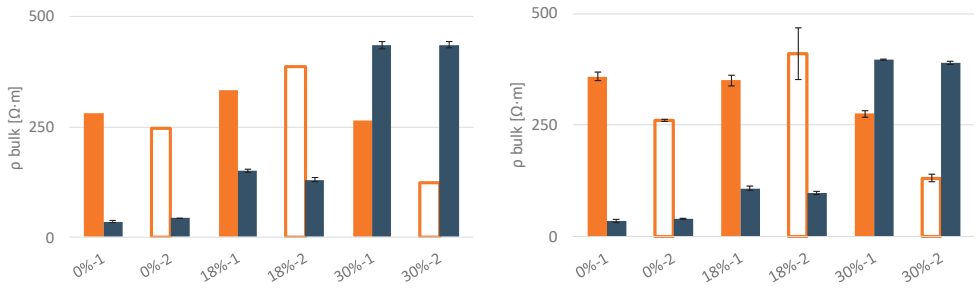

Figure 4: Left: the electrical resistivity of concrete (ρ) measured before coupling for C/A=1.6: orange bars are an A sample (1 measurement), and dark bars are the C samples (average of 2 measurements). Right: the electrical resistivity of concrete (ρ) measured before coupling for C/A=5.0: orange bars are the A samples (average of 4 measurements), and dark bars are the C samples (average of 2 measurements). Error bars indicate the range. Colour legend given in Figure 3

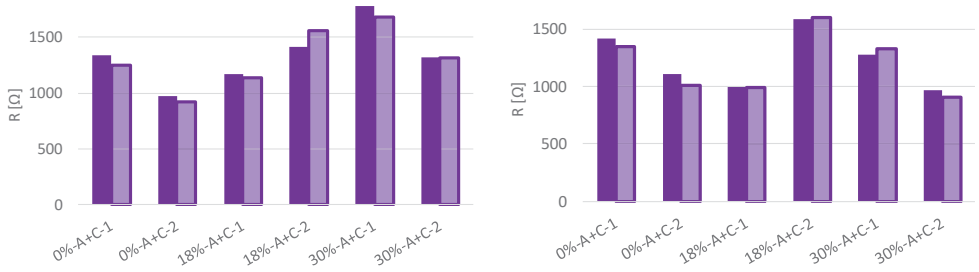

Figure 5: Left: the electrical resistance measured between reinforcement embedded in A and C samples ($R_{A\text{-}C}$) before macrocoupling for C/A=1.6 (solid purple bar) and after disconnection (light purple). Right: the electrical resistance measured between reinforcement embedded in A and C samples ($R_{A\text{-}C}$) before macrocoupling for C/A=5.0 (solid purple bar) and after disconnection (light purple). Colour legend given in Figure 3

3.2. Potentiodynamic polarization curves

Figure 6 presents the polarization curves measured for the A samples (area≈80 cm^2) and the C samples (the three reinforcement bars connected, area≈400 cm^2). The parameters derived from the PDPs are summarized in Table 3. They are the slopes of the lines fitted to the PDPs assuming activation control in

the polarization range of the macrocouples. They are not necessarily the Tafel slopes of the anodic and cathodic reactions, because they were taken in a higher polarization range than the range in which Tafel slopes are usually calculated. The results were used for modelling the macrocell corrosion process

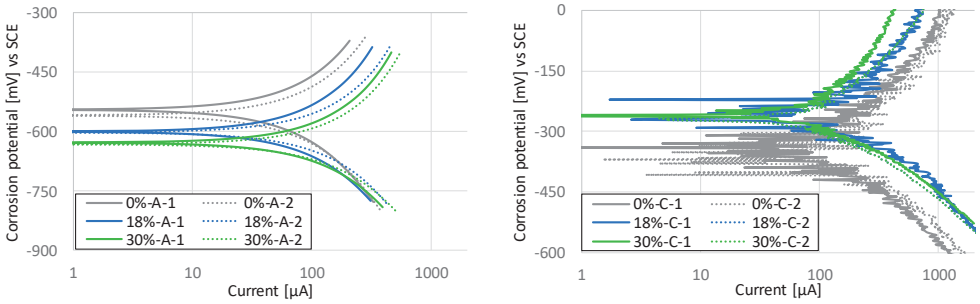

Figure 6: Left: potentiodynamic polarization curves for A samples (carbonated, area≈ 80 cm²). Right: potentiodynamic polarization curves for C samples (non-carbonated, area ≈ 400 cm²). Colour legend given in Figure 3

Table 3: Electrochemical parameters derived from the PDP (slope of regression lines assuming activation control) [mV/Dec]

		Fly ash content		
		0 %	18 %	30 %
A samples (carbonated concrete)	$m_{A\text{-}an}$	340	330	290
	$m_{A\text{-}cath}$	360	360	320
C samples (non-carbonated concrete)	$m_{C\text{-}an}$	8000	6000	7000
	$m_{C\text{-}cath}$	260	280	280

3.3. Microcell corrosion

The microcell current density was determined for the A samples before coupling, see Figure 7. The data includes daily measurements over four consecutive days before the coupling.

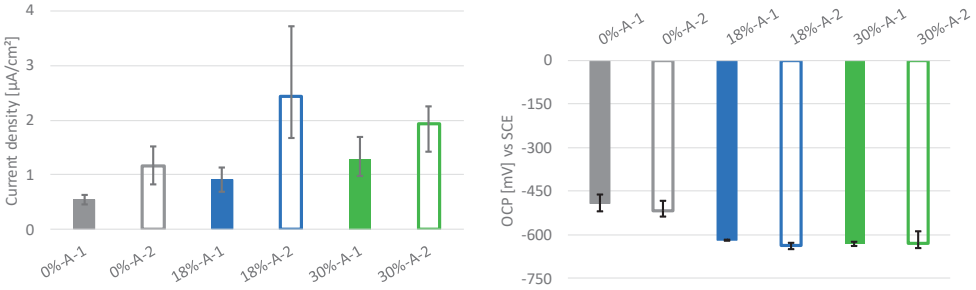

Figure 7: Left: microcell current density in the A samples before macrocoupling. Right: OCP in the A samples before macrocoupling. Average (bars) and range (error bars) of 4 measurements taken on consecutive days. Colour legend given in Figure 3

3.4. Macrocell corrosion

Figure 8 gives a summary of the OCP results before the A and C samples were connected, and 10 days after connecting them (A+C).

Figure 9 shows the galvanic current and the OCP of the macrocouples over time (C/A=5.0).

Figure 10 presents the macrocell current densities determined after 10 days of coupling for C/A=5.0 (left) and for C/A=1.6 (right).

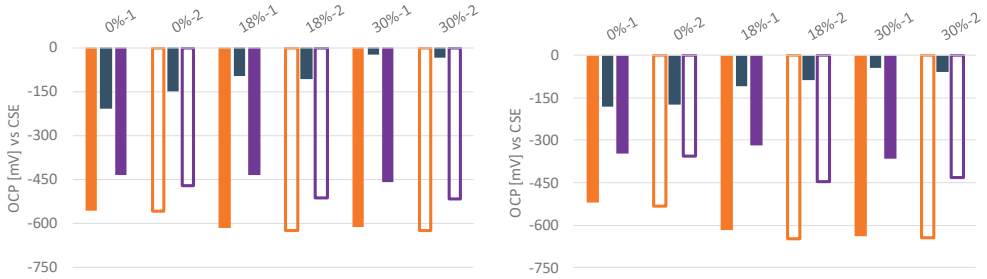

Figure 8: Left: the OCP measured before coupling (A and C samples) and after 10 days of coupling (A+C samples) for C/A=1.6. Right: the OCP measured before coupling (A and C samples) and after 10 days of coupling (A+C samples) for C/A=5.0. Colour legend given in Figure 3

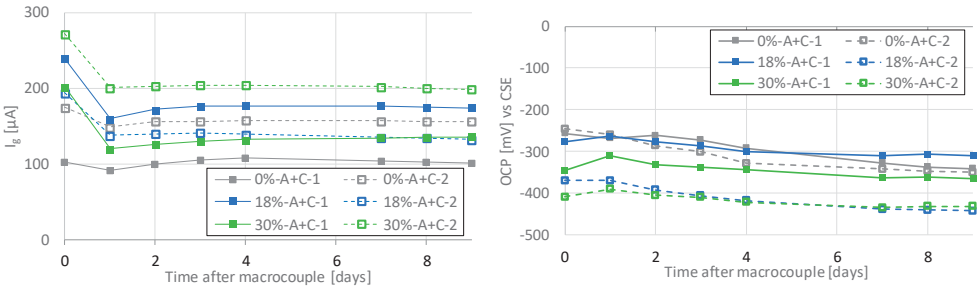

Figure 9: Left: the galvanic current (I_g) of macrocouples over time for C/A=5.0. Right: the OCP of macrocouples over time for C/A=5.0. The colour legend given in Figure 3 is followed depending on the FA amount even where samples A+C are represented

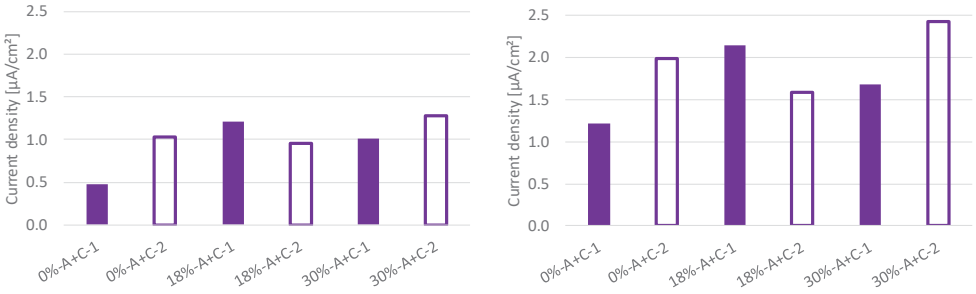

Figure 10: Left: the macrocell current density determined after 10 days of coupling for C/A=1.6. Right: the macrocell current density determined after 10 days of coupling for C/A=5.0. Colour legend given in Figure 3

4. Macrocell contribution in carbonated PC and PCFA concrete

The microcell current densities determined when the carbonated (A) samples were not coupled with the non-carbonated (C) samples were compared with the macrocell current densities determined when they were coupled. The corrosion rate was assessed using the classification of severity suggested by Andrade et al. [19] among others, see Table 4.

Table 4: Ranges of corrosion rates in reinforcement embedded in concrete according to [19-21]

Severity	Negligible	Low	Moderate	High	Very high
Corrosion rate [$\mu A/cm^2$]	≤ 0.1	0.1-0.5	0.5-1	1-10	10-100

The microcell current density range measured in this investigation is in agreement with the data reported in the literature and in the moderate to high range according to Table 4. Two parameters were investigated: the influence of the fly ash and the influence of the microstructure (casting position).

Slightly higher microcell corrosion rates were measured in the PCFA samples than in the PC samples. This is in agreement with most studies in the literature (see Figure 1). Moreover, fly ash led to more negative OCP values (ca. 100 mV) than in PC samples.

Systematically higher microcell corrosion rates were measured in the samples cast in the top position than in samples cast in the bottom position. The impact of casting position was greater than the impact of binder composition. OCP values were not affected by the casting position.

The macrocell current densities were in the moderate to high range for C/A=1.6, and in the high range for C/A=5.0 according to Table 4, similar to the ranges Castel et al. [12-14] reported for PC samples with C/A=2.0 and C/A=5.0.

Figure 11 illustrates the microcell corrosion current density determined in the A samples before coupling ($i_{mi\text{-}A}$), and the total current density (i_{tot}) determined from the galvanic current (i_g) and microcell contribution ($i_{mi\text{-}A+C}$) when the A and C samples were connected. The stacked bars in Figure 11 (i_{tot}: lower bar $i_{mi\text{-}A+B}$ and upper bar i_g) take into account the local changes in the active reinforcement due to anodic polarization, as shown in Figure 12. The red dashed line indicates the threshold value for the corrosion rate being considered high according to Table 4. The total current density is classified as high for all the cement types, casting positions, and C/A ratios tested in this study. The PCFA presented slightly higher total corrosion rates than the PC samples.

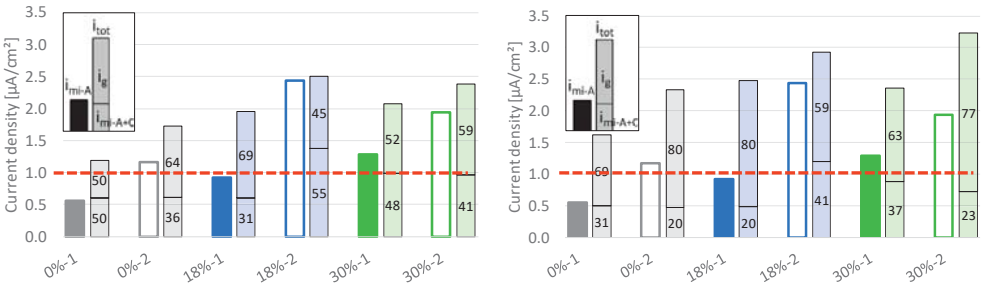

Figure 11: Left: the microcell current density for the A samples (i_{mi-A}) two hours before coupling, and the total current density (i_{tot}) when the samples were coupled (A+C), for C/A=1.6. Right: the microcell current density for the A samples (i_{mi-A}) two hours before coupling, and the total current density (i_{tot}) when the samples were coupled (A+C), for C/A=5.0. The numbers in the bars show the contributions of the macrocell (i_g) and microcell (i_{mi-A+C}) as a percentage of the whole. The red dashed line indicates the threshold for high current density according to Table 4

4.1.1. Influence of fly ash on macrocell corrosion

We expected that because the electrical resistivity of the non-carbonated PCFA is higher than that of PC, this would increase R_{A-C} and overall limit the galvanic current in the macrocell. However, this effect was not observed in the materials and conditions tested. The following section discusses the parameters which did affect the result: the resistivity of carbonated and non-carbonated concrete, the driving potential, and the slope of the activation control lines.

Figure 4 presents the electrical resistivity of the concrete determined in the A (carbonated) and the C (non-carbonated) samples before they were coupled. When concrete is non-carbonated, the higher the amount of fly ash, the higher the electrical resistivity. When concrete is carbonated, the resistivity of the PC and PCFA samples is similar. The electrical resistivity of our non-carbonated concrete samples cannot be directly compared with the electrical resistivity of our carbonated concrete samples due to the different age and preconditioning of the samples. Figure 5 presents the electrical resistance between the reinforcement bars (electrodes) embedded in the A and C samples right before the electrical connection was established and right after disconnection (after 10 days of connection). The electrical resistance between the electrodes did not change during this period, which indicates that there were limited changes in the moisture state of the samples during the coupling.

If we compare the electrical resistance in PC and PCFA (30%), see Figure 5, it seems the C/A did not influence the electrical resistance determined in the PC samples. However, in the PCFA (30%) samples, the electrical resistance increased for the lower C/A. This can be explained by the electrical resistivity of the non-carbonated PCFA being higher than that of PC. The more reinforcement is embedded in non-carbonated concrete, the higher becomes the possible beneficial influence of the fly ash in the form of higher electrical resistance. This could give PCFA an advantage over PC when the C/A is high, e.g. when a macrocouple starts to develop.

The driving potential between the carbonated and non-carbonated samples was higher in the PCFA samples than in the PC samples, see Figure 8 (the A samples presented more negative values while the C

samples presented more positive values in the PCFA than in the PC samples). In addition, the slope of the cathodic activation control lines of the PCFA samples was slightly higher than those of PC (see Table 3), which means higher current for the same polarization in the PCFA samples.

The parameters described above may explain the differences between expectations and observations. The results are limited to the moisture condition (≈100% RH) and C/A ratios tested (1.6 and 5.0).

4.1.2. Influence of microstructure in macrocell corrosion

The casting position has previously been found to introduce casting defects under reinforcement bars in the upper part of the mould [15]. According to Castel et al. [12-14], the so-called "top-bar effect" does not influence the microcell corrosion in carbonated concrete, but does have an impact on the galvanic current once a macrocouple is established. They explain this as due to the higher driving potential observed in the samples with defects in the concrete-steel interface.

In the current investigation, we studied the influence of the position of the reinforcement during the casting: A-1 samples (bottom position) and A-2 samples (top position). Systematically higher microcell current density was observed in the A-2 samples than in the A-1 samples, but similar OCP. And when we compared the galvanic current of the macrocouples (Figure 9), systematically higher values were measured in the A-2 samples than in the A-1 samples (except for the 18%-A+C-2 sample). The reason in this case is probably not the difference in the driving potential, which was similar in samples from positions 1 and 2 (Figure 8), but the electrical resistance between the reinforcement embedded in carbonated concrete and non-carbonated concrete before they were connected (Figure 5). Overall, when we compared the total current density, systematically higher values were measured in the samples from position 2 than in samples from position 1. In a previous investigation [2], we found microstructural defects in terms of crack patterns that depended on the relative position of the reinforcement during the casting, so this may be the parameter that affects the microcell and macrocell corrosion processes.

4.2. Macrocell corrosion mechanism in carbonated concrete

The mechanism of macrocell corrosion in carbonated concrete has been described by Bertolini et al. [1] and Castel et al. [13] amongst others. Here we describe the macrocell mechanism using parameters which can be experimentally retrieved.

Figure 12 uses Evans diagrams to present a simplified model which illustrates the influence of coupling active reinforcement embedded in carbonated concrete (an A sample) with passive reinforcement embedded in non-carbonated concrete (a C sample). The vertical axis is the corrosion potential (E_{corr}) against the saturated calomel reference electrode (SCE), and the horizontal axis is the current in logarithmic scale. The sketch presented here shows one of the couplings tested in this investigation with C/A=5.0.

When the reinforcement embedded in carbonated concrete (the A sample) is coupled with reinforcement embedded in non-carbonated concrete (the C sample), the A sample is anodically polarized (ΔE_A) to more positive E_{corr} values, while the C sample is cathodically polarized (ΔE_C) to more negative E_{corr} values. According to this simplified model, there is a difference in potential between the active and passive reinforcement ($\Delta E_{A\text{-}C}$) which equals to the electrical resistance ($R_{A\text{-}C}$) between them times the current

flowing (I_g). The equilibrium of the macrocell depends on the anodic and cathodic polarization curves of the two samples. The oxidation current in the C sample is almost constant (practically a vertical line), while the oxidation current in the A increases with the anodic polarization. It is possible to maintain this higher oxidation rate due to the additional reduction of oxygen in the C sample. Figure 12 illustrates how the microcell current density is affected by the coupling.

This model together with the PDPs make it possible to quantify the contribution of the partial processes involved in macrocell corrosion: the cathodic polarization of the C sample (ΔE_C), the difference in potential between the A and C samples (ΔE_{A-C}), and the anodic polarization of the A sample (ΔE_A). Moreover, we can investigate local changes in the A sample due to the anodic polarization: the decrease in microcell current density (due to the lower reduction of oxygen in the A sample) and the increase in total current density (due to the galvanic couple).

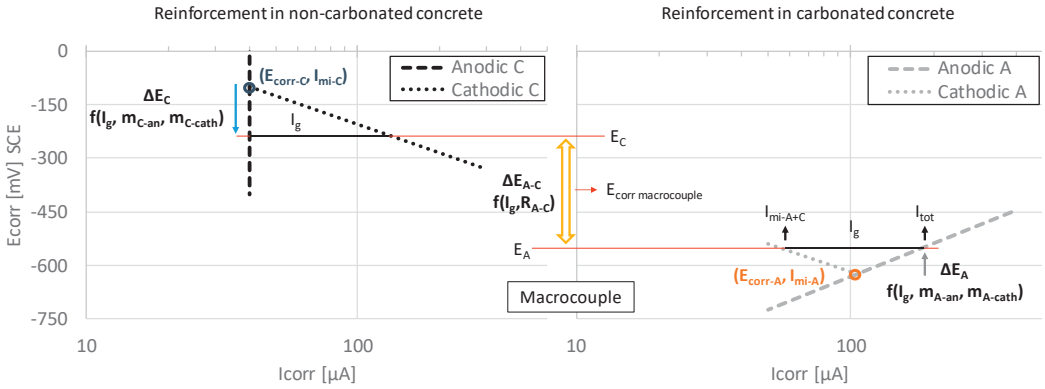

Figure 12: Proposed schematic representation of macrocell corrosion between reinforcement embedded in non-carbonated concrete (passive) and reinforcement embedded in carbonated concrete (active) based on Evans diagrams. The sketch presented here is based on experimental data for C/A=5.0

Figure 13 presents a comparison of the differences in potential between the A and C samples determined experimentally before they were connected (purple bars) and the values obtained by applying the model presented in Figure 12 and the electrochemical parameters presented in Table 3 for C/A=1.6 and C/A=5.0. The contribution of the three partial processes involved in the macrocell is depicted: the cathodic polarization of the C ($\Delta E_C=f(I_g, m_{C\text{-}an}, m_{C\text{-}cath})$); the difference in potential between the A and C samples ($\Delta E_{A\text{-}C}=f(I_g, R_{A\text{-}C})$); and the anodic polarization of the A ($\Delta E_A=f(I_g, m_{C\text{-}an}, m_{C\text{-}cath})$).

For C/A=1.6, the ΔE_C dissipates about 60% of the driving potential, the ΔE_{A-C} dissipates about 25%, and the remaining 15% is due to ΔE_A. ΔE_C depends on the ability of the cathode to reduce oxygen, and for C/A=1.6, it is needed higher polarization compared to C/A=5.0 to sustain the increased oxidation rate of iron in the A sample. ΔE_{A-C} becomes less relevant due to the lower galvanic current than in C/A=5.0.

For C/A=5.0, the ΔE_C dissipates about 30% of the driving potential, the ΔE_{A-C} dissipates about 50%, and the remaining 20% is due to ΔE_A. In this case, the reduction rate of oxygen can be sustained with a relatively small polarization. ΔE_{A-C} is the process which dissipates more potential due to the high galvanic current.

ΔE_A is the partial process which dissipates least potential in both cases tested (C/A=1.6 and C/A=5.0).

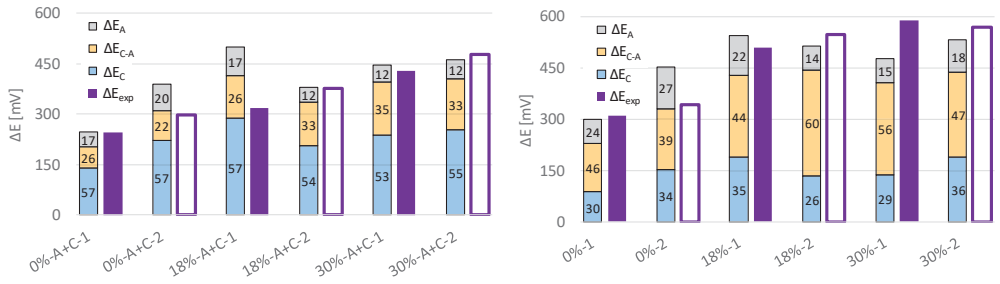

Figure 13: Left: calculated contribution (in percentage terms) of the three partial processes involved in macrocell corrosion (stacked bars) and measured driving potential (purple bars) for C/A=1.6. Right: calculated contribution (in percentage terms) of the three partial processes involved in macrocell corrosion (stacked bars) and measured driving potential (purple bars) for C/A=5.0

Figure 14 presents the relationship between the difference in potential in the carbonated and non-carbonated samples before connecting them and the macrocell current density once connected. The driving force for macrocell corrosion is the difference in potential between the active and passive steel before coupling them. To make it possible to compare the results of the current investigation with the results reported by Castel et al. [12-14], their data have been treated as expressed in terms of current density.

Castel et al. [13] concluded that there is an exponential correlation between the macrocell driving potential and the current density that mirrors the polarization curves of the system (linear in log scale, see Figure 6). Our data set compares to their observations as illustrated in Figure 12. The driving potential is a decisive parameter, but on its own does not make it possible to determine the galvanic current. Additional parameters need to be considered, e.g. the cathodic polarization of the passive steel, the electrical resistance between active and passive steel, and the anodic polarization of the active steel.

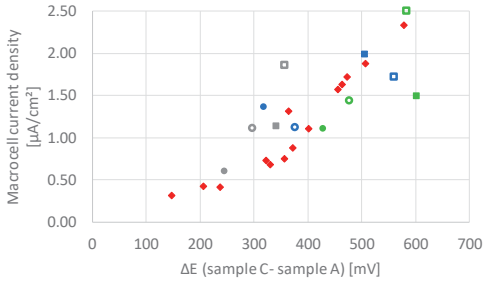

Figure 14: Relationship between the difference in the corrosion potential before coupling and the macrocell current density after coupling. Squares indicate C/A=5.0, circles indicate C/A=1.6, and red diamonds indicate values after [12-14]

4.2.1. Influence of the cathode-to-anode ratio on macrocell corrosion

According to Table 4, the total current density is classified as high for all the samples tested in the current investigation. It is slightly higher for the PCFA samples than for the PC samples for the two C/A ratios tested. In all cases, the 0%-1 sample gave the lowest microcell and total current density. The microcell and macrocell activity contribution is greatly influenced by the C/A. For C/A=1.6, the galvanic contribution varies in the range of 45-70% of i_{tot}, while for C/A=5.0, the galvanic contribution is about 60% to 80%. When the microcell current density before macrocoupling is compared with the total current density once connected, the ratio varies between 1.1 and 3 regardless of the amount of fly ash present.

The model presented in this investigation made it possible to determine the relative influence of each of the partial processes involved in macrocell corrosion. This section discusses the influence of the cathode-to-anode ratio. In the modelling, the size of the cathode was varied while the size of the anode was fixed. In addition to C/A=5, two other cases were calculated, one low (C/A=0.5) and the other high (C/A=50), to illustrate the impact of the C/A ratio. The electrochemical parameters of the passive steel were determined from the PDPs (Figure 6) assuming they were proportional to the exposed area of reinforcement. The electrochemical parameters of the active steel were also determined from the PDPs (Figure 6). The data retrieved from the PC samples was used for this numerical application. The electrical resistance between the electrodes was assumed constant (1000 Ω), based on (Figure 5) and the discussion in [22]. Figure 15 summarizes the results.

When we compare the relative influence of the three partial processes involved in the macrocell mechanism, the higher the C/A, the more relevant becomes the difference in potential between the active and passive steel ($\Delta E_{A\text{-}C}$), and the lower the C/A, the more important the role played by the cathodic polarization of the passive steel (ΔE_C). The anodic polarization of the active steel (ΔE_A) seems to play a similar role when the C/A is high.

The higher the C/A, the higher is the total current density and the galvanic contribution becomes more relevant than the microcell contribution. The calculation showed that even if the active steel is coupled with a limited amount of passive steel (C/A=0.5), the macrocell effect is not negligible for this moisture condition (a factor of 1.4 when the total and microcell current densities are compared).

The total current density is the value which should be considered when making a service life prediction, otherwise a non-conservative calculation can be made. The exposure condition investigated might be considered representative of a period of wetness in a reinforced concrete structure in service.

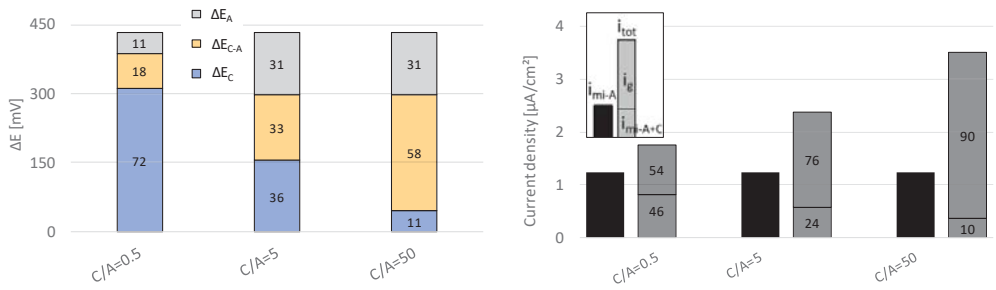

Figure 15: Left: Calculated contribution (In percentage terms) of the three partial processes involved in macrocell corrosion (stacked bars). Right: Microcell current density and calculated total current density contributions (in percentage terms)

5. Conclusion

The corrosion activity of reinforcement in carbonated concrete samples was measured with and without electrical connection to reinforcement in non-carbonated samples; i.e. microcell and macrocell corrosion were measured. The cathode-to-anode ratio (C/A) was either 1.6 or 5.0, and the samples were kept in a moist environment (≈100% RH). Three binder compositions were used, differing in fly ash content (0%, 18% or 30%). All the concretes were prepared with the same water-to-cement ratio (0.55), which is not in accordance with NS-EN 206 where more restrictive limitations are given for the fly ash blends than Portland cement. The concrete resistivity of every sample was measured individually, and the electrical resistance between the reinforcement embedded in carbonated and non-carbonated concrete was determined. Microcell corrosion rates and corrosion potentials were measured in the reinforcement in the carbonated samples. After the non-carbonated and carbonated samples were connected, the corrosion potential and galvanic currents of the macrocouple were monitored. A model was introduced to quantify the partial processes involved in the macrocell corrosion. The following conclusions can be drawn:

- The microcell current density in the carbonated concretes was moderate-to-high for the exposure condition tested. The impact of casting position (microstructure) was greater than the impact of cement composition. The microcell current density was slightly higher in the Portland-fly ash concretes than in plain Portland concrete
- In all cases, the macrocell current density was of the same magnitude as the microcell current density and not negligible
- The total current density was calculated taking into account the local changes in the active steel due to the anodic polarization. The total current density was high in all cases and slightly higher in the Portland-fly ash concretes than in plain Portland concrete
- Macrocell effects due to coupling between reinforcement in carbonated and non-carbonated concrete should be considered when making service life predictions. The exposure investigated in this study might be considered representative of a period of wetness in a field structure
- The macrocell corrosion mechanism was assessed based on Evans diagrams. The contributions of the different partial processes involved in the macrocell corrosion were modelled: cathodic polarization of passive reinforcement, the difference in potential between active and passive reinforcement, and anodic polarization of active reinforcement. It was shown that the macrocell

current depends on the C/A ratio, and that for high C/A the potential drop between the active and passive steel was the dominant partial process, whereas for low C/A the polarization of the cathode was the dominant partial process.

6. Acknowledgements

This project is part of a larger research project, 'Lavkarbsem' (NFR project no. 235211/O30), which is supported by the Norwegian Research Council and the following companies: Mapei AS, Norbetong AS, Norcem AS, Skanska AS, and Rambøll Engineering AS. The data was obtained partly using samples prepared in collaboration with NTNU/POLIMI.

7. References

[1] L. Bertolini, B. Elsener, P. Pedeferri, E. Redaelli, R.B. Polder, Corrosion of Steel in Concrete: Prevention, Diagnosis, Repair, 2nd Edition, Wiley-VCH Verlag GmbH & Co, Weinheim, Germany, 2013.
[2] A. Belda Revert, K. De Weerdt, K. Hornbostel, M.R. Geiker, Carbonation-induced corrosion: Investigation of the corrosion onset, Construction and Building Materials, 162 (2018) 847–856.
[3] J. Gulikers, Theoretical considerations on the supposed linear relationship between concrete resistivity and corrosion rate of steel reinforcement, Materials and Corrosion, 56 (2005) 393–403.
[4] C. Andrade, I.R. Maribona, S. Feliu, J.A. González, S. Feliu, The effect of macrocells between active and passive areas of steel reinforcements, Corrosion Science, 33 (1992) 237–249.
[5] NS-EN 206:2013+NA:2014 Concrete, Specification, performance, production and conformity, Standard Norge, 2014.
[6] EN-1992-1-1 Eurocode 2. Design of concrete structures – Part 1–1: General rules and rules for buildings, 2004.
[7] C. Alonso, C. Andrade, J.A. González, Relation between resistivity and corrosion rate of reinforcements in carbonated mortar made with several cement types, Cement and Concrete Research, 18 (1988) 687–698.
[8] R.K. Dhir, M.R. Jones, M.J. McCarthy, Pulverized-fuel ash concrete: carbonation-induced reinforcement corrosion rates, Proceedings of the Institution of Civil Engineers – Structures and Buildings, 94 (1992) 335–342.
[9] A.D.M. Arachchige, Influence of cement content on corrosion resistance, Proceedings of the Institution of Civil Engineers – Construction Materials, 161 (2008) 31–39.
[10] E. Zornoza, J. Payá, P. Garcés, Carbonation rate and reinforcing steel corrosion rate of OPC/FC3R/FA mortars under accelerated conditions, Advances in Cement Research, 21 (2009) 15–22.
[11] M. Messina, A. Belda Revert, M.R. Geiker, M. Gastaldi, Correlation between corrosion current density and electrical resistivity of carbonated concrete (In preparation).
[12] A. Castel, A. Nasser, Microcell versus galvanic corrosion currents in carbonated concrete, Magazine of Concrete Research, 66 (2014) 697–707.
[13] A. Nasser, A. Clément, S. Laurens, A. Castel, Influence of steel–concrete interface condition on galvanic corrosion currents in carbonated concrete, Corrosion Science, 52 (2010) 2878–2890.
[14] A. Castel, A. Nasser, Influence of pre-existing oxides layer and interface condition with carbonated concrete on active reinforcing steel corrosion, Materials and Corrosion, 66 (2015) 206–214.
[15] R. Zhang, A. Castel, R. François, Influence of steel–concrete interface defects owing to the top-bar effect on the chloride-induced corrosion of reinforcement, Magazine of Concrete Research, 63 (2011) 773–781.

[16] M.G. Sohail, S. Laurens, F. Deby, J.P. Balayssac, Significance of macrocell corrosion of reinforcing steel in partially carbonated concrete: numerical and experimental investigation, Materials and Structures, 48 (2015) 217–233.
[17] M. Stern, A.L. Geary, Electrochemical Polarization: I. A Theoretical Analysis of the Shape of Polarization Curves, Journal of the Electrochemical Society, 104 (1957) 56–63.
[18] C. Andrade, V. Castelo, C. Alonso, J. González, The Determination of the Corrosion Rate of Steel Embedded in Concrete by the Polarization Resistance and AC Impedance Methods, ASTM International Symposium on the Corrosion Effect of Stray Currents and the Techniques for Evaluating Corrosion of Rebars in Concrete, (1986) 43–63.
[19] C. Andrade, C. Alonso, Corrosion rate monitoring in the laboratory and on-site, Construction and Building Materials, 10 (1996) 315–328.
[20] C. Andrade, C. Alonso, Test methods for on-site corrosion rate measurement of steel reinforcement in concrete by means of the polarization resistance method, Materials and Structures, 37 (2004) 623–643.
[21] H.S. So, S.G. Millard, Electrochemical transient techniques for the evaluation of reinforcement corrosion in concrete, Insight – Non-Destructive Testing and Condition Monitoring, 49 (2007) 390–396.
[22] K. Hornbostel, U.M. Angst, B. Elsener, C.K. Larsen, M.R. Geiker, On the limitations of predicting the ohmic resistance in a macro-cell in mortar from bulk resistivity measurements, Cement and Concrete Research, 76 (2015) 147–158.

Part III- Appendices

Appendix I

Microstructural appearance carbonated concrete

External report prepared by Ulla Hjorth Jakobsen (Danish Technological Institute)

Appendix in: Reinforcement corrosion in carbonated fly ash concrete

Andres Belda Revert

Thesis for the degree of Philosophiae Doctor

Trondheim, May 2018

Norwegian University of Science and Technology
Faculty of Engineering, Science and Technology
Department of Structural Engineering

DANISH
TECHNOLOGICAL
INSTITUTE

Gregersensvej
DK-2630 Taastrup
Tel. +45 72 20 20 00
Fax +45 72 20 20 19

info@teknologisk.dk
www.teknologisk.dk

NTNU, Trondheim
Microstructural appearance carbonated concrete

Performed for:
Andres Belda
Department of Structural Engineering
Faculty of Engineering Science and Technology
Norwegian University of Science and Technology (NTNU)
NO-7491 Trondheim
Norway

Performed by:
Ulla Hjorth Jakobsen
Danish Technological Institute
Gregersenvej 4
2630 Taastrup
Denmark

Project no.: 735718
Date: February 7, 2017

DANISH TECHNOLOGICAL INSTITUTE

Content

Attached: Plate 1-9; Photo documentation

1. Introduction

The following report is prepared on the request of Andres Belda, NTNU, Trondheim, Norway.

Nine laboratory made concrete samples were, December 21th 2016, received for petrographic analysis. Details regarding the samples are in Table 1 below.

Table 1: Data supplied by NTNU.

Sample	Exposure	Thin Section	Polished Section	Name (Label)	Carbonated depth [mm]
CEM I	60% RH 1% CO_2	x 1	x 1	I-60	12-15[1]
CEM II/B-M		x 1	x 1	II-60	17-20
CEM II/B-V		x 1	x 1	III-60	22-25
CEM I	90% RH 5% CO_2	x 1	x 1	I-90	5-17
CEM II/B-M		x 1	x 1	II-90	8-16
CEM II/B-V		x 1	x 1	III-90	6-20
CEM I	Natural carbonation (sheltered)	x 1	x 1	I-N	2.8-3
CEM II/B-M		x 1	x 1	II-N	3.5-5
CEM II/B-V		x 1	x 1	III-N	2.5-4

The three analyzed binders contain various fly ash replacements: CEM I (0% FA), CEM II/B-M (18% FA), and CEM II/B-V (30% FA). The concretes were exposed to different conditions (Table 1).

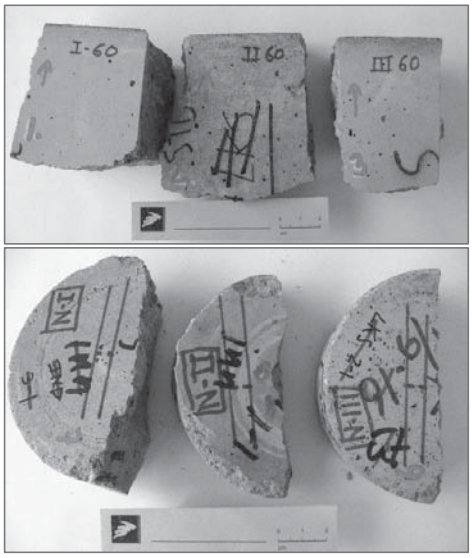

The appearance of the samples as received.

Numbers in red are DTI identification numbers. Specimens made from the samples have the lab number 7842.

1.1 Scope of Analysis

The scope of this examination is to perform a petrographic analysis of each concrete sample using optical fluorescent microscopy and SEM-EDX.

Special emphasis is on the effect of 3 different exposure conditions on the appearance and composition of the cement paste.

Detailed petrographic analysis as well as photo plates are attached to this document.

2. Result

The following observations were obtained during the petrographic analysis of nine concrete samples:

Generally, all the concrete appears with a plane and intact surface (Figure 1), though in most of the concrete several small micro-cracks formed in the plastic stage are present in the surface. The concrete containing CEM II, 18%FA seem to have the highest amount of surface defects.

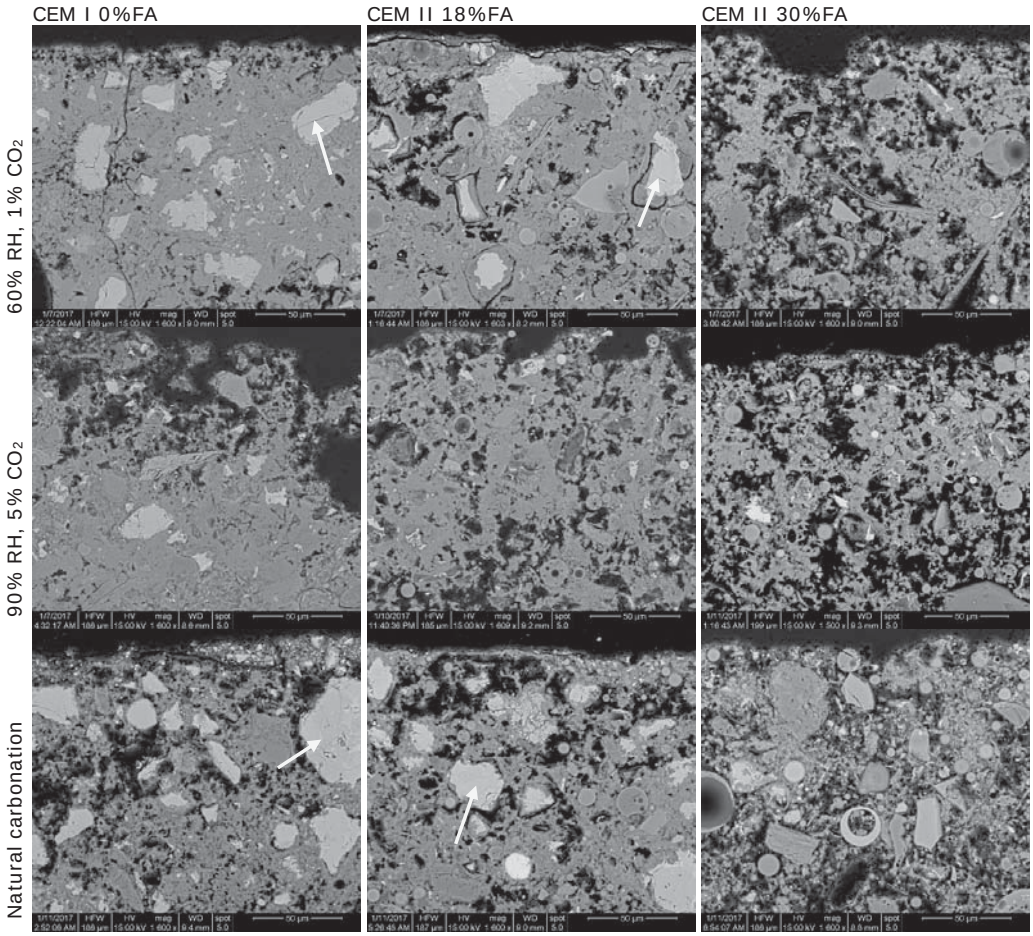

Figure 1: Appearance of the carbonated surface of the 9 concrete samples.Relatively many partially hydrated and non-carbonated cement grains are seen in the surface region of 4 of the concrete (light grey phases, arrows). All images are takein the same magnification and in backscatter mode.

A summary of observations is seen in Table 2a and 2b. All of the concrete has a relatively porous paste as well as having a somewhat inhomogeneous paste texture with alternating porous and less porous areas (patchy). Furthermore, adhesions defects (formed in the plastic stage) between paste and aggregate are observed in most of the concrete samples.

The paste of the concrete is, dependent on exposure condition carbonated to varying depths. Deepest carbonation and the sharpest carbonation front is seen in concrete exposed to 60% RH and 1% CO_2. The carbonation is also deep in concrete exposed to 90% RH and 5% CO_2, but the

carbonation front is very uneven varying from 4-15mm. Lowest depth of carbonation is seen in the natural exposed concrete where the max. carbonation depth is 5mm (Table 2).

Table 2a: Summary of petrographic observations; ordered after exposure condition

Petrographic Observations													
	Paste		Carbonation zone					Interface zone		CH			
Sample ID	Patchy	Porosity	mm	Front	Popcorn carb.	Non-carb. areas	Porosity	mm	Porosity	In paste	In voids	Air, amount	Adhesion cracks
I-60	Distinct	High	12	Even	-	Many	Slightly increased	1.2	-	High	Present	High	Some
II-60	Somewhat	Medium	12-14	Relative even	-	Some	Slightly increased	1.2	-	Medium	None	Low	Many
III-60	Weak	Medium	20-22	Relative even	X	None	Slightly increased	-	-	Low	None	Low	Some
I-90	Distinct	High	4-14	Un-even	-	Many	Increased	1	Decreased	High	Present	High	Few
II-90	Somewhat	Medium	7-14	Un-even	-	Few	Increased	1	Decreased	Medium	None	Low	Few
III-90	Somewhat	Medium	11-15	Un-even	X	Some	Increased	-	Decreased	Low	None	Low	Few
I-N	Somewhat	High	2-5	Un-even	-	Some	Slightly increased	0.8	-	High	Present	High	Few
II-N	Somewhat	Medium	2-5	Un-even	-	None	Slightly increased	0.8	Decreased	Medium	None	Low	Some
III-N	Somewhat	Medium	4	Even	X	Few	Slightly increased	1	-	Low	None	Low	Some

Table 2b: Summary of petrographic observations; ordered after binder type

Petrographic Observations													
	Paste		Carbonation zone					Interface zone		CH			
Sample ID	Patchy	Porosity	mm	Front	Popcorn carb.	Non-carb. areas	Porosity	mm	Porosity	In paste	In voids	Air, amount	Adhesion cracks
I-60	Distinct	High	12	Even	-	Many	Slightly increased	1.2	-	High	Present	High	Few
I-90	Distinct	High	4-14	Un-even	-	Many	Increased	1	Decreased	High	Present	High	Few
I-N	Somewhat	High	2-5	Un-even	-	Some	Slightly increased	0.8	-	High	Present	High	Few
II-60	Somewhat	Medium	12-14	Relative even	-	Some	Slightly increased	1.2	-	Medium	None	Low	Some
II-90	Somewhat	Medium	7-14	Un-even	-	Few	Increased	1	Decreased	Medium	None	Low	Few
II-N	Somewhat	Medium	2-5	Un-even	-	None	Slightly increased	0.8	Decreased	Medium	None	Low	Some
III-60	Weak	Medium	20-22	Relative even	X	None	Slightly increased	-	-	Low	None	Low	Some
III-90	Somewhat	Medium	11-15	Un-even	X	Some	Increased	-	Decreased	Low	None	Low	Few
III-N	Somewhat	Medium	4	Even	X	Few	Slightly increased	1	-	Low	None	Low	Some

Generally, the cement in the concrete samples are well hydrated, but in all sample larger partially hydrated cement grains are visible.

Partially hydrated and non-carbonated cement grains are present in the carbonated, especially surface region, of some of the concrete. This feature is most pronounced in concrete containing CEM I and CEM II w. 18%FA and exposed naturally and at 60% RH (Figure 1). In concrete containing CEM II w. 30%FA, and in concrete exposed to 90% RH most of the cement grains are fully hydrated.

Generally, no sign of calcium hydroxide, CH is seen in carbonated pasta.

As the paste in generally has a patchy appearance the carbonated paste also appears patchy with less carbonated "islands" in a zone of carbonated paste (see Plate 1-9). The most distinct patchy feature is seen in concrete containing CEM I, and to some extent in concrete exposed to 90% RH.

Most of the concrete except those containing 30% FA, has a normal carbonation texture (Figure 2). In concrete containing 30% FA a popcorn-like texture is observed (Figure 2).

The concrete containing CEM I has an apparent very high capillary porosity similar or higher than our w/c reference of 0.70. The other concrete has an apparently lower capillary porosity. Generally, an increased porosity of the carbonated paste is seen in all concrete (Table 2).

An about 1mm wide, somewhat opaline zone containing very little CH, is recognized in most concrete except in the concrete containing 30% FA and lab-exposed.

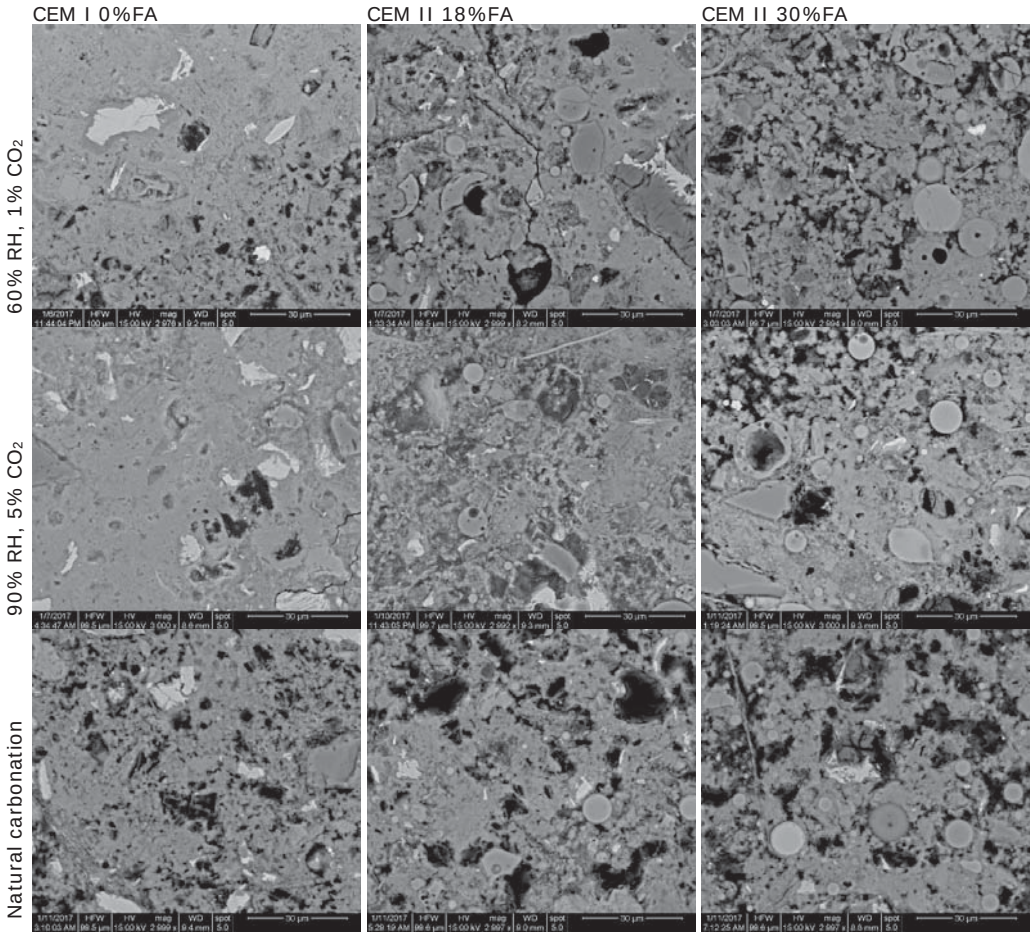

Figure 2: Appearance of the carbonated paste of the 9 concrete samples. A popcorn-like texture is seen in the concrete containing 30% FA. All images are takein the same magnification and in backscatter mode.

Phase analysis performed from EDX analysis on carbonated versus non-carbonated paste is presented in Figure 3.

The analysis shows generally that phase composition generally depends on the cement composition.

CEM I
Non-carbonated paste in concrete with CEM I, mainly consist of a mixture of CH and CSH and when exposed to 90% RH or natural conditions, ettringite seem to be more frequent.

CEM II 18%FA
Non-carbonated paste in concrete with CEM II 18%FA, consist of a mixture of mainly CSH, ettringite and monosulphate.

CEM III 30%FA
Non-carbonated paste in concrete with CEM III 30%FA, consist of a mixture of mainly CSH and monosulphate.

A certain amount of mono-carboaluminate hydrate phases is present in all concrete.

The carbonate phases present in carbonated paste is quite similar in composition to CSH (when plottet in the S/Al diagram), except in concrete with 30%FA where the phases have a distinct lower and more uniform S/Ca ratio.

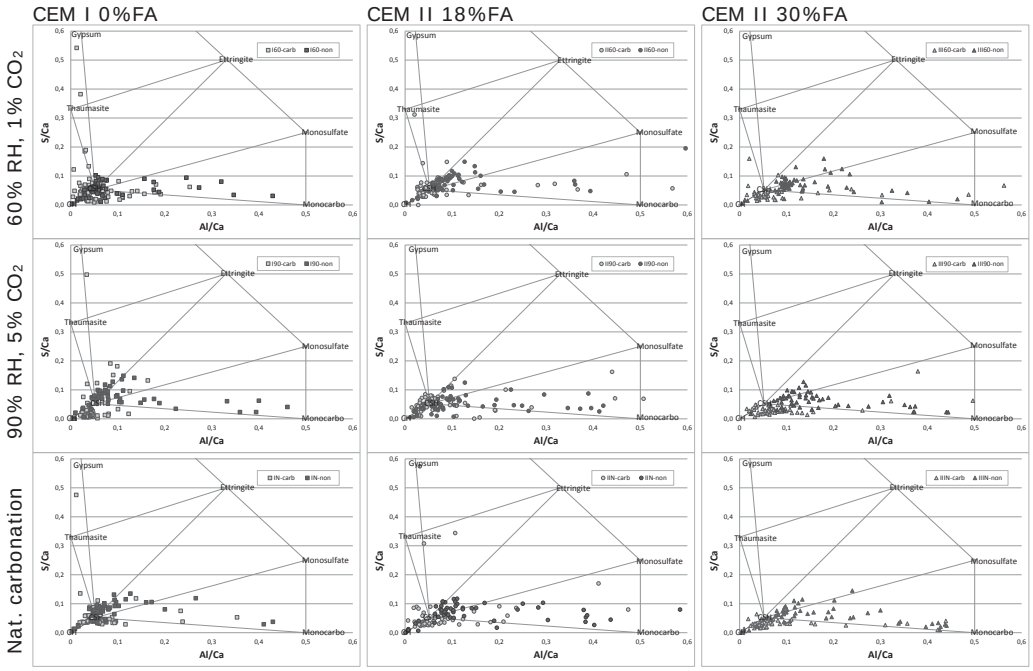

Figure 3: Phase analysis performed on carbonated and non-carbonated paste of the 9 concrete samples.

No distinct differences in phase composition is observed comparing binder type versus exposure condition (Figure 3).

Table 3 shows the average Si/Ca ratio of the carbonated and non-carbonated paste ordered after binder type and exposure condition. As seen, the Si/Ca ratio is in general lower in carbonated paste compared to non-carbonated paste. When ordered after binder type the lowest Si/Ca ratio in non-carbonated paste is in concrete with CEM I, and there is a tendency to it is also lowest in carbonated paste.

Table 3: Average Si/Ca ratios in carbonated and non-carbonated paste ordered after exposure condition and binder type, respectively

#	Carbonated paste	Non-carbonated paste
I60	0.25	0.35
II60	0.32	0.43
III60	0.29	0.43
I90	0.25	0.36
II90	0.27	0.38
III90	0.29	0.45
IN	0.30	0.37
IIN	0.29	0.40
IIIN	0.30	0.40

#	Carbonated paste	Non-carbonated paste
I60	0.25	0.35
I90	0.25	0.36
IN	0.30	0.37
II60	0.32	0.43
II90	0.27	0.38
IIN	0.29	0.40
III60	0.29	0.43
III90	0.29	0.45
IIIN	0.30	0.40

February 15, 2017

Ulla Hjorth Jakobsen
Phone: +45 7220 2198
Email: uhj@teknologisk.dk

3. Analytical Methods

3.1 Petrography

The petrographic analysis (both macroscopic and microscopic examination) is carried out according to ASTM C856 "Standard Practice for Petrographic Examination of Hardened Concrete". The samples are for documentation photographed when received.

The microscopic examination is performed on totally 9 fluorescent impregnated thin sections. A section represents an area of 30 x 45 mm. The section is positioned from the surface and 45 mm into the concrete. The cast surface is indicated with an arrow on the section. All photographs taken, are positioned with the cast surface facing up.

The thin section is made by vacuum impregnating a slice of the sample with an epoxy resin containing a fluorescent dye. Subsequently, the impregnated slice is mounted on a glass plate, and ground to a thickness of 0.020 mm (20 µm). Finally, the section is covered by a cover glass. The thin section is then examined in a polarizing optical microscope using transmitted light, crossed polarized light, and blue transmitted light with a yellow blocking filter (fluorescent mode).

Three photographs using the three light modes have been taken from 3 position in each section; carbonated paste, interface between carbonated and non-carbonated paste, and non-carbonated paste. The photographs are presented in nine Plates attached.

The vacuum impregnation of the sample with epoxy causes all voids and cavities in the sample to be filled with fluorescent epoxy. By transmitting fluorescent light through the thin section in the microscope, the fluorescent epoxy in the various porosities will emit yellow light that makes voids, cavities and cracks easy to identify. The fluorescent epoxy also impregnates the capillary pores in the hardened cement paste causing a dense cement paste with low water to cement ratio to appear darker green while a more porous cement paste with a high water to cement ratio appears lighter green. By this, the water to cement ratio (w/c) of the concrete is estimated, by comparing to known references, with an accuracy of ± 0.02.

The table below gives definitions of petrographic terms used in the text.

Terms	Definition
Micro cracks	Cracks that are less than 0.01 mm wide
Fine cracks	Cracks that are between 0.01 and 0.1 mm wide
Coarse cracks	Cracks that are more than 0.1 mm wide
Adhesion cracks	Half moon shaped cracks (defects) along the paste/aggregate interface. The cracks mirror the aggregate surfaces. Forms in non-hardened concrete often as a result of bleeding
Totally carbonated	All calcium hydroxide, and all CSH phases are carbonated
Partly carbonated	All calcium hydroxide is carbonated but partly un-hydrated cement grains remain non-carbonated
Hadley Holes	Term describing holes or imprints after former cement grains, now hydrated. When viewed in fluorescent light they appear bright yellow (holes) with the shape of former alite grains. These features are especially distinct in the cement paste of rapid hardening cement

3.2 Scanning Electron Microscopy

SEM-EDX analysis is performed on 9 polished sections using a Quanta 400 from FEI at DTI. An accelerating voltage of 15 KeV, spot size 5 and a working distance of around 10 mm are used during analysis. The data are Proza corrected. The analyses were performed using carbon-coated polished sections in high vacuum mode.
Paste analysis is performed on each sample by analyzing 50 point in carbonated area and 50 points in non-carbonated area.

4. PETROGRAPHIC ANALYSIS

Project No.	735718	**Sample No.:**	I-60	**Section #:**	7842-1	**Size:**	30x45mm

Petrographic Analysis

Binder type:	CEM I, 0%FA
Paste:	The cement is well hydrated. The paste appears distinctly patchy throughout with alternating highly porous and less porous areas. Generally, the paste appears highly porous with an apparent w/c ratio equal or higher to our 0.70 reference. A slightly higher porosity is seen in the carbonated surface area.
$Ca(OH)_2$:	Present throughout the paste and in many air voids as relatively large crystals. The content of CH is highest in the most porous areas. CH is observed in few voids of the carbonated zone.
Opaline paste:	Not observed.
Carbonation (mm):	12mm, relatively even front. The zone contains many non-carbonated areas where the cement grains are only partially hydrated. Larger cement grains in the carbonated zone is non-carbonated. A 1.2mm thick slightly opaline zone, with very little CH, is present in front of the carbonated paste.
Surface:	The surface appears plane and intact with few plastic cracks.
Interior cracks:	Few adhesion cracks are observed.
Ettringite:	Not observed.
Air (type, est. vol%):	Many small air voids present, well-distributed, estimated to 5-6vol%.

Phase Analysis

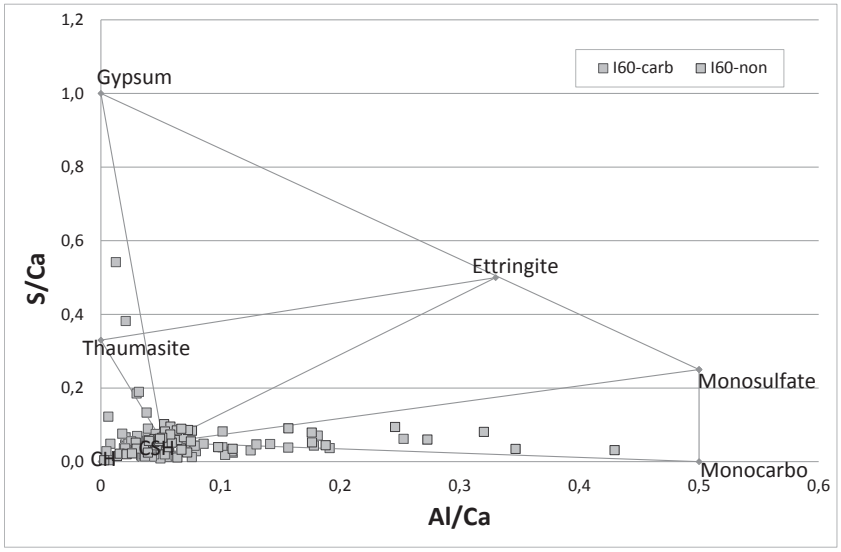

SEM-EDX analysis

Project No.	735718	**Sample No.:**	I-60	**Section #:**	7842-1	**Size:**	30x45mm

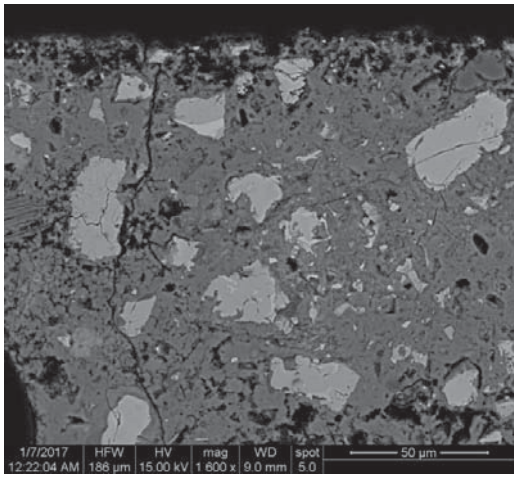

Overview, carbonated surface; several un-hydrated cement grains

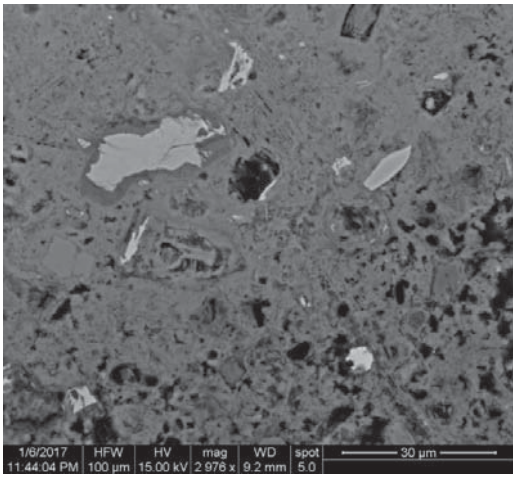

Carbonated paste

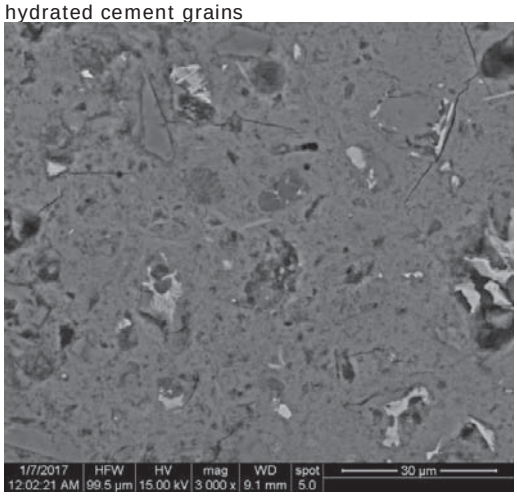

Carbonated paste

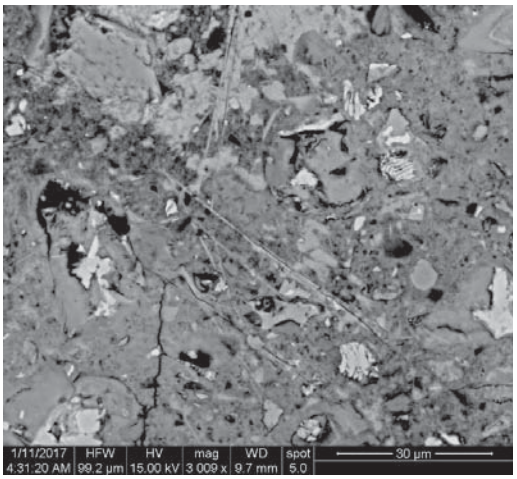

Non-carbonated paste

PETROGRAPHIC ANALYSIS

Project No.	735718	**Sample No.:**	II-60	**Section #:**	7842-2	**Size:**	30x45mm

Petrographic Analysis

Binder type:	CEM II, 18%FA
Paste:	The cement is well hydrated. The paste appears somewhat patchy with alternating porous and less porous areas. Generally, the paste is porous, with a slightly higher porosity in the carbonated surface area.
$Ca(OH)_2$:	Present throughout the paste, small crystals. CH is not observed in air voids.
Opaline paste:	Somewhat opaline in non-carbonated areas.
Carbonation (mm):	12-14mm, relatively even front. The zone contains some non-carbonated areas where the cement grains are visible. Larger cement grains in the carbonated zone, especially near the surface, is non-carbonated. A 1.2mm thick slightly opaline zone, with very little CH, is present in front of the carbonated paste.
Surface:	The surface appears plane and intact with many plastic cracks.
Interior cracks:	Some adhesion cracks are observed.
Ettringite:	Not observed.
Air (type, est. vol%):	Few, large air voids present.

Phase Analysis

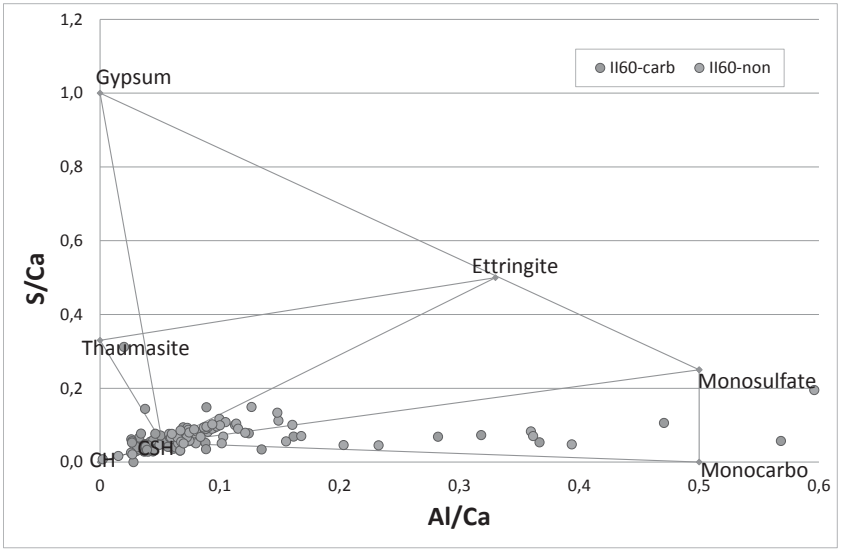

SEM-EDX analysis

Project No.	735718	**Sample No.:**	II-60	**Section #:**	7842-2	**Size:**	30x45mm

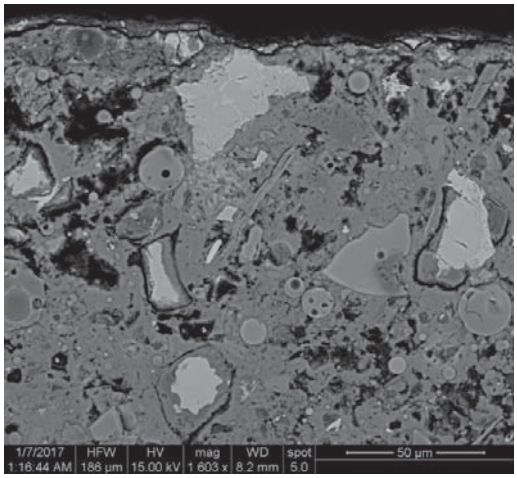

Overview, carbonated surface; several unhydrated cement grains

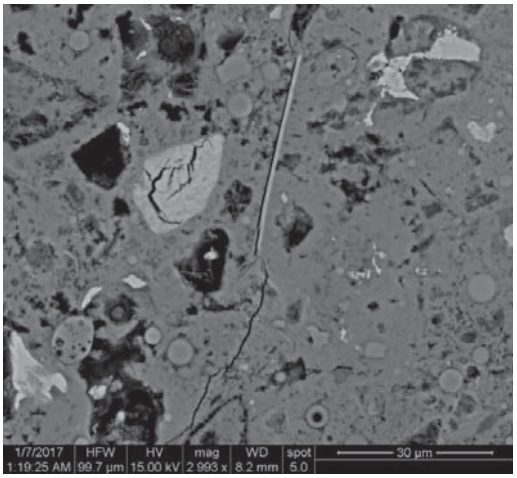

Carbonated paste

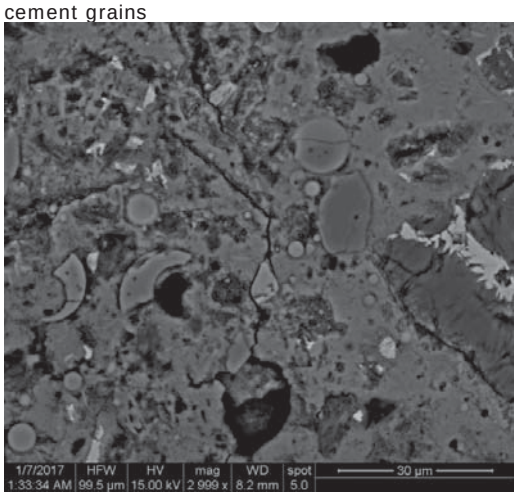

Carbonated paste

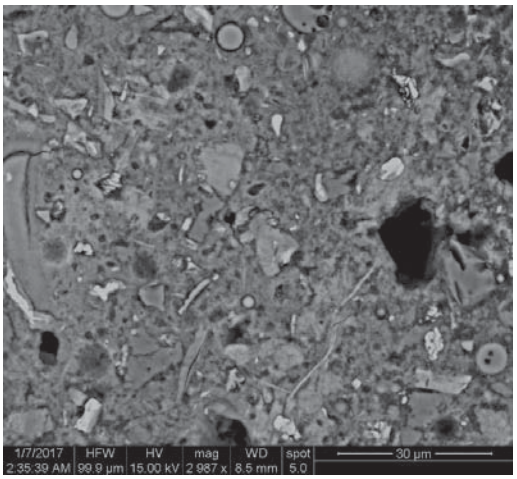

Non-carbonated paste

PETROGRAPHIC ANALYSIS

Project No.	735718	**Sample No.:**	III-60	**Section #:**	7842-3	**Size:**	30x45mm

Petrographic Analysis

Binder type:	CEM II, 30%FA
Paste:	The cement is well hydrated. The paste appears relatively homogeneous throughout. Generally, the paste is porous, with a slightly higher porosity in the carbonated surface area.
$Ca(OH)_2$:	Difficult to observe due to the distinct opalinity of the paste, but present throughout. CH is not observed in air voids.
Opaline paste:	Distinctly opaline in non-carbonated areas.
Carbonation (mm):	20-22mm, relatively even front. Only few larger cement grains in the carbonated zone is non-carbonated. The texture of the carbonated paste looks like popcorn. No distinct interface zone between carbonated and non-carbonated paste is recognized.
Surface:	The surface appears plane and intact with few plastic cracks.
Interior cracks:	Some adhesion cracks are observed.
Ettringite:	Not observed.
Air (type, est. vol%):	Few, large air voids present.

Phase Analysis

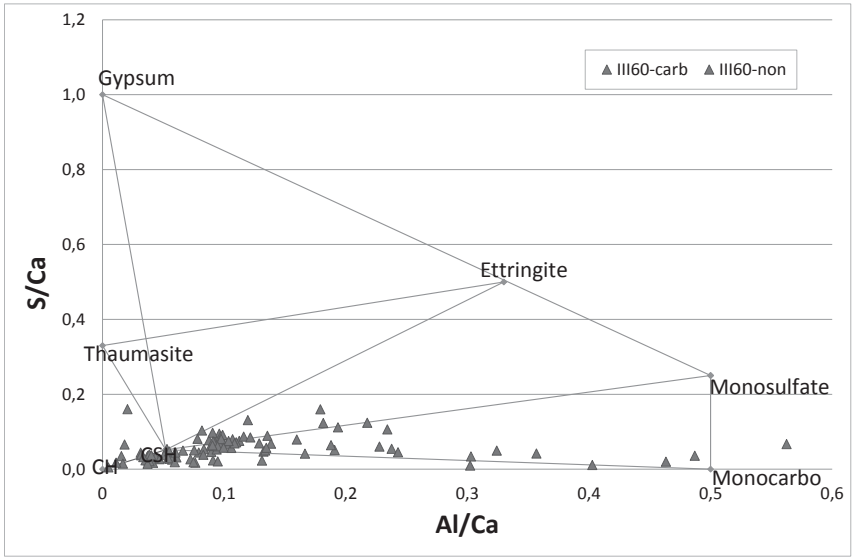

SEM-EDX analysis

Project No.	735718	**Sample No.:**	III-60	**Section #:**	7842-3	**Size:**	30x45mm

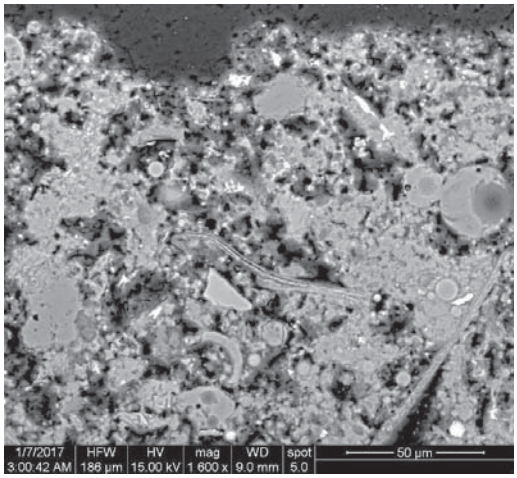

Overview, carbonated surface

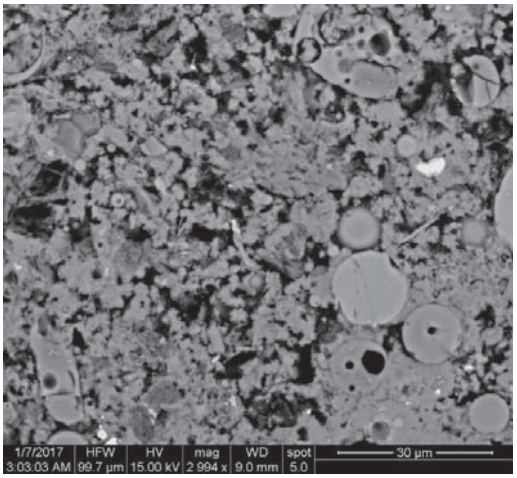

Carbonated paste

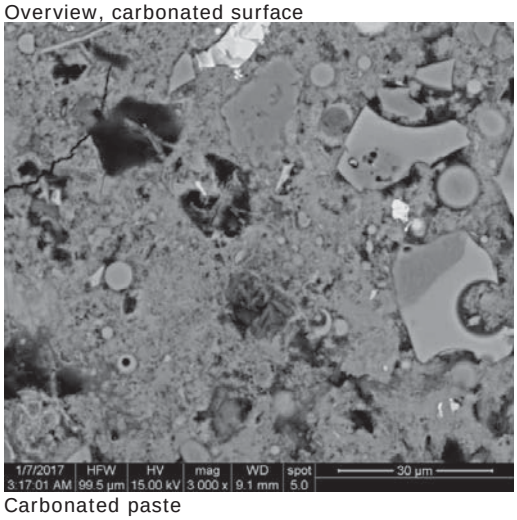

Carbonated paste

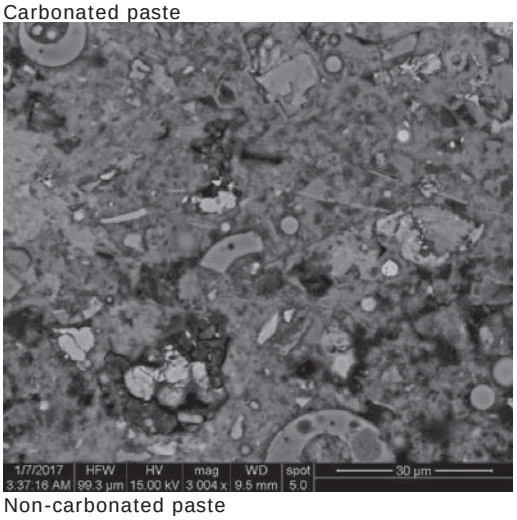

Non-carbonated paste

DANISH TECHNOLOGICAL INSTITUTE

PETROGRAPHIC ANALYSIS

Project No.	735718	**Sample No.:**	I-90	**Section #:**	7842-4	**Size:**	30x45mm

Petrographic Analysis

Binder type:	CEM I, 0%FA
Paste:	The cement is well hydrated. The paste appears distinctly patchy throughout with alternating highly porous and less porous areas (bleeding?). Generally, the paste is highly porous with an apparent w/c ratio equal or higher to our 0.70 reference, however a distinct lower porosity is seen in the interface zone between carbonated and non-carbonated paste.
$Ca(OH)_2$:	Present throughout the paste and in many air voids as relatively large crystals.
Opaline paste:	Not observed.
Carbonation (mm):	4-14mm, highly un-even front, difficult to draw a line. The zone contains many non-carbonated areas where the cement grains are visible. Many larger cement grains in the carbonated zone is only partially hydrated and non-carbonated. An approximate 1mm thick slightly opaline zone, with very little CH, is present in front of the carbonated paste.
Surface:	The surface appears plane and intact with few plastic cracks.
Interior cracks:	Few adhesion cracks are observed.
Ettringite:	Observed within the non-carbonated paste of the carbonated zone.
Air (type, est. vol%):	Many small air voids present, well-distributed, estimated to 5-6vol%.

Phase Analysis

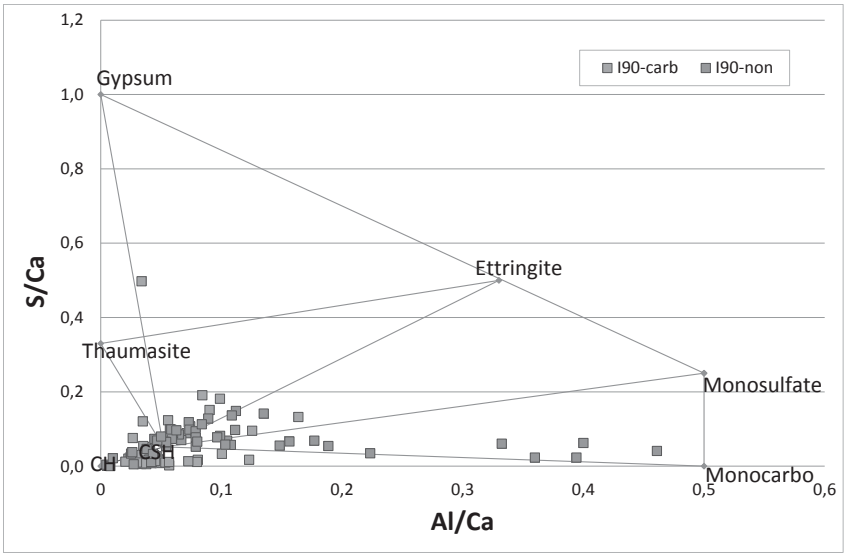

SEM-EDX analysis

Project No.	735718	**Sample No.:**	I-90	**Section #:**	7842-4	**Size:**	30x45mm

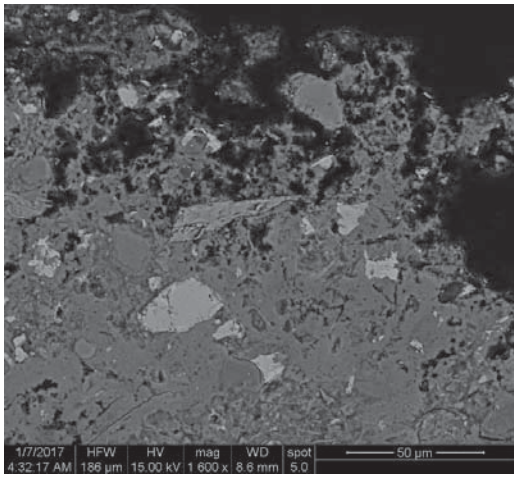

Overview, carbonated surface, some un-hydrated cement grains

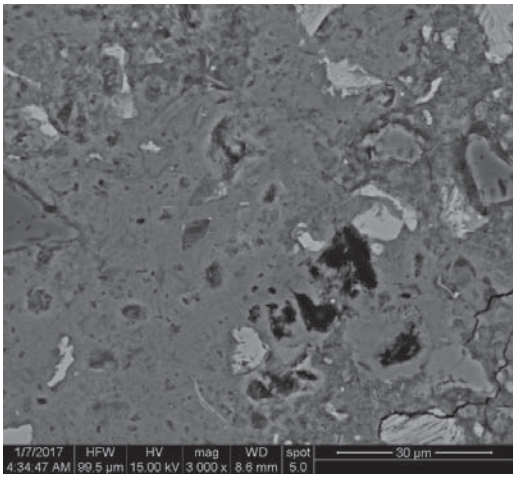

Carbonated paste

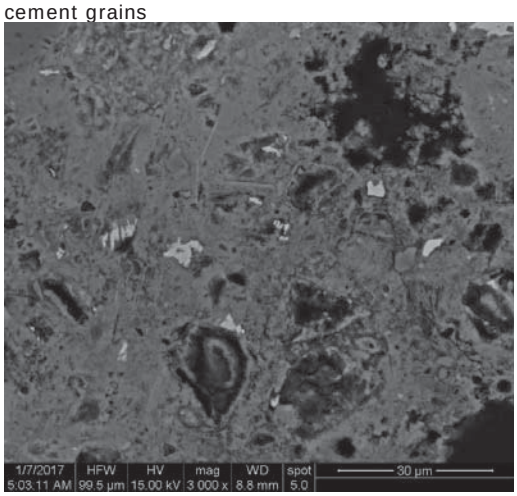

Carbonated paste

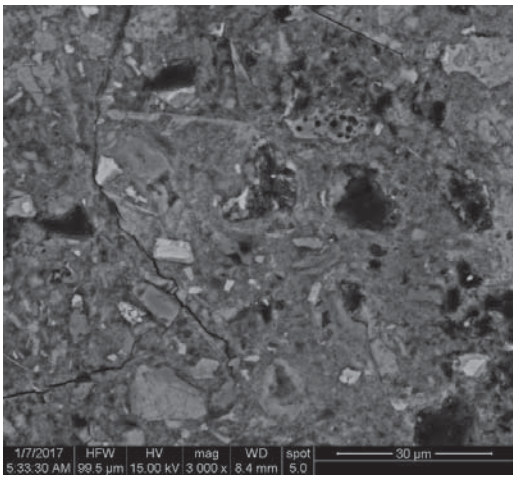

Non-carbonated paste

PETROGRAPHIC ANALYSIS

Project No.	735718	**Sample No.:**	II-90	**Section #:**	7842-5	**Size:**	30x45mm

Petrographic Analysis

Binder type:	CEM II, 18%FA
Paste:	The cement is well hydrated. The paste appears somewhat patchy with alternating porous and less porous areas (most distinct in non-carbonated paste). Generally, the paste is porous, with a slightly higher porosity in the carbonated surface area. A distinct lower porosity is observed at the interface between carbonated and non-carbonated paste.
$Ca(OH)_2$:	Present throughout the paste. CH is not observed in air voids.
Opaline paste:	Somewhat opaline in non-carbonated areas.
Carbonation (mm):	7-14mm, relatively un-even front. The zone contains few non-carbonated areas where the cement grains are visible. Few larger cement grains in the carbonated zone appears non-carbonated. An approximate 1mm thick slightly opaline zone, with very little CH, is present in front of the carbonated paste.
Surface:	The surface appears plane and intact with some plastic cracking.
Interior cracks:	Few adhesion cracks are observed.
Ettringite:	Not observed.
Air (type, est. vol%):	Few, large air voids present.

Phase Analysis

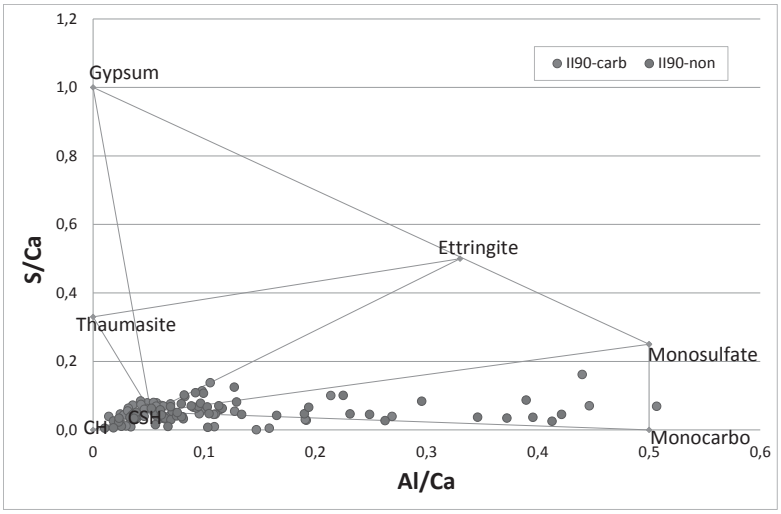

SEM-EDX analysis

Project No.	735718	**Sample No.:**	II-90	**Section #:**	7842-5	**Size:**	30x45mm

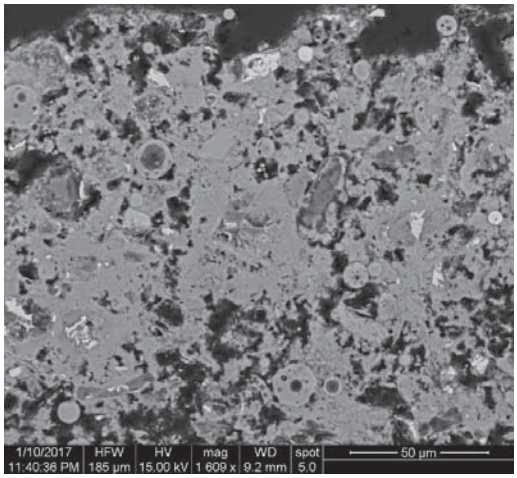

Overview, carbonated surface

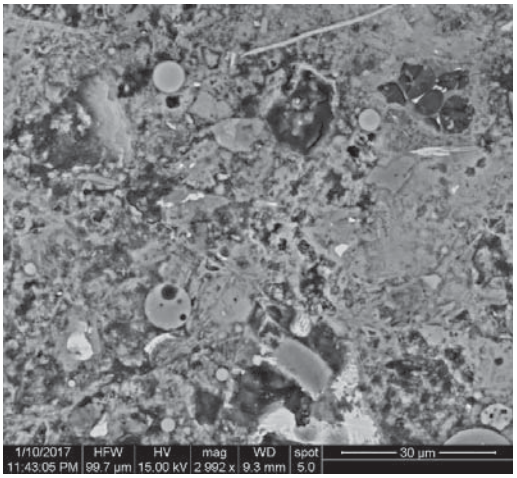

Carbonated paste

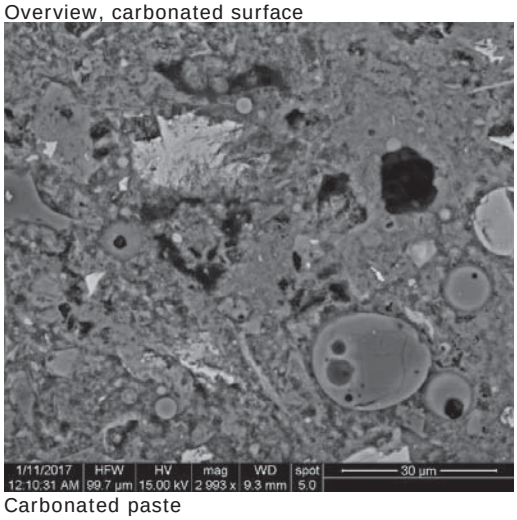

Carbonated paste

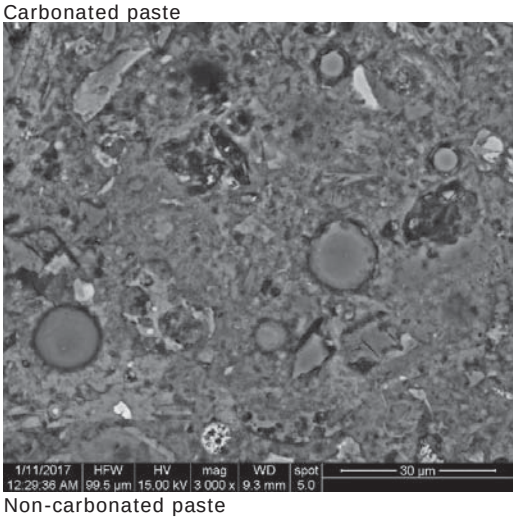

Non-carbonated paste

PETROGRAPHIC ANALYSIS

Project No.	735718	**Sample No.:**	III-90	**Section #:**	7842-6	**Size:**	30x45mm

Petrographic Analysis

Binder type:	CEM II, 30%FA
Paste:	The cement is well hydrated. The paste appears somewhat inhomogeneous with patchy areas (especially in non-carbonated areas). Generally, the paste is porous, with a somewhat higher porosity in the carbonated surface area.
$Ca(OH)_2$:	Difficult to observe due to distinct opalinity of paste, but present throughout.
Opaline paste:	Distinctly opaline in non-carbonated areas.
Carbonation (mm):	11-15mm, somewhat un-even front. Non-carbonated paste is present along some of the coarse aggregate particles. Only few larger cement grains in the carbonated zone is non-carbonated. The texture of the carbonated paste appears like popcorn. No distinct interface zone between carbonated and non-carbonated paste is recognized.
Surface:	The surface is plane and intact with few plastic cracks.
Interior cracks:	Few adhesion cracks are observed.
Ettringite:	Not observed.
Air (type, est. vol%):	Few, large air voids present.

Phase Analysis

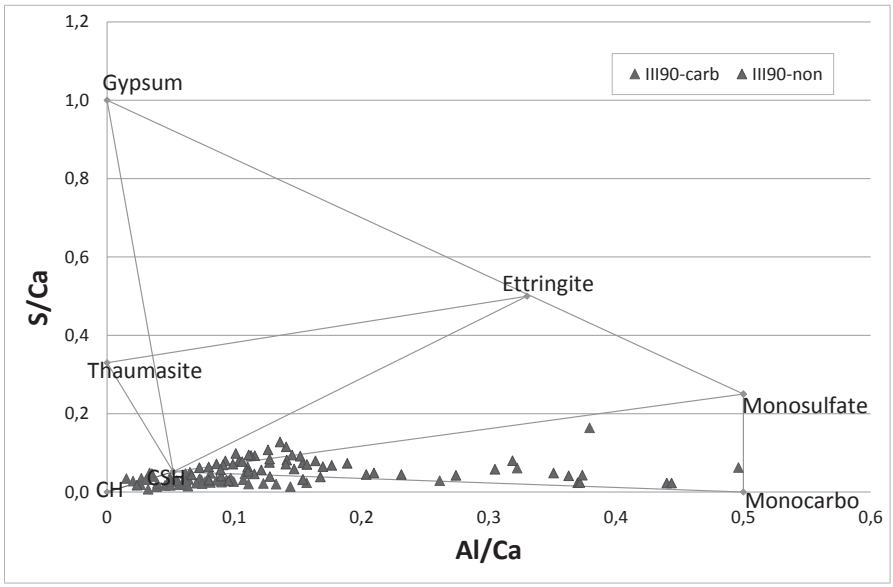

SEM-EDX analysis

Project No.	735718	**Sample No.:**	III-90	**Section #:**	7842-6	**Size:**	30x45mm

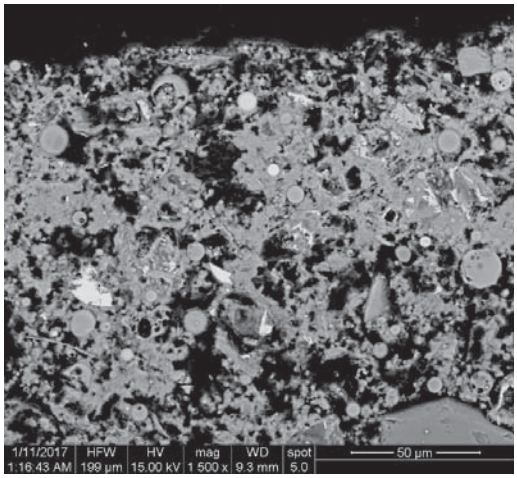

Overview, carbonated surface, popcorn carbonated

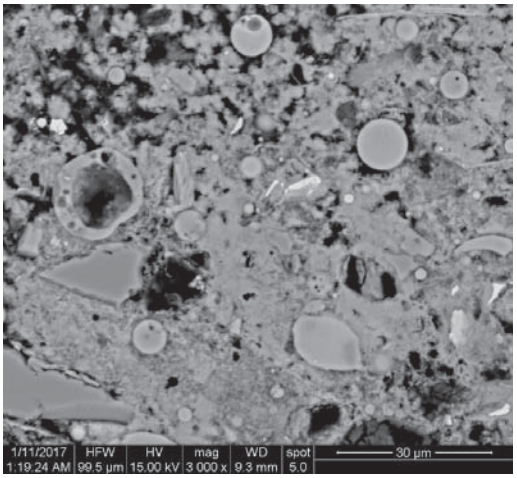

Carbonated paste

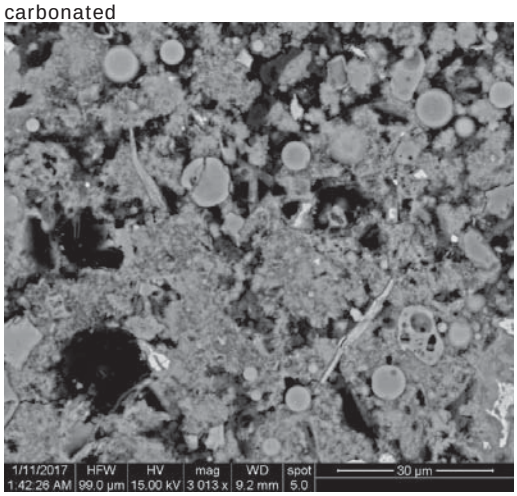

Carbonated paste

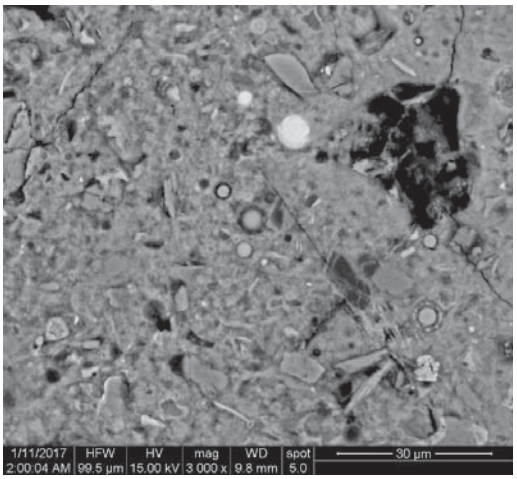

Non-carbonated paste

PETROGRAPHIC ANALYSIS

Project No.	735718	**Sample No.:**	I-N	**Section #:**	7842-7	**Size:**	30x45mm

Petrographic Analysis

Binder type:	CEM I, 0%FA
Paste:	The cement is well hydrated. The paste appears patchy throughout with alternating highly porous and less porous areas. Generally, the paste is highly porous with an apparent w/c ratio equal or higher to our 0.70 reference.
$Ca(OH)_2$:	Present throughout the paste and in many air voids as relatively large crystals.
Opaline paste:	Not observed.
Carbonation (mm):	2-5mm, somewhat un-even front. The zone contains some less-carbonated areas where non-carbonated cement grains are visible; these areas are most distinct near the surface. Larger cement grains in the carbonated zone, especially near the surface, is only partially hydrated and non-carbonated. A 0.8mm thick slightly opaline zone, with very little CH, is present in front of the carbonated paste.
Surface:	The surface is plane and intact with some plastic cracking.
Interior cracks:	Few adhesion cracks are observed.
Ettringite:	Not observed.
Air (type, est. vol%):	Many small air voids present, well-distributed, estimated to 5-6vol%.

Phase Analysis

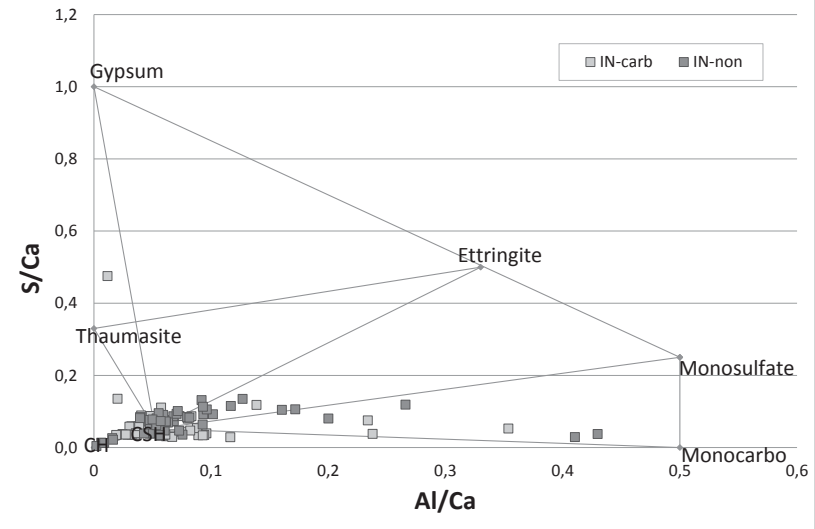

SEM-EDX analysis

Project No.	735718	**Sample No.:**	I-N	**Section #:**	7842-7	**Size:**	30x45mm

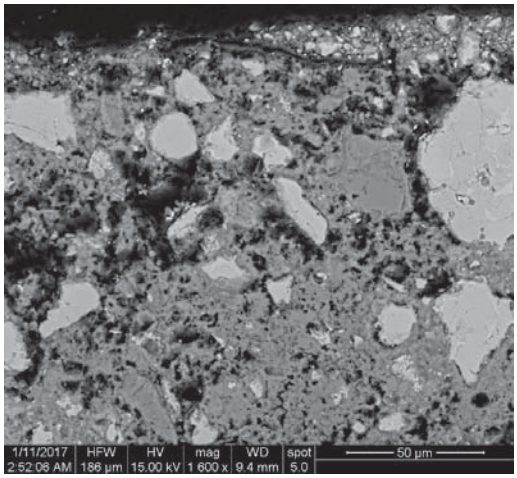

Overview, carbonated surface, several un-hydrated cement grains

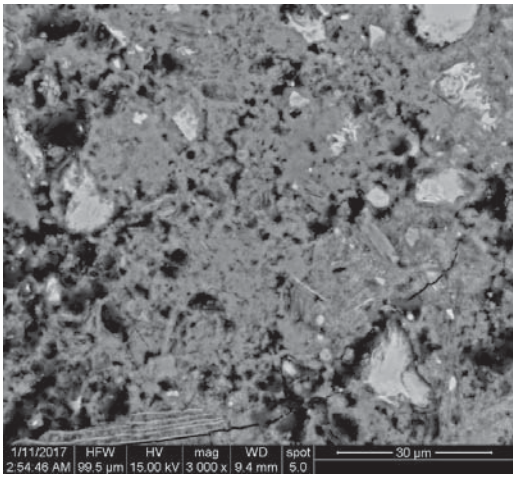

Carbonated paste

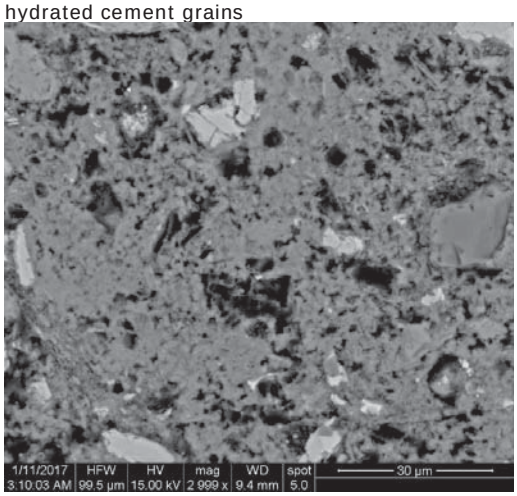

Carbonated paste

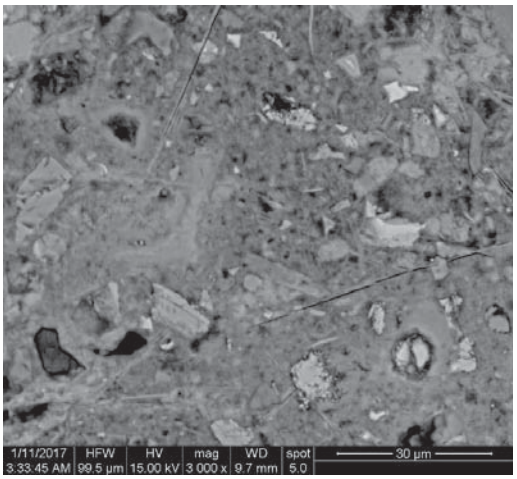

Non-carbonated paste

PETROGRAPHIC ANALYSIS

Project No.	735718	**Sample No.:**	II-N	**Section #:**	7842-8	**Size:**	30x45mm

Petrographic Analysis

Binder type:	CEM II, 18%FA
Paste:	The cement is well hydrated. The paste appears somewhat patchy. Generally, the paste is porous, with a slightly higher porosity in the carbonated surface area. A distinct lower porosity is observed at the interface between carbonated and non-carbonated paste.
$Ca(OH)_2$:	Present throughout the paste. CH is not observed in air voids.
Opaline paste:	Slightly opaline in non-carbonated areas.
Carbonation (mm):	2-5mmmm, relatively un-even front. Many larger cement grains in the carbonated zone, near the surface, are less hydrated and non-carbonated. An approximate 0.8mm thick slightly opaline zone, with very little CH, is present in front of the carbonated paste.
Surface:	The surface is plane and intact, with a high number of plastic cracks.
Interior cracks:	Some adhesion cracks are observed.
Ettringite:	Not observed.
Air (type, est. vol%):	Few, large air voids present.

Phase Analysis

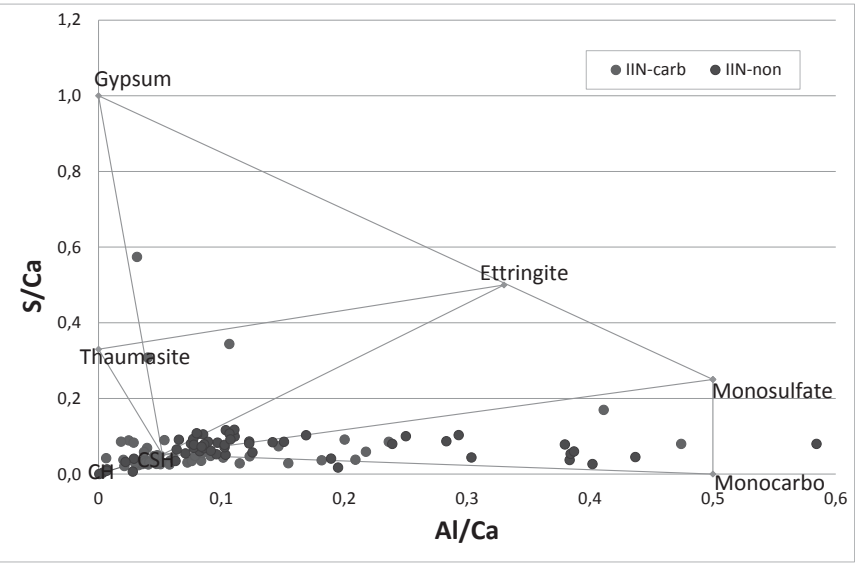

SEM-EDX analysis

Project No.	735718	**Sample No.:**	II-N	**Section #:**	7842-8	**Size:**	30x45mm

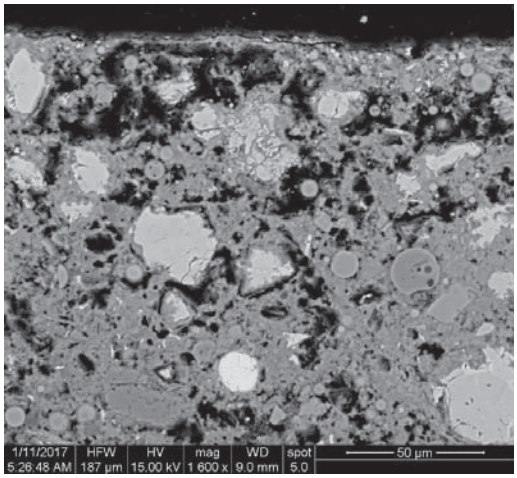

Overview, carbonated surface with many unhydrated cement grains

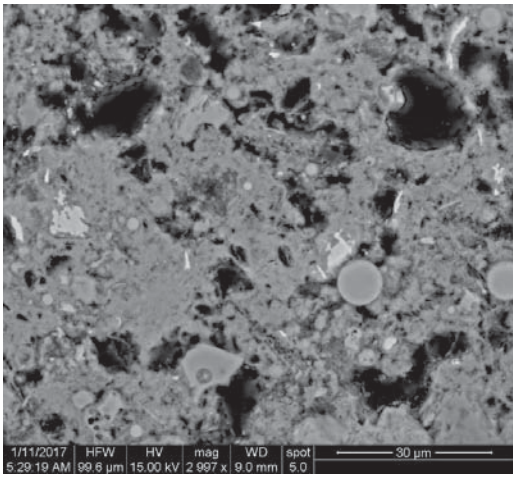

Carbonated paste

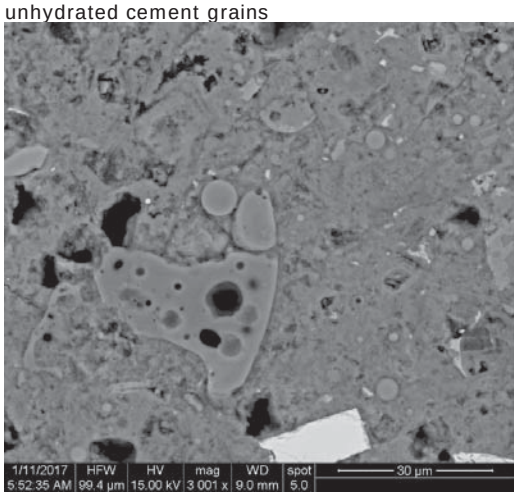

Carbonated paste

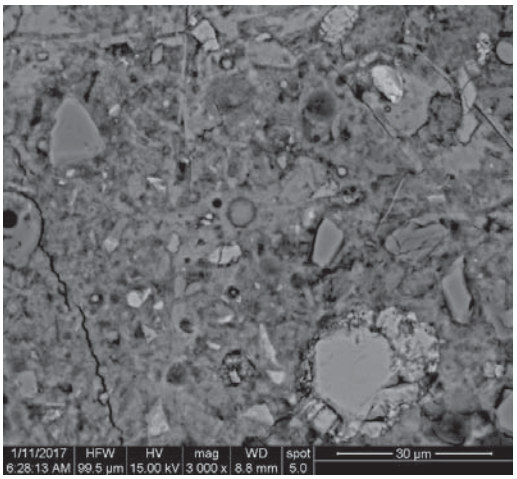

Non-carbonated paste

PETROGRAPHIC ANALYSIS

Project No.	735718	**Sample No.:**	III-N	**Section #:**	7842-9	**Size:**	30x45mm

Petrographic Analysis

Binder type:	CEM II, 30%FA
Paste:	The cement is well hydrated. The paste appears somewhat patchy. Generally, the paste is porous, with a somewhat higher porosity in the carbonated surface area.
$Ca(OH)_2$:	Difficult to observe, but present throughout the paste.
Opaline paste:	Distinctly opaline in non-carbonated areas.
Carbonation (mm):	4mm, rather even front. Most cement grains in the carbonated zone is hydrated and carbonated. The texture of the carbonated paste looks like popcorn. An approximate 1mm thick slightly opaline zone, with very little CH, is present in front of the carbonated paste.
Surface:	The surface is plane and intact with few plastic cracks.
Interior cracks:	Some adhesion cracks are observed.
Ettringite:	Not observed.
Air (type, est. vol%):	Few, large air voids present but larger agglomerates are observed.

Phase Analysis

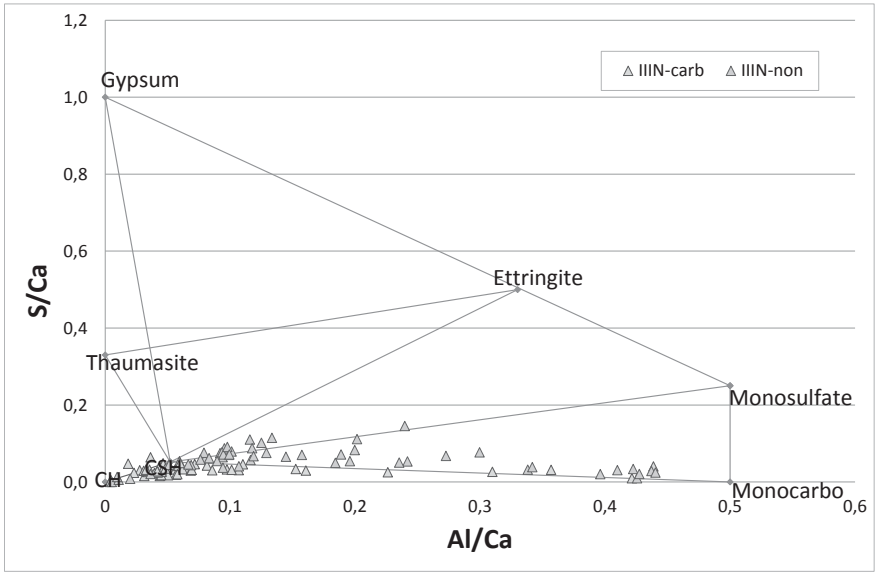

SEM-EDX analysis

Project No.	735718	**Sample No.:**	III-N	**Section #:**	7842-9	**Size:**	30x45mm

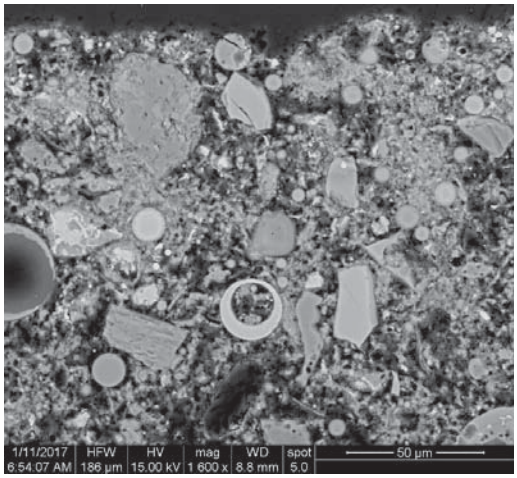

Overview, porous carbonated surface

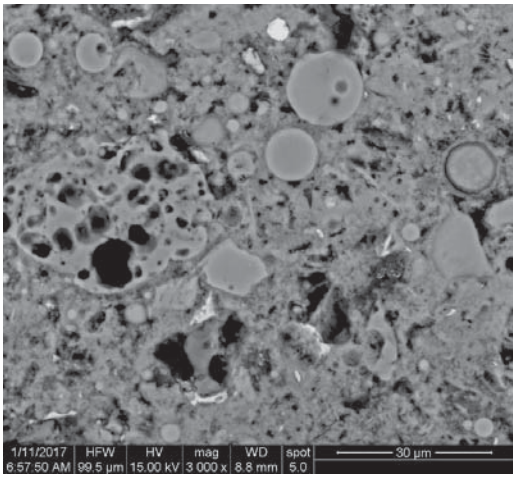

Carbonated paste

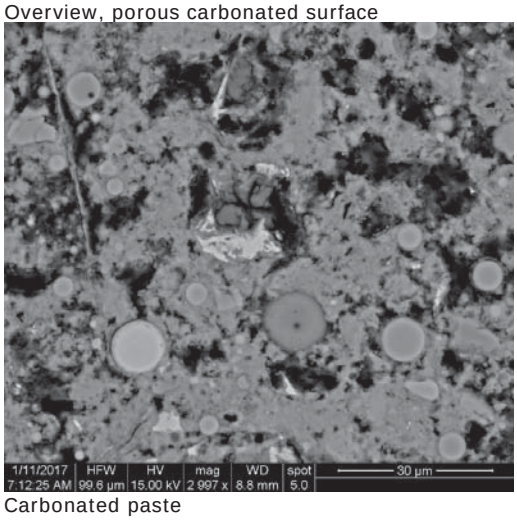

Carbonated paste

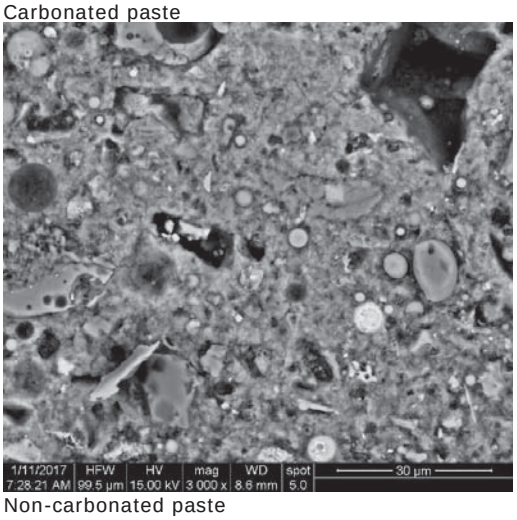

Non-carbonated paste

Plate 1: I-60, CEM I

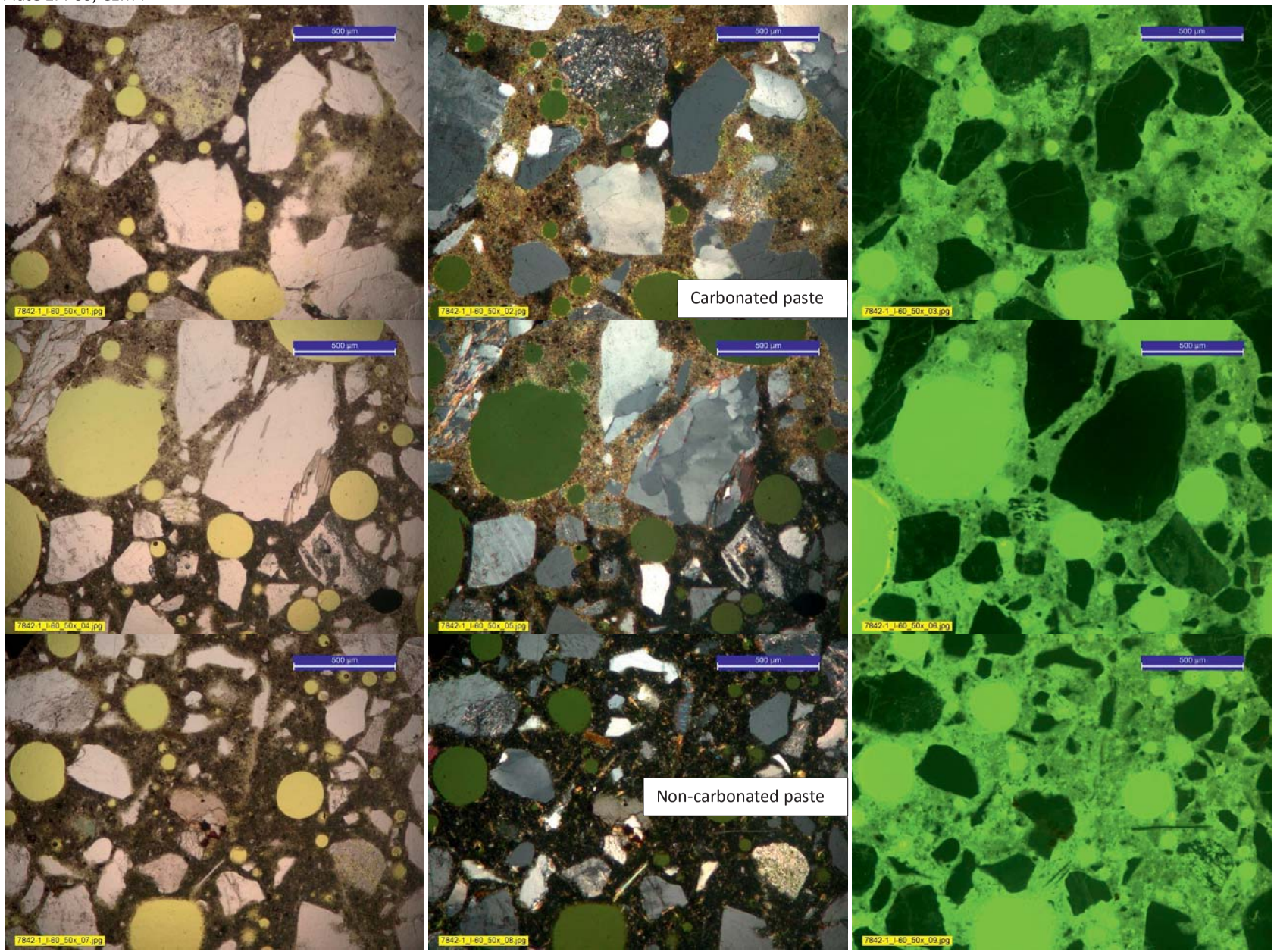

Plate 2: II-60, CEM II/B-M

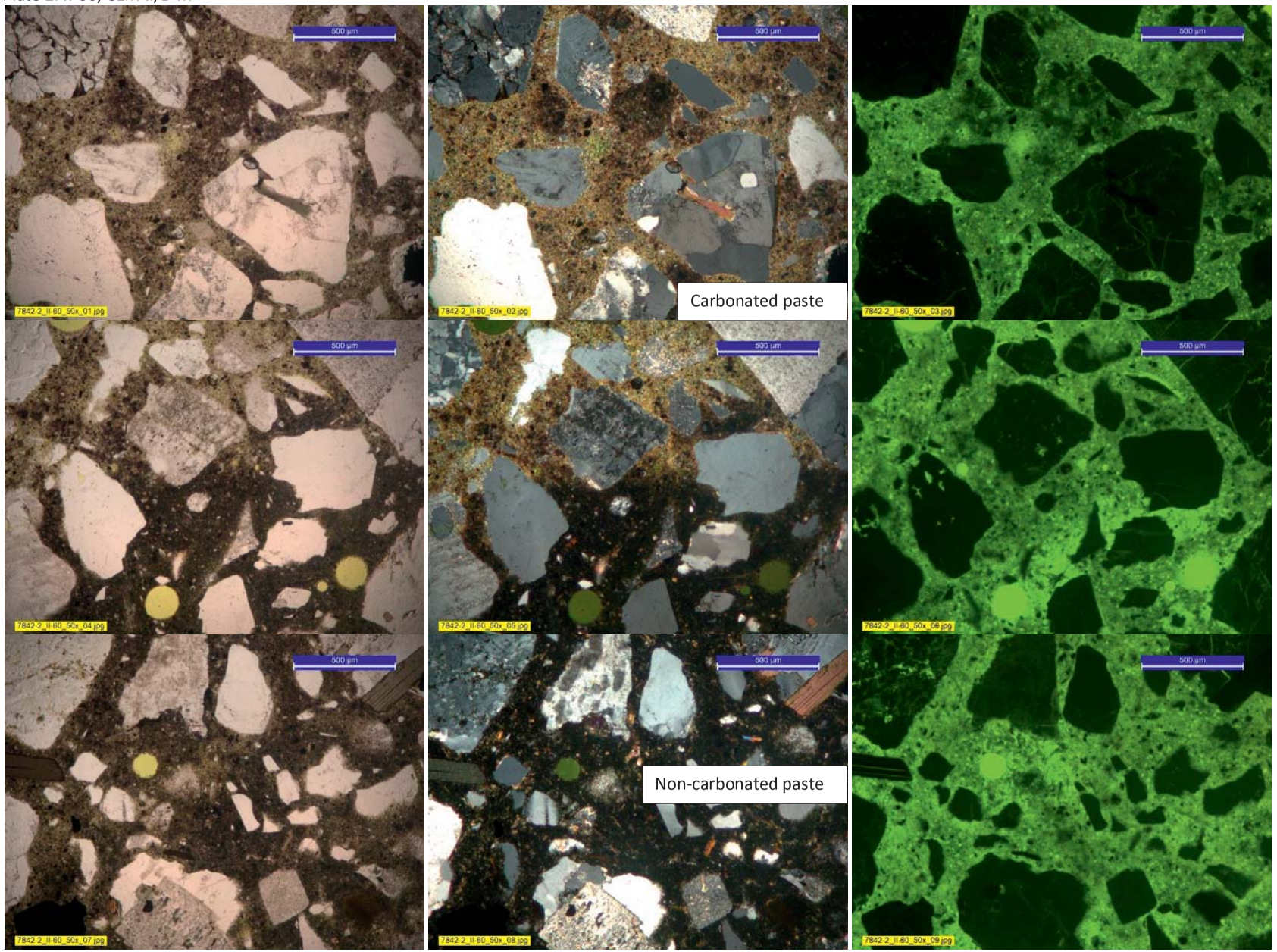

Plate 3: III-60, CEM II/B-V

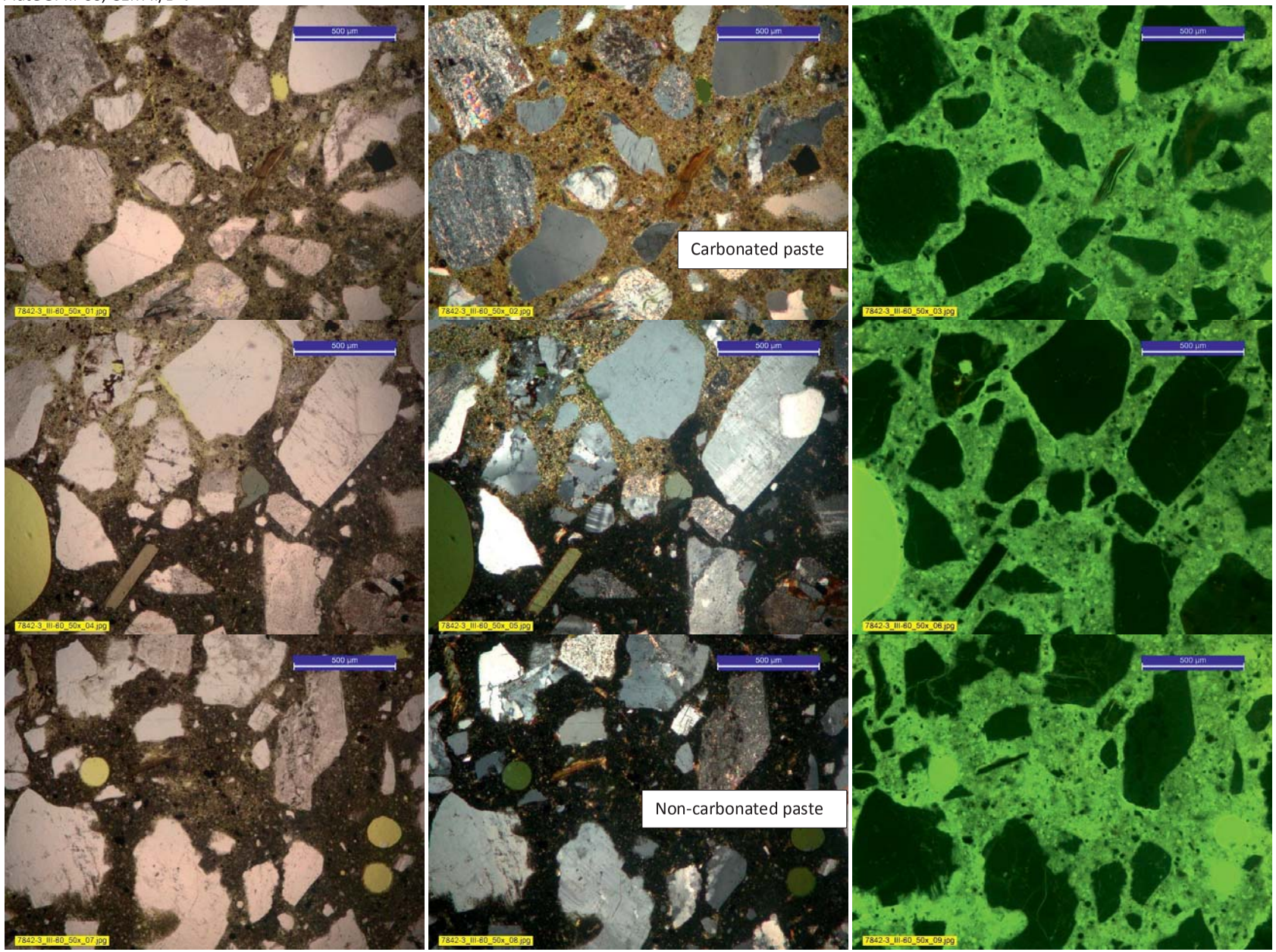

Plate 4: I-90, CEM I

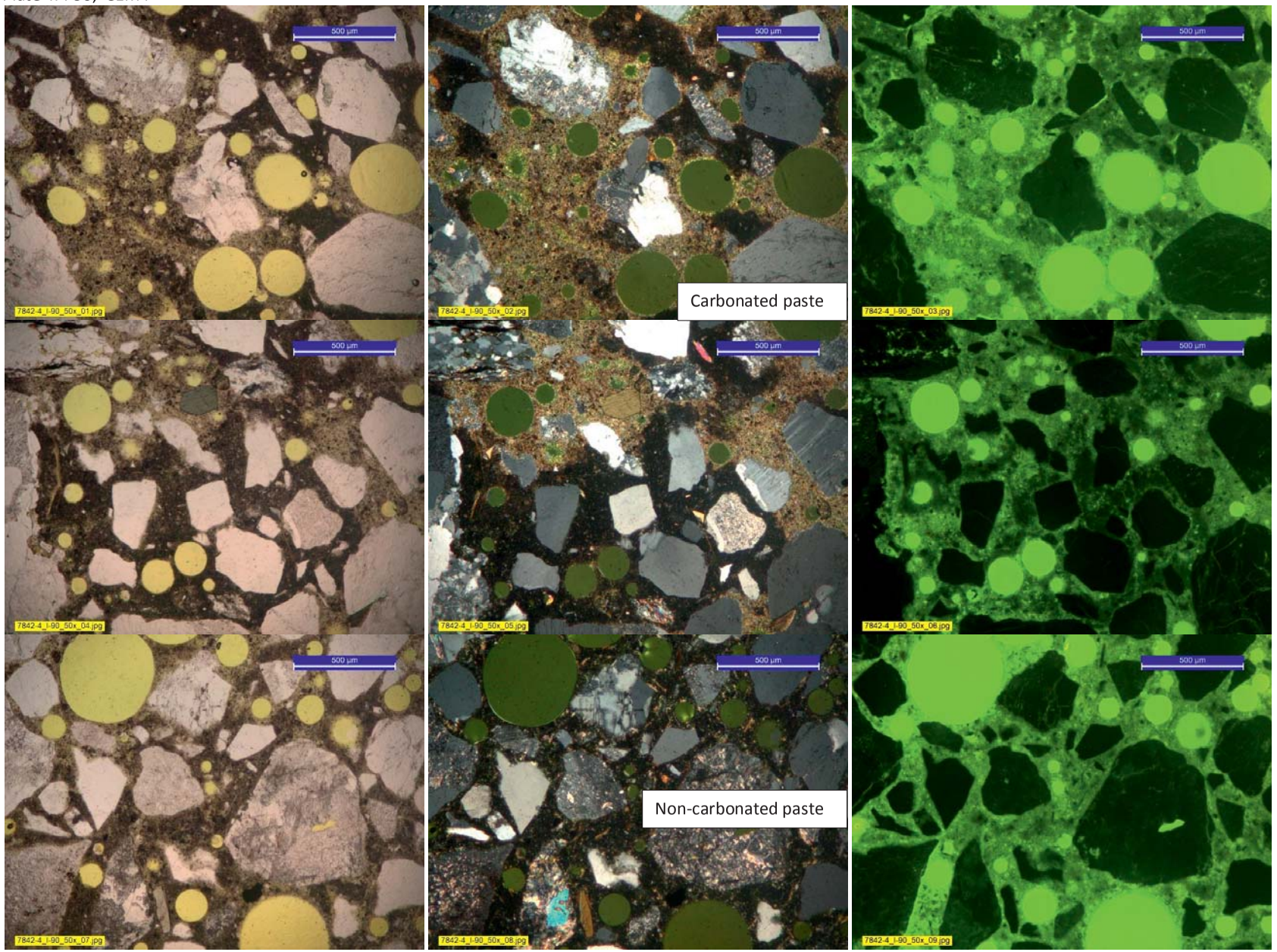

Plate 5: II-90, CEM II/B-M

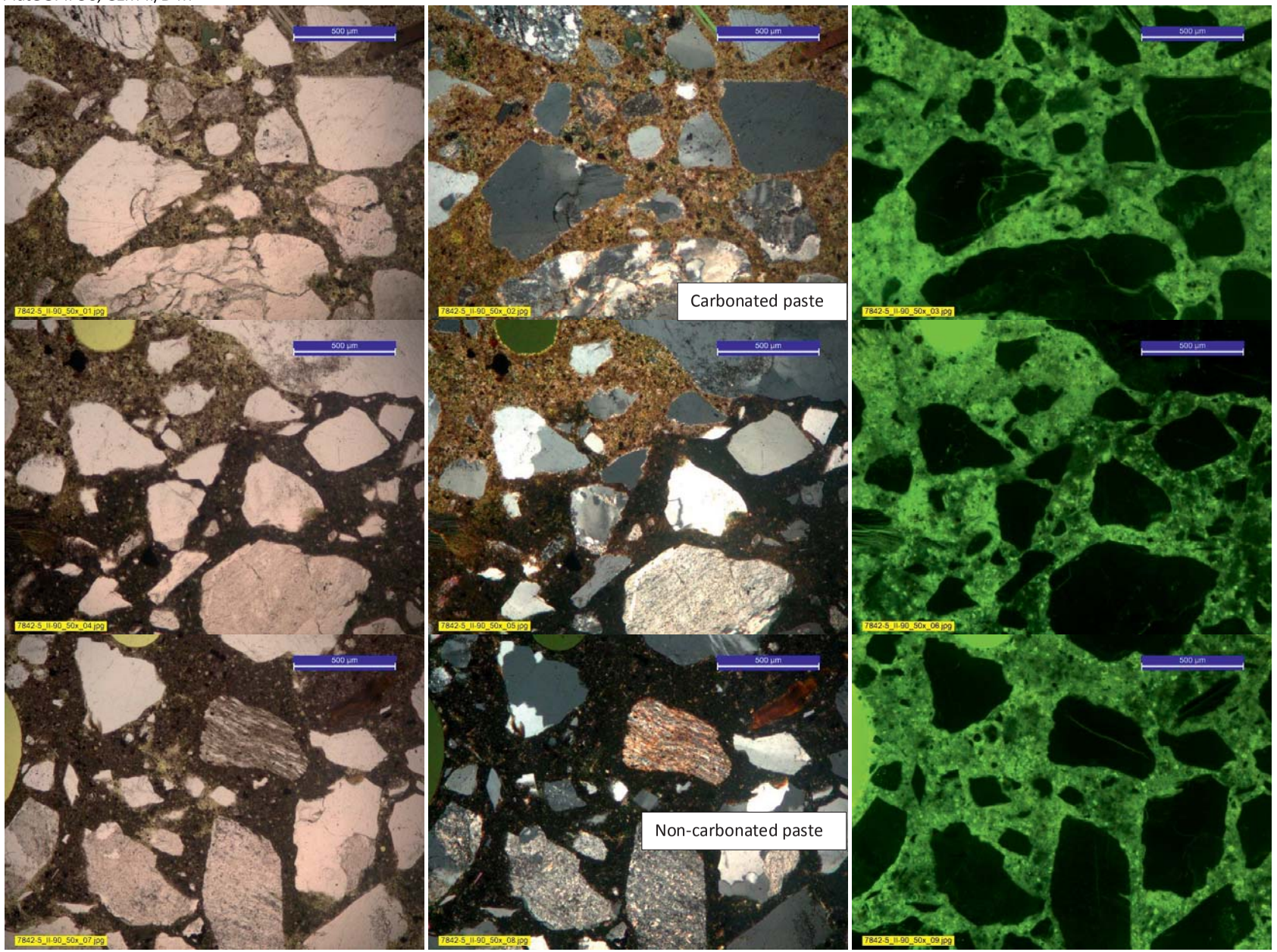

Plate 6: III-90, CEM II/B-V

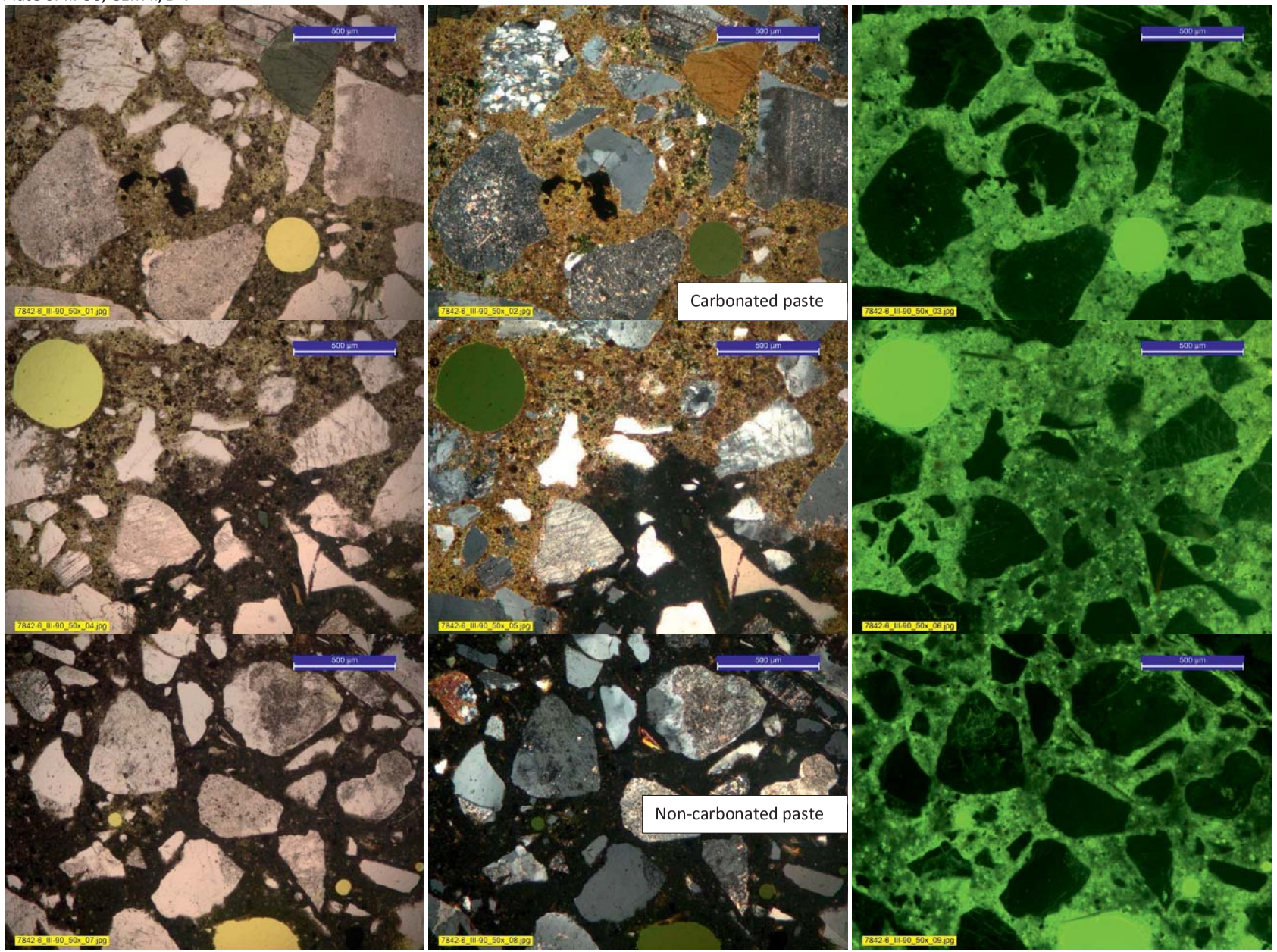

Plate 7: I-N, CEM I

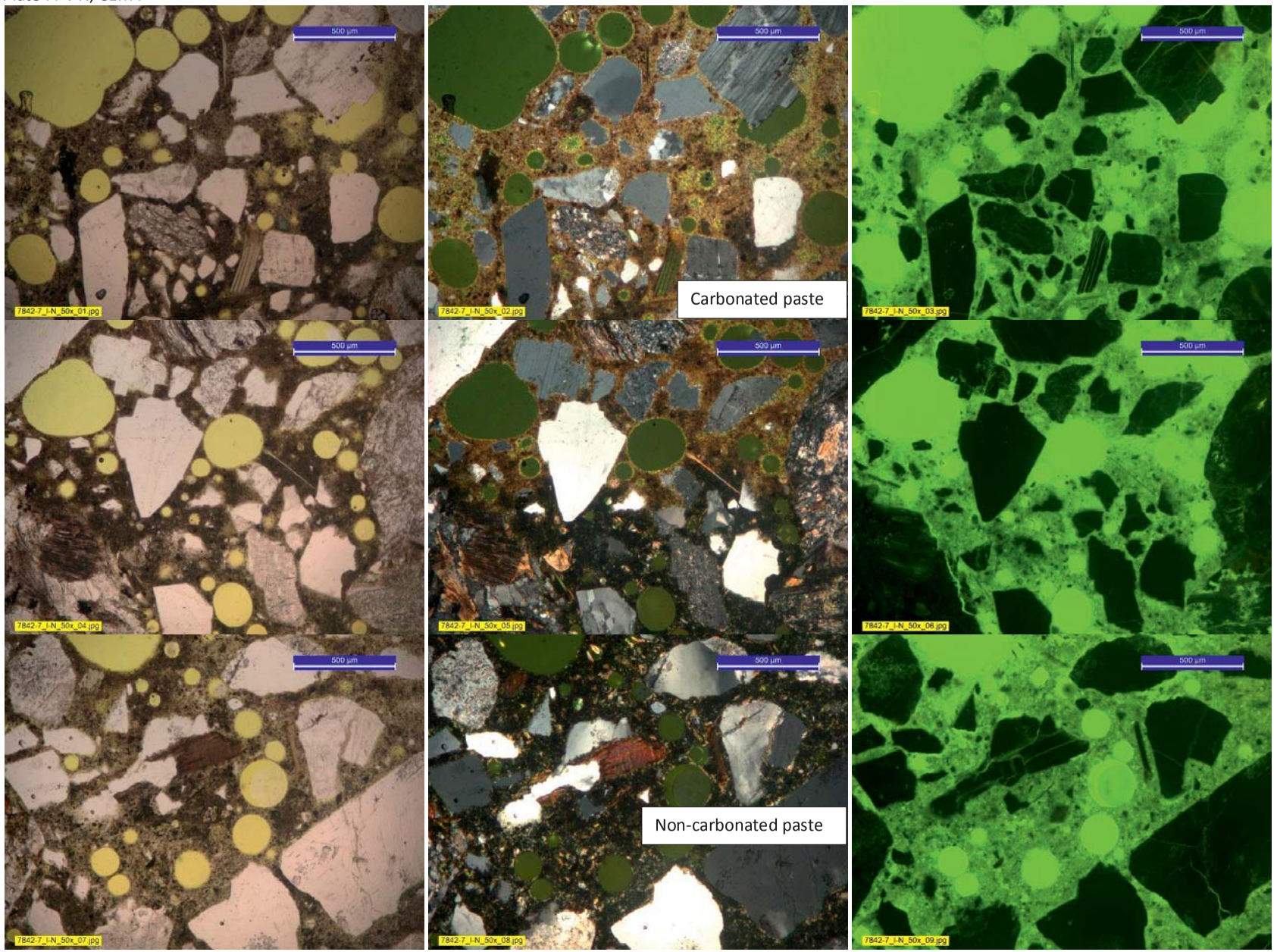

Plate 8: II-N, CEM II/B-M

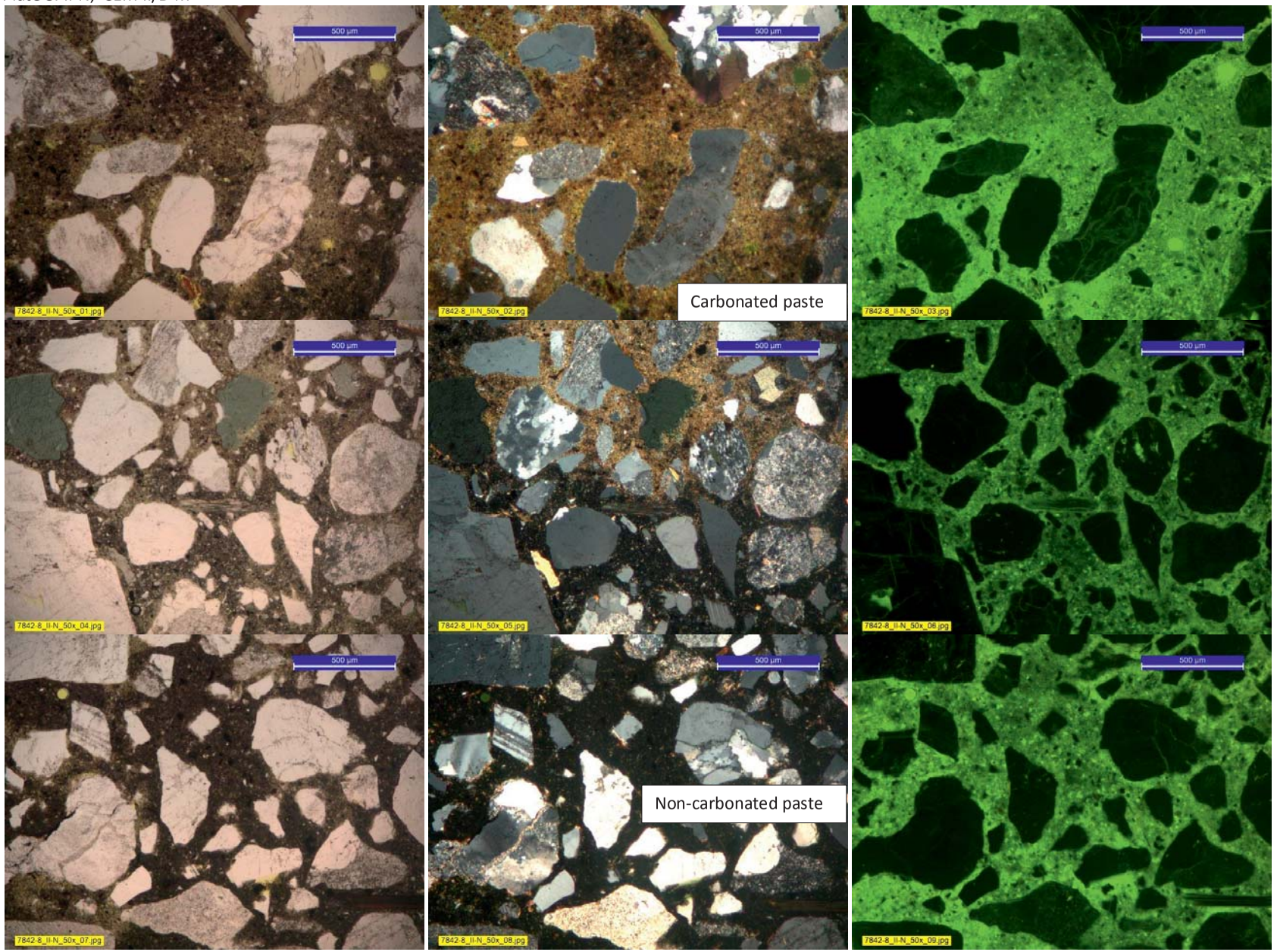

Plate 9: III-N, CEM II/B-V

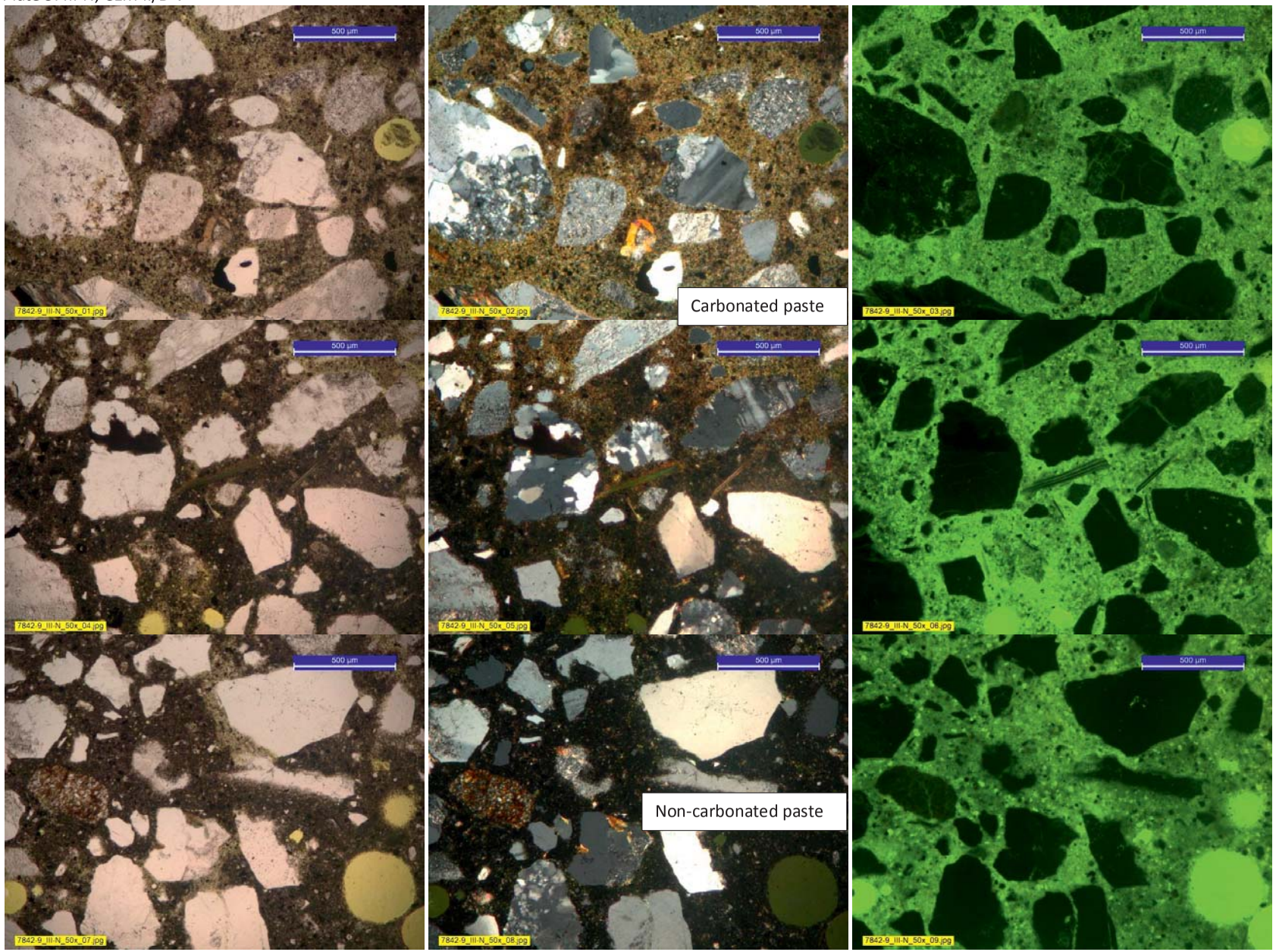

Appendix II

Impact of carbonation on the electrical resistivity of concrete

Appendix in: Reinforcement corrosion in carbonated fly ash concrete

Andres Belda Revert

Thesis for the degree of Philosophiae Doctor

Trondheim, May 2018

Norwegian University of Science and Technology

Faculty of Engineering, Science and Technology

Department of Structural Engineering

NTNU
Norwegian University of
Science and Technology

Contents

1. Introduction

Concrete samples were prepared to investigate the influence of carbonation on the electrical resistivity of concrete. Some of the samples where used in complementary investigations [1-4].

2. Experimental

100-mm concrete cubes were wet-saw cut in slices and the two central slices (25 mm in thickness) of each cube were kept and exposed to carbonation or a reference environment, see Table 1 and Figure 1.

Table 1: Experimental matrix (label of slices and exposure)

Cement	FA [%]	90% RH, 0% CO_2, 20°	90% RH, 5% CO_2, 20°
CEM I	0	0%-2, 0%-4	0%-1, 0%-3
CEM II/B-M	18	18%-2, 18%-4	18%-1, 18%-3
CEM II/B-V	30	30%-2, 30%-4	30%-1, 30%-3

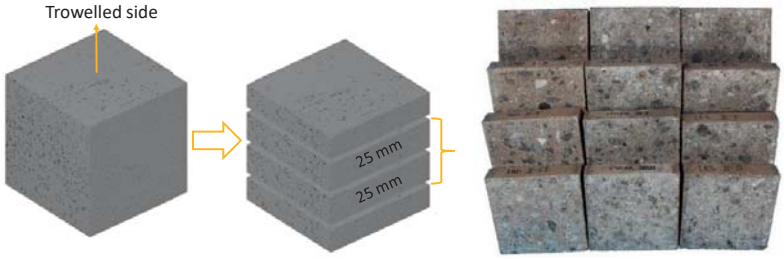

Figure 1: 100-mm concrete cubes and sampling

2.1. Concretes

Table 2 gives the chemical composition by XRF of the three investigated cements. Concretes were prepared aiming at w/b ratio 0.55. Table 3 presents the concrete composition.

Table 2: Chemical composition of the investigated binders determined by XRF facilitated by NORCEM AS [% by mass]

Cement	Label	SiO_2	Al_2O_3	Fe_2O_3	CaO	MgO	SO_3	P_2O_5	K_2O	Na_2O
CEM I	0%	19.6	4.9	3.1	60.8	2.3	3.7	0.1	0.9	0.5
CEM II/B-M	18%	25.5	7.6	4.2	50.7	2.1	3.3	0.2	1.1	0.6
CEM II/B-V	30%	28.4	8.8	4.4	46.9	2.2	2.7	0.2	1.2	0.6

Table 3: Concrete compositions [kg/m^3]. Weight of the aggregates given in saturated-surface dry condition

Constituent	CEM I	CEM II/B-M	CEM II/B-V
Cement	371.4	369.8	369.5
Sand 0/8 mm	1173.2	1166.9	1160.3
Gravel 5/16 mm	624.2	628.5	629.6
Free Water	206.9	202.9	200.9
Superplasticiser (Dyn. XTend)	3.78	3.69	3.68
Stabilisor (Viscostar 6K)	0.55	0.55	0.55
w/c	0.56	0.55	0.54

2.2. Preparation

The concretes were cast and prepared at a Norwegian precast factory in batches of 1 m^3. The concrete was poured in the moulds and gentled compaction was applied on the sides until no air bubbles appeared on the surface. The cubes were kept in the moulds for two weeks and subsequently kept in a laboratory environment (60± 10% RH, 20± 4°C) for 6 months.

The cubes were cut in four slices using wet-saw cutting. The cutting direction was parallel to the casting side. The two inner slices of each cube were kept. The actual dimensions of each slice were measured using a Vernier calliper. Three measuring points were determined on the cross section of the slices and the area was 10x10 cm^2 for all the slices (dimensions of the moulds). Once the cubes were cut, they slides were wrapped in wet clothes for a week before the first resistivity measurement.

The samples exposed to the reference environment were kept in a desiccator containing saturated barium chloride solution and soda lime sticks to remove any trace of CO_2 (Figure 2) at 20ºC.

The samples exposed to carbonation were kept in a climate cabinet at 20ºC, 90% RH, 5% CO_2. A climate cabinet with forced ventilation was set to ensure steady conditions (Figure 2).

Table 4 describes the conditions to which the samples have been exposed including the dates.

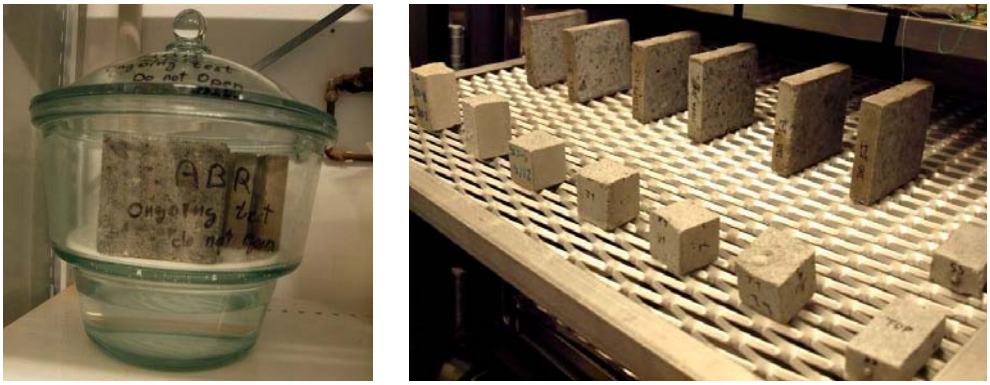

Figure 2: Reference samples (left) and samples exposed to carbonation (right)

Table 4: Dates and conditions for casting, curing and exposure

	Date	T [ºC]	RH [%]	CO_2 [%]
Casting	28-04-2016	20	-	0.04
Curing	28-04-2016 12-05-2016	20	Sealed	
Conditioning	12-05-2016 21-11-2016	20	60	0.04
Exposure	21-11-2016 Ongoing by the submission of the PhD Thesis	20	90	5/0
Last measurement	16-03-2018	20	90	5/0

2.3. Measurement of electrical resistivity of concrete

The resistivity was calculated from the resistance determined using the two-plate method. An LCR meter was used adjusting the frequency to obtain the lowest phase angle (square pulse circa 0.9 V). Two pieces of wet cloth were used during the measurement to provide electric contact. The cell constant was individually determined for each sample. Based on the geometry of the samples the following equation applies to obtain resistivity from resistance:

$$\rho = \frac{A}{w} \cdot R = k \cdot R$$

Where

- ρ: electrical resistivity of concrete [Ω·m]
- A: cross section of the slice [m^2]
- w: thickness of the slice [m]
- R: electrical resistance of concrete [Ω]

3. Results

The electrical resistivity of the concrete was determined on the samples before starting the exposure. The electrical resistivity was similar for each cement before the exposure to carbonation started. The electrical resistivity and the mass change were determined over time, see Figure 3.

Based on samples containing the same cements and exposed to the same environment (further description is given in Appendix III), the slices were fully carbonated after 50 weeks of exposure. The electrical resistivity of the carbonated samples seemed comparable within the two last measurements. However, Figure 3 right shows that the change in mass of the carbonated samples did not reach a plateau, suggesting non-equilibrium conditions. The samples exposed to the reference environment seemed to have reached moisture equilibrium.

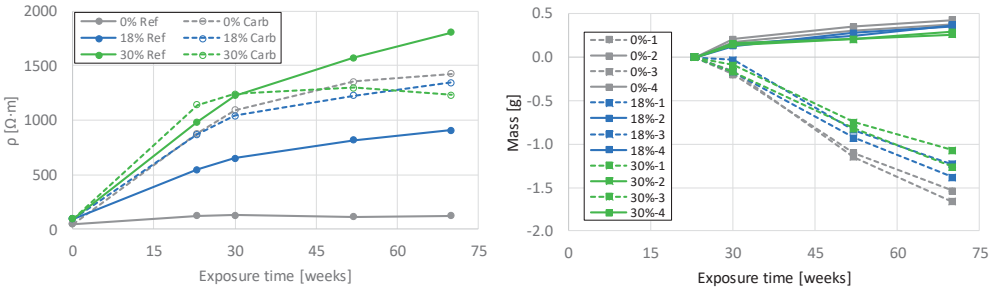

Figure 3: Left: electrical resistivity of concrete over time exposed to reference environment (continuous line) or carbonation (dashed line), each series is the average value of two measurements. Right: mass change (related to mass after 23 weeks of exposure) of the concrete slices over time exposed to reference environment (continuous line) or carbonation (dashed line), each point represents a sample (slide)

4. Further research

The results were non-conclusive as the samples appear not have reached equilibrium conditions within the test period. It is suggested to keep the samples exposed to carbonation and reference environment and repeat the measurement e.g. each 25 weeks until equilibrium conditions are reached (week 37 in 2018 next measurement).

5. References

[1] A. Belda Revert, K. De Weerdt, M.R. Geiker, U.H. Jakobsen, SEM-EDS analysis of products formed under natural and accelerated carbonation of concrete with CEM I, CEM II/B-M and CEM II/B-V in: XXIIIth Symposium on Nordic Concrete Research & Developement, Aalborg, Denmark, 2017.
[2] A. Belda Revert, K. Hornbostel, K. De weerdt, M.R. Geiker, Determination of the polarization resistance of steel in carbonated fly-ash concrete- effect of measurement technique, in: EUROCORR- 20th International corrosion congress-Corrosion of Steel in Concrete, Prague, 2017.
[3] M. Messina, A. Belda Revert, K. Hornbostel, M.R. Geiker, M. Gastaldi, Corrosion current density as a function of electrical resistivity of carbonated concrete, (In preparation).
[4] A. Belda Revert, K. Hornbostel, K. De Weerdt, M.R. Geiker, Macrocell corrosion in carbonated Portland and Portland-fly ash concrete - contribution and mechanism, Submitted to Cement and Concrete Research, (2018).

6. Raw data

The raw data from the measurements is included in the following tables (geometry including cell constants and the measurements). The orange cells refer to the samples which were exposed to carbonation. The mass, frequency, real part of the impedance (Zre), imaginary part of the impedance (Zim), phase angle and determined electrical resistivity are included in the tables.

	0%-1	0%-2	0%-3	0%-4	18%-1	18%-2	18%-3	18%-4	30%-1	30%-2	30%-3	30%-4
Thickness [mm]	22.21	22.44	22.52	22.6	22.54	22.56	22.31	22.46	22.36	22.23	22.71	22.42
	22.18	22.36	22.68	22.53	22.47	22.39	22.31	22.54	22.57	22.34	22.54	22.42
	22.01	22.57	22.63	22.72	22.57	22.42	22.41	22.35	22.51	22.31	22.53	22.33
Area [m²]	0.01	0.01	0.01	0.01	0.01	0.01	0.01	0.01	0.01	0.01	0.01	0.01
k [m]	0.45	0.45	0.44	0.44	0.44	0.45	0.45	0.45	0.44	0.45	0.44	0.45

INITIAL MEASUREMENT

	0%-1	0%-2	0%-3	0%-4	18%-1	18%-2	18%-3	18%-4	30%-1	30%-2	30%-3	30%-4
Frequency [Hz]	40000	40000	40000	40000	15000	15000	15000	15000	10000	10000	10000	10000
Zre [Ω]	116.5	122.5	106.3	112.3	230.4	223.3	188.6	210.0	206.5	212.1	225.1	226.3
Zimg [Ω]	-1.1	-1.2	-0.9	-1.1	-3.9	-4.0	-3.1	-3.8	-4.1	-4.4	-4.7	-4.8
Phase	-0.54	-0.57	-0.48	-0.55	-0.98	-1.01	-0.93	-1.03	-1.14	-1.18	-1.19	-1.21
ρ [Ω·m]	53	55	47	50	102	99	84	94	92	95	100	101

23 weeks exposure

	0%-1	0%-2	0%-3	0%-4	18%-1	18%-2	18%-3	18%-4	30%-1	30%-2	30%-3	30%-4
Frequency [Hz]	100	100	100	100	100	100	100	100	100	100	100	100
m [g]	484.7	484.9	492.9	489.4	516.7	516.2	511.4	516.2	529.8	521.6	528.6	523.2
Zre [Ω]	1980.0	272.4	1960.0	297.9	1960.0	1200.0	1950.0	1260.0	2540.0	2190.0	2600.0	2200.0
Phase	-2.40	-0.80	-2.40	-0.70	-2.00	-0.70	-2.00	-0.70	-1.50	-0.90	-1.50	-0.90
ρ [Ω·m]	895	121	867	132	870	534	873	561	1130	982	1151	983

30 weeks exposure

	0%-1	0%-2	0%-3	0%-4	18%-1	18%-2	18%-3	18%-4	30%-1	30%-2	30%-3	30%-4
Frequency [Hz]	100	100	100	100	100	100	100	100	100	100	100	100
m [g]	484.9	484.7	493.1	489.2	516.7	516.1	511.6	516.1	529.9	521.5	528.8	523.0
Zre [Ω]	2480.0	267.0	2402.0	306.0	2380.0	1448.0	2290.0	1480.0	2830.0	2812.0	2770.0	2659.0
Phase	-2.30	-0.70	-2.30	-0.70	-2.00	-0.70	-2.00	-0.70	-1.50	-1.00	-1.50	-1.00
ρ [Ω·m]	1120	119	1062	135	1057	645	1025	659	1259	1261	1226	1188

Appendix II

52 weeks exposure

	0%-1	0%-2	0%-3	0%-4	18%-1	18%-2	18%-3	18%-4	30%-1	30%-2	30%-3	30%-4
Frequency [Hz]	100	100	100	100	100	100	100	100	100	100	100	100
m [g]	485.8	484.6	494.1	489.0	517.5	515.9	512.4	516.0	530.6	521.4	529.4	523.0
Zre [Ω]	3060.0	248.0	3010.0	263.0	2750.0	1800.0	2760.0	1870.0	2875.0	3580.0	2970.0	3450.0
Phase	-2.30	-0.60	-0.60	-0.60	-2.30	-0.80	-2.30	-0.80	-1.50	-1.10	-1.60	-1.10
ρ [Ω·m]	1383	110	1331	116	1221	802	1235	833	1279	1606	1315	1541

70 weeks exposure

	0%-1	0%-2	0%-3	0%-4	18%-1	18%-2	18%-3	18%-4	30%-1	30%-2	30%-3	30%-4
Frequency [Hz]	100	100	100	100	100	100	100	100	100	100	100	100
m [g]	486.22	484.49	494.56	488.95	517.91	515.85	512.81	515.87	530.87	521.37	529.88	522.91
Zre [Ω]	3300.0	270.0	3080.0	300.0	3000.0	2000.0	3040.0	2070.0	2800.0	4150.0	2750.0	3910.0
Phase	-2.30	-1.30	-2.40	-1.30	-2.40	-0.80	-2.40	-0.90	-1.50	-1.20	-1.60	-1.10
ρ [Ω·m]	1491	120	1362	133	1332	891	1361	922	1246	1862	1217	1746

Appendix III

Microcell and macrocell corrosion in carbonated reinforced Portland-fly ash concrete exposed to 20°C, 90% RH, 5% CO_2, preliminary data and discussion

Appendix in: Reinforcement corrosion in carbonated fly ash concrete

Andres Belda Revert

Thesis for the degree of Philosophiae Doctor

Trondheim, May 2018

Norwegian University of Science and Technology

Faculty of Engineering, Science and Technology

Department of Structural Engineering

NTNU
Norwegian University of Science and Technology

Contents

1. Introduction

Plain and reinforced (with or without additional embedded instrumentation) concrete samples were prepared to investigate microcell and macrocell corrosion in carbonated Portland-fly ash concrete. The set of samples was not fully conditioned during the PhD study. Some of the samples where used in complementary investigations [1-4]. Microstructural analysis of these concretes is presented in Appendix I.

The aim of this study was to investigate macrocell corrosion in carbonated concrete and to which extent it is relevant compared to microcell corrosion.

2. Experimental

Table 1 presents the experimental matrix, Table 2 the performed measurements, and Figure 1 an overview of the samples.

The plain samples were prepared to monitor the carbonation development.

The reinforced samples contained two carbon steel reinforcement bars, placed in the middle of the sample either close to the bottom or top side, 20 mm concrete cover.

The reinforced samples including instrumentation (referred as "instrumented" in the following) contain six carbon steel (CS) reinforcement bars (WE): three on the top and three on the bottom, 20 mm concrete cover, two stainless steel (SS) bars (CE) which are positioned in the middle of the prism, one reference electrode ERE 20 (RE), and one pseudo-reference electrode made from a piece of titanium mesh.

Table 1: Original experimental matrix. In rounded brackets samples left for future investigations

Cement	Sample Label (laboratory)	DataLabel (report)	Plain 150x120x260	Reinforced 150x120x260	Instrumented 320x120x3000
CEM I	IND	0%	3 (1)	3 (2)	1 (1)
CEM II/B-M	STDFA	18%	3 (1)	3 (2)	1 (1)
CEM II/B-V	LKS	30%	3 (1)	3 (1)	1 (1)

Table 2: Summary of the performed measurements

Measurement	Sample	Reinforcement
Carbonation depth (pH indicator)	Plain	-
Open circuit potential	Reinforced	1, 2
Open circuit potential	Instrumented	1, 2, 3, 4, 5, 6
Microcell corrosion	Instrumented	1, 2, 3, 4, 5, 6
ρ concrete cover	Instrumented	1-2, 2-3, 4-5, 5-6
ρ concrete bulk	Instrumented	SS1-SS2
Electrical resistance between CS and SS	Instrumented	1-SS1, 3-SS2, 4-SS1, 6-SS2

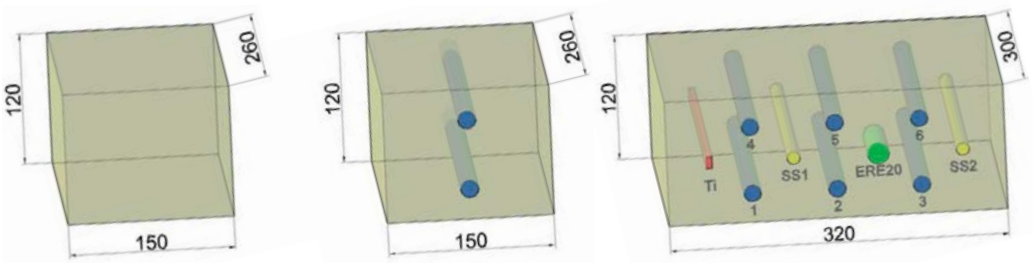

Figure 1: Plain, reinforced and instrumented concrete samples [mm]. Blue: carbon steel, yellow: stainless steel, green: reference electrode (ERE 20), and red: pseudo reference electrode (titanium mesh)

2.1. Materials

2.1.1. Cements

The XRF analysis of the cements is given in Table 3.

Table 3: Chemical composition of the investigated binders determined by XRF facilitated by NORCEM AS [% by mass]

Binder	SiO_2	Al_2O_3	Fe_2O_3	CaO	MgO	SO_3	P_2O_5	K_2O	Na_2O
CEM I	19.6	4.9	3.1	60.8	2.3	3.7	0.1	0.9	0.5
CEM II/B-M	25.5	7.6	4.2	50.7	2.1	3.3	0.2	1.1	0.6
CEM II/B-V	28.4	8.8	4.4	46.9	2.2	2.7	0.2	1.2	0.6

2.1.2. Embedded elements

Carbon steel diameter 16 mm B500NC was used as reinforcement, Table 4 presents the limitations on the chemical composition according to NS 3576 NS-3576-3 [5]. The steel was received in straight lengths of 6 meters, cut in 29.5-mm in length pieces using a mechanical saw, both ends were polished to round the sharp edges, and an electric connection was set in one of each of the ends. Then, the bars were weighted and finally a 50-mm length of each of the ends was coated with bee wax by dipping each end of the bar twice in melted beeswax. The steel was cleaned with acetone to remove dirt and grease, and then embedded in the concrete.

Table 4: Limitations on the chemical composition of steel B500NC [%] according to NS 3576 [5]

Element	C	Si	Mn	P	S	N	Cu
Upper limit	0.24	0.65	1.7	0.055	0.055	0.014	0.85

Stainless steel reinforcement bars were embedded to be used as cathodes in the macrocell corrosion measurements. Stainless steel diameter 12 mm (AISI 2250, X2CrNiMoN22-5-3 (number 1.4462) according to NS-EN-10088 [6]) was used, see Table 5.

Table 5: Limitations on the chemical composition of steel number 1.4462 [%] according to NS-EN-10088 [6]

Element	C	Si	Mn	P	S	Cr	Mo	Ni	N
Upper limit	0.03	1	2	0.035	0.015	21-23	2.5-3.5	4.5-6.5	0.1-0.22

ERE 20 (supplied by FORCE Technology) is an embeddable reference electrode based on the equilibrium of manganese dioxide (MnO_2) in an alkaline electrolyte (NaOH). The chemicals are placed in a stainless steel case which is covered with a plastic isolator. A shift in potential of 30 mV/unit-of-pH is expected if carbonation reaches the sensor. The potential of the ERE 20 reference electrode was measured against an external saturated calomel electrode to check the stability.

A 20-mm width strip titanium mesh (diamond opening 3.5 x 6 mm, thickness 2 mm) was used as pseudo-reference electrode. Table 6 presents the chemical composition.

Table 6: Chemical composition of the titanium mesh (given by Wuxi Advanced Titanium Technology Co.) [% in mass]

Element	N	C	H	Fe	O	Ti
Upper limit	0.02	0.01	0.009	0.11	0.06	Balance

2.2. Concretes

Concretes w/b 0.55 containing Portland cement and Portland-fly ash cements according to EN-197-1 [7] were prepared, see Table 7. The concretes were prepared at a Norwegian precast factory in batches of 1 m^3. The concrete was poured in the moulds and gentled compaction was applied on the sides until no air bubbles appeared on the surface. The samples were kept in the moulds covered with a plastic wrap for 72 hours after casting, then demoulded and wrapped in plastic at 20°C for 11 days in a sealed container. The curing time was 14 days before starting the exposure.

Table 7: Concrete compositions [kg/m^3]. Weight of the aggregates given in saturated-surface dry condition

Constituent	CEM I	CEM II/B-M	CEM II/B-V
Cement	371.4	369.8	369.5
Sand 0/8 mm	1173.2	1166.9	1160.3
Gravel 5/16 mm	624.2	628.5	629.6
Free Water	206.9	202.9	200.9
Superplasticiser (Dyn. XTend)	3.78	3.69	3.68
Stabilisor (Viscostar 6K)	0.55	0.55	0.55
w/c	0.56	0.55	0.54

2.3. Exposure

Samples were exposed to accelerated carbonation (20°C, 90% RH and 5% CO_2) after the sealed curing. Climate cabinets with forced ventilation were set up to ensure homogeneous exposure conditions on the samples.

Table 8 describes the conditions to which the samples have been exposed.

Table 8: Dates and conditions for casting, curing and exposure

	Date	T [°C]	RH [%]	CO_2 [%]
Casting	28-04-2016	20	-	0.04
Curing	28-04-2016 12-05-2016	20	Sealed	-
Exposure	12-05-2016 Ongoing by the submission of the PhD Thesis	20	90	5
Last measurement	26-03-2018	20	90	5

2.4. Methods

2.4.1. Carbonation

Carbonation was detected on the plain samples. Samples 50 mm in thickness were obtain using a mechanical splitter. The freshly split surface was sprayed with thymolphthalein solution. The solution was prepared by dissolving 1 gram of thymolphthalein in powder (grade "ACS, Reag. Ph Eur" (VWR)) in a mix of 30 ml of deionized water and 70 ml of ethanol. The pH threshold of thymolphthalein is in the range of 9.5 to 10.5, below it becomes colourless and above it presents an intense blueish colour. The carbonation depth distribution was characterized using image analysis as described in [8].

2.4.2. Open circuit potential

The open circuit potential of the reinforcement was monitored using the embedded ERE 20 reference electrode during the exposure time. The OCP was additionally determined using an external SCE applied on the concrete surface in the middle length of each reinforcement bar. A custom-made acquisition system with an internal impedance of 10 MΩ was used.

2.4.3. Linear polarization resistance

The polarization resistance of the reinforcement was determined using LPR technique without compensating for the ohmic drop. The reinforcement was polarized ±10 mV from the OCP potential at a rate of 0.167 mV/min. The ohmic drop between the RE and WE was determined using AC Electrochemical impedance spectroscopy (EIS). EIS was performed applying an alternative sinusoidal voltage of 10 mV in the range of 500 kHz to 1 Hz. The ohmic drop was associated with the lowest phase angle of the Bodo plot. The microcell current density was determined from the polarization resistance using Stern-Geary equation [9] and assuming the B values given by [10].

2.4.4. Electrical resistivity of concrete

The electrical resistivity of concrete was determined using EIS in a two-cell probe arrangement. The resistivity of the concrete cover was determined using pairs of neighbouring carbon steel reinforcement bars. EIS was performed applying an alternative sinusoidal voltage of 10 mV in the range of 500 kHz to 1 Hz and the resistance associated with the lowest phase angle of the Bodo plot was determined. The cell factor of the setup was empirically determined in a sample with same geometry containing same instrumentation using an electrolyte of known resistivity.

2.4.5. Galvanic currents

The galvanic current can be measured coupling the reinforcement embedded in carbonated concrete with the stainless steel reinforcement using a zero-resistance ammeter.

3. Preliminary results

3.1. Carbonation detection

Table 9 presents the carbonation depth distribution determined over time. Note that the carbonation distributions were determined in the plain samples. The carbonation development may differ in plain and reinforced samples due to microstructural defects [8].

Table 9: Carbonation depth distribution determined on plain samples over exposure time

Exposure time [Weeks]	Carbonation depth [mm]								
	0% FA			18% FA			30% FA		
	Mean	SD	COV	Mean	SD	COV	Mean	SD	COV
8	7.8	1.9	24.3	8.3	2.3	27.7	11.1	3.2	29.2
31	10.4	2.8	27.2	10.9	2.2	20.5	14.4	3.1	21.8
45	10.1	3.3	32.4	14.3	3.1	21.8	20.1	5.6	28.0
72	12.6	3.0	23.9	17.0	4.2	24.5	20.7	4.3	20.9
100	12.6	4.0	32.1	19.0	3.3	17.3	24.7	5.9	23.7

3.2. Microcell corrosion (instrumented samples)

The open circuit potential and microcell current density determined after 100 weeks of exposure in the instrumented samples are presented in Figure 2. Each bar includes the measurement of one reinforced-instrumented sample (6 measurements per sample).

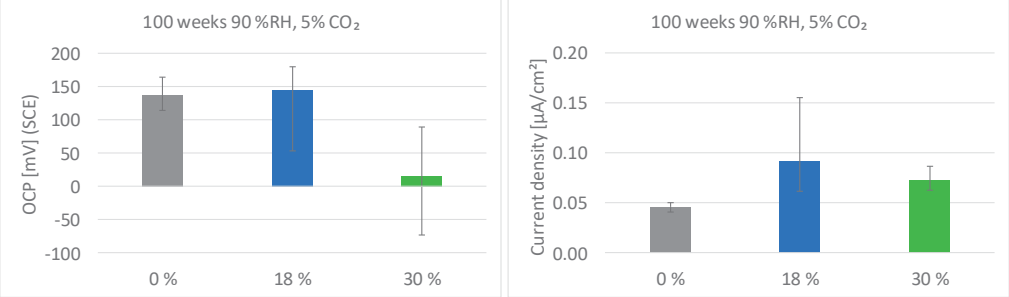

Figure 2: Open circuit potential and microcell current density. Solid bar (average) and error bar (range)

3.3. Electrical resistivity of concrete

Figure 3 presents the electrical resistivity of the concrete cover determined in the instrumented samples using the reinforcement bars as electrodes (4 measurements per sample).

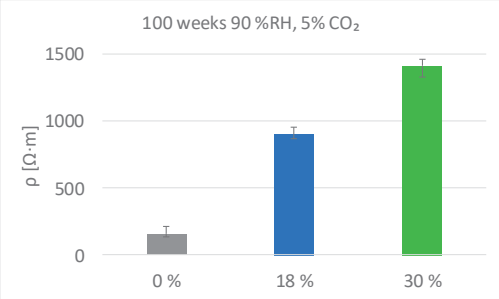

Figure 3: Electrical resistivity of the concrete cover (solid bars) determined between each two neighboring carbon steel reinforcement bars after 100 weeks exposed to 90% RH and 5% CO_2. Error bars indicate the range

3.4. Electrical resistance between reinforcement bars and stainless steel bar

Figure 4 presents the electrical resistance between each carbon steel reinforcement bar and the nearest stainless steel bar (instrumented samples). Six measurements were performed per sample.

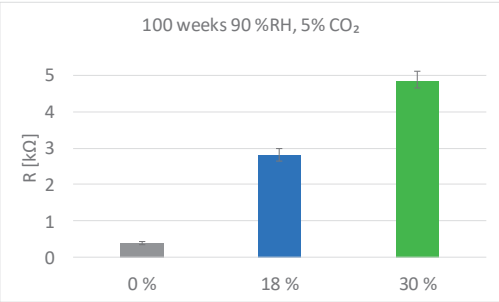

Figure 4: Electrical resistance between each carbon steel reinforcement bar and the nearest stainless steel bar after 100 weeks exposed to 90% RH and 5% CO_2

4. Preliminary discussion

4.1. Carbonated fraction of the concrete-steel interface

Figure 5 left presents the carbonation distributions determined after 100 weeks of exposure including the position of the reinforcement (20 mm cover, 16 mm in diameter). Figure 5 right illustrates the carbonation depth distributions determined in plain samples overtime including the position of the reinforcement (20 mm cover, 16 mm in diameter).

The samples used for further discussion are the 18% and 30% FA due to the potential limited fraction of reinforcement embedded in carbonated concrete in the 0% samples. According to Figure 5, most of the reinforcement is embedded in carbonated concrete after 100 weeks of exposure for the 30% FA samples and part of it for the 18% FA samples. These carbonation measurements were performed in plain samples, while faster carbonation development was observed in reinforced samples due to microstructural defects [8]. Thus, a higher fraction of the reinforcement than shown in Figure 5 could be embedded in fully carbonated concrete.

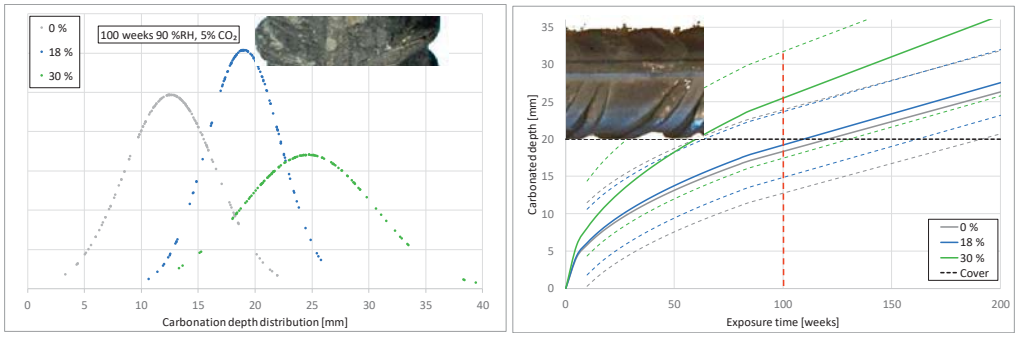

Figure 5: Left: carbonation depth distribution determined after 100 weeks of exposure in the plain samples. Right: carbonation depth distributions determined on the plain samples over time (8, 31, 45, 72 and 100 weeks) and development assuming square root law (solid line average, dashed lines 5% and 95% of the carbonation distribution). Concrete exposed to 90% RH and 5% CO_2. The reinforcement indicates the position and size (concrete cover 20 mm and diameter 16 mm).

4.2. Microcell corrosion in carbonated concrete: OCP, i_{corr} and ρ

The determined OCPs after 100 weeks of exposure compares to passivity in aerated concrete or negligible corrosion in dry carbonated and chloride-free concrete according to [11]. The current densities determined on this condition are assessed as low to negligible according to [12].The electrical resistivity determined in these samples compares to the one determined in carbonated concrete slices which contain the same materials and were exposed to the same condition (Appendix II).

Figure 6 presents a comparison of the data retrieved in [3] and the data retrieved from the 18% and 30 % FA samples in the current investigation (blue and green arrows). Note that the data retrieved in [3] was determined in samples exposed to drying, so equilibrium conditions were not reached. The data determined at 90% RH is comparable but on the low side of the corrosion rate-concrete electrical resistivity trend found in [3]. When comparing the OCP-corrosion rate relationship comparable OCP was measured in both cases.

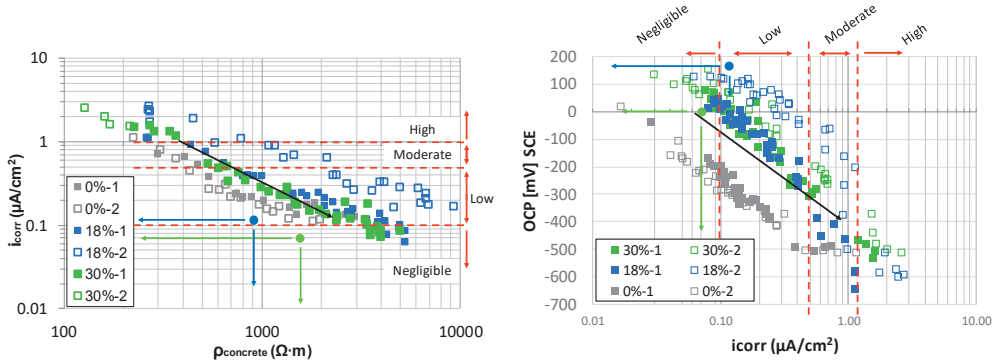

Figure 6: Left: relationship between microcell current density and concrete electrical resistivity of carbonated concrete. Right: relationship between open circuit potential and microcell current density. From capillary saturated condition upon drying in the laboratory [Paper S-VIII],[3]. Blue and green arrows indicate the parameters determined in the 18 and 30% FA samples exposed to 90% RH and 5% CO_2 for 100 weeks

The corrosion rate in the 30% FA exposed to 90% RH was low to negligible. Higher corrosion rates were expected for this external humidity [13]. However, carbonated concrete presents lower moisture compared to non-carbonated concrete exposed to the same external conditions [14, 15]. The limited amount of electrolyte seems to limit the corrosion propagation in carbonated concrete. Only when carbonated concrete is in direct contact with water, high corrosion rates were measured as presented in Figure 6 left (left side) and Figure 6 right (right side).

4.3. Macrocell corrosion in carbonated concrete

The electrical resistance between the reinforcement bars (CC) and the stainless steel bars (SS) is highly influenced by the amount of fly ash. If a macrocouple is stablished between the CC (embedded in carbonated concrete) and the SS, the high electrical resistance of the fly ash samples is expected to limit the galvanic current compared to the Portland cement samples. The model presented in [4] is applied to investigate the potential influence of the electrical resistance between the reinforcement embedded in carbonated concrete and the reinforcement embedded in the non-carbonated concrete on macrocell corrosion. From Figure 4, a factor of 10 is observed when comparing the electrical resistance determined in the 0% to the 30% samples. For the tested conditions, the hypothetical galvanic current flowing between the CS and SS when connected is calculated using the model presented in [4]. The galvanic current is lowered from 5 µA to 4 µA when the electrical resistance is increased from 400 Ω (0% FA samples) to 5000 Ω (30% FA samples). The addition of fly ash could present an advantage compared to PC and reduces the galvanic current for these conditions. The electrochemical parameters derived in [4] are used and the following hypothesis are taken (see Figure 7):

- Area of CS 100 cm^2, and area of SS 75 cm^2
- The anodic polarization of the SS is a vertical line
- The cathodic polarization of the CS has a slope of 300 mV/Dec
- Corroding CS in carbonated concrete:
  - OCP -60 mV vs SCE, i_{corr} 0.08 µA/cm^2
- The anodic polarization of the CC has a slope of 300 mV/Dec
- The cathodic polarization of the CS has a slope of 300 mV/Dec
- The electrical resistance between the CS and the CC is either 400 Ω (0% FA) or 5000 Ω (30% FA)

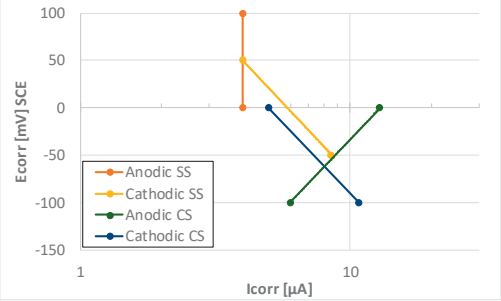

Figure 7: Application of macrocell corrosion model presented in [4] based on Evans diagram of CS (active) and SS

5. Further research

When the carbon steel bars are fully embedded in carbonated concrete the microcell corrosion should be determined. Macrocell corrosion when coupled with the stainless steel bars should be determined also. Based on Figure 5 this assessment can be performed after 150 weeks (March 2019).

The microcell current density determined was assessed as low, either because of the low carbonated fraction of the concrete-reinforcement interface or due to the limited moisture content in carbonated concrete exposed to 90% RH (too low to sustain active corrosion).

The numerical calculation shown that the fly ash could reduce the galvanic current 20% compared to PC thanks to the higher electrical resistance when non-carbonated.

6. References

[1] A. Belda Revert, K. De Weerdt, M.R. Geiker, U.H. Jakobsen, SEM-EDS analysis of products formed under natural and accelerated carbonation of concrete with CEM I, CEM II/B-M and CEM II/B-V in: XXIIIth Symposium on Nordic Concrete Research & Developement, Aalborg, Denmark, 2017.
[2] A. Belda Revert, K. Hornbostel, K. De weerdt, M.R. Geiker, Determination of the polarization resistance of steel in carbonated fly-ash concrete- effect of measurement technique, in: EUROCORR- 20th International corrosion congress-Corrosion of Steel in Concrete, Prague, 2017.
[3] M. Messina, A. Belda Revert, K. Hornbostel, M.R. Geiker, M. Gastaldi, Corrosion current density as a function of electrical resistivity of carbonated concrete, (In preparation).
[4] A. Belda Revert, K. Hornbostel, K. De Weerdt, M.R. Geiker, Macrocell corrosion in carbonated Portland and Portland-fly ash concrete - contribution and mechanism, Submitted to Cement and Concrete Research, (2018).
[5] NS-3576-3, NS-3576-3:2012. Armeringsstål. Mål og egenskaper. Del 3: Kamstål B500NC. (Steel for the reinforcement of concrete. Dimensions and properties. Part 3: Ribbed carbon steel B500NC). (2012).
[6] NS-EN-10088, NS-EN 10088-1: Stainless steels. Part 1: List of stainless stells, in, 2014.
[7] EN-197-1, EN 197-1 Cement - Part 1: Composition, specifications and conformity criteria for common cements, in, 2011.
[8] A. Belda Revert, K. De Weerdt, K. Hornbostel, M.R. Geiker, Carbonation-induced corrosion: Investigation of the corrosion onset, Construction and Building Materials, 162 (2018) 847-856.
[9] M. Stern, A.L. Geary, Theoretical Analysis of the Shape of Polarization Curves, Journal of the Electrochemical Society, 104 (1957) 7.
[10] C. Andrade, V. Castelo, C. Alonso, J. González, The Determination of the Corrosion Rate of Steel Embedded in Concrete by the Polarization Resistance and AC Impedance Methods, ASTM International, (1986) 20.
[11] L. Bertolini, B. Elsener, P. Pedeferri, E. Redaelli, R. Polder, Corrosion of Steel in Concrete, Wiley-VCH Verlag GmbH & Co, Weinheim, Germany, 2013.
[12] C. Andrade, C. Alonso, Corrosion rate monitoring in the laboratory and on-site, Construction and Building Materials, 10 (1996) 315-328.
[13] K. Tuutti, Corrosion of steel in concrete, in, Swedish Cement and Concrete Research Institute, Stockholm, 1982.
[14] S.L. Langedal, Investigation of resistivity, porosity and pore solution composition in carbonated mortar prepared with ordinary Portland cement and Portland-fly ash cement, in: Department of Structural Engineering, Norwegian University of Science and Technology, Trondheim, 2018, pp. 96.
[15] H. Justnes, T. Østnor, J. Skocek, Mechanism of increased carbonation rate, in, SINTEF, Trondheim, 2018.

7. Raw data: reinforced samples, OCP vs SCE

	0% samples (Reinforcement position- Concrete sample number)					
	Top-1	Bottom-1	Top-2	Bottom-2	Top-3	Bottom-3
26.01.2017	143	151	135	160	150	173
03.02.2017	160	168	121	146	117	138
14.02.2017			119	139	115	137
17.02.2017			132	155	130	150
21.02.2017			170	190	128	149
24.02.2017			160	177	128	150
28.02.2017			129	149	128	148
07.03.2017			160	191	130	149
10.03.2017			164	191	136	152
14.03.2017			165	193	130	150
17.03.2017			138	160	143	162
21.03.2017			120	143	108	130
24.03.2017			156	178	120	139
28.03.2017			133	154	120	137
31.03.2017			163	186	124	141
07.04.2017			137	157	135	152
18.04.2017			129	152	89	108
21.04.2017			187	204	140	157
24.04.2017			172	190	127	144
02.05.2017			166	184	124	140
05.05.2017			156	170	122	137
09.05.2017			169	187	121	136
12.05.2017			137	154	120	133
16.05.2017			164	180	127	140
19.05.2017			170	186	124	136
23.05.2017			122	138	123	135
26.05.2017			155	172	119	131
30.05.2017			149	164	124	136
02.06.2017			140	155	115	126
25.07.2017			137	149	125	132
15.09.2017			150	160	130	140
26.10.2017			168	176	157	155
02.11.2017			146	154	145	152
13.11.2017			161	169	156	160

	18% samples (Reinforcement position- Concrete sample number)					
	Top-1	Bottom-1	Top-2	Bottom-2	Top-3	Bottom-3
26.01.2017	140	160	130	182	152	194
03.02.2017	158	184	114.8	169	127	167
14.02.2017			83	134	104	138
17.02.2017			65	121	116	154
21.02.2017			72	120	115	153
24.02.2017			71	121	111	148
28.02.2017			85	132	120	155
07.03.2017			89	137	122	158
10.03.2017			93	138	124	161
14.03.2017			95	142	124	161
17.03.2017			109	154	133	172
21.03.2017			78	126	108	150
24.03.2017			91	138	117	156
28.03.2017			93	138	117	154
31.03.2017			97	142	121	159
07.04.2017			108	155	125	167
18.04.2017			73	120	98	140
21.04.2017			122	162	139	175
24.04.2017			105	153	127	164
02.05.2017			109	155	128	166
05.05.2017			107	154	128	167
09.05.2017			117	165	140	180
12.05.2017			111	160	136	174
16.05.2017			112	156	130	168
19.05.2017			105	152	125	164
23.05.2017			108	154	127	165
26.05.2017			103	149	122	159
30.05.2017			107	154	128	165
02.06.2017			99	149	121	159
25.07.2017			117	160	134	161
15.09.2017			110	162	149	173
26.10.2017			141	185	167	150
02.11.2017			136	180	159	166
13.11.2017			131	179	159	170

	30% samples (Reinforcement position- Concrete sample number)					
	Top-1	Bottom-1	Top-2	Bottom-2	Top-3	Bottom-3
26.01.2017	72	181	121	190	110	172
03.02.2017	74	182	124	187	128	171
14.02.2017			80	144	100	137
17.02.2017			89	158	108	146
21.02.2017			95	160	105	144
24.02.2017			87	157	101	140
28.02.2017			90	163	106	147
07.03.2017			85	166	94	128
10.03.2017			94	164	96	114
14.03.2017			96	167	97	121
17.03.2017			96	174	88	125
21.03.2017			81	154	52	107
24.03.2017			81	159	55	112
28.03.2017			72	159	49	124
31.03.2017			72	159	52	113
07.04.2017			96	166	68	125
18.04.2017			43	160	38	89
21.04.2017			74	179	55	115
24.04.2017			76	166		
02.05.2017			70	168		
05.05.2017			75	170		
09.05.2017			78	186		
12.05.2017			92	178		
16.05.2017			78	165		
19.05.2017			68	163		
23.05.2017			63	165		
26.05.2017			60	160		
30.05.2017			66	168		
02.06.2017			72	164		
25.07.2017			11	87		
15.09.2017			35	102		
26.10.2017			53	100		
02.11.2017			51	122		
13.11.2017			44	98		

8. Raw data: Instrumented samples, OCP vs ERE 20, OCP vs Ti, OCP vs SCE

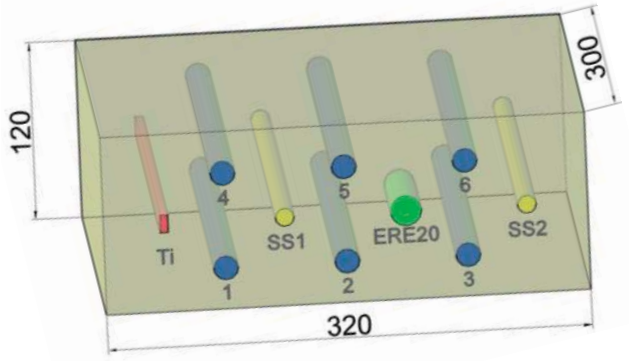

Table 10: OCP Instrumented samples 05/13/2016 (before starting exposure condition)

OCP vs. ERE 20							OCP vs. ERE 20							OCP vs. ERE 20						
Reinf	SAMPLE 0%- INSTRUMENTED						Reinf	SAMPLE 18%- INSTRUMENTED						Reinf	SAMPLE 30%- INSTRUMENTED					
	1	2	3	4	5	6		1	2	3	4	5	6		1	2	3	4	5	6
[mV]	-268	-266	-259	-271	-261	-260	[mV]	-258	-252	-254	-266	-257	-252	[mV]	-266	-266	-269	-263	-266	-265
OCP vs. Ti							OCP vs. Ti							OCP vs. Ti						
Reinf	SAMPLE 0%- INSTRUMENTED						Reinf	SAMPLE 18%- INSTRUMENTED						Reinf	SAMPLE 30%- INSTRUMENTED					
	1	2	3	4	5	6		1	2	3	4	5	6		1	2	3	4	5	6
[mV]	176	182	185	173	183	184	[mV]	196	201	199	187	197	201	[mV]	138	138	136	141	138	138
Corrosion potential Ti vs. ERE 20							Corrosion potential Ti vs. ERE 20							Corrosion potential Ti vs. ERE 20						
[mV]	-445						[mV]	-455						[mV]	-405					
Corrosion potential ERE 20 vs. SCE							Corrosion potential ERE 20 vs. SCE							Corrosion potential ERE 20 vs. SCE						
[mV]							[mV]							[mV]						

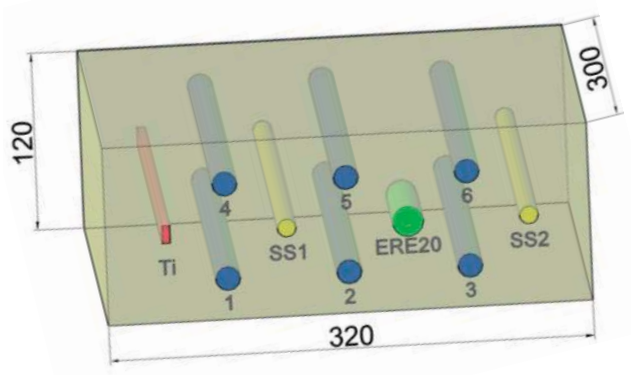

Table 11: OCP Instrumented samples 06/29/2016

OCP vs. ERE 20							OCP vs. ERE 20							OCP vs. ERE 20						
Reinf	SAMPLE 0%- INSTRUMENTED						Reinf	SAMPLE 18%- INSTRUMENTED						Reinf	SAMPLE 30%- INSTRUMENTED					
	1	2	3	4	5	6		1	2	3	4	5	6		1	2	3	4	5	6
[mV]	-232	-220	-226	-238	-227	-220	[mV]	-229	-226	-226	-247	-231	-235	[mV]	-242	-251	-248	-245	-259	-247
OCP vs. Ti							OCP vs. Ti							OCP vs. Ti						
Reinf	SAMPLE 0%- INSTRUMENTED						Reinf	SAMPLE 18%- INSTRUMENTED						Reinf	SAMPLE 30%- INSTRUMENTED					
	1	2	3	4	5	6		1	2	3	4	5	6		1	2	3	4	5	6
[mV]	173	184	178	166	178	184	[mV]	163	166	165	144	161	157	[mV]	111	102	105	108	94	106
Corrosion potential Ti vs. ERE 20							Corrosion potential Ti vs. ERE 20							Corrosion potential Ti vs. ERE 20						
[mV]	-405						[mV]	-392						[mV]	-352					
Corrosion potential ERE 20 vs. SCE							Corrosion potential ERE 20 vs. SCE							Corrosion potential ERE 20 vs. SCE						
[mV]	364						[mV]	362						[mV]	367					

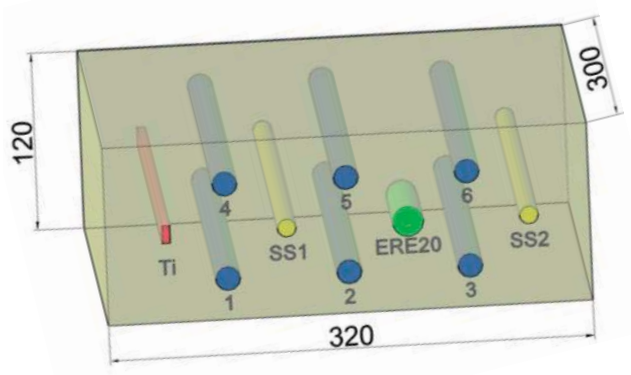

Table 12: OCP Instrumented samples 08/01/2016

OCP vs. ERE 20							OCP vs. ERE 20							OCP vs. ERE 20						
Reinf	SAMPLE 0%- INSTRUMENTED						Reinf	SAMPLE 18%- INSTRUMENTED						Reinf	SAMPLE 30%- INSTRUMENTED					
	1	2	3	4	5	6		1	2	3	4	5	6		1	2	3	4	5	6
[mV]	-226	-211	-222	-224	-223	-219	[mV]	-223	-221	-220	-245	-230	-232	[mV]	-237	-246	-243	-241	-278	-244
OCP vs. Ti							OCP vs. Ti							OCP vs. Ti						
Reinf	SAMPLE 0%- INSTRUMENTED						Reinf	SAMPLE 18%- INSTRUMENTED						Reinf	SAMPLE 30%- INSTRUMENTED					
	1	2	3	4	5	6		1	2	3	4	5	6		1	2	3	4	5	6
[mV]	169	184	173	171	172	176	[mV]	155	156	157	133	148	146	[mV]	106	97	100	102	66	99
Corrosion potential Ti vs. ERE 20							Corrosion potential Ti vs. ERE 20							Corrosion potential Ti vs. ERE 20						
[mV]	-396						[mV]	-378						[mV]	-343					
Corrosion potential ERE 20 vs. SCE							Corrosion potential ERE 20 vs. SCE							Corrosion potential ERE 20 vs. SCE						
[mV]	342						[mV]	370						[mV]	373					

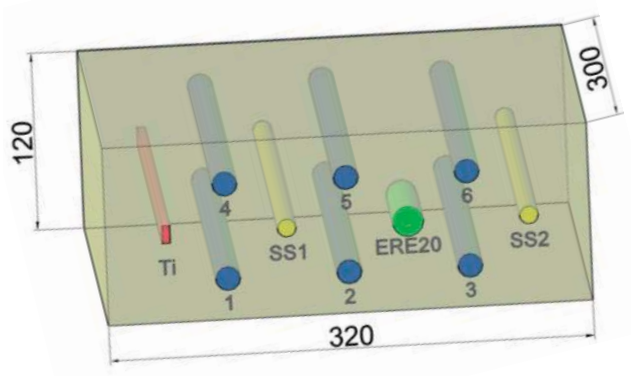

Table 13: OCP Instrumented samples 09/29/2016

OCP vs. ERE 20							OCP vs. ERE 20							OCP vs. ERE 20						
Reinf	SAMPLE 0%- INSTRUMENTED						Reinf	SAMPLE 18%- INSTRUMENTED						Reinf	SAMPLE 30%- INSTRUMENTED					
	1	2	3	4	5	6		1	2	3	4	5	6		1	2	3	4	5	6
[mV]	-224	-207	-228	-228	-220	-220	[mV]	-224	-216	-219	-230	-233	-234	[mV]	-230	-238	-237	-254	-282	-256
OCP vs. Ti							OCP vs. Ti							OCP vs. Ti						
Reinf	SAMPLE 0%- INSTRUMENTED						Reinf	SAMPLE 18%- INSTRUMENTED						Reinf	SAMPLE 30%- INSTRUMENTED					
	1	2	3	4	5	6		1	2	3	4	5	6		1	2	3	4	5	6
[mV]	158	175	154	154	162	161	[mV]	139	146	143	86	129	128	[mV]	100	93	94	77	49	75
Corrosion potential Ti vs. ERE 20							Corrosion potential Ti vs. ERE 20							Corrosion potential Ti vs. ERE 20						
[mV]	-382						[mV]	-362						[mV]	-331					
Corrosion potential ERE 20 vs. SCE							Corrosion potential ERE 20 vs. SCE							Corrosion potential ERE 20 vs. SCE						
[mV]	387						[mV]	390						[mV]	379					

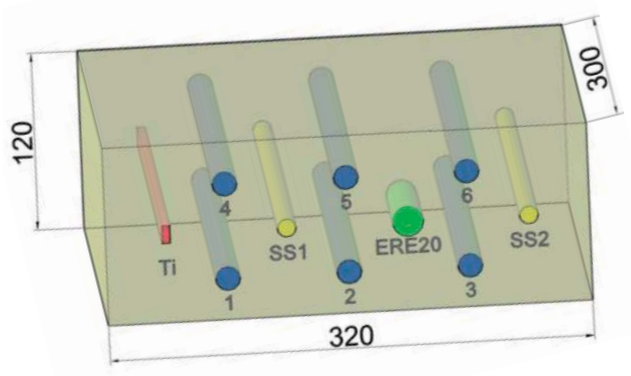

Table 14: OCP Instrumented samples 11/09/2016

OCP vs. ERE 20							OCP vs. ERE 20							OCP vs. ERE 20						
Reinf	SAMPLE 0%- INSTRUMENTED						Reinf	SAMPLE 18%- INSTRUMENTED						Reinf	SAMPLE 30%- INSTRUMENTED					
	7	8	9	10	11	12		13	14	15	16	17	18		1	2	3	4	5	6
[mV]	-224	-211	-228	-225	-220	-220	[mV]	-228	-216	-221	-266	-233	-235	[mV]	-229	-236	-236	-246	-234	-240
OCP vs. Ti							OCP vs. Ti							OCP vs. Ti						
Reinf	SAMPLE 0%- INSTRUMENTED						Reinf	SAMPLE 18%- INSTRUMENTED						Reinf	SAMPLE 30%- INSTRUMENTED					
	1	2	3	4	5	6		1	2	3	4	5	6		1	2	3	4	5	6
[mV]	151	164	148	150	155	155	[mV]	127	138	134	89	122	120	[mV]	99	92	91	81	94	88
Corrosion potential Ti vs. ERE 20							Corrosion potential Ti vs. ERE 20							Corrosion potential Ti vs. ERE 20						
[mV]	-375						[mV]	-355						[mV]	-327					
Corrosion potential ERE 20 vs. SCE							Corrosion potential ERE 20 vs. SCE							Corrosion potential ERE 20 vs. SCE						
[mV]	389						[mV]	412						[mV]	365					

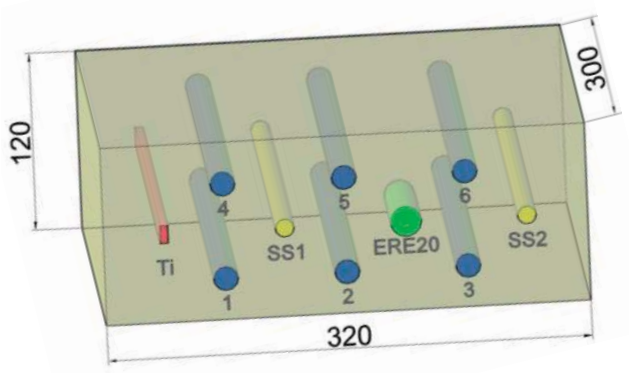

Table 15: OCP Instrumented samples 02/03/2017

OCP vs. ERE 20							OCP vs. ERE 20							OCP vs. ERE 20						
Reinf	SAMPLE 0%- INSTRUMENTED						Reinf	SAMPLE 18%- INSTRUMENTED						Reinf	SAMPLE 30%- INSTRUMENTED					
	7	8	9	10	11	12		13	14	15	16	17	18		1	2	3	4	5	6
[mV]	-223	-216	-226	-219	-219	-219	[mV]	-230	-221	-226	-421	-235	-238	[mV]	-228	-233	-235	-244	-234	-283
OCP vs. SCE							OCP vs. SCE							OCP vs. SCE						
Reinf	SAMPLE 0%- INSTRUMENTED						Reinf	SAMPLE 18%- INSTRUMENTED						Reinf	SAMPLE 30%- INSTRUMENTED					
	1	2	3	4	5	6		1	2	3	4	5	6		1	2	3	4	5	6
[mV]	196	147	139	145	147	149	[mV]							[mV]	142	169	167	158	169	121
Corrosion potential Ti vs. ERE 20							Corrosion potential Ti vs. ERE 20							Corrosion potential Ti vs. ERE 20						
[mV]							[mV]							[mV]						
Corrosion potential ERE 20 vs. SCE							Corrosion potential ERE 20 vs. SCE							Corrosion potential ERE 20 vs. SCE						
[mV]	380						[mV]	410						[mV]	330					

Appendix IV

Supplementary discussion to paper S-VIII:

"Correlation between corrosion current density and electrical resistivity of carbonated concrete"

Appendix in: Reinforcement corrosion in carbonated fly ash concrete

Andres Belda Revert

Thesis for the degree of Philosophiae Doctor

Trondheim, May 2018

Norwegian University of Science and Technology

Faculty of Engineering, Science and Technology

Department of Structural Engineering

NTNU
Norwegian University of
Science and Technology

Appendix IV presents a supplementary discussion to Paper S-VIII: "*Correlation between corrosion current density and electrical resistivity of carbonated concrete*" by Marco Messina, Andres Belda Revert, Karla Hornbostel, Matteo Gastaldi and Mette Rica Geiker.

Appendix IV has been prepared by Andres Belda Revert, Karla Hornbostel, and Mette Rica Geiker

Contents

1. Description

This Appendix includes a supplementary discussion of the data presented in Paper S-VIII. Further description of the samples and methods can be found in [1, 2]. A brief description of the samples and methods is given and a supplementary discussion is presented supporting that the corrosion process in carbonated concrete is under anodic resistance control.

2. Experimental

Concrete reinforced samples 150x120x260 mm were cast with water-to-cement ratio of 0.55 containing two reinforcement bars 260 mm in length (cover 20 mm) were prepared. Both ends of the bars were coated with beeswax to a length of 50 mm. The concrete was poured into the moulds and gentle compaction was applied by tapping on the sides with a rod until no air bubbles appeared on the surface.

The samples were sealed cured for 14 days and then longitudinally cut into two samples differing only in casting position (casting position 1 (bottom) and 2 (top)). The samples were carbonated using a high CO_2 concentration (5% for 10 months and ≈100% until fully carbonated (detected using pH indicator thymolphthalein)). Probes were embedded in one of the longitudinal sides on each sample and a pseudo-reference electrode (a piece of activated titanium 25 mm in length and 1 mm in diameter) was embedded close to the reinforcement.

Once the samples were carbonated they were immersed in water until capillary saturated condition. Then, the samples were exposed to drying in the laboratory while monitoring the corrosion current density (i_{corr}) of the reinforcement using LPR, the open circuit potential (OCP) using an external saturated calomel reference electrode and a voltmeter, and the electrical resistivity of carbonated concrete (ρ) determined using the embedded probes by using a conductivity meter.

Table 1 presents the description of the samples investigated. They are referred to by the amount of fly ash (0%, 18% or 30%) and the position of the reinforcement during the casting (bottom (1) or top (2)).

The data presented in Figure 1 and Figure 2 is a summary of the corrosion current density, the open circuit potential and the electrical resistivity of concrete monitored from capillary saturated condition of the samples over drying in the laboratory.

Table 1: Label of the samples

	CEM I	CEM II/B-M	CEM II/B-V
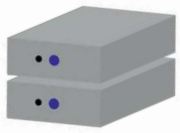	0%-2	18%-2	30%-2
	0%-1	18%-1	30%-1

3. Supplementary discussion to Paper S-VIII

Alonso et al. [3] found a linear trend when plotting the electrical resistance of carbonated mortar containing various cement types versus the corrosion current density (i_{corr}) of the embedded reinforcement in log-log scale (Andrade et al. [4] post-treated the data and presented the i_{corr}-electrical resistivity (ρ) of carbonated mortar relationship). The higher the electrical resistivity, the lower the i_{corr}. Based on the observations, they proposed that the corrosion process in carbonated mortar is under "*resistance control"*. Glass et al. [5] found the same trend investigating reinforced PC mortar samples. In addition, they compared the open circuit potential (OCP) and i_{corr}; the higher the i_{corr}, the lower the OCP. They argued that resistance control alone could not explain the OCP-i_{corr} relationship and proposed that the anodic reaction is limited by the electrical resistance of the matrix. The mechanism was termed as "*anodic resistance control"*. According to this theory, the OCP-i_{corr} data set should mirror a cathodic polarization curve: the reduction of oxygen remains unaffected while the anodic reaction changes depending on the electrical resistivity of the matrix (as presented in Fig 9 in [5]).

The i_{corr}-ρ relationship obtained in the current investigation is presented in Figure 1. Additionally, the regression lines reported by Alonso et al. [3, 4] are included in Figure 1. In agreement with Alonso et al. [3] the i_{corr}-ρ relationship appears to be binder independent within the scatter of the measurements. In addition, sample (18%-2), showed a systematically higher i_{corr} compared to the other samples which could not be explained.

The OCP-i_{corr} relationship obtained in the present investigation is given in Figure 2. Additionally the regression line reported by Glass et al. [5] and the regression lines determined from the data published by Alonso et al. [3] (they presented the OCP and i_{corr} data separately) are showed in Figure 2. For low current densities, the OCP-i_{corr} trend of the FA samples compares to the trend of the PC samples, but is shifted ca. 300 mV towards more positive values. In addition, there appears to be an impact of the sample position (bottom or top) during the casting, especially for the PCFA mortars. For high current densities, the OCP-i_{corr} relationship changes, especially for the OPC samples towards a more horizontal trend, and seems to be affected by other parameters. Glass et al. [5] observed similar behavior but they did not discuss the observations.

The potential parameters which could have influenced the OCP-i_{corr} relationship are: a) pore solution composition, e.g. [6], b) pore structure (pore water availability), e.g. [7], c) steel-concrete interface characteristics, e.g. [8], and electrical resistivity (influenced by a) – c)), *e.g.* [9].

As mentioned by Glass al. [5], the OCP-i_{corr} data seems to mirror a cathodic polarization curve. From our understanding, this means that the anodic reaction is affected by the change in moisture in a much more pronounced way than the cathodic reaction. All samples showed comparable behaviour indicating that the corrosion process is under anodic resistance control regardless the cement type. The shift between OPC and PCFA samples indicate that the addition of fly ash could have influenced the cathodic reaction. The data taken from Alonso et al. [3] also depicts an influence of fly ash, but in their case the shift was observed in the opposite direction.

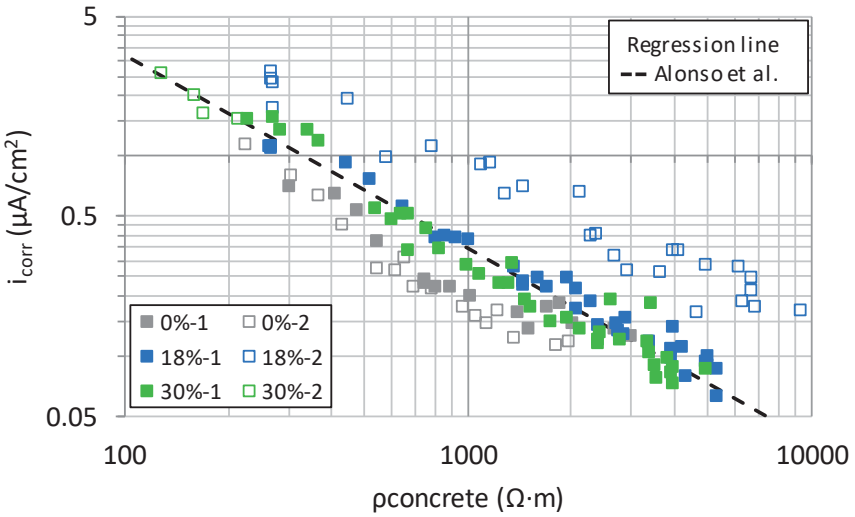

Figure 1: Corrosion current density of reinforcement versus electrical resistivity of carbonated concrete from capillary saturated condition (left side) over drying in laboratory exposure (to the right)

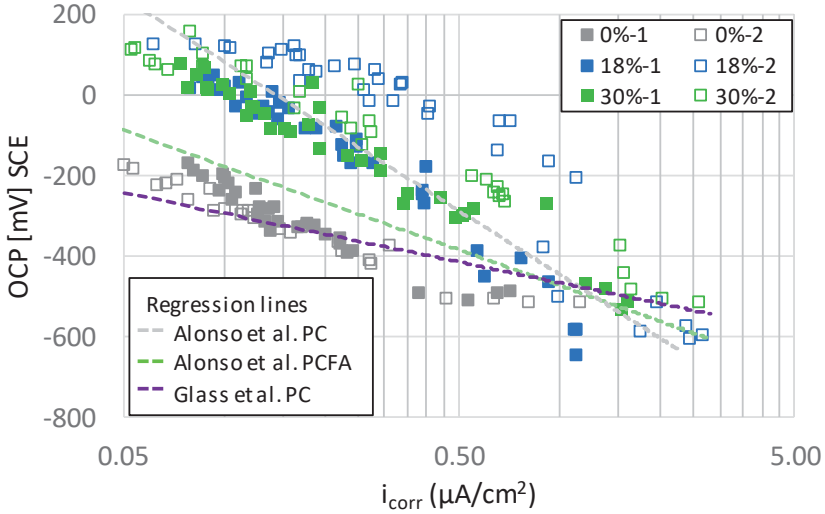

Figure 2: Open circuit potential versus corrosion current density of reinforcing steel from capillary saturated condition (right side) over drying in laboratory exposure (to the left)

An alternative way of presenting the data is given in Figure 3. In this case the ratio between the ohmic resistance (R_Ω) between the reinforcement and the reference electrode, and the polarization resistance of the reinforcement (R_p) is presented versus the weight loss due to water evaporation during the laboratory exposure. When comparing the data, similar trends are observed for all samples. An initial plateau is observed in the R_Ω/R_p until a certain weight loss (critical weight loss), when an abrupt increase in the R_Ω/R_p takes places. The critical weight loss seems to depend on the amount of fly ash added.

This alternative presentation of the data may illustrate a change of the partial process controlling the corrosion process over drying. In very moist conditions, the R_Ω of the concrete and the R_p of the reinforcement change similarly, whereas after the critical weight loss the R_Ω increases more rapidly than the R_p. When comparing Figure 1, Figure 2, and Figure 3 changes upon drying are observed. In Figure 1, the scatter of the trend for each sample increases over drying. In Figure 2, a change in the OCP–i_{corr} relation from the high current density range towards lower current densities is observed while in Figure 3 a remarkable change in the R_Ω/R_p is detected after the critical weight.

This is a preliminary discussion of the governing partial process of carbonation-induced corrosion, which we expect to continue.

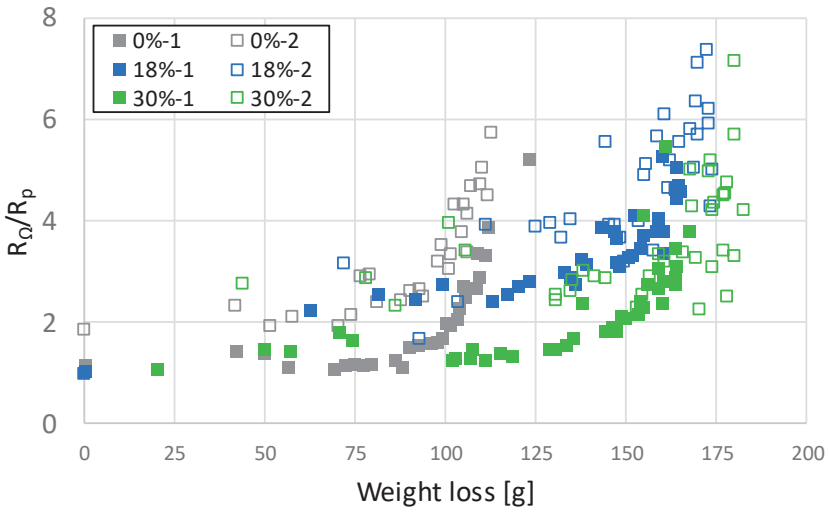

Figure 3: R_Ω/R_p ratio versus weight loss due to water evaporation. From capillary saturated condition (left side) over drying in laboratory exposure (to the right)

4. Summary

The data suggests that the corrosion process in carbonated concrete is under anodic resistance control. However, the controlling partial process may vary depending on the moisture conditions.

We found that under the accelerated carbonation conditions tested here, the i_{corr}-ρ relationship is not binder dependent, while the OCP-i_{corr} relationship is binder dependent.

5. References

[1] M. Messina, A. Belda Revert, K. Hornbostel, M.R. Geiker, M. Gastaldi, Corrosion current density as a function of electrical resistivity of carbonated concrete, (In preparation).
[2] A. Belda Revert, K. Hornbostel, K. De Weerdt, M.R. Geiker, Macrocell corrosion in carbonated Portland and Portland-fly ash concrete - contribution and mechanism, Submitted to Cement and Concrete Research, (2018).
[3] C. Alonso, C. Andrade, J. González, Relation between resistivity and corrosion rate of reinforcements in carbonated mortar made with several cement types, Cement and Concrete Research, 18 (1988) 687-698.
[4] C. Andrade, C. Alonso, Corrosion rate monitoring in the laboratory and on-site, Construction and Building Materials, 10 (1996) 315-328.
[5] G.K. Glass, C.L. Page, N.R. Short, Factors affecting the corrosion rate of steel in carbonated mortars, Corrosion Science, 32 (1991) 1283-1294.
[6] S.L. Langedal, Investigation of resistivity, porosity and pore solution composition in carbonated mortar prepared with ordinary Portland cement and Portland-fly ash cement, in: Department of Structural Engineering, Norwegian University of Science and Technology, Trondheim, 2018, pp. 96.
[7] M. Stefanoni, U. Angst, B. Elsener, Corrosion rate of carbon steel in carbonated concrete – A critical review, Cement and Concrete Research, 103 (2018) 35-48.
[8] U.M. Angst, M.R. Geiker, A. Michel, C. Gehlen, H. Wong, O.B. Isgor, B. Elsener, C.M. Hansson, R. François, K. Hornbostel, R. Polder, M.C. Alonso, M. Sanchez, M.J. Correia, M. Criado, A. Sagüés, N. Buenfeld, The steel–concrete interface, Materials and Structures, 50 (2017) 143.
[9] B. Elsener, C. Andrade, J. Gulikers, R. Polder, M. Raupach, Half-cell potential measurements – Potential mapping on reinforced concrete structures- a RILEM TC-154 technical recommendation, Materials and Structures, 36 (2003) 461-471

Part IV- Supplementary Papers

Paper S-I

Carbonation front characterization: pH colour indicators

Revert, Andres Belda; De Weerdt, Klaartje; Geiker, Mette Rica

Proceedings of the 35th Cement and Concrete Science Conference, Aberdeen, Scotland (2015)

35th Cement & Concrete Science Conference
26-28 August 2015 Paper Number 0052
University of Aberdeen

Carbonation front characterization
pH colour indicators

A. Belda, K. De Weerdt, M.R. Geiker

Norwegian University of Science and Technology (NTNU). Dept. of Structural Engineering

Summary: A PhD project dealing with carbonation induced corrosion has been initiated at NTNU in 2015. The main goal of the project is to obtain improved understanding of parameters controlling carbonation induced corrosion: onset and development. Emphasis is put on studying low carbon footprint cements, specifically blends of Portland cement and fly ash. This paper presents some preliminary results on carbonation front characterization for mortar samples subjected to accelerated carbonation.

Keywords: *phenolphthalein, thymolphthalein, thymol blue, rainbow indicator, image analysis*

1. Introduction

CO_2 from the atmosphere can diffuse into the concrete cover. Through reaction with the pore solution and hydration phases, the CO_2 can cause a decrease in the pH of the pore solution from about 13 to values below 9 (Schiessl, 1976). The thickness of the concrete layer from the exposed surface inwards affected by CO_2 is called the carbonation depth. In sound concrete the steel reinforcement is protected from corrosion by the high pH of the pore solution. However, when the carbonation front reaches the steel corrosion may initiate.

The most common way to measure the carbonation depth is by spraying a freshly broken surface with a pH colour indicator such as phenolphthalein as recommended in EN-13295. Carbonated concrete remains colourless while sound concrete (pH above 9) is coloured by the indicator. However, phenolphthalein has recently been classified as carcinogenic by the Norwegian Environment Agency and therefore alternative indicators need to be identified.

It should be noted that the carbonation depth determined by a pH indicator only shows where the pH of the pore solution drops below a certain level, but does not give any information regarding the extent of carbonation of the solids. The carbonation was early observed to cause a more gradual change in the pH of the pore solution and in the composition of the hydrates (Schiessl 1976 and Tuutti 1982). Hence alternative techniques are required to investigate the changes at the carbonation front, methods such as thermogravimetric analysis (TGA), X-ray diffraction (XRD) or Fourier transformed infrared spectroscopy (FTIR) on profiles ground powder (Chang et al. 2006) have been used.

In this preliminary study different pH indicators were tested and compared with TGA analysis of profile ground powder. This paper presents a critical evaluation of the different pH indicators used on mortars prisms subjected to accelerated carbonation testing.

2. Experimental methods

2.1. Sample preparation

Standard mortar prisms 40 x 40 x 160 mm were prepared according to EN 196-1. Standard CEN sand was used (d_{max} 2 mm).Two binders were investigated: CEM I containing 4% limestone powder and CEM II/B-V containing 30% fly ash and 4% limestone powder, both with two different water-binder ratios: 0.5 and 0.55. After casting, the mortar prisms were stored in the moulds covered with a plastic at 20°C during 24 hours. Then, they were

demoulded, wrapped in plastic and store at 20°C during 13 days in a sealed barrel over water. Fourteen days after casting, samples were exposed for four weeks to the following conditions: temperature 20 °C ± 0.5 °C, relative humidity 60% ± 1.5% and CO_2 concentration 1.45% ± 0.1%.

2.2. pH indicators

Carbonation depth was measured after four weeks of accelerated carbonation for both binders and w/b ratios. The following indicators and concentrations (% in mass) were used: phenolphthalein (P) 1% and 0.1%, thymolphthalein (T) 1% and 0.1%, thymol blue (TB) 0.2% and 0.04% and rainbow indicator (R) acquired premixed. The solid indicators were dissolved in ethanol: water solutions with a volume ratio of 70:30. The indicators were sprayed on freshly broken surfaces. After one hour, pictures were taken with constant light conditions. The pH threshold values given by the supplier are shown in Figure 1 Left. Depending on the indicator the colour change can start from 7.8 (TB) to 10.5 (T).

Image analysis free-ware, Plotdigitizer (http://plotdigitizer.sourceforge.net/), was used to measure carbonation depth. The following procedure was applied: scaling of the picture, dividing into 4 x 4 mm grid; measuring manually 30 points from the six central grids of each side i.e. top (no contact with mould during casting), bottom, left and right. The average, standard deviation, maximum and minimum value were calculated. Only the images for the highest indicator dosages and rainbow indicator were treated.

3. Experimental results

Figure 2 shows the fractured surfaces of the samples with different binders and water-binder ratios sprayed with the tested pH indicators. The average value and standard deviation of the carbonation depths are given in Figure 1 Right (using data from the four sides of the prism). Table 1 gives the carbonation depth depending on the side of the prism for the CEM II/B-V, w/b 0.55 sprayed with T 1%.

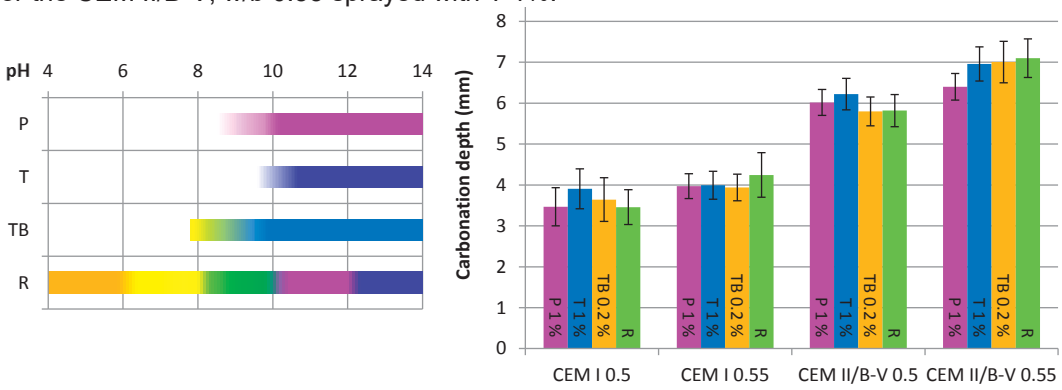

Figure 1: Left - pH threshold values given by supplier; Right – carbonation depth.

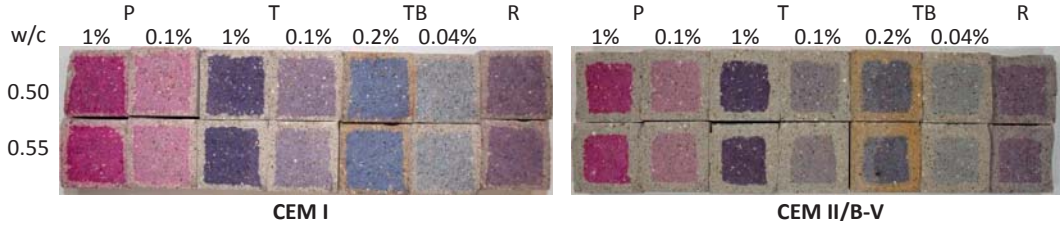

Figure 2: Carbonation depth for the different indicators, binder types and w/c ratios tested.

4. Discussion

From Figure 2 it can be seen that higher concentrations of the pH indicators give a darker colour, which makes it easier to assess the difference between the un-coloured and coloured area. The best contrast was obtained with T 1% and P 1%.

According to the Figure 1 Left, the measured carbonation depth values should have the following sequences: TB< P< T<R. However, as can be seen from Figure 1 Right, there is no considerable difference between the carbonation depths determined with the different indicators. This suggests that the pH drops abruptly at the carbonation front. The pH levels from the different indicators (8-10) were obtained at approximately the same depth. Carbonation depth determination by spraying with a pH indicator is therefore relatively insensitive for the indicator used (within the 8-10 pH range).

The carbonation depth seems to be strongly dependent on the binder type, as expected (Figure 1 Right). The CEM I has a lower carbonation rate compared to the CEM II for the investigated conditions due to its higher buffer capacity and possibly lower early age porosity. The effect of the w/b is rather small for the CEM I mortars and slightly larger for the ones with CEM II in the investigated range.

From Table 1 a slight reduction in the carbonation depth can be observed for the bottom side compared to the other sides of the prism. Further investigation is required to find the cause of this discrepancy.

Table 1: Carbonation depths [mm]: CEM II/B-V, w/b 0.55 sprayed with T 1%.

	Bottom	Right	Top	Left
Average	5.5	7.5	7.4	7.3
Standard Deviation	0.24	0.26	0.24	0.29
Maximum value	6.1	8	8	8.1
Minimum value	5.1	6.8	7	6.7

It should be noted that there is a range of important factors which also affects the carbonation depth measurements for example the presence and size of aggregates, bleeding or segregation and air voids.

5. Conclusions

Thymolphthalein 1% (T 1%) is an equally good pH indicator for the determination of the carbonation depth as the traditionally used and potentially carcinogenic phenolphthalein 1% (P 1%) for the tested mortar compositions and exposure conditions.

6. Acknowledgements

NFR project no. 235211/O30: LAVKARBSEM.

7. References

Schiessl, P. 1976. Zur Frage de zulässigen Rissbreite und der erforder lichen Betondeckung im Stahlbetonbau- unter besonderer Berücksichtigung der Karbonatisierung des Betongs. DAfS, Heft 255. Berlin.

K. Tuuti. 1982. “Corrosion of Steel in Concrete “, PhD thesis, Swedish Cement and Concrete Research Institute (CBI), Stockholm.

Chang, Cheng Feng, and Jing Wen Chen. 2006. “The Experimental Investigation of Concrete Carbonation Depth.” Cement and Concrete Research 36 (9): 1760–67.

Paper S-II

Investigation of the effect of partial replacement of Portland Cement by Fly Ash on carbonation using TGA and SEM-EDS

Revert, Andres Belda; De Weerdt, Klaartje; Hornbostel, Karla; Geiker, Mette Rica

Proceedings of the International RILEM Conference Materials, Systems and Structures in Civil Engineering , Lyngby, Denmark (2016)

International RILEM Conference on Materials, Systems and Structures in Civil Engineering
Conference segment on Concrete with Supplementary Cementitious Materials
22-24 August 2016, Technical University of Denmark, Lyngby, Denmark

INVESTIGATION OF THE EFFECT OF PARTIAL REPLACEMENT OF PORTLAND CEMENT BY FLY ASH ON CARBONATION USING TGA AND SEM-EDS

Andres Belda Revert[(1)], Klaartje de Weerdt[(1)], Karla Hornbostel[(1)], Mette Rica Geiker[(1)]

[(1)] Department of Structural Engineering, NTNU, Norwegian University of Science and Technology, Trondheim, Norway

Abstract
The aim of this paper is to investigate the effect of partial replacement of Portland cement by fly ash on the phase changes upon carbonation and the resulting CO_2-binding capacity. Two mortars with water-to-binder ratio 0.55 and two different binders, Portland cement (CEM I) and Portland fly ash cement (CEM II/B-V) were cured sealed for 14 days at 20ºC and subsequently exposed to accelerated carbonation (20ºC, 60% RH and 1.5% CO_2) for 4 weeks. The changes in the phase assemblage upon carbonation were studied by TGA and SEM-EDS. TGA allowed the quantification of changes in Portlandite and calcium carbonate content. SEM-EDS was used to investigate changes in the C-S-H composition and the microstructure. It was observed that both binders formed similar amounts of carbonates upon accelerated carbonation, even though their CaO content differed. This could be attributed to differences in the reaction degree of the Portland clinker and a larger contribution to the uptake of CO_2 by C-S-H for the fly ash containing cement. Hence care should be taken when applying the CaO content as a measure for the CO_2-binding capacity.

1. Introduction

Carbonation is the spontaneous reaction of CO_2 present in the air with the cement paste, which causes, among others, a drop in the pH of the pore solution. Once the carbonation front reaches reinforcement, embedded steel is no longer passivated and corrosion may start depending on the exposure [1]. Carbonation-induced corrosion is one of the major causes of premature deterioration of reinforced concrete structures [2].

Carbonation is a stepwise reaction which causes gradual changes in the cement paste. First CO_2 is dissolved in the pore solution and carbonic acid is formed. Then the carbonic acid reacts with Ca ions from the different cement phases and calcium carbonate ($C\underline{C}$) is formed. Portlandite (CH) is the first to react, followed by monosulphate (AFm) and ettringite [3]. Calcium silicate hydrate (C-S-H) decalcifies gradually once CH is consumed until it becomes silica gel [4, 5]. Additionally, unhydrated phases as alite and belite can be carbonated [6].

Replacing Portland cement partially with fly ash results in changes of the overall CaO content and the phase assemblage such as consumption of CH by the pozzolanic reaction, and lowering of the Ca/Si ratio of the C-S-H [7]. This affects the CO_2-binding capacity of the resulting binder [3, 8].

The most common way to identify carbonation in concrete is to spray a freshly split surface with a pH indicator (EN 13295 [9]). It is a simple, non-expensive and reliable method to determine the carbonation depth [10]. However, pH indicators do neither reveal information about the changes in the phase assemblage nor the microstructure upon carbonation.

The authors used thermogravimetric analysis (TGA) to quantify the content of CH and $C\underline{C}$ on homogenized profile ground samples and scanning electron microscopy with energy dispersive spectrometry (SEM-EDS) to investigate differences in morphology and elemental composition upon carbonation on polished sections. The aim was to investigate the effect of partial replacement of Portland cement by fly ash on the phase changes upon carbonation and the resulting CO_2-binding capacity. In this paper, two mortars with water-to-binder ratio 0.55 and two binders, Portland cement (CEM I) and Portland fly ash cement (CEM II/B-V), exposed to accelerated carbonation (20ºC, 60% RH and 1.5% CO_2) were investigated.

The present study is part of a PhD project on carbonation of Portland fly ash cement. The final aim of the project is to improve the understanding of the mechanisms affecting the service life of concrete structures with Portland fly ash cements. Both the initiation period (carbonation) and the propagation period (corrosion) are considered.

2. Experimental

Figure 1 provides an overview of the experimental techniques and the sampling undertaken on mortar prisms.

2.1 Mortar samples

Mortar prisms 40 x 40 x 160 mm with two binders were investigated. The binders were: CEM I containing 4% limestone powder and CEM II/B-V containing 30% fly ash and 4% limestone powder. Table 1 presents the chemical composition of the binders determined by XRF. Clinker with similar mineralogy was used for both cements. The mortar composition (water-to-binder ratio 0.55) was 450 g binder, 1350 g standard CEN sand (d_{max} 2 mm) and 247.5 g water per batch. The mortars were mixed according to EN 196 [11]. The prisms were stored in the moulds covered with a plastic wrap at 20°C for 24 hours after casting. Then, they were demoulded, wrapped in plastic and stored at 20°C for 13 days in a sealed container.

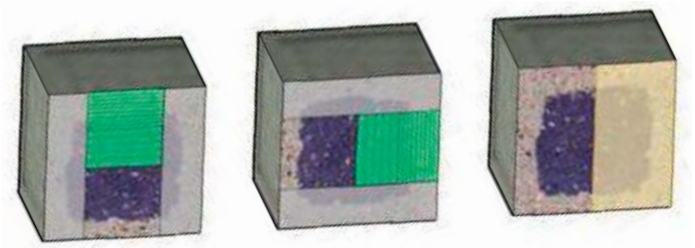

Profile ground samples: ***TGA*** **Polished sections:** ***SEM-EDS***

Figure 1: Schematic overview of the undertaken experimental techniques including sampling. The blue area indicates the non-carbonated mortar identified by thymolphthalein.

Table 1: Chemical composition of the investigated binders determined by XRF [% by mass]

Compound	SiO_2	Al_2O_3	Fe_2O_3	CaO	MgO	SO_3	P_2O_5	K_2O	Na_2O
CEM I	20.4	4.8	3.4	61.7	2.2	3.5	0.2	0.9	0.5
CEM II/B-V	29.5	10.8	4.5	44.6	2	3.2	0.4	1.1	0.5

2.2 Exposure

Fourteen days after casting, the mortar prisms were exposed for four weeks to accelerated carbonation conditions: 20 ± 0.5ºC, 60 ± 1.5% RH and 1.45 ± 0.1% CO_2. Note that the short curing period only allows for a limited degree of reaction of the fly ash [7, 13].

2.3. Methods

TGA was performed on profile ground samples. To study carbonation as a one dimensional phenomenon, the lateral sides (10 mm on each) were removed by dry cutting before profile grinding, see Figure 1. The right (R) and top (T) side were studied. The outer 0-1 mm step was omitted as different paste content was expected. The grinding steps were 1 mm for the first 10 mm and 2 mm-steps for the rest of the sample. The TGA was performed with a Mettler Toledo TGA/DSC 3+, on samples of approximately 300 mg loaded in aluminum oxide crucibles. The samples were heated from 40 to 900ºC at a rate of 20ºC/min while the oven was purged with N_2 at 50 ml/min. The weight loss of the samples was monitored as a function of the temperature. The amounts of CH and C$\underline{C}$ were calculated according to equation (1). However, the exact boundaries were taken from the derivative curve:

$$CH\ \% = \frac{W_{400\,℃} - W_{550\,℃}}{W_{850\,℃}} \cdot \frac{74}{18} \cdot 100\%\ ; \qquad \underline{CC}\ \% = \frac{W_{550\,℃} - W_{850\,℃}}{W_{850\,℃}} \cdot \frac{100}{44} \cdot 100\% \tag{1}$$

Polished sections were prepared according to [12]. All polished sections were carbon coated. Images were taken in back scatter electron (BSE) mode using a Quanta 400 ESEM from FEI operated at high vacuum mode at an accelerating voltage of 20 kV. SEM-EDS point analysis was performed using a JEOL JXA – 8500F Electron Probe Micro analyzer and a Hitachi S-3400N equipped with an Oxford EDS at an accelerating voltage of 15 kV. The following elements were analysed Al, Ca, Cl, Fe, K, Na, Mg, S, and Si. The points were manually selected avoiding sand grains and unreacted fly ash and clinker grains.

3. Results

3.1 TGA

Figure 2 presents an example of both mass loss and derivative curve for a sound sample (dark) and a carbonated sample (grey) determined by TGA for both CEM I (left) and CEM II/B-V (right) mortar after 2 weeks curing and 4 weeks of exposure. It can be seen that the carbonate peak for the carbonated sample (450-850 ºC) has broad shoulders extending from temperatures as low as 450ºC up to 850ºC. This could relate to the decomposition of different C$\underline{C}$ polymorphs which decompose at lower temperatures compared to calcite. However, XRD analysis reported in [10] did not indicate the presence of polymorphs such as vaterite or aragonite. The broadness of the carbonation peak is therefore attributed to large amount of C$\underline{C}$ present and to the variation in crystallinity of the C$\underline{C}$ formed. The carbonation of CH has been observed to result in more crystalline C$\underline{C}$ which decomposes at higher temperatures. Carbonation of C-S-H, on the other hand, results in microcrystalline C$\underline{C}$, of which the decomposition starts at temperatures as low as 450 ºC [13]. This is in agreement with the results presented in Figure 2 where the decarbonation peak related to more crystalline C$\underline{C}$ at about 800 ºC seems to be larger for the carbonated CEM I mortar compared to the CEM II/B-V one, as more of the C$\underline{C}$ originate from CH carbonation for the former compared to the latter. Note that the AFm peak at about 200 ºC disappears upon carbonation.

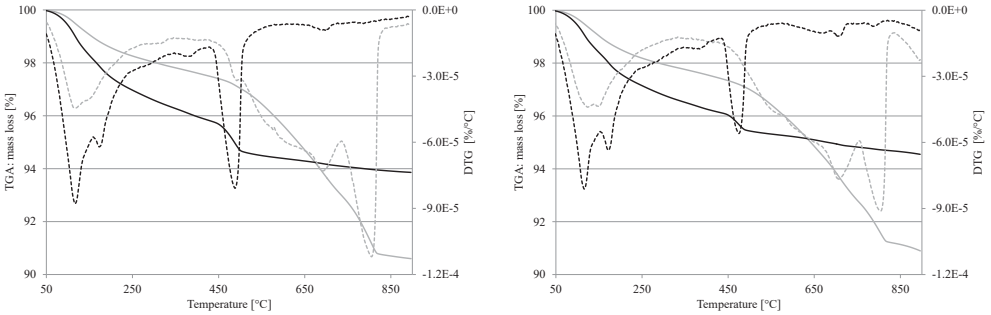

Figure 2: TGA (solid) and DTG (dotted) of sound sample (black), and carbonated sample (grey). Left: CEM I sample. Right: CEM II/B-V sample.

Figure 3 shows the CH and C$\underline{C}$ profiles determined by TGA on profile ground powder. The horizontal axes indicate the depth inwards, with the origin at the exposed surface. The outer 4-6 mm for CEM I and 6-8 mm for CEM II/B-V are affected by carbonation. Carbonation is associated with a decrease in the CH content and an increase in the C$\underline{C}$ content. The amount of C$\underline{C}$ seems to be stable in the carbonated zone, and both binders appear to form comparable amounts of C$\underline{C}$ upon carbonation. Except for the first measurement on the top side of the CEM I mortar prism (depth 1-2 mm) which indicates a higher amount of C$\underline{C}$ compared to the other measurements. However, this might be due to a higher paste content at the top surface caused by e.g. instability in fresh state.

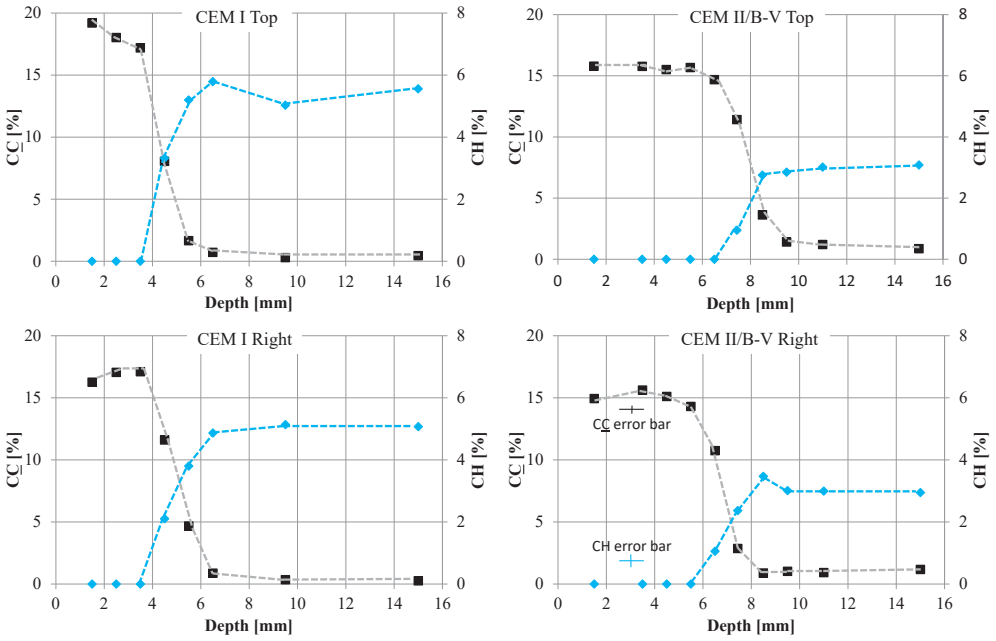

Figure 3: The amount of CH (diamonds) and C$\underline{C}$ (squares) in function of the depth determined on profile ground powder using TGA. The horizontal axis represents the depth (0 outer surface and positive inwards) while the vertical axis presents the C$\underline{C}$ content to the left and CH content to the right in each graph. Note the difference between the scales for C$\underline{C}$ and CH. The typical error for the C$\underline{C}$ estimation was not larger than 0.4 percentage points and 0.3 percentage points for the CH estimation. The error of position is considered the grinding step; 1 mm for the first 10 mm and 2 mm for the rest of the sample.

In the non-carbonated mortar, the amount CH seems to be stable for both binders. The CH content in the CEM II/B-V (about 3%) is notably lower than for the CEM I mortar (about 5%). This lower content is expected both due to the dilution of clinker by the fly ash (dilution effect: 5%·66/96=3.4%) resulting in less clinker to form CH, as well as the pozzolanic reaction of the fly ash consuming part of the CH formed by the clinker (difference between measured CH content in the CEM II/B-V, 3%, and the diluted content due to fly ash, 3.4%: the 0.4% is consumed by the pozzolanic reaction).

It should be noted that for profile grinding in the case of TGA, the content of the different phases is homogenized over the depth of the step (1 or 2 mm). Gradual variations in the CH and C$\underline{C}$ content, between 4-6 mm for CEM I and 6-8 mm for CEM II/B-V, could therefore be partially due to spatial variations in the carbonation depth as stated in [10].

3.2 SEM-EDS

Figure 4 shows BSE images of the carbonated side of CEM I and CEM II/B-V after 2 weeks curing and 4 weeks of exposure.

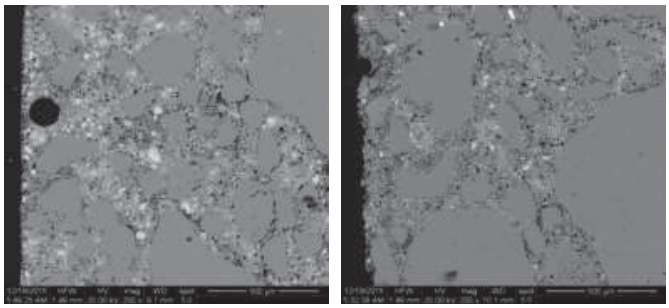

Figure 4: BSE image of side of mortar samples. Left: CEM I. Right: CEM II/B-V (scale indicates 500 μm).

A remarkable difference between the two mortars is the presence of lots of unhydrated cement particles (brighter particles size 10-20 μm) in the CEM I mortar and the near absence of them in the CEM II/B-V mortar. This indicated that the degree of hydration of the cement clinker is considerable higher in the CEM II/B-V mortar compared to the CEM I mortar. The explanation for this might be the higher effective water to clinker ratio in the CEM II/B-V mortar. The observation indicates that unhydrated cement grains resist carbonation within the period of exposure.

It should be noted that SEM-BSE imaging is not the most recommended technique to detect carbonation [10]. Detection of the carbonation is far more efficient using optical microscopy with cross polarized light on thin sections, as calcium carbonate crystals formed upon carbonation change the colour of the cement paste from dark brown to bright opaline colours. Nevertheless, one can distinguish between carbonated and non-carbonated paste in BSE images, tracing CH, as indicated in Figure 5. In the carbonated paste CH can no longer be observed. The presence or absence of CH is, however, difficult to identify, especially for the CEM II/B-V sample containing a lower amount of CH.

Figure 6 shows SEM-EDS dot-plots for carbonated and non-carbonated paste of the mortars. During an EDS point analysis the elements in a certain volume are analysed, e.g. 1 μm^3. This volume comprises generally a mixture of phases. In order to be able to identify phases the results are expressed in ratios. Hence if a mixture of phases is analysed, the result should lie in between the ideal stoichiometry of these phases.

The SEM-EDS analyses of the non-carbonated pastes indicate the presence of hydration phases such as AFm, CH and C-S-H. The C-S-H composition of the two binders seems to be slightly different. The Ca/Si ratio of the CEM I mortar seems to be 1.8 (Si/Ca = 0.56) compared to 1.55 (Si/Ca = 0.65) in the case of CEM II-B/V. The C-S-H of the CEM II-B/V also seems to have a slightly higher Al/Si ratio compared to CEM I, respectively 0.14 versus 0.09. These findings are in agreement with [14, 15].

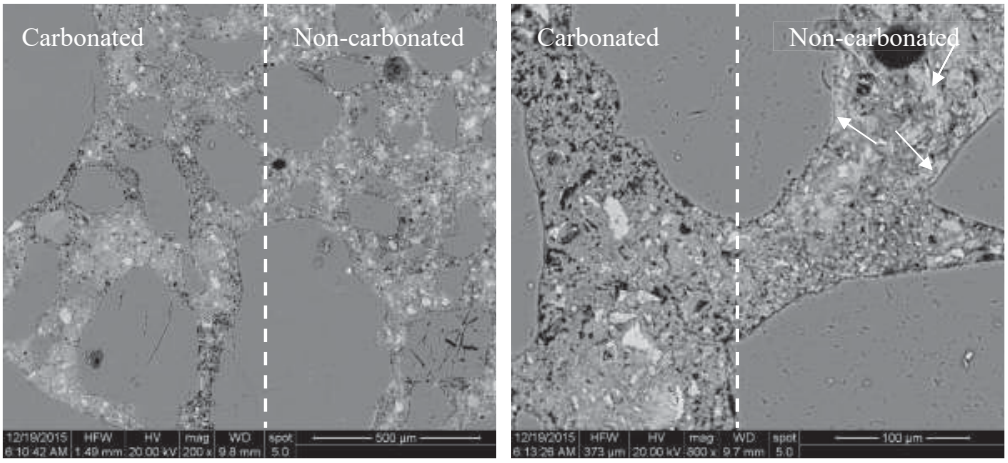

Figure 5: Identification of carbonated and non-carbonated paste in BSE images of CEM I mortar based on presence or absence of CH (scale indicates Left - 500 µm. Right – 100 µm). CH with its typical grey tone is indicated with arrows.

Upon carbonation the data points move to lower Si/Ca ratios. The majority of the points gather around a Si/Ca ratio of 0.25 and an Al/Ca ratio of 0.05. This is contradictory to what is expected. Carbonation results in decalcification of the C-S-H and hence in an increased Si/Ca ratio [5]. However, as mentioned before during SEM-EDS point analysis a volume comprising a combination of phases is analyzed. The lower Si/Ca ratio might indicate a consistent intense intermixing between decalcified C-S-H and C$\underline{C}$.

Due to the fine intermixing, EDS on smaller volumes e.g. combined with TEM is required in order to differentiate between the calcite and the decalcified C-S-H and the Ca/Si ratio of the decalcified C-S-H [13]. Alternatively, other techniques e.g. Si NMR could be used as in [5].

4. Discussion

From Figure 3 it can be seen that both binders, CEM I and CEM II/B-V seem to bind comparable amounts of C$\underline{C}$ in the carbonated cement paste, being slightly higher in the case of CEM I binder. This is unexpected as CEM I has a considerably higher CaO content compared to CEM II/B-V (see Table 1). Calculations of CO_2-binding capacities of binders are commonly related in one way or another to the CaO content of the cement [3, 8, 16].

Hence, one would expect considerably higher amounts of C$\underline{C}$ in the carbonated zone of the CEM I mortar compared to the CEM II/B-V mortar. However, in this investigation it was observed that even though the CaO content in the Portland cement was 40% higher than in the fly ash cement, the amount of C$\underline{C}$ was only about 10% higher in the Portland cement sample upon carbonation. Thus it seems that other factors should be considered when estimating the binding capacity of a given concrete/mortar.

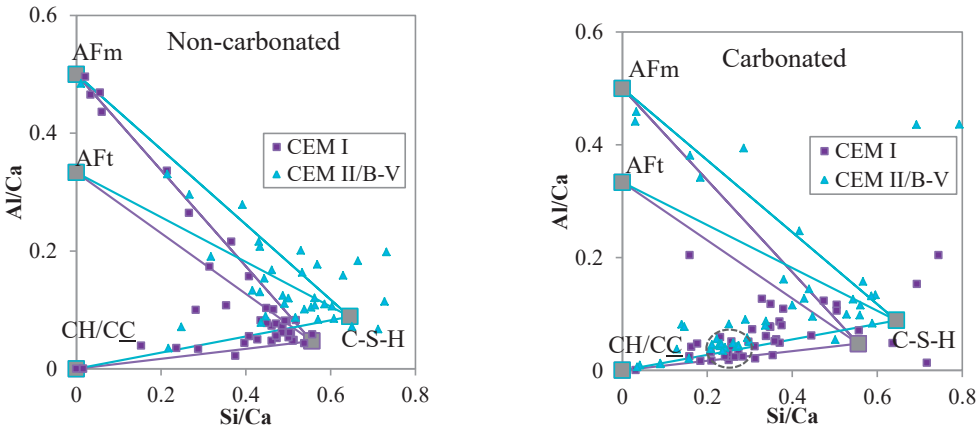

Figure 6: SEM-EDS point analysis of non-carbonated (Left) and carbonated (Right) paste expressed as molar ratios of Si/Ca versus Al/Ca. The ideal composition of ettringite (AFt), monosulphate (AFm), and portlandite (CH), as well as the assumed composition of C-S-H for the different binders is marked.

In order to understand this apparent discrepancy, the origin of the CC was estimated. Figure 7 presents the different contributions for the carbonated section at 1-2 mm depth. To be able to calculate the different contributions, the CC and CH content of the non-carbonated samples (depth 12-14 mm) were determined by TGA. These samples contained CC due to minor limestone additions to the binders (L). The CC originating from the carbonation of CH were calculated based on the amount of CH in the non-carbonated samples (CC=100/74·CH). The remaining amount of CC was assumed to originate from carbonation of C-S-H. For the CEM I a larger part of the formed CC originates from the carbonation of CH compared to CEM II/B-V. This can be expected as CEM II/B-V contains less CH compared to CEM I due to both dilution of Portland clinker and the pozzolanic reaction of the fly ash.

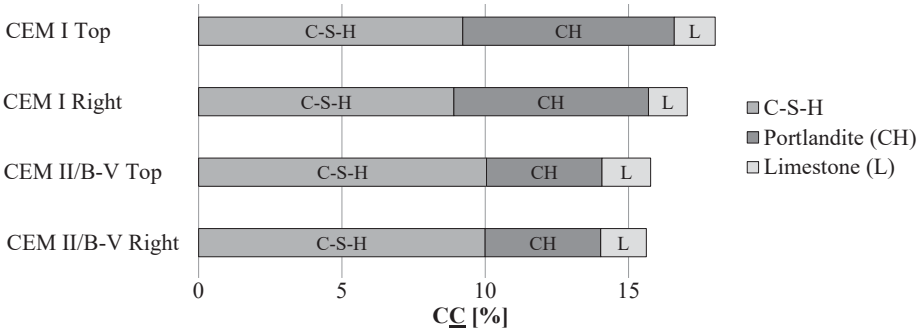

Figure 7: Estimated origin of carbonates (CC) for carbonated samples. CH and L content taken from sound sample (depth 12-14 mm) and total CC content from carbonated sample.

The CEM II/B-V seems to bind more CO_2 through carbonation of C-S-H compared to CEM I. Based on the results presented two potential explanations can be put forward for the similar CO_2-binding capacity of the two binders even though their CaO contents differ:

- First, the degree of reaction of the clinker is considerably higher in the CEM II/B-V mortar compared to the CEM I (Figure 4). This results in an increased CO_2-binding capacity relative to the clinker content for the CEM II/B-V mortar compared to the CEM I mortar, as the unreacted clinker grains do not seem to have carbonated.
- In addition, the CEM II/B-V binder seems to bind more CO_2 during the carbonation of the C-S-H compared to CEM I (Figure 7). This might be both due to differences in the amount of C-S-H formed and due to the binding capacity of the C-S-H for the two mortars. In the CEM II/B-V mortar, potentially more C-S-H can have formed due to the combination of higher reaction degree of the clinker and the pozzolanic reaction of the fly ash. The binding capacity of the C-S-H will also be influenced by the composition of the non-carbonated and the carbonated C-S-H. With the applied techniques, we are neither able to quantify the amount of C-S-H formed nor to identify the Ca/Si ratio of the carbonated C-S-H. Therefore, we cannot at present quantify the contributions of the before named effects on observed difference in CO_2-binding in the C-S-H for the two mortars.

Even though both binders seem to have a similar CO_2-binding capacity, their carbonation rate is very different. As Figure 3 shows that C$\underline{C}$ was found at greater depth for the CEM II/B-V mortar compared to the CEM I for the same accelerated carbonation conditions. This indicates the CO_2-binding capacity is not a rate limiting factor for carbonation. Additional investigations are needed to identify the parameters determining the carbonation rate i.e. porosity.

5. Conclusions

- The TGA results show that the CEM I mortar contains more CH than the CEM II/B-V mortar, as expected. The TGA also reveals that both binders, CEM I and CEM II/B-V, bind a similar total amount of CO_2 upon accelerated carbonation. As both binders, CEM I and CEM II/B-V, differ considerably in CaO content, respectively 62 and 45%, the CO_2-binding capacity can therefore not be related to the CaO content of the binders.
- SEM-EDS analyses indicate that both binders form similar reaction products upon carbonation, i.e. finely inter-mixed decalcified C-S-H with calcium carbonate. The BSE images reveal a large difference in the reaction degree of the clinker in the two binders. The partial replacement of Portland cement by fly ash leads to a near to complete reaction of the clinker whereas lots of unreacted clinker grains were observed for the pure Portland cement. The unreacted clinker did not seem to carbonate.
- CEM II/B-V has a similar CO_2-binding capacity compared to CEM I, which can be explained by a higher degree of reaction of the clinker and a larger contribution of C-S-H to the uptake of CO_2 for the CEM II/B-V mortar compared to CEM I.

7. Acknowledgements

The authors acknowledge the Norwegian Research Council for facilitating the research (NFR project no. 235211/O30: LAVKARBSEM) and the financial support provided by the partners of the LAVKARBSEM project: Heidelberg Technology Center GmbH, Mapei AS, Norbetong AS, Norcem AS, NTNU, Rambøll Engineering AS, SINTEF Byggforsk avd Trondheim, Skanska Norge AS, Spenncon AS. Also, the authors would like to acknowledge Ulla Hjorth Jakobsen (DTI) for the assistance with microscopy and Tone Østnor (SINTEF) for the assistance with TGA.

8. References

[1] Bertolini, L., et al., Chapter 5: Carbonation-induced corrosion, in *Corrosion of Steel in Concrete*, Weinheim, (2013), 79-91

[2] Bamforth, P., Enhancing Reinforced Concrete Durability, Concrete Society Technical Report, (2004)

[3] Lagerblad, B., Carbon dioxide uptake during concrete life cycle – State of the art report, Swedish Cement and Concrete Research Institute (2006)

[4] Chang, C. F. and J. W. Chen, The experimental investigation of concrete carbonation depth, Cement and Concrete Research, (2006), 1760-1767

[5] Sevelsted, T. F. and J. Skibsted, Carbonation of C–S–H and C–A–S–H samples studied by ^{13}C, ^{27}Al and ^{29}Si MAS NMR spectroscopy, Cement and Concrete Research, (2015), 56-65

[6] Papadakis, V. G., et al., Fundamental modelling and experimental investigation of concrete carbonation, American Concrete Institute Materials Journal (1991), 363-373

[7] De Weerdt, K., et al., Hydration mechanisms of ternary Portland cements containing limestone powder and fly ash, Cement and Concrete Research (2011), 279-291.

[8] Engelsen, C. J. and H. Justnes, CO_2- binding by concrete, SINTEF, Oslo (2014)

[9] EN 13295:2003: Products and systems for the protection and repair of concrete structures. Test methods. Determination of resistance to carbonation (2003)

[10] Belda, A., et al., Carbonation Characterization of Mortar with Portland Cement and Fly Ash, Comparison of Techniques, Nordic Concrete Research, (in preparation)

[11] EN 196-1:2005: Methods of testing cement – Part 1: Determination of strength (2005)

[12] Detwiler, R. J., et al., Preparing specimens for microscopy, Concrete International (2001), 51-58

[13] Herterich, J., et al., Microstructure and phase assemblage of low-clinker cements during early stages of carbonation, 14th International Congress on the Chemistry of Cement Beijing (2015)

[14] Richardson, I. G., The nature of the hydration products in hardened cement pastes, Cement and Concrete Composites (2000), 97-113

[15] Deschner, F., et al., Hydration of Portland cement with high replacement by siliceous fly ash, Cement and Concrete Research (2012), 1389-1400

[16] Fridh, K., et al., A model to calculate the CO_2-uptake in a country's concrete structures during service life and after, XXII Nordic concrete research symposia, Reykjavik (2014)

Paper S-III

SEM-EDS of products formed at natural and accelerated carbonation of concrete from CEM I, CEM II/B-M and CEM II/B-V

Revert, Andres Belda; De Weerdt, Klaartje; Geiker, Mette Rica; Hjorth, Ulla Jakobsen

XXIII Nordic Concrete Research Symposium, Aalborg, Denmark (2017)

SEM-EDS analysis of products formed under natural and accelerated carbonation of concrete with CEM I, CEM II/B-M and CEM II/B-V

Andres Belda Revert*
PhD student
e-mail:
andres.b.revert@ntnu.no

Mette Rica Geiker*
PhD, Professor
e-mail:
mette.geiker@ntnu.no

Klaartje De Weerdt*
PhD, Associate Professor
e-mail:
klaartje.d.weerdt@ntnu.no

*
Norwegian University of Science and Technology (NTNU),
Department of Structural Engineering
Richard Birkelands vei 1 A, 7491. Trondheim

Ulla Hjorth Jakobsen
PhD, Senior Consultant
Danish Technological Institute (DTI)
Concrete Centre
Gregersensvej 4, DK 2630 Taastrup
e-mail: uhj@teknologisk.dk

ABSTRACT
Carbonation resistance of concrete is usually tested under accelerated conditions, i.e. by elevating the CO_2 concentration compared to natural conditions and keeping the RH close to 60%. However, it is not clear if these conditions mirror the natural process. Using SEM-EDS we investigated the composition of the reaction products of carbonated and non-carbonated concrete containing 0, 18 and 30% fly ash exposed to three different carbonation conditions. In non-carbonated concrete the reaction products depended on the binder. However, in carbonated concrete the reaction products were similar in composition in all the concretes and exposure conditions tested.

Key words: Carbonation, Supplementary Cementitious Materials (SCM), Testing

1. INTRODUCTION

Carbonation is a spontaneous reaction of the cement paste with the CO_2 present in the atmosphere. It is a slow process under natural conditions (0.03% CO_2) and is therefore accelerated for testing purposes by controlling the relative humidity (50-65%) and using increased CO_2 concentration (e.g. 1 to 50%, see summary in [1]). Carbonation causes changes in microstructure, phase composition and pH of the pore solution in the cement paste [2]. It is, however, not clear if the accelerated exposure conditions cause similar changes compared to natural carbonation.

The investigation is part of a PhD study on carbonation-induced corrosion in fly ash concrete. In the project two different accelerated conditions were used in addition to natural conditions: one to accelerate carbonation (60% RH and 1% CO_2) and one where also corrosion in carbonated concrete is facilitated (90% RH and 5% CO_2). The aim of the investigation is to check if the tested accelerated conditions mirror the natural carbonation process. The phase composition, pore solution and other microstructural features in the carbonated concrete, especially in the vicinity of the reinforcement, will influence reinforcement corrosion. In this paper, we focus on the composition of the reaction products.

2 EXPERIMENTAL

Concretes containing three different cements water-to-binder ratio 0.54-0.56 and 370 kg/m^3 cement were prepared. The cements contained limestone addition (4%) and different amounts of fly ash CEM I (0%), CEM II/B-M (18%) and CEM II/B-V (30%), see Table 1. The concrete samples were kept in the mould for three days and when demoulded wrapped in plastic for 11 days. After this period, they were carbonated for 20 weeks. Three exposure conditions were used: "N": natural carbonation sheltered from rain, "1-60": 60% RH and 1% CO_2, and "5-90": 90% RH and 5% CO_2. The temperature was in all cases close to 20ºC. Polished epoxy impregnated sections were prepared at the Danish Technological Institute (DTI). All polished sections were carbon coated before testing. A scanning electron microscope Quanta 400 ESEM from FEI operated at high vacuum mode, accelerating voltage of 15 kV, spot size 5 and working distance of around 10 mm was used. The data was Proza corrected. 50 points were manually taken selecting the outer reaction products in carbonated ("Carb") and non-carbonated ("Non") areas of each sample.

3 RESULTS AND DISCUSSION

Figure 1 presents the data obtained by SEM-EDS point analysis. The horizontal axis shows the Si/Ca molar ratio and the vertical the Al/Ca molar ratio. The ideal stoichiometry of the following phases is indicated: calcium hydroxide (CH) and calcium carbonate (C$\underline{\text{C}}$) in the origin, and on the vertical axes ettringite (AFt) and monosulphate (AFm). The estimated composition of the C-S-H for the tested non-carbonated concretes is marked with large black squares. During the SEM-EDS point analysis a certain volume is analysed, which generally includes a mixture of phases and the resulting point lies in between the ideal stoichiometry of the phases in the mixture. The points taken in the non-carbonated areas indicate the presence of AFm, AFt, CH/C$\underline{\text{C}}$ and C-S-H. In the carbonated areas less AFm and AFt phases seem to be present as fewer points are found between the C-S-H and AFt or AFm compositions. The points associated with C-S-H in the carbonated concrete seem to gather mainly around a Si/Ca ratio from 0.15-0.35. This is opposite of what one would expect. Upon carbonation C-S-H decalcifies [3] and one would expect the data point to move to higher Si/Ca ratios. A possible reason for the observation is that during SEM-EDS point analysis a volume comprising several phases is analysed. The lower Si/Ca ratio may originate from fine intermixing of decalcified C-S-H and C$\underline{\text{C}}$. This is in line with recent TEM observations indicating the formation of finely dispersed C$\underline{\text{C}}$ crystals in C-S-H upon carbonation [4].

Table 1 – Chemical composition of the cements determined by XRF [% by mass]

Cement	Label	SiO_2	Al_2O_3	Fe_2O_3	CaO	MgO	SO_3	P_2O_5	K_2O	Na_2O
CEM I	A	20.4	4.8	3.4	61.7	2.2	3.5	0.2	0.9	0.5
CEM II/B-M	B	27.5	8.4	3.9	52.7	1.6	2.6	0.2	0.6	0.5
CEM II/B-V	C	29.5	10.8	4.5	44.6	2	3.2	0.4	1.1	0.5

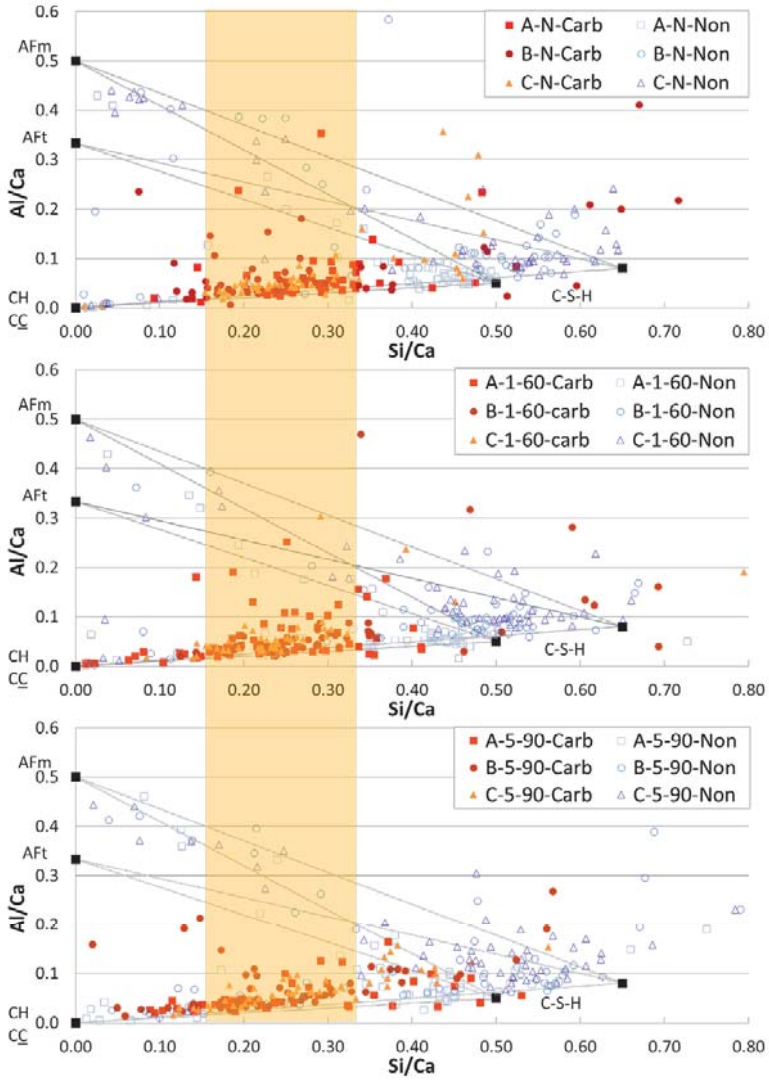

Figure 1 – SEM-EDS point analysis, Si/Ca versus Al/Ca ratios. The ideal composition of ettringite (AFt), monosulphate (AFm), portlandite (CH) and calcium carbonate (C$\underline{C}$), as well as the estimated compositions of C-S-H in the non-carbonated concretes with fly ash (Si/Ca=0.65) and without fly ash (Si/Ca=0.5) are marked. The shaded area indicates the data points in carbonated concrete (0.15-0.35 Si/Ca) where decalcified C-S-H is finely intermixed with C$\underline{C}$.

The lowering of the Si/Ca ratio of C-S-H related points upon carbonation indicates that Ca redistributes in the system. For example, Ca originating from portlandite will dissolve and precipitate as very small C$\underline{C}$ crystals finely intermixed with the decalcified C-S-H. Note that a mass balance of the Ca cannot be performed as only few manually selected points were analysed. Similar observations using SEM-EDS point analysis on mortars containing similar binders exposed to 60% RH and 1% CO_2 were reported earlier [5]. The results presented in this paper show that upon carbonation decalcified C-S-H is finely intermixed with C$\underline{C}$ independently of the binder as well as the exposure conditions. As the reaction products are in equilibrium with the pore solution, the results indicate that the composition of the pore solutions upon carbonation might not be that different either. Assuming similar pore structure, it could lead to comparable concrete resistivity in carbonated concrete. Further research is needed to confirm this.

5 CONCLUSION

Concretes with varying fly ash content were exposed to natural and accelerated carbonation and the reaction products were investigated using SEM-EDS. The data shows that the reaction products upon carbonation are similar for the tested concretes and exposures conditions even if the initial hydration products were different.

AKNOWLEDGEMENTS

The current paper is part of a larger research project 'Lavkarbsem' (NFR project no. 235211/O30). The project is supported by the Norwegian Research Council and the following companies, Engineering AS, HTC (Heidelberg Technology Center), Mapei AS, Norbetong AS, Norcem AS, Rambøll AS and Skanska AS.

REFERENCES

[1] Harrison, T., Jones, M., Newland, M. Kandasami, S. and Khanna, G. “Experience of Using the prTS 12390-12 Accelerated Carbonation Test to Assess the Relative Performance of Concrete.” Magazine of Concrete Research 64 (8): 737–47 (2012)

[2] Bertolini, L., Elsener, B., Pedeferri, P., Redaelli, E. and Polder, R.: “Corrosion of Steel in Concrete”, Wiley-VCH Verlag GmbH & Co, Weinheim, Germany, pp. 79-91 (2013)

[3] Sevelsted, T. F. and Skibsted, J.: “Carbonation of C–S–H and C–A–S–H samples studied by ^{13}C, ^{27}Al and ^{29}Si MAS NMR spectroscopy”, Cement and Concrete Research, Vol. 71, pp. 56-65 (2015)

[4] Herterich, J., Black, L. and Richardson, I.: “Microstructure and phase assemblage of low-clinker cements during early stages of carbonation”, 14th International Congress on the Chemistry of Cement, Beijing, China (2015)

[5] Revert, A. B., De Weerdt, K., Hornbostel, K. and Geiker, M.R.: “Investigation of the effect of partial replacement of Portland cement by fly ash on carbonation using TGA and SEM-EDS”, International RILEM Conference on Materials, Systems and Structures in Civil Engineering, Lyngby, Denmark, pp. 413-422 (2016)

Paper S-IV

Carbonation-induced corrosion, impact of sampling technique on predicted service life

Revert, Andres Belda; De Weerdt, Klaartje; Hornbostel, Karla; Geiker, Mette Rica

Proceedings of the International RILEM 4th Conference on Service Life Design for Infrastructures, Delft, Netherlands (2018)

CARBONATION-INDUCED CORROSION, IMPACT OF SAMPLING TECHNIQUE ON PREDICTED SERVICE LIFE

A. Belda Revert (1), K. De Weerdt (1), K. Hornbostel (2), M.R. Geiker (1)

(1) Department of Structural Engineering, Norwegian University of Science and Technology (NTNU), 7491 Trondheim, Norway

(2) Norwegian Public Roads Administration (Statens vegvesen), Trondheim, Norway

Abstract

Limit state equations for the depassivation of reinforcement due to carbonation are available in guidelines and standards. The physical uncertainty of the carbonation process due to the inherent nature of the concrete is taken into account by using probabilistic modelling and statistical distributions of the material properties. The probability of failure, and thus the service life of a reinforced concrete structure, is determined comparing the carbonation depth distribution to the concrete cover distribution. In this investigation, the influence of the sampling technique on the carbonation depth distribution and the predicted service life are discussed.

Keywords: Carbonation, corrosion onset, probabilistic design

1. INTRODUCTION

The carbonation depth is the depth measured from the exposed surface inwards at which the pH indicator phenolphthalein (1% in mass solution) sprayed on a freshly split surface changes from colourless to pink according to [1]. The carbonation distribution is determined manually by taking five points per side on mortar (40x40x160 mm) or concrete (100x100x400 mm) samples. [1] There are other standards and recommendations, which suggest different procedures, *e.g.* [2-5]. The carbonation development of the bulk (plain) concrete is assumed to represent the carbonation development in reinforced concrete. However, systematic variations may be introduced due to microstructural changes in the vicinity of the reinforcement [6].

The (design) service life of a structure is defined as "*the assumed period for which a structure or part of it is to be used for its intended purpose with anticipated maintenance but without major repair being necessary*" according to [7]. To quantify the service life a limit state and the level of reliability (or probability of failure) for not passing it in a period should be defined [8]. A limit state equation for the depassivation of reinforcement due to carbonation is available in *e.g.* [8], which also recommends a probability of failure (P_f) of 10%.

The aim of the paper is to illustrate the impact of the sampling technique on the statistical distribution of the measured carbonation depth and implications of this on the predicted service life.

2. EXPERIMENTAL

Concrete prisms (*w/b*=0.55) 120x120x260 mm and wall elements 1500x1300x250 mm were prepared containing Portland and Portland-fly ash cement (18% or 30% FA), maximum aggregate size 16 mm. The prisms and wall elements were cured for two weeks wrapped in plastic. Subsequently, the prisms were exposed to 20°C, 90% RH and 5% CO_2 in a climate chamber and the wall elements were exposed to natural carbonation ((XC3) according to EN 1992 [9]) at a field station in Trondheim [10], Norway.

Carbonation was detected by spraying thymolphthalein on a freshly split surface of prisms or drilled cores and quantified either manually (M), selecting five points taken per side according to [1], or by image analysis (I), using pictures taken by an Olympus E-630 camera attached to a setup with fixed lighting conditions. The pictures were scaled, and the sample/non-carbonated areas were determined using ImageJ freeware (https://imagej.net/Welcome). 140 measuring points were taken per sample (3 points/cm). The carbonation depths were determined avoiding the corner effect (due to the ingress from two directions). [6]

3. RESULTS AND DISCUSSION

Table 1 presents the carbonation depth distribution determined using the image analysis (samples exposed to 20°C, 90% RH and 5% CO_2) and the manual approach (samples exposed to XC3, or to 20°C, 90% RH and 5% CO_2 for 72 weeks). Figure 1 illustrates the impact of the sampling technique on the measured carbonation depth distributions after 72 weeks accelerated exposure. When using the manual approach, the measurements are operator dependent and the average of the determined distribution can be higher or lower compared to the real carbonation distribution. In addition, the manual approach leads to a lower standard deviation (the tails of the distribution are “cut off”). The overlapping area between carbonation distributions and concrete cover distribution indicates the probability of failure. The calculated values (P_f) assuming a concrete cover distribution of 30 ± 5 mm (average ± standard deviation) are given in Figure 1.

Assuming square root-time dependency, the carbonation rates (coefficients) were determined for the two exposure conditions, see Table 2. The carbonation coefficients when exposed to XC3 compare to coefficients found in well-cured and compacted concrete [11].

The service life for structures made from the three concrete compositions was determined using the data from Table 1, and assuming P_f=10%, concrete cover 30 ± 5 mm. Table 3 illustrates that for the present data, the sampling technique has limited impact on the predicted service life.

The applicability of data from the accelerated exposure condition is supported by SEM-EDS point analysis [12], which showed comparable chemical composition of the reaction products in the same concretes investigated here which were carbonated under natural and different accelerated conditions. Further investigations of the microstructure are ongoing.

Table 1: Determined carbonation depth distributions. t: time in weeks, x̃: average value, COV: coefficient of variation, I: image analysis, M: manual

Exposure	t [w]	Carbonation depth [mm]						Sampling			
		0% FA		18% FA		30% FA		Approach	Points	Length [cm]	Points /cm
		$\tilde{x}$	COV	$\tilde{x}$	COV	$\tilde{x}$	COV				
20°C, 90% RH, 5% CO_2	8	7.8	24	8.3	28	11.1	29	I	160	54	3
	31	10.4	27	10.9	21	14.4	22	I	160	54	3
	45	10.1	32	14.3	22	20.1	28	I	160	54	3
	72	12.6	24	17	25	20.7	21	I	160	54	3
		13.1	18	18.2	22	20.4	16	M	20	54	0.4
XC3	20	2.8	13	3.8	13	4.1	10	M	5	10	0.5
	78	4.7	23	5.2	12	6.3	16	M	5	10	0.5

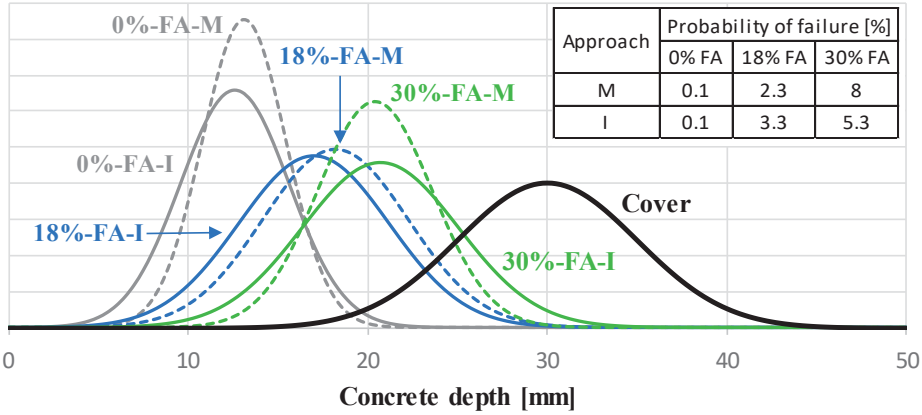

Approach	Probability of failure [%]		
	0% FA	18% FA	30% FA
M	0.1	2.3	8
I	0.1	3.3	5.3

Figure 1: Determined carbonation depth distributions using image analysis (I) or manual (M) approach (72 w, 20°C, 90% RH, 5% CO_2). Calculated P_f assuming concrete cover 30 ± 5 mm

Table 2: Calculated carbonation rates (mm/year$^{0.5}$)

Exposure	0% FA	18% FA	30% FA
20°C, 90% RH, 5% CO_2	11.8	15.0	19.5
XC3	4.0	4.6	5.4

Table 3: Calculated service life [years] for XC3, concrete cover 30 ± 5 mm, P_f=10%

Approach	0% FA	18% FA	30% FA
M	48	26	18
I	48	23	20

4. CONCLUSIONS

The influence of the sampling technique on the carbonation depth distribution and the predicted service life was quantified. The manual approach described in [1] was compared to an image analysis approach. Only limited impact on the predicted service life was observed using carbonation depth distribution of Portland cement concrete with and without fly ash exposed to 20°C, 90% RH and 5% CO_2. The carbonation depth determined manually is representative of the real carbonation distribution.

5. AKNOWLEDGEMENTS

The current investigation is part of a larger research project, 'Lavkarbsem' (NFR project no. 235211/O30). The project is supported by the Norwegian Research Council and the following companies: Mapei AS, Norbetong AS, Norcem AS, Skanska AS, and Rambøll Engineering AS. The authors would like to thank Associate Professor Daniel Cantero (NTNU) for discussion of the calculations.

6. REFERENCES

[1] EN-12390-10, Testing hardened concrete - Part 10: Determination of the relative carbonation resistance of concrete, 2007.
[2] prEN-12390-10, Testing hardened concrete - Part 10: Determination of the relative carbonation resistance of concrete, In revision.
[3] ISO 1920-12, Testing of concrete — Part 12: Determination of the carbonation resistance of concrete. Accelerated carbonation method, 2015.
[4] S. Greve-Dierfeld, C. Gehlen, Performance-based durability design, carbonation part 2 - Classification of concrete, Structural Concrete, 17 (2016) 523-532.
[5] NT Build 357. Concrete, repairing materials and protective coating: carbonation resistance, NORDTEST, 1989.
[6] A. Belda Revert, K. De Weerdt, K. Hornbostel, M.R. Geiker, Carbonation-induced corrosion: Investigation of the corrosion onset, Construction and Building Materials, 162 (2018) 847-856.
[7] ISO 2394: General principles on reliability for structures, 2015.
[8] International Federation for Structural Concrete, fib, Model Code for Service Life Design, Bulletin no 34, Lausanne, Switzerland, 2006.
[9] EN-1992, EN 1992: Design of concrete structures, 2004.
[10] T. Østnor, O.Skjølsvold, A. Belda Revert, SINTEF report SBF 218:00081- Restricted.
[11] L. Bertolini, B. Elsener, P. Pedeferri, E. Redaelli, R. Polder, Chapter 5: Carbonation-induced corrosion, Corrosion of Steel in Concrete, Wiley-VCH Verlag GmbH & Co, Weinheim, Germany, 2013, pp. 79-91.
[12] A. Belda Revert, K. De Weerdt, M.R. Geiker, U.H. Jakobsen, SEM-EDS analysis of products formed under natural and accelerated carbonation of concrete with CEM I, CEM II/B-M and CEM II/B-V XXIIIth Symposium on Nordic Concrete Research & Developement, Aalborg, Denmark, 2017.

Paper S-V

Impact of accelerated carbonation on microstructure and phase assamblage

Revert, Andres Belda; De Weerdt, Klaartje; Hjorth, Ulla Jakobsen; Geiker, Mette Rica

Submitted to Nordic Concrete Research

Impact of accelerated carbonation on microstructure and phase assemblage

	Andres Belda Revert PhD student Norwegian University of Science and Technology (NTNU), Department of Structural Engineering Richard Birkelands vei 1 A, 7491. Trondheim andres.b.revert@ntnu.no
	Klaartje De Weerdt PhD, Associate Professor Norwegian University of Science and Technology (NTNU), Department of Structural Engineering Richard Birkelands vei 1 A, 7491. Trondheim klaartje.d.weerdt@ntnu.no
	Ulla Hjorth Jakobsen PhD, Senior Consultant Danish Technological Institute (DTI) Concrete Centre Gregersensvej 4, DK 2630 Taastrup uhj@teknologisk.dk
	Mette Rica Geiker PhD, Professor Norwegian University of Science and Technology (NTNU), Department of Structural Engineering Richard Birkelands vei 1 A, 7491. Trondheim mette.geiker@ntnu.no

ABSTRACT

The current investigation presents a summary of the characterization of the microstructure and phase assemblage of carbonated mortar and concrete samples containing Portland and Portland-fly ash cement, which were exposed to various conditions. Different characterization techniques were used: thermogravimetric analysis to study the solid phases, SEM-EDS point analysis to investigate the chemical composition of the solid phases, optical microscopy to investigate the microstructure, and cold water extraction to characterize the chemical composition of the pore solution. The combined results on microstructure and phase assemblage indicate that carbonation up to 5% CO_2 appears representative for natural carbonation.

Key words: Carbonation, microstructure, solid phases, pore solution, Portland-fly ash cement

1. INTRODUCTION

Carbonation is the reaction of the CO_2 present in the atmosphere with the phases in the hydrated cement paste. Carbonation causes a change in the microstructure, solid phases, and lowers the pH of the pore solution [1]. Carbonation in natural exposure is a slow process. For performance testing, carbonation is therefore usually accelerated by means of optimal relative humidity (60-70%) [1] and increased CO_2 concentration (25-250 times than natural) [2]. However, it is not clear to which extent the microstructure and phase assemblage developed upon accelerated carbonation mirrors that for natural carbonation.

Castellote et al. [3] investigated cement paste exposed to various CO_2 concentrations (0.03 (natural), 3, 10 and 100%). The samples were prepared with Portland cement and a water-to-binder ratio (*w/b*) of 0.5. Phase changes due to carbonation were investigated using ^{29}Si MAS-NMR, TGA and XRD. The authors concluded that accelerated carbonation up to 3% CO_2 gives similar products compared to natural carbonation. For 10% and 100% CO_2 the C-S-H was more extensively carbonated and silica gel was formed.

Auroy et al. [4] investigated cement paste (*w/b*=0.40) containing a ternary blend (50% PC + 25% FA + 25% GGBFS). Exposure conditions were 25°C, 55% RH, and 0.04 or 3% CO_2. Carbonation was investigated using XRD, TGA and ^{29}Si NMR3. They found that similar products were formed upon carbonation at the two CO_2 concentrations. Some calcium hydroxide was found in the carbonated area, and C-S-H decomposed to a Ca-enriched silica gel (Ca/Si ≈ 0.5). The calcium hydroxide and carbonate contents were similar in both exposures. After further research using XRD, TGA and ^{29}Si NMR they confirmed that the carbonation products formed at 3% CO_2 were representative of the products formed at long term natural carbonation [5]. In agreement, Shah et al. using XRD, TGA and SEM-EDS point analysis found that the products formed at 60% RH and 3% CO_2 compared to products formed at natural carbonation [6]. No results on carbonation at relative humidity higher than 75% were found.

Table 1 presents the summary of pore solution investigations of carbonated cementitious materials found in the literature. For the studies reported in [7, 8], the pore solution was obtained by high pressure squeezing on moisturized samples. Carbonated concrete is usually dry and therefore pore solution squeezing by mechanical procedures requires that the samples are moisturized. The water added in the samples in [7, 8] was however not reported and the dilution was not taken into account when determining the pore solution composition. For the studies reported in [9, 10] cold water extraction (CWE), a rapid leaching method on ground mortar or concrete was used to study the pore solution composition.

All studies show that the amount of alkali metals (Na and K) in the carbonated pore solution is reduced compared to pore solution of non-carbonated samples [11]. Anstice et al. [7] found similar amounts of alkali metals in the pore solution of carbonated mortars (first carbonated and then moisturized) at different CO_2 concentrations while higher amounts of sulphates and chlorides were found in the samples exposed to 100% CO_2. Pu et al. [8] reported higher amounts of free alkali metals compared to [7]. The addition of fly ash reduces the amount of alkali metals in the pore solution in non-carbonated samples [11]. The studies reported in [9, 10] using CWE showed that the amount of free alkali metals in the pore solution of carbonated Portland cement was similar to the content in carbonated Portland-fly ash cement.

The current paper summarizes observations of the impact of different exposure conditions on the microstructure and phase assemblage of carbonated mortar and concrete. Various techniques were applied: SEM-EDS point analysis (chemical composition of the solid phases), optical microscopy (microstructure), cold water extraction (chemical composition of the pore solution), and thermogravimetric analysis (solid phases). The aim was to investigate the influence of the exposure conditions on the carbonation reaction products. The impact of the exposure condition was found to be minor compared to the changes upon carbonation.

Table 1: Summary of pore solution investigations in carbonated mortar and cement paste found in the literature. T is given in [°C], RH in [%] and CO_2 in [%]

Ref	Cement	*w/b*	Exposure			Technique	Composition				Unit
			T	RH	CO_2		Na	K	Cl	S	
[7]	CEM I	0.6	22	75[a]	100	Squeezed pore solution (300 MPa) + Ion chromatographic analysis	4	10	21	17	mmol/l
		0.6	22		5		4	9	13	20	
		0.6	22		0.03		3	15	4	1	
		0.6	22	65[b]	100		2	6	11	15	
		0.6	22		5		7	16	12	24	
		0.6	22		0.03		4	13	8	11	
		0.6	22	55[c]	100		5	11	23	18	
		0.6	22,		5		0	1	8	2	
		0.6	22		0.03		3	26	8	2	
		0.6	22	55[d]	100		10	17	23	20	
		0.6	22		5		1	1	11	7	
		0.6	22		0.03		1	1	9	5	
[8]	CEM I	0.5	20	40[e]	0	Squeezed pore solution (300 MPa) + pH meter	1.1	1020	-	-	mmol/l
		0.5	20	40[e]	5		0.2	190	-	-	
	CEM II/B-V (15% FA)	0.5	20	40[e]	0		0.9	580	-	-	
		0.5	20	40[e]	5		0.2	190	-	-	
[9]	CEM I	0.55	20	60[e]	0	CWE + ICP-MS	24	30	1	3	mmol/kg
		0.55	20	60	1		6	2	2	11	
		0.55	20	90[f]	0		26	30	0	1	
		0.55	20	90	5		10	10	8	1	
	CEM II/B-V (30% FA)	0.55	20	60[e]	0		17	23	1	1	
		0.55	20	60	1		5	2	2	12	
		0.55	20	90[f]	0		17	24	0	0	
		0.55	20	90	5		5	3	15	18	
[10]	CEM I	0.55	20	Sealed		CWE + ICP-MS	26	30	-	-	mmol/kg
	CEM I	0.55	20	60	1		4	2	-	-	
	CEM II/B-V (30% FA)	0.55	20	Sealed			18	22	-	-	
		0.55	20	60	1		3	1	-	-	
		0.40	20	60	1		3	1	-	-	

Salt solutions used to keep RH at a certain value: [a]: sodium chloride, [b]: ammonium nitrate, [c]: magnesium nitrate, [d]: sodium dichromate, [e]: sodium chloride, [f]: barium chloride

2. EXPERIMENTAL

The experimental investigation comprises three series of tests. The investigated materials and exposure conditions (including the used legends) are given in Table 2 and Table 3, respectively. The legends for the samples combine material and exposure, <% FA>-<% RH>-<% CO2>, e.g. 30-60-1 is a sample containing 30% fly ash which was exposed to 60% RH and 1% CO_2.

Table 2: Material and cement compositions investigated

Description		Cement type according to EN 197 [12] and fly ash content (FA)		
		CEM I (0% FA)	CEM II/B-M (18% FA)	CEM II/B-V (30% FA)
Series 1	Concrete prisms	x	x	x
Series 2	Mortar prisms			x
Series 3	Mortar disks	x		x

Table 3: Exposure conditions investigated (all 20°C except XC3)

	Non-carbonated			Carbonated			
	Sealed cured	Dried at 60%	Non-carb. sample	Natural XC3	60% RH, 1% CO_2	90% RH, 5% CO_2	60% RH, 100% CO_2
Legend	<%FA>-Sealed	<%FA>-60-0	<%FA>-Bulk	<%FA>-XC3	<%FA>-60-1	<%FA>-90-5	<%FA>-60-100
Series 1			x	x		x	
Series 2	x			x	x		
Series 3	x	x			x		x

2.1 Samples

Table 4 and Table 5 provide the chemical composition of the cements used.

Table 4: Chemical composition and fineness of the cements used in Series 1, as determined by XRF facilitated by NORCEM AS [% by mass]

Cement	% FA	SiO_2	Al_2O_3	Fe_2O_3	CaO	MgO	SO_3	P_2O_5	K_2O	Na_2O	Blaine [m^2/kg]
CEM I	0%	19.6	4.9	3.1	60.8	2.3	3.7	0.1	0.9	0.5	548
CEM II/B-M	18%	25.5	7.6	4.2	50.7	2.1	3.3	0.2	1.1	0.6	477
CEM II/B-V	30%	28.4	8.8	4.4	46.9	2.2	2.7	0.2	1.2	0.6	459

Table 5: Chemical composition and fineness of the cements used in Series 2 and Series 3, as determined by XRF facilitated by NORCEM AS [% by mass]

Cement	% FA	SiO_2	Al_2O_3	Fe_2O_3	CaO	MgO	SO_3	P_2O_5	K_2O	Na_2O	Blaine [m^2/kg]
CEM I	0%	20.4	4.8	3.4	61.7	2.2	3.5	0.2	0.9	0.5	420
CEM II/B-V	30%	29.5	10.8	4.5	44.6	2	3.2	0.4	1.1	0.5	501

For Series 1, concretes prism (120x150x260 mm) and wall elements (1200x1500x250) were cast at a concrete plant from concrete (*w/b*=0.55) containing three cements: CEM I (0% FA), CEM II/B-M (18% FA) or CEM II/B-V (30% FA). Further information on casting and compaction can be found in [13]. The concrete prisms were kept in the mould for three days and when demoulded

wrapped in plastic for 11 days. After this period, the prisms were exposed to accelerated carbonation for 20 weeks. The walls were exposed to natural carbonation in sheltered condition (XC3). Drilled cores with a diameter of 100 mm were investigated.

For Series 2, mortar prisms (140x40x160 mm) containing CEM II/B-V and having *w/b*=0.40 or 0.55 and paste-to-sand ratio (*p/s*) of 0.73 in volume were prepared. Further information on casting and compaction can be found in [10]. The mortars were cast in steel moulds and compacted using a vibrating table. Two 20-mm layers were compacted by applying 5 seconds of vibration for the *w/b*=0.55 and 10 seconds for the *w/b*=0.40 on each layer. After casting, the prism were covered with plastic for one day and subsequently stored sealed in plastic at 20 °C for 13 days. At the age of 14 days, the mortar prisms were exposed for 9 weeks to different conditions.

For Series 3, mortars (*w/b*=0.55) containing CEM I and CEM II/B-V were mixed and cast in polyethylene bottles 50 mm in diameter and 100 mm in height. Further information in casting and compaction can be found in [9]. Each bottle was filled in three layers and each layer jolt-compacted applying 30 strokes. The bottles were kept sealed at 20°C for two weeks and then wet-cut in disks of 15 mm in thickness using a saw. At the age of 14 days the disks were exposed to different carbonation conditions until they were fully carbonated. When the samples did not show any change in colour after spraying thymolphthalein on a freshly split sample they were classified as "fully carbonated". ¨

2.2 Methods

Table 6 provides an overview of methods applied and the types of samples used.

Carbonation depth was detected spraying a pH indicator (thymolphthalein, 1%) on a freshly split surface. For Series 1, carbonation depths were also determined on the thin sections using crossed polarized light.

Thin sections were prepared by the Danish Technological Institute according to NT Build 361 [14]. The concrete samples were impregnated with an epoxy resin containing fluorescent dye, mounted on a glass plate, ground to a thickness of 20 µm, and then covered with a glass. The thin sections were investigated with a Leica DM 2500P microscope using polarized, crossed polarized and fluorescent light.

Polished sections containing carbonated, transition zone, and non-carbonated concrete were prepared by the Danish Technological Institute according to [15]. The polished sections were investigated using scanning electron microscope Quanta 400 ESEM from FEI operated at high vacuum mode, accelerating voltage of 15 kV, spot size 5 and working distance of 10 mm were used. The specimens were carbon coated and the data was Proza corrected. The points were manually selected (typical 50 points in each zone) in the outer hydration products in carbonated and non-carbonated areas avoiding unreacted fly ash, clinker grains and aggregates. During SEM-EDS point analysis a volume of approx. 1 µm3 comprising a combination of different phases is analyzed.

Cold water extraction (CWE) was applied as described in [16] on homogenized ground powder. The powder was passed through 80 µm mesh sieve and mixed with deionized water and filtrated.

The filtrated solution was diluted and acidified. The composition of the filtrated solution was analysed using Inductively Coupled Plasma Mass Spectrometry (ICP-MS). The chemical composition of the pore solution was determined in mmol/kg of mortar.

Thermogravimetric analysis (TGA) was performed on homogenized ground powder using a Mettler Toledo TGA/DSC 3+. Aluminium oxide crucibles were loaded with ca. 300 mg of powder. The samples were heated from 40°C to 900°C at a rate of 10°C/min while the oven was purged with N_2 at 50 ml/min. The weight loss of the samples was monitored as a function of the temperature.

Table 6: Methods applied

Method		Carbonation depth	Microstructure	Solid phases		Pore solution
		pH indicator	Optical microscopy	SEM-EDS	TGA	CWE
Type of sample		Freshly split surface	Fluorescent thin section	Polished section	Powder	Powder
Series 1	Concrete prisms	x	x	x		x
Series 2	Mortar prisms	x				x
Series 3	Mortar disks	x			x	x

3. RESULTS

3.1 Microstructure

Table 7 presents a summary of the characteristics of the microstructure of the partly carbonated concrete samples investigated in Series 1. Micrographs illustrating the transition from carbonated (top) to non-carbonated (bottom) concrete are given in Figure 1. The micrographs were taken on a CEM II/B-V concrete sample exposed to 90% RH, 5% CO_2 using different light settings.

The carbonation depths determined by the pH indicator, and on the thin sections using crossed polarized light were comparable, taking into account the spatial variation of the carbonation depths [17], see Table 7.

When examining the surface in some of the samples a denser layer was observed. In other cases a slightly more open layer close to the surface was observed. It is not clear if these differences in microstructure were caused by carbonation or could be due to local inhomogeneities prior to carbonation. Areas of higher capillary porosity close to the exposed surfaces are often observed in field samples.

In order to investigate and compare the capillary porosity in carbonated and non-carbonated concrete, an image analysis system was used. This system uses the green tone intensity of the paste when illuminated in UV light as a measure of the capillary porosity. The lower the intensity the lower the capillary porosity, and vice versa. From the comparison, it was concluded that the variability of the microstructure due to local, initial defects was stronger than the potential changes in the microstructure caused by carbonation.

Other characteristics, which were investigated, were the presence of CH in the carbonated area or in the bulk, the width of the transition zone from carbonated to non-carbonated concrete, adhesion and surface cracks, and the air content.

A characteristic feature of the samples exposed to 90% and 5% CO_2 was a densification in front of the carbonation front. This issue should be investigated in more detail, potentially it is due to an accumulation of sulphates.

Overall, the microstructure of the carbonated concretes depended more on inhomogeneities prior to carbonation than on the exposure conditions.

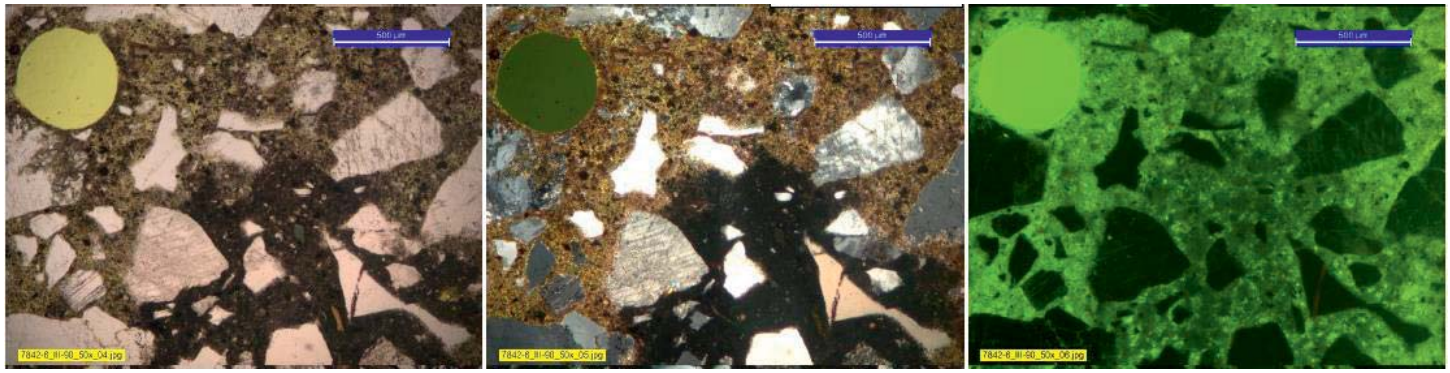

Figure 1: Micrographs illustrating transition from carbonated (top) to non-carbonated (bottom) in 30-90-5 (Series 1). Optical microscopy on fluorescence epoxy impregnated thin sections. From left to right: polarized, crossed polarized and fluorescent light

Table 7: Characteristics of the microstructure of carbonated and non-carbonated concrete (Series 1)

Label	x_c OM [mm]	x_c pH [mm]	Denser surface upon carb.	Higher porosity surface[1]	Capillary porosity (carb.) GT	Capillary porosity bulk (non-carb.) GT	Non-carb islands carb. zone	Adhesion cracks	Surf. cracks	Densification in front of the front	CH bulk	Air content	Transition zone [mm]
0-60-1	12	12-15	No	No	120	125	Yes	Yes	No	No	Yes	5-6%	1.2
18-60-1	12-14	17-20	Yes	No	100	115	Slight	No	No	No	No	Low	1.2
30-60-1	20-22	22-25	No	No	130	135	Slight	Yes	No	No	Yes	Low	0
0-90-5	4-14	5-17	No	Yes	100	120	Yes	Yes	Yes	Yes	Yes	5-6%	1
18-90-5	7-14	8-16	No	Yes	120	120	Slight	Yes	No	Yes	Yes	Low	1
30-90-5	11-15	6-20	No	Yes	130	110	Slight	No	No	Yes	Yes	Low	spotty
0-XC3	2-5	2.5-3	No	No	130	130	Yes	Yes	No	No	Yes	5-6%	0.8
18-XC3	2-5	3.5-5	No	Yes	138	120	Slight	No	No	Slight	Yes	None	0.8
30-XC3	4	2.5-4	No	No	132	120	Slight	No	No	No	No	Low	1

x_c: carbonation depth, OM: optical microscopy, pH: thymolphthalein, GT: green tone intensity rounded to nearest 5 (settings: 160x, Exp:12, gain: 0, gamma: 4, saturation: 200, N=10)

[1] Higher porosity in the samples prior to exposure

3.2 Solid phases

Figure 2 presents the differential weight loss curves of the investigated mortar disks. Table 8 presents the calculated amounts of CH and C$\underline{C}$ related to the weight at 850°C. Additionally, it includes the maximum theoretical amount of C$\underline{C}$, which can be formed upon carbonation if all the CaO available in the systems carbonates, and the degree of carbonation related to this maximum amount.

Even for the samples exposed to 100% CO_2, the calculated degree of carbonation was not 100%. This is probably due to incomplete carbonation of the clinker grains. When comparing the plain Portland cement (0%) samples, an increased amount of carbonates is formed at 100% CO_2 compared to 1% CO_2 which is reflected also in a relative increase in the degree of carbonation from around 70% to 90%. Compared to 1% CO_2 exposure, the 100% CO_2 exposure led to a reduction of the peak(s) in the temperature range 100-150°C corresponding to C-S-H, AFt, AFm and gypsum. Similar trends are observed for both cements.

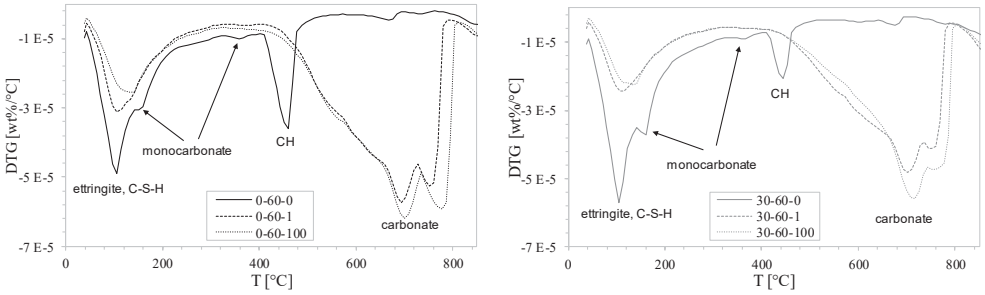

Figure 2: Differential weight loss (DTG) for mortar disks (Series 3) exposed to 0%, 1% and 100% CO2 and 60% RH after [9]

Table 8: Measured amounts of CH and CC [% of weight at 850°C] and calculated degree of carbonation (rounded to nearest 5) for mortar disks (Series 3) exposed to 0%, 1% and 100% CO_2 and 60% RH.

	CH [%]	C$\underline{C}$ [%]	C$\underline{C}$ [%] Theoretical fully carbonated	Degree of carbonation [%]
0-60-0	4.5	1	25	0
0-60-1	-	18		70
0-60-100	-	22		90
30-60-0	2	1	18	0
30-60-1	-	15		80
30-60-100	-	17		90

The chemical composition of the carbonation reaction products was investigated using SEM-EDS on the polished sections of carbonated and non-carbonated parts of the concrete samples (Series 1). This investigation is also reported in [18]. Figure 3 presents a summary of the data. SEM-EDS point analysis data are presented as Si/Ca versus Al/Ca molar ratios in order to identify phases. In a dot plot, a data point lays in between the ideal stoichiometry of the phases it comprises. The ideal composition of the following hydration phases are included: ettringite (AFt), monosulphate (AFm), and portlandite (CH), in addition calcium carbonate (C$\underline{C}$) is added.

The approximate C-S-H composition of the non-carbonated concretes with fly ash (Si/Ca=0.65) and without fly ash (Si/Ca=0.5) was determined. The Si/Ca decreased to 0.15-0.35 upon carbonation due to the fine intermixing of decalcified C-S-H with CC. Based on the results presented in Figure 3 no clear difference in the composition of the reaction products in the carbonated concretes for the tested cements and exposures conditions could be observed.

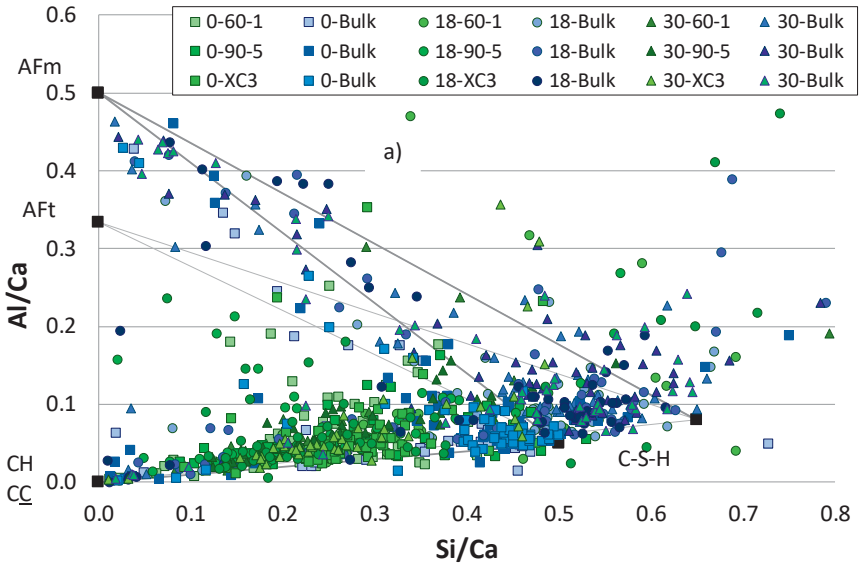

Figure 3: SEM-EDS point analysis data presented as Si/Ca versus Al/Ca molar ratios for carbonated and non-carbonated concrete samples (Series 1). Squares: CEM I (0% FA), circles: CEM II/B-M (18% FA), triangles: CEM II/B-V (30% FA). Green colours: carbonated, blue colours: non-carbonated. After [18]

3.3 Pore solution composition

Data for pore solution analysis of mortar samples from Series 2 are given in Figure 4. The results include data of the fully carbonated depths (according to the pH indicator) and sealed samples. The free alkali metal ion (Na and K) concentrations were lower in the carbonated samples compared to the sealed samples. The sodium and potassium concentrations in the carbonated mortars were not influence by the *w/b* (0.40 (30*-60-1) versus 0.55 (30-60-1)). In addition to the data given in Figure 4, the sodium and potassium concentrations of the samples exposed to natural carbonation were measured. These were found to be slightly higher (Na 7, and K 5 mmol/kg) than those of the same samples exposed to 60% RH and 1% CO_2 However, the measured higher free alkali metal contents in the samples exposed to natural carbonation could be due to contamination of the samples with non-carbonated material due to a limited carbonation depth, about 2 mm, after 9 weeks of exposure. Further analysis will be performed to verify these results.

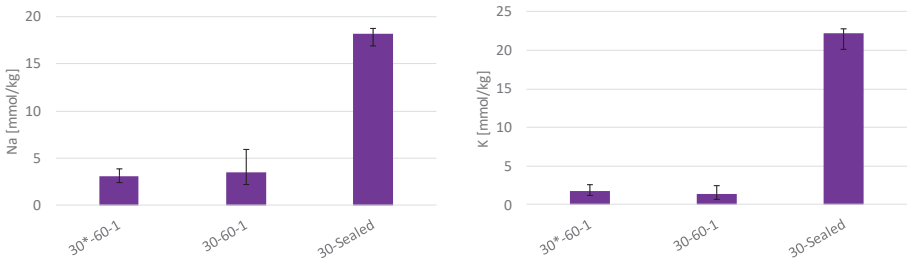

Figure 4: Free alkali metal (Na and K) content (mmol/kg of mortar) using CWE on mortar samples from Series 2. Solid bars (average) and error bars (range) of 3 measurements. Sample 30-60-1 has w/b=0.40 and 30-60-1 w/b=0.55. Partly after [10]*

Figure 5 presents the free alkali metals, sulphur and chlorine content of the mortar samples exposed to 1% and 100% CO_2 as well as sealed samples as a reference (Series 3). The pore solution composition obtained using CWE yielded a comparable sodium and potassium content in the carbonated mortars, irrespective of the cement composition and the exposure. Similar to observations for Series II (Figure 4), the free sodium and potassium content was significantly reduced by carbonation. The free sulphur and chlorine content were considerably higher in the carbonated mortars compared to the non-carbonated mortars. The free sulphur content in the carbonated mortars was comparable for the two cements but higher in the samples exposed to 100% CO_2 than in the samples exposed to 1% CO_2. The free chlorine content was, in contrast to expectations, slightly lower in the samples exposed to 100% CO_2 than the samples exposed to 1% CO_2.

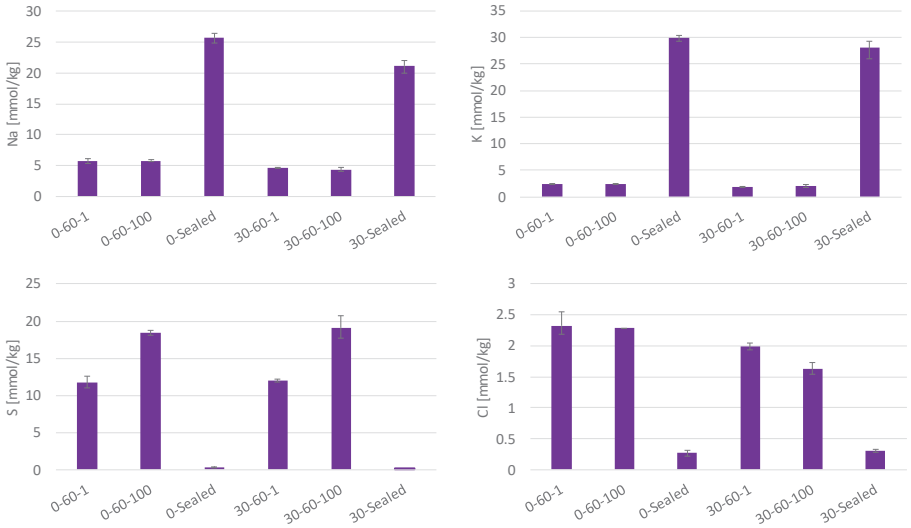

Figure 5: Free alkali metal (Na and K), sulphur (S) and chlorine (Cl) content (mmol/kg of mortar) using CWE on mortars from Series 3. Solid bars (average) and error bars (range) of 3 measurements. Partly after [9]

4. DISCUSSION

The pore solution composition and microstructure of concrete plays a decisive role on the propagation of reinforcement corrosion. The aim of the current paper was to investigate the influence of the accelerated exposure conditions on the microstructure and phase assemblage in carbonated concrete.

Petrographic analysis of thin sections revealed that the microstructure of the carbonated samples (natural carbonation (XC3), 60% RH and 1% CO_2, or 90% RH and 5% CO_2) depended more on local inhomogenities prior to carbonation than on the exposure condition or cement type.

TGA indicated that the solid phase assemblage of samples carbonated at 1% and 100% CO_2 (60% RH, 20°C) are comparable. However, the samples exposed to 100% CO_2 had a reduced peak(s) in the temperature range 100-150°C (corresponding to C-S-H, AFt, AFm and gypsum) and an increased peak in the carbonate range, indicating a higher degree of carbonation than the samples carbonated at 1% CO_2.

SEM-EDS point analysis showed that the composition of the outer reaction products formed upon carbonation were independent of the exposure condition (XC3, 60% RH and 1% CO_2, or 90% RH and 5% CO_2) and cement type (0-30% fly ash) tested.

The pore solution analysis of the carbonated samples showed that sodium and potassium are bound by the reaction products upon carbonation, while sulphate and chloride are released into the pore solution. Higher amounts of alkali were found in the naturally carbonated samples compared to samples exposed to 1% CO_2, but it is not clear whether this was due to either the exposure condition or intermixing of carbonated and non-carbonated material during the sampling. When comparing the influence of the exposure conditions, carbonation at 100% CO_2 led to a similar amount of free alkali metals as for 1% CO_2 exposure. The impact of accelerated carbonation on the free chlorine content was non-conclusive. For exposure to 100% CO2, higher amounts of sulphates were released into the pore solution compared to the 1% CO_2 exposure. This is in agreement with results by Anstice et al. [7]. The increased sulphur content in the pore solution upon carbonation suggests further carbonation of the cement hydration phases containing sulphate (e.g. AFm and AFt). TGA results support this showing higher amounts of carbonates formed at 100% CO2 compared to 1% CO_2 exposure and reduced peak(s) in the temperature range 100-150°C.

Table 9 presents a summary of the findings. The results are presented in three sets as the methods were only applied on a selection of the samples and exposure conditions. According to the literature [3-6], carbonation up to 3% CO_2 (RH<75%) is representative for natural carbonation (no data on carbonation above 75% RH was found). Based on our data, the range could be extended up to 5% CO_2. In agreement with literature reporting increased degree of carbonation at 10% and 100% CO_2 [3], we found slightly increased degree of carbonation of samples carbonated at 100% compared to samples carbonated at 1% CO_2.

Considering the impact of different exposure conditions, it should be noted that the influence of the exposure conditions was minor compared to the changes upon carbonation (from non-carbonated to carbonated condition).

Table 9: Summary of the of findings on the difference in microstructure and phase assemblage due to variation in exposure conditions

Exposure	Method	Findings
XC3 60% RH, 1% CO_2	Optical microscopy	• The microstructure of carbonated samples was similar regardless cement type and exposure condition.
90% RH, 5% CO_2	SEM-EDS	• The chemical composition of the outer reaction products was similar regardless type and exposure condition
60% RH, 1% CO_2 60% RH, 100% CO_2	CWE + ICP-MS	• The amount of free alkali metals (Na and K) upon carbonation was similar regardless the exposure condition and cement type • The amount of sulphates increased upon carbonation at 100% CO_2 compared to 1% CO_2 exposure • Data on chloride content are non-conclusive
	TGA	• Carbonation at 100% CO_2 slightly increased the amount of carbonates and reduced the phase in the 100-150 °C range compared to carbonation at 1% CO_2
XC3 60% RH, 1% CO_2	CWE + ICP-MS	• Non-conclusive; either due to the impact of the exposure or the limited carbonation of the naturally carbonated samples

5. CONCLUSIONS

The investigation of thin sections with optical microscopy showed that the microstructure of carbonated samples was similar regardless the cement type and the exposure conditions, i.e. natural (0.04%), 1% or 5% CO_2. Any observed variation in microstructure within the samples was attributed to local inhomogeneities prior to carbonation. The microstructure was not investigated for carbonation at 100% CO_2.

A similar chemical composition of the outer reaction products was observed using SEM-EDS point analysis for natural (0.04%), 1% or 5% CO_2 carbonated samples. The outer reaction products were not investigated for carbonation at 100% CO_2.

A similar decrease in the free alkali metal content was observed using cold water extraction on mortars with and without fly ash when carbonated at 1% and 100% CO_2. For both exposures, carbonation causes an increase in the content of sulphate and chloride ions in the pore solution. However, higher amounts of sulphates were present in the pore solution when the samples were exposed to 100% CO_2. This observation was supported by TGA, which indicated a slight decrease in the AFm and AFt phases and higher amount of calcium carbonate in the samples exposed to 100% CO_2. The data for the free chlorine content was non-conclusive. Pore solution analysis was non-conclusive for natural carbonation and was not investigated for 5% CO_2.

Carbonation up to 5% CO_2 appears representative for natural carbonation. An increased degree of carbonation and an increase in the free sulphur content were observed at 100% CO_2. It should be noted that the impact of the various exposure conditions was minor compared to the changes upon carbonation (from non-carbonated to carbonated condition).

ACKNOWLEDGEMENTS

The current investigation is part of a larger research project, 'Lavkarbsem' (NFR project no. 235211/O30). The project is supported by the Norwegian Research Council and the following companies: Mapei AS, Norbetong AS, Norcem AS, Skanska AS, and Rambøll Engineering AS. The authors would like to thank Gilles Plusquellec and Simon Langedal for their work, which made possible to prepare this summary paper.

REFERENCES

1. L. Bertolini, B. Elsener, P. Pedeferri, E. Redaelli, R. Polder, Chapter 5: Carbonation-induced corrosion, in: Corrosion of Steel in Concrete, Wiley-VCH Verlag GmbH & Co, Weinheim, Germany, 2013, pp. 79-91.
2. T.A. Harrison, M.R. Jones, M.D. Newlands, S. Kandasami, G. Khanna, Experience of using the prTS 12390-12 accelerated carbonation test to assess the relative performance of concrete, Magazine of Concrete Research, 64 (2012) 737-747.
3. M. Castellote, L. Fernandez, C. Andrade, C. Alonso, Chemical changes and phase analysis of OPC pastes carbonated at different CO2 concentrations, Materials and Structures, 42 (2009) 515-525.
4. M. Auroy, S. Poyet, L.B. P., J.-M. Torrenti, T. Charpentier, M. Moskura, X. Bourbon, Representativeness of accelerated carbonation testing of cement pastes, in: N.c. federation (Ed.) XXII Nordic concrete research symposia, Norsk betongforening, Reykjavik, Iceland, 2014.
5. M. Auroy, S. Poyet, P. Le Bescop, J.-M. Torrenti, T. Charpentier, M. Moskura, X. Bourbon, Comparison between natural and accelerated carbonation (3% CO2): Impact on mineralogy, microstructure, water retention and cracking, Cement and Concrete Research, 109 (2018) 64-80.
6. V. Shah, K. Scrivener, B. Bhattacharjee, S. Bishnoi, Changes in microstructure characteristics of cement paste on carbonation, Cement and Concrete Research, 109 (2018) 184-197.
7. D.J. Anstice, C.L. Page, M.M. Page, The pore solution phase of carbonated cement pastes, Cement and Concrete Research, 35 (2005) 377-383.
8. Q. Pu, L. Jiang, J. Xu, H. Chu, Y. Xu, Y. Zhang, Evolution of pH and chemical composition of pore solution in carbonated concrete, Construction and Building Materials, 28 (2012) 519-524.
9. S.L. Langedal, Investigation of resistivity, porosity and pore solution composition in carbonated mortar prepared with ordinary Portland cement and Portland-fly ash cement, in: Department of Structural Engineering, Norwegian University of Science and Technology, Trondheim, 2018, pp. 96.
10. K. De Weerdt, G. Plusquellec, A. Belda Revert, M.R. Geiker, B. Lothenbach, Effect of carbonation on the pore solution of mortar, In preparation, (2018).
11. A. Vollpracht, B. Lothenbach, R. Snellings, J. Haufe, The pore solution of blended cements: a review, Materials and Structures, (2015) 1-27.
12. EN-197-1, EN 197-1 Cement - Part 1: Composition, specifications and conformity criteria for common cements, in, 2011.
13. A. Belda Revert, K. Hornbostel, K. De Weerdt, M.R. Geiker, Macrocell corrosion in carbonated Portland and Portland-fly ash concrete - contribution and mechanism, Submitted to Cement and Concrete Research, (2018).

14. Nordtest, Concrete, hardened: Water-cement ratio - NT Build 361, in, 1991.
15. R.J. Detwiler, L.J. Powers, U.H. Jakobsen, W.U. Ahmed, K. Scrivener, K.O. Kjellsen, Preparing Specimens for Microscopy, Concrete International, (2001).
16. G. Plusquellec, M.R. Geiker, J. Lindgård, J. Duchesne, B. Fournier, K. De Weerdt, Determination of the pH and the free alkali metal content in the pore solution of concrete: Review and experimental comparison, Cement and Concrete Research, 96 (2017) 13-26.
17. A. Belda Revert, K. De Weerdt, K. Hornbostel, M. Geiker, Carbonation Characterization of Mortar with Portland Cement and Fly Ash, Comparison of Techniques Nordic Concrete Research, (2016) 60-76.
18. A. Belda Revert, K. De Weerdt, M.R. Geiker, U.H. Jakobsen, SEM-EDS analysis of products formed under natural and accelerated carbonation of concrete with CEM I, CEM II/B-M and CEM II/B-V in: XXIIIth Symposium on Nordic Concrete Research & Developement, Aalborg, Denmark, 2017.

Paper S-VI

Determination of the polarization resistance of steel in carbonated fly-ash concrete-effect of measurement technique

Revert, Andres Belda; Hornbostel, Karla; De Weerdt, Klaartje; Geiker, Mette Rica

Proceedings EUROCORR 2017, Prague, Czech Republic (2017)

Determination of the polarization resistance of steel in carbonated fly-ash concrete- effect of measurement technique

Belda Revert Andres[1], Hornbostel Karla[2], De Weerdt Klaartje [1], Geiker Mette[1]

[1]Norwegian University of Science and Technology (NTNU), Trondheim, Norway, andres.b.revert@ntnu.no
[2] Norwegian Public Road Administration, Trondheim, Norway

Abstract
The polarization resistance (R_p) of a metal gives an indication of the corrosion condition at a given time. The R_p of embedded reinforcement in concrete is usually determined using the linear polarization resistance or the galvanostatic pulse technique. The relatively high electrical resistivity of concrete is a challenging factor when determining R_p. The electrical resistance becomes higher when adding supplementary cementitious materials to Portland cement or upon carbonation. Reinforced concrete prisms with 16-mm carbon steel reinforcement and concrete cover 20 mm were prepared using Portland-fly ash cement. The prisms were sealed-cured for two weeks and subsequently completely carbonated. The R_p of the reinforcement was determined using the linear polarization resistance and galvanostatic pulse techniques, and electrochemical impedance spectroscopy. The possible influence of using an embedded or an external reference electrode was investigated. Overall, comparable R_p values were determined with the three investigated techniques using either the external or the embedded reference electrode.

Keywords
Carbonation-induced corrosion, Portland-fly ash concrete, Linear polarization resistance, Galvanostatic pulse, AC electrochemical impedance spectroscopy

Introduction

When performing electrochemical measurements, there is a potential drop between the elements in the cell due to the resistivity of the electrolyte (ohmic drop). When testing steel in electrolytes, the test solution can be changed in order to lower the resistivity. However, when testing steel embedded in concrete the resistivity is a material property which cannot be modified. The addition of supplementary cementitious materials to Portland cement makes this point even more challenging due to an increased concrete resistivity. Reported values vary from a factor of two to an order of magnitude compared to Portland cement depending on the type of addition and amount, and additionally, carbonation leads to even higher electrical resistivity compared to non-carbonated concrete [1].

For steel in solution, Oelßner et al. discussed the possibilities for compensation of the ohmic drop using a corrosion test cell where the reference electrode (RE) is in contact with the working electrode (WE) via a Lugging capillary and the counter electrode (CE) is directly immersed in the test solution [2]. The corrosion cell for steel embedded in concrete differs from this. The reference electrode is usually applied on the external concrete surface (the distance between the WE and RE is the concrete cover) but embeddable reference electrodes are also available. The counter electrode is usually an external electrode placed on the concrete surface but also embedded electrodes can be used. Figure 1 represents a corrosion equivalent circuit describing this three-probe arrangement. When performing an electrochemical measurement the open circuit potential is monitored between the RE and WE while a current or potential difference is applied between the CE and WE. Figure 1 includes the following idealized electronic components: R_c, resistance of the concrete between CE and the RE, and R_Ω, resistance of the concrete between the RE and the WE. The potential is measured between the RE and the WE, thus the resistance between the RE and the WE is the one to be considered. R_Ω can be reduced by placing the RE close to the WE, however if the RE is placed too close to the WE the current density distribution is disturbed [2]. Figure 1 does not include the WE response, which varies depending on the applied electrochemical technique.

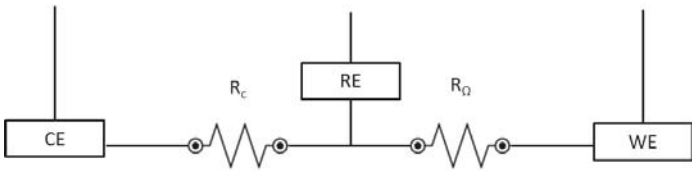

Figure 1: Equivalent circuit for three-probe corrosion cell of reinforcement embedded in concrete. CE: counter electrode, RE: reference electrode, WE: working electrode, Rc: concrete resistance between CE and RE, R_Ω: concrete resistance between RE and WE

Polarization resistance measurements allow to investigate the response of the embedded steel when the potential is changed from the open circuit potential. The potential can be changed by applying an external potential difference (potentiostatic, e.g. linear polarization resistance technique (LPR)) or applying an external current (galvanostatic, e.g. galvanostatic pulse technique (GVP)). If both anodic and cathodic reactions are activation-controlled, a linear relationship between current density and potential is observed close to the corrosion potential [3]. The LPR has been widely used in reinforced concrete, it allows to investigate the instantaneous polarization resistance of embedded steel (R_p) by polarizing potentiostatically the steel in the range of 10-25 mV in both anodic and cathodic directions [4]. Andrade et al. found good agreement comparing corrosion rate estimated from LPR and the actual reinforcement gravimetric loss [5]. Glass et al. discussed the applicability of polarization resistance for corrosion measurements in carbonated concrete and concluded that LPR is

suitable, even if the anodic reaction is not activation-controlled [6]. The treatment of the data is straightforward to determine the R_p, it is the slope of the potential-current response. However, the R_p determination using LPR is highly dependent on the ohmic drop compensation, as both the response from the reinforcement and the concrete contribution (R_Ω) are included in the response. GVP consists of galvanostatically polarizing the embedded steel in a small range by forcing a current (μA) and recording the response, e.g. Glass et al. proposed a polarization range of 15 mV [7]. The R_Ω and R_p can be determined by fitting the response to an equivalent circuit which includes a resistor (R_Ω) connected in series with a capacitator and resistor (R_p) in parallel [4]. AC electrochemical impedance spectroscopy (EIS) allows to investigate the response of the concrete-reinforcement system when applying a sinusoidal alternating potential signal, e.g. 10 mV. Depending on the frequency, different regions can be investigated: the bulk (concrete) in the high frequency range, and the electrode (reinforcement) in the low frequency range [8]. The response might be complex and fitting an equivalent circuit may be challenging, and even if the circuit fits the response the elements might not have any physical meaning [9]. There are investigations on the influence of the measuring technique on the corrosion rate determination of embedded steel in concrete, [10, 11, 12], see the Discussion section for further details. However, these investigations were performed on chloride-contaminated samples. No quantitative comparison for carbonation-induced corrosion has been found.

The purpose of this study is to compare the polarization resistance of reinforcement embedded in carbonated concrete determined by the linear polarization resistance and galvanostatic pulse techniques, and electrochemical impedance spectroscopy using either an embedded or an external reference electrode. Comparable polarization resistance values were obtained with the three investigated techniques using either the external or the embedded reference electrode.

Experimental

Materials and samples

Figure 2 presents a sketch of the investigated samples. Concrete was prepared with water-to-cement ratio 0.55 containing Portland-fly ash cement (30% fly ash) and maximum aggregate size 16 mm. The reinforcement was ribbed carbon steel diameter 16 mm. The steel was cut in 260-mm pieces, cleaned with acetone, and 50 mm of both ends were coated with bee wax. The concrete was mixed and cast at a Norwegian precast plant. The samples were sealed cured for two weeks, cut in two halves and fully carbonated. Each half (S-1 and S-2) has an approximate thickness of 55 mm, which gave an approximate concrete cover of 20 mm on both sides. The carbonated samples were immersed in tap water and a pseudo-reference electrode (25-mm piece of mixed metal oxide titanium (Ti), 1 mm in diameter) was embedded by drilling a hole and applying grout. Once the change in weight in immersed conditions was considered negligible (<0.003% per 24 hours, obtained after two weeks of immersion, "capillary saturated conditions"), the electrochemical measurements were performed. Further details on the samples are given in [13].

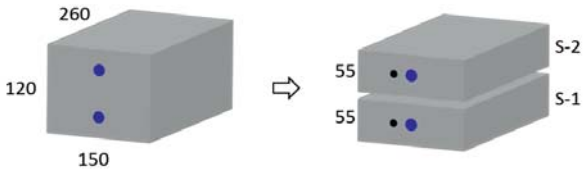

Figure 2: Overview of sample prepraration. Blue: reinforcement (Ø 16 mm), black: embedded Ti RE (Ø 1 mm). Dimensions in mm

Methods

The electrochemical techniques were performed using a potentiostat PARSTAT 2273 with a three-probe corrosion cell which consisted of a working electrode (WE, reinforcement), counter electrode (CE, external titanium mesh (diamond opening 3.5 x 6 mm, thickness 0.7 mm)) and reference electrode (RE) as depicted in Figure 3. Two reference electrodes were used, an external saturated calomel (SCE, XR 150 from Nerliens Meszansky) placed on the concrete surface and an embedded pseudo-reference electrode (Ti) embedded at 10 mm from the reinforcement. The measurements were performed on the samples immersed in a water bath.

Linear polarization resistance (LPR) measurements were performed by polarizing the reinforcement 10 mV in both anodic and cathodic directions (polarization range 20 mV), at a rate of 0.167mV/s and step height 0.1 mV. Two alternatives were used, LPR using automatic compensation (current-interruption method), and LPR without compensation. Galvanostatic pulse (GVP) measurements were performed supplying a current of 50 µA during 30 seconds, which polarized the reinforcement approximately 10 mV in the anodic direction. AC electrochemical impedance spectroscopy (EIS) was applied using a sinusoidal wave of 10 mV and a frequency range of 500 kHz to 4 mHz.

Figure 4 illustrates the schematic response of each technique and the determination of the resistance values, polarization resistance of reinforcement (R_p) and ohmic drop (R_Ω):

- LPR with automatic compensation (LPR-C): The slope of the response is the R_p.
- LPR without compensation (LPR-NC): The slope of the response is the R_T ($R_p + R_\Omega$). The R_Ω is determined from the other techniques (average value from GVP and EIS).
- GVP: The R_p and the R_Ω were obtained from the instantaneous potential drop and following potential transient, respectively, by fitting the response to an equivalent circuit.
- EIS: In the range of high to low frequencies (Nyquist plot) the point with the lowest phase angle is attributed to R_Ω. In the range of low frequencies, the response is broken down into a semicircle plus a line and the diameter of the semicircle is attributed to the R_p.

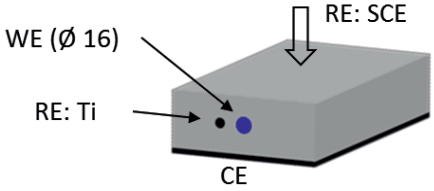

Figure 3: Investigated three-probe corrosion cell

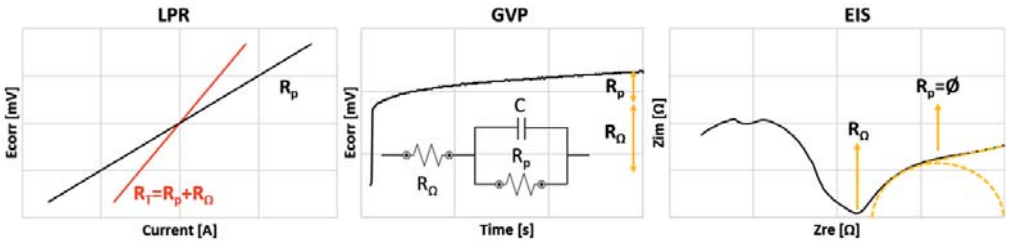

Figure 4: Schematic response of each of the electrochemical test and determination of parameters (R_p and R_Ω). LPR (red LPR-NC, and black LPR-C), GVP including equivalent circuit, and EIS indicating lowest phase angle and diameter of the fitted circle

Results

Figure 5, Figure 6 and Figure 7 present the results of the electrochemical measurements performed using either the embedded or the external reference electrode. Note that the axes have been adjusted for each sample to better illustrate the response.

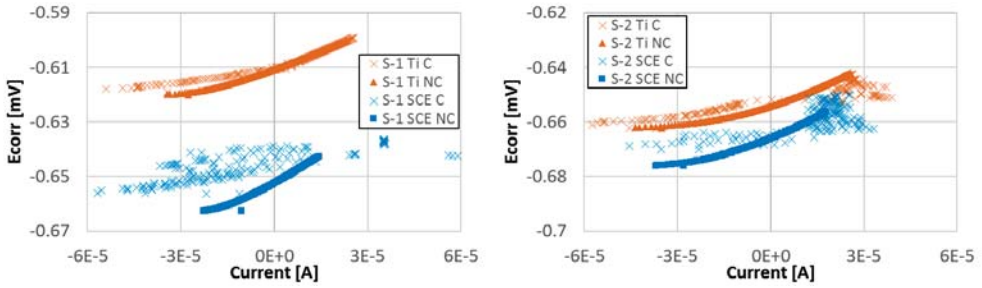

Figure 5: Results of LPR measurements with automatic compensation (C) and without compensation (NC) using embedded (Ti) and external (SCE) RE. Note adjusted axes

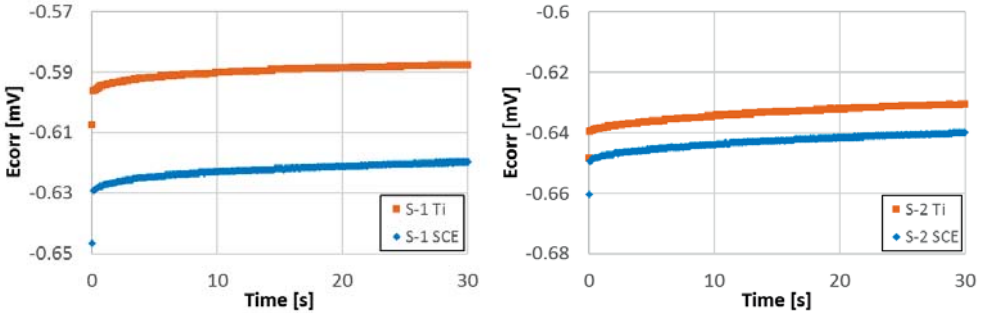

Figure 6: Results of GVP measurements using embedded (Ti) and external (SCE) RE. Note adjusted axes

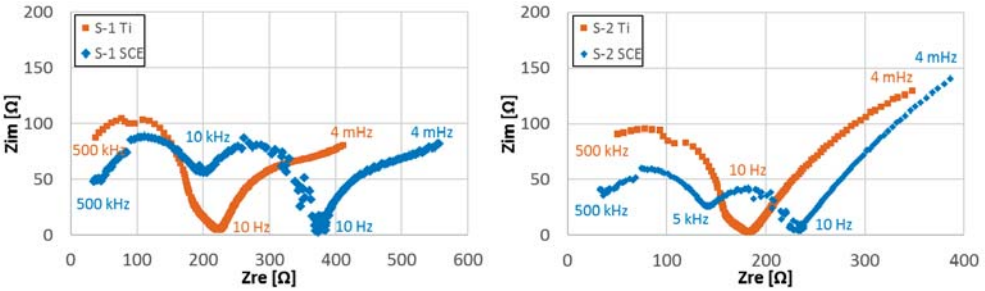

Figure 7: Results of EIS measurements. Nyquist plots using embedded (Ti) and external (SCE) RE. Frequencies of interest are indicted (max., min. and transition points). Note adjusted axes

Discussion

Sample 1 and 2 showed similar response when LPR and GVP were performed, and the Nyquist plots of the EIS data were comparable in the high frequency range. However, the response in the low frequency range differed. The Table 2 presents a summary of the resistance values determined with the three techniques using either the embedded or the external RE. When performing LPR with automatic compensation, the data was scattered and

the polarization resistance was not considered reliable. The R_p determined using LPR-NC was obtained by subtracting the average R_Ω determined with GVP and EIS from the R_T.

Table 1: Summary of the obtained resistance values. Shaded cells indicate that these values were obtained assuming average R_Ω determined from GVP and EIS. Figure 2 illustrates nomenclature used

		Ti	SCE	Ti	SCE	Ti	SCE
		R_T [Ω]		R_Ω [Ω]		R_p [Ω]	
LPR-NC	S-1	420	590	-	-	180	210
	S-2	360	400	-	-	180	170
GVP	S-1			250	380	150	170
	S-2			190	240	200	190
EIS	S-1			230	380	240	270
	S-2			180	230	-	-

Techniques for measuring corrosion rate in carbonated concrete

The LPR without compensation resulted in a linear potential-current relationship. This relationship includes both the R_p and the R_Ω. We have assumed that the resistance of concrete does not change during the test. A limitation of this approach is that the R_Ω could not be constant during the LPR test e.g. due to different polarization of the concrete during the varying DC current which is registered through the LPR test. However, as a linear potential-current relationship was observed when not compensating for the R_Ω, and a linear relationship is expected between the "true" potential and current, it indicates that the R_Ω is constant. The LPR test took 2 minutes with the used parameters, and the slope of the response was easily obtained from the raw data.

GVP gives both information on the R_Ω and the R_p in a relative short time. However, the data has to be treated in a more complex way compared to LPR and an equivalent circuit is assumed. The parameters which polarize the reinforcement in the desired range cannot be known in advance and "trial-error" is required until the proper polarization range is obtained. For this corrosion cell and concrete condition, the application of 50 µA during 30 seconds led to a polarization of the reinforcement in the range of 10 mV.

EIS is a time consuming technique, for the investigated conditions each measurement took approximately 90 minutes. The interpretation of the data is even more complex compared to the GVP technique and it is challenging to fit an equivalent circuit to the response. The response from S-1 was treated to determine the R_p by breaking down the data into a semicircle plus a line in the low frequency range as described in [8]. However, it was not possible to determine R_p in S-2.

The R_p values obtained using LPR and GVP are comparable without systematic under or overestimation (between 10 to 25 % compared to LPR). The R_p values determined from EIS are 25 % higher compared to LPR. Nygaard and Geiker investigated the influence of polarization current and time using GVP in chloride contaminated samples [11]. They concluded that polarization times from 20 to 50 s gave comparable R_p values to LPR, but always on the lower side. In this investigation we used GVP with polarization time 30 s. Andrade et al. aimed at comparing the R_p values obtained with LPR and EIS on not-corroding, chloride contaminated and carbonated samples [10]. However, the EIS Nyquist plot of the carbonated samples did not show a semicircle and the R_p value could not be determined. Videm compared R_p determined on chloride contaminated samples using LPR,

GVP and EIS measurements among other techniques [12]. He did not find good agreement when comparing them and concluded that was because part of the current sent during the electrochemical test is consumed by other processes apart from the corrosion reaction, e.g. corrosion product changing from ferric to ferrous state.

Ohmic drop determination

The automatic R_Ω compensation feature for LPR measurement using our equipment did not seem to work for the two corrosion cells investigated. The data was scattered and did not show the expected potential-current linear relationship (not possible to fit a line). According to the user manual, the automatic R_Ω compensation is performed by the current-interruption method. A short current interruption is applied at the end of each measuring step and the potential drop during this interruption is assumed to be related to the resistance of the electrolyte.

The R_Ω obtained by GVP and EIS were comparable. However, EIS gives information on the dielectric properties of concrete, which is not only showing pure resistance behaviour but also including some capacitance in the high frequency range.

Location of RE

The R_Ω values obtained using the external RE are higher compared to the embedded RE. This is in agreement with expectations as the embedded RE is separated 10 mm from the WE while the external RE is separated 20 mm. The R_p values obtained with each of the two RE are comparable, the difference for each measurement is smaller than 15 % and there was no systematic trend.

EIS response: Nyquist plot

The recorded response using the embedded RE shows two arcs (time constants), one attributed to the bulk (high frequency range) and the other to the corrosion process (low frequency range) while the response using the external RE includes an additional time constant in the high frequency range. According to [14], the two first arcs observed at high frequency using the external RE are related to percolating and closed porosity. However, they should have been observed using both the external and the embedded RE. Newton and Sykes observed three arcs when investing chloride contaminated mortar samples and proposed an equivalent circuit with three time constants for corroding reinforcement embedded in concrete using an external RE which compares to the response we have recorded using the external RE [15].

McCarter et al. reported that when using fly ash in concrete, a plateau is observed between the response of the bulk and the response of the electrode in the Nyquist plot, and the higher the fly ash replacement the larger the extension of the plateau [16]. We have not observed a plateau, but a line with negative slope between the response of the bulk and the response of the electrode. Koleva et al. observed a plateau between the response of the bulk and the electrode in chloride contaminated samples and concluded that the plateau was due to a change of the pore wall surface in the chloride contaminated samples compared to the reference samples without chlorides [17]. The observed plateau influences on the determination of the R_Ω if a circle is fitted or the lowest phase angle is chosen. In this investigation we have found a good agreement comparing the R_Ω determined using GVP and EIS (lowest phase angle point, in all the cases the phase angle was < 2 °).

Possible field limitations

The measurements were performed on samples which contained one piece of reinforcement. The samples were fully carbonated and capillary saturated before the electrochemical tests were performed. If one assumes that the reinforcement corrodes uniformly along the entire area, only microcell corrosion and uniform field distribution when performing the electrochemical tests are expected.

Field measurements, on the other hand, are affected by additional factors. Factors which might pay a decisive role for the R_p determination on structures are e.g. varying current confinement, uncertain area of reinforcement which is polarized or galvanic macro couples.

Conclusion

The polarization resistance of reinforcement embedded in carbonated, capillary saturated concrete was determined by three different methods (LPR, GVP and EIS). A three-cell probe corrosion arrangement was used which consisted of a working electrode (reinforcement), an external counter electrode (titanium mesh), and either an embedded pseudo-reference electrode (Ti) or an external saturated calomel reference electrode (SCE). The determined polarization resistance for the three methods was comparable (factor of 0.75 to 1.25 compared to LPR). The automatic compensation feature for LPR measurement of the potentiostat used in this study was found not suitable, and LPR without compensation requires knowledge on the ohmic drop. EIS resulted in slightly higher R_p compared to LPR which may be related to the fitting of the data. GVP was found the most suitable technique as it can be executed in a short time and gives separate information about the ohmic drop and the polarization resistance. The location of the reference electrode only influenced the ohmic drop, comparable polarization resistance was determined for both arrangements (external and embedded RE) using the three methods applied.

The measurements were performed on samples with well-defined geometry and fixed counter electrode to working electrode ratio. However, for field measurements additional factors could influence the determination of R_p, e.g. macrocell effects or insufficient current confinement.

Aknowledgements

The data was obtained using samples prepared in collaboration with POLIMI. The NTNU PhD study is part of “Lavkarbsem” project (NFR project no. 235211/O30), which is supported by the Norwegian Research Council and the following companies, Mapei AS, Norbetong AS, Norcem AS, Skanska AS, and Rambøll Engineering AS.

References

1. R. B. Polder, "Test methods for on site measurement of resistivity of concrete — a RILEM TC-154 technical recommendation," Construction and Building Materials, vol. 15, pp. 125-131, 2001.
2. W. Oelßner, F. Berthold, and U. Guth, "The iR drop – well-known but often underestimated in electrochemical polarization measurements and corrosion testing," Materials and Corrosion, vol. 57, no. 6, pp. 455-466, 2006.
3. M. Stern and A. L. Geary, "Theoretical Analysis of the Shape of Polarization Curves," Journal of the Electrochemical Society, vol. 104, p. 7, 1957.
4. C. Andrade and C. Alonso, "Test methods for on-site corrosion rate measurement of steel reinforcement in concrete by means of the polarization resistance method," Materials and Structures, vol. 37, no. 9, pp. 623-643, 2004.

5. C. Andrade and J. A. González, "Quantitative measurements of corrosion rate of reinforcing steels embedded in concrete using polarization resistance measurements," Materials and Corrosion, vol. 29, no. 8, pp. 515-519, 1978.
6. G. K. Glass, C. L. Page, and N. R. Short, "Factors affecting the corrosion rate of steel in carbonated mortars," Corrosion Science, vol. 32, no. 12, pp. 1283-1294, 1991.
7. G. K. Glass, C. L. Page, N. R. Short, and S. W. Yu, "An investigation of galvanostatic transient methods used to monitor the corrosion rate of steel in concrete," Corrosion Science, vol. 35, no. 5, pp. 1585-1592, 1993.
8. D. A. Jones, Principles and prevention of corrosion. Pearson Education, 1991.
9. D. A. Koleva, K. van Breugel, J. H. W. de Wit, E. Van Westing, N. Boshkov, and A. L. A. Fraaij, "Electrochemical Behavior, Microstructural Analysis, and Morphological Observations in Reinforced Mortar Subjected to Chloride Ingress," Journal of The Electrochemical Society, vol. 154, no. 3, pp. 45-56, 2007.
10. C. Andrade, V. Castelo, C. Alonso, and J. González, "The Determination of the Corrosion Rate of Steel Embedded in Concrete by the Polarization Resistance and AC Impedance Methods," ASTM International, p. 20, 1986.
11. P. V. Nygaard and M. R. Geiker, "Measuring the corrosion rate of steel in concrete – effect of measurement technique, polarisation time and current," Materials and Corrosion, vol. 63, no. 3, pp. 200-214, 2012.
12. K. Videm, "Phenomena disturbing electrochemical corrosion rate measurements for steel in alkaline environments," Electrochimica Acta, vol. 46, no. 24, pp. 3895-3903, 2001.
13. M. Messina, A. Belda Revert, M. Gastaldi, and M. R. Geiker, "Joint investigation on the relationship between corrosion rate and resistivity in carbonated concrete," In preparation.
14. J. M. Deus, B. Díaz, L. Freire, and X. R. Nóvoa, "The electrochemical behaviour of steel rebars in concrete: an Electrochemical Impedance Spectroscopy study of the effect of temperature," Electrochimica Acta, vol. 131, pp. 106-115, 2014.
15. C. J. Newton and J. M. Sykes, "A galvanostatic pulse technique for investigation of steel corrosion in concrete," Corrosion Science, vol. 28, no. 11, pp. 1051-1074, 1988/01/01/ 1988.
16. W. J. McCarter, G. Starrs, and T. M. Chrisp, "The complex impedance response of fly-ash cements revisited," Cement and Concrete Research, vol. 34, no. 10, pp. 1837-1843, 2004.
17. D. A. Koleva et al., "Correlation of microstructure, electrical properties and electrochemical phenomena in reinforced mortar. Breakdown to multi-phase interface structures. Part II: Pore network, electrical properties and electrochemical response," Materials Characterization, vol. 59, no. 6, pp. 801-815, 2008.

Paper S-VII

Karbonatisering av miljøvennlig betong

Revert, Andres Belda; De Weerdt, Klaartje; Hornbostel, Karla; Geiker, Mette Rica

Byggeindustrien (7), page 47, 2016

NYTT FRA NTNU

Karbonatisering av miljøvennlig betong

En ulempe med miljøvennlig betong er redusert motstand mot karbonatisering og dermed økt fare for armeringskorrosjon. I prosjektet LAVKARBSEM er målet å bidra til en bærekraftig anvendelse av miljøvennlige sementer i betongkonstruksjoner utsatt for karbonatisering.

Andres Belda Revert, Klaartje De Weerdt, Karla Hornbostel, Mette R Geiker

Inst. for konstruksjonsteknikk

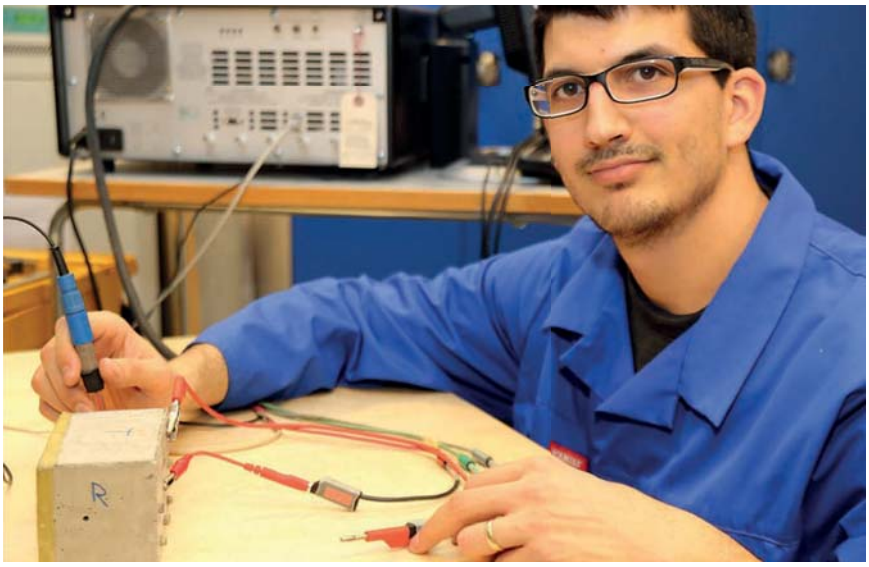

PhD kandidat Andres Belda Revert undersøker korrosjon av stålarmeringen i karbonatisert mørtel ved hjelp av elektrokjemiske teknikker. Foto: Giedrius Zirgulis

Norcem AS jobber kontinuerlig med utvikling av nye, mer miljøvennlige sementer for det norske markedet. Sementindustrien står for 5-8% av menneskeligskapt CO2. En av måtene som er brukt for å redusere CO2-utslippet i sementproduksjon på, er å øke erstatningen av den vanlige Portland sementen med andre mineralske stoffer som for eksempel flygeaske. Flygeaske er et biprodukt fra kullfyrte kraftverk, men denne erstatningen har vist seg å redusere motstanden mot karbonatisering av betongen. Dette gjelder spesielt for betong brukt i fasader, balkonger og andre bygningsdeler som er særlig utsatt for karbonatisering.

Karbonatisering

Karbonatisering er en prosess der CO2 fra atmosfæren trenger inn i betongen, og binder seg opp i sementpastaen. Dette har som følge at pH-en i selve betongen som opprinnelig er rundt 13, går ned til mellom 8 og 9. Ved den opprinnelige høye pH-en er stålarmering inni betongen beskyttet mot korrosjon, men denne beskyttelsen forsvinner når pH-en synker til pH 9 og lavere. Armeringen i en karbonatisert betong kan altså korrodere. Dette vil føre til riss og avskalling av betong og reduksjon i armeringstverrsnitt, som over tid kan sette bæreevnen til konstruksjonen i faren.

Forskning

LAVKARBSEM prosjektet (NFR prosjekt no. 235211/O30) er støttet av Norges Forskningsrådet og prosjektpartnere er: Norcem AS, NTNU, SINTEF, Skanska Norge AS, Mapei, Rambøll, Norbetong, og HeidelbergCement Technology Center. Målet for prosjektet er å oppnå en bedre forståelse av hvilke faktorer som påvirker karbonatisering av betong og karbonatiseringsindusert armeringskorrosjon. Forståelsen vil danne bakgrunn for bærekraftig anvendelse av miljøvennlige sementer.

Innenfor LAVKARBSEM prosjektet vil vi fokusere på å øke tiden det tar før karbonatiseringsfronten når stålarmeringen. Sentralt i prosjektet er PhD kandidat Andres Belda Revert som ved hjelp av elektrokjemiske teknikker karakteriserer korrosjonen av armeringen i karbonatisert betong. Prof. Mette R Geiker er hovedveileder, og førsteamanuensis Klaartje De Weerdt og post doc Karla Hornbostel er medveiledere.

Bruk tymolftalein til å måle karbonatisering

Andres har i innledende forsøk sett nærmere på bestemmelsen av karbonatiseringsfronten. Karbonatiseringsfronten blir vanligvis bestemt ved å spraye en fersk splittet betongoverflate med en pH indikator. Typisk blir en 0.1% fenolftaleine løsning brukt, men fenolftalein er klassifisert som helsefarlig av Miljødirektoratet, og bruken av dette produktet bør unngås. Andres har bekreftet at 1% tymolftalein løsning er like bra til å identifisere karbonatiseringsfronten på mørtel. Resultatet er bekreftet gjennom parallellprøving utført av SINTEF. Tymolftalein (1%) som ikke er klassifisert som helsefarlig burde dermed både i regelverket og praksis erstatte det helsefarlige fenolftaleinet (0.1%).

Måle korrosjonshastighet

Neste fase i prosjektet er nå i gang. Anders ser nå nærmere på korrosjonshastigheten av stålarmeringen i karbonatisert betong ved hjelp av elektrokjemiske teknikker.

Sammenligning av 1 prosent fenolftalein løsning (venstre) og 1 prosent tymolftalein løsning (høyre) som pH indikator sprayet på en fersk splittet overflate av karbonatisert mørtel. Farget mørtel angir ukarbonatisert område. Foto: NTNU

Litteratur

Belda Revert, A; De Weerdt, K; Geiker, MR (2015) Carbonation front characterization: pH color indicators. 35th Cement & Concrete Science Conference, Aberdeen.

Paper S-VIII

Correlation between corrosion current density and electrical resistivity of carbonated concrete

Messina, Marco; Revert, Andres Belda; Hornbostel, Karla; Gastaldi, Matteo; Geiker, Mette Rica;

To be submitted

Correlation between corrosion current density and electrical resistivity of carbonated concrete

M. Messina [1], A. Belda Revert [2], K. Hornbostel [3], M. Gastaldi [4], M.R. Geiker [5]

[1,*]PhD student, email: marco.messina@polimi.it. Politecnico di Milano, Department of Chemistry, Materials and Chemical Engineering "G. Natta", Via Mancinelli 7, 20131 Milan, Italy.

[2,*]PhD student, email andres.b.revert@ntnu.no Norwegian University of Science and Technology. Institutt for konstruksjonsteknikk, Materialteknisk, 3-225, Gløshaugen, Richard Birkelands vei 1a, Trondheim.

[3,*]Senior engineer Norwegian Public Roads Administration, email: karla.hornbostel@vegvesen.no. Trondheim, Norway.

[4,*]Assistant professor at Politecnico di Milano, Department of Chemistry, Materials and Chemical Engineering "G. Natta", Via Mancinelli 7, 20131 Milan, Italy.

[5,*]Professor at Norwegian University of Science and Technology, email: mette.geiker@ntnu.no. Institutt for konstruksjonsteknikk, Materialteknisk, 3-225, Gløshaugen, Richard Birkelands vei 1a.

Keywords:

concrete, carbonation-induced corrosion, corrosion current density, corrosion potential, electrical resistivity

ABSTRACT

In this study, corrosion current density of steel reinforcement in carbonated concrete made of ordinary portland cement, ordinary portland cement with 18% and 30% of fly ash was investigated varying the moisture exposure from capillary saturation to laboratory conditions. A high correlation coefficient was found between the corrosion current density of reinforcement and the electrical resistivity of concrete, which suggests that they depend on the same factors. Compared to moisture, the concrete composition was found to be less influencing. The data indicates that microcell corrosion in carbonated concrete is under anodic resistance control.

1 INTRODUCTION

Steel reinforcement in concrete is protected against corrosion thanks to the alkaline pore solution, but the protection can be lost when the pore solution is neutralized by carbon dioxide (CO_2). This process is named *carbonation* [1]. Corrosion of steel reinforcement in carbonated concrete was widely studied, despite this different mechanisms of control were suggested [2]. Alonso et Al. [3] found a linear trend when plotting the electrical resistance of carbonated mortar (R) containing various cement types versus the corrosion current density (i_{corr}) of the embedded reinforcement in log-log scale (Alonso et Al. [4] post-treated the data and presented the i_{corr}-electrical resistivity (ρ) of carbonated mortar relationship). The higher the electrical resistivity, the lower the corrosion current density. Based on the observations, they proposed that the corrosion process is under "*resistance control*". Glass et Al. [5] found the same trend investigating reinforced mortar specimen made of ordinary portland cement. In addition, a comparison between the corrosion potential (E_{corr}) and the corrosion current density was done. The higher the corrosion current density, the lower the corrosion potential. They argued that the resistance control alone could not explain the i_{corr}-E_{corr} relationship and proposed that the anodic reaction is limited by the electrical resistance of the matrix. The mechanism was termed as "*anodic resistance control*". However, the data was determined only in reinforced mortar made of ordinary portland cement.

In this work, the correlation between reinforcement corrosion current density and electrical resistivity of carbonated concrete as well as the controlling mechanism of corrosion in carbonated concrete is discussed. Reinforced concrete specimens made of ordinary portland cement, ordinary portland cement with 18% and 30% of fly ash were used. The corrosion current density and corrosion potential of reinforcement as well as the concrete electrical resistivity were monitored at submerged condition and in the course of laboratory exposure. The corrosion current density was measured by means of the linear polarization resistance technique. The electrical resistivity of concrete was measured by means of specific probe that was post-embedded at the same depth as the reinforcement.

2 MATERIALS AND METHODS

2.1 Concrete specimens

Concrete was prepared with three different types of cement, as illustrated in Table 1. The water to cement ratio was 0.55 for all types of concrete. Chemical composition of each cement type is summarized in Table 2. One reinforced and one plain large specimen of 150x260x120 mm were cast for each type of concrete. Then, each large specimen was longitudinally cut in two 150x260x~60 mm halves ("specimen" in the remaining text), as shown in Figure 1. The two reinforced specimens for each type of concrete were instrumented and used mainly for electrochemical investigation, whilst the other two plain specimens were used for checking the progress of carbonation. The two instrumented specimens of each concrete type are referred in the text with the following names: OPC-1 and OPC-2 for ordinary portland cement; 18%FA-1 and 18%FA-2 for blended cement with 18% of fly ash; 30%FA-1 and 30%FA-2 for blended cement with 30% of fly ash.

2.2 Instrumentation

Carbon steel reinforcement (B500NC) of diameter 16 mm and length 270 mm was placed in the middle of each specimen, as illustrated in Figure 2. The surface of reinforcement was cleaned with acetone to remove dirt and grease. The ends of the reinforcement were covered by wax, while the central length of 160 mm was exposed in contact with the concrete. Four probes were post-installed in the specimens after fully carbonation. A description of each probe is reported in Table 3. The pseudo-reference electrode consists of a mixed-metal oxide activated titanium rod of diameter 1 mm and length 25 mm, which was placed alongside each rebar at the distance of about 10 mm (see Figure 2). Probe A consists of two stainless steel rods (AISI 316) of 2 mm in diameter and 45 mm in length, which were placed 50 mm apart. Heat-shrinkable tubing was used for covering a length of 40 mm of the two rods and the last 5 mm were uncovered to be in contact with the injected grout. Epoxy-based paint was used for covering the tips of the rods. This probe was post-embedded at the same depth as the reinforcement (see Figure 2), and was used for measuring the combined electrical resistivity of injected grout and carbonated concrete in the vicinity of reinforcement. Probe B is similar to probe A, but the length of the two stainless steel rods is 20 mm. This probe was also post-embedded at the same depth as the reinforcement but at the horizontal distance of about 45 mm. Probe B was used in the specimen 1 for studying the potential influence of the reinforcement on electrical current distribution between the emitter electrode and the receiver electrode in measuring the electrical resistivity. Probe C consists of two titanium rods of diameter

2 mm and length 5 mm, which were placed 4 mm apart. Heat-shrinkable tubing was used for covering a length of 40 mm of the two rods and the last 5 mm were uncovered to be in contact with the injected grout. Epoxy-based paint was used for covering the tips of the rods. This probe was also post-embedded at the same depth as the reinforcement (see Figure 2). Probe C was used for measuring the electrical resistivity of injected grout. All the probes were post-embedded in the specimens by drilling holes, which were subsequently filled with injected cement grout. Ready pre-mixed product (Nonset 50 from Mapei) was used to prepare the grout. Tap water (132 g) and sieved sand (100 g, max diameter of 250 μm) were added to 300 g of Nonset 50. The holes for installing the pseudo-reference electrode, probe A and probe B were made by a drill with bit of 6 mm in diameter, while a bit of 8 mm was used for installing the probe C. Before and after the installation of the probes, the specimens were kept in submerged condition.

2.3 Conditioning and exposure conditions

The specimens were prepared in plywood moulds and kept sealed for 14 days. After 14 days of curing, the specimens were subjected to accelerated carbonation using a climatic chamber with forced ventilation at 20°C, 90% R.H. and 5% of CO_2 for 10 months. Then, the specimens were longitudinally cut in two 150x260x~60 mm halves (Figure 1) and subjected to carbonation in a chamber filled of CO_2 at 20°C and 60% R.H. until complete carbonation. Specimens of OPC, 18%FA and 30%FA became fully carbonated after 202, 122 and 62 days respectively. Once the reinforced concrete specimens were fully carbonated, they were submerged in tap water. The probes were post-embedded after some days in submerged condition. The lateral surfaces of the specimens were sealed with epoxy-based paint before starting the laboratory exposure. The laboratory exposure started when the mass change measurement between two consecutive measurements in 24 hours was lower than 0.01%. The relative humidity (R.H.) and temperature (T) of laboratory during test are reported in Figure 3a-c.

2.4 Measurements

A portable high impedance voltmeter ($>10^{12}\Omega$) was used to measure the corrosion potential of the reinforcement ($E_{corr.}$) against the standard calomel reference electrode (SCE) [6]. The external reference electrode was applied on the horizontal surface of the specimen in correspondence to the reinforcement by interposing a wet sponge. When the potential influence of reinforcement on the electrical resistivity

measurement was investigated, the corrosion potential was monitored against the post-embedded activated titanium electrode (Ti MMO).

A portable conductivity meter was used to measure the electrical conductivity. Alternating current with square wave voltage of 80 mV peak to peak and frequency in the range of 40-1000 Hz (automatically selected by the instrument) was used as measurement signal. The measurement of electrical conductivity was converted into electrical resistivity (ρ) by means of a specific cell constant, which was experimentally determined for each probe. The electrical resistivity of concrete reported in the results and discussion section was obtained by means of numerical compensation using the electrical resistivity of grout and the combined electrical resistivity of grout and pre-existing concrete. The description of the compensation procedure is given in the preparatory work [7].

A potentiostat was used to estimate the corrosion current density ($i_{corr.}$) by means of the linear polarization resistance technique (LPR). The polarization was performed with a three-probe cell arrangement imposing a potential steps of ±10 mV (scan rate of 0.166 mV/s and step height 0.1 mV) versus the free corrosion potential of the reinforcement (WE), which was measured against the embedded activated titanium electrode (RE). The electrical current was applied by an external mesh of titanium (150x260mm CE) placed on the surface of concrete by interposing a wet sponge. The corrosion current density (i_{corr} in mA/m^2) was calculated by the ratio between the B constant (26 mV [8]) and the polarization resistance ($i_{corr}=B/R_p$) [9-10]. Electrochemical impedance spectroscopy (EIS) and galvanostatic pulse (GVP) were used for measuring the ohmic drop [11]. During the EIS measurement, a difference of 10 mV between the free corrosion potential of reinforcement and the potential of the embedded activated titanium electrode was imposed with frequency between 500 kHz and 50 mHz. In the GVP measurement, direct current (DC) of 20 µA for few seconds between the counter-electrode (CE) and the working-electrode (WE) was applied.

Relative humidity and temperature of the exposure conditions were measured using a Testo 605-H1 compact thermal hygrometer (±0.5 °C and ±3% R.H.).

Measurement of mass of the specimens was performed by means of a balance of accuracy 0.005 g. Mass change (Δm) was determined by the difference between the mass over time and the last measurement of mass in submerged condition (steady condition).

3 RESULTS AND DISCUSSION

Figure 4 shows, as an example, the trends of grout electrical resistivity (probe C), combined grout-concrete electrical resistivity (probe A) and concrete electrical resistivity from capillary saturated condition (area 1) to laboratory dry out (area 2). The same trends were observed in all the specimens. The numerical compensation of grout effect on the combined grout-concrete electrical resistivity measurement (probe A) was necessary because of the significant low grout electrical resistivity (probe C), which was alkaline. The compensated concrete electrical resistivity resulted higher than the combined grout-concrete resistivity. The solid line in Figure 4 shows the time in which the possible influence of reinforcement on the measurement of electrical resistivity was studied. This effect was studied by monitoring the corrosion potential of reinforcement before, during and after the measurement of electrical resistivity by means of the probe A and probe B (Figure 5). Figure 5 shows that the corrosion potential does not change during the electrical resistivity measurement carried out by the probe A (in the vicinity of reinforcement) and probe B (far from the reinforcement), thus no electrical current flows through the reinforcement during the electrical resistivity measurement, but rather the electrical current remains in the concrete [12]. The lack of alternative paths with lower resistance suggests that the electrical resistivity measurements carried out by the probe A was not affected by the presence of the reinforcement.

The measurements of electrical resistivity (ρ), corrosion current density ($i_{corr.}$), corrosion potential (E_{corr}) and the mass change (Δm) of the specimens against time are reported in Figures 6(a-b) for OPC specimens, in Figures 6(c-d) for 18%FA specimens and in Figures 6(e-f) for 30%FA specimens. In general, the decrease of water from capillary saturated condition to the end of laboratory exposure caused a significant increase of concrete electrical resistivity and corrosion potential while the corrosion current density and specimen mass decreased.

Corrosion current density of reinforcement as a function of relative water decrease is reported in Figure 7. Relative water decrease is the ratio between the mass change over time and the last measurement of mass at submerged condition. The maximum corrosion current density in OPC was between 7 and 12 mA/m^2, while in FA was almost twice at 0% of relative water decrease which corresponds to the submerged condition. Moreover, the relative water decrease should be higher in FA than OPC to reach negligible corrosion current density (lower than 1 mA/m^2). This confirms that the maximum corrosion current density does not depend

only on the exposure condition (e.g. submerged condition) but also on the microstructure of concrete, in agreement with previous work [4]. The relative water decrease affected inversely the electrical resistivity of concrete, as shown in Figure 8. Figure 8 shows a horizontal asymptote at 0% relative water decrease as seen in Figure 7 for the maximum corrosion current density. This means that also the electrical resistivity of concrete changes according to the microstructure of concrete at equal exposure condition. Moreover, from Figure 7 and 8 appear an impact of the sample position (bottom or top) during the casting, especially for the fly ash samples. Corrosion current density of reinforcement as a function of electrical resistivity of carbonated concrete at submerged condition is shown in Figure 9. The symbols represent the average value, while the horizontal and vertical lines represent the range of variation in measurements of electrical resistivity and corrosion current density respectively. Figure 9 shows that the maximum corrosion current density increases when decreasing the electrical resistivity of concrete. Furthermore, similar values of electrical resistivity correspond to similar values of corrosion current density, apart from the specimen 18%FA-2 that showed a systematically higher i_{corr} compared to the specimen 18%FA-1 which could not be explained.

The ρ-i_{corr} correlation obtained in the current investigation is presented in Figure 10. Additionally, the regression lines reported by Alonso et al. [3] and Messina et Al. [13] are included in Figure 10. In agreement with Alonso et Al. [3], the ρ-i_{corr} correlation was found to be concrete composition independent. The high correlation coefficient suggests that corrosion current density of reinforcement and electrical resistivity of concrete depends on the same factors. The scatter increased upon drying (towards higher ρ).

The corrosion potential as a function of corrosion current density is reported in Figure 11. The regression line suggested by Glass et Al. [5], Messina et Al. [14] (limestone-porland cement) and the regression lines determined from data published by Alonso et Al. [3] (they presented the E_{corr} and i_{corr} data separately) are also given in Figure 11. No general correlation was found between these two parameters. All specimens showed comparable behaviour indicating that the corrosion process is mainly under anodic resistance control, but the corrosion potential differs in each specimen.

4 CONCLUSIONS

The high correlation coefficient found between the corrosion current density of reinforcement and the electrical resistivity of concrete suggests that they depends on the same factors. The concrete composition was found to be less influencing compared to the moisture changes. The experimental data suggests that the corrosion current density in carbonated concrete is mainly under anodic resistance control. The relationship between corrosion potential and corrosion current density of reinforcement was found to be concrete depended.

5 ACKNOWLEDGMENTS

This work is part of the joint collaboration between Politecnico di Milano (POLIMI) and Norwegian University of Science and Technology (NTNU).The research was financed by the Italian Ministry of Education, University and Research (MIUR) for the project entitled “Predicting the residual service life of reinforced concrete structures by monitoring the electrical resistivity of concrete” and “Lavkarbsem (NFR project no. 235211/O30) project, which is supported by the Norwegian Research Council and the following companies: Mapei AS, Norbetong AS, Norcem AS, Skanska AS, and Rambøll Engineering AS.

References

[1] L. Bertolini, B. Elsener, P. Pedeferri, E. Redaelli, R.B. Polder, Corrosion of steel in concrete, Wiley-VCH Verlag GmbH & Co. (2013).

[2] Stefanoni, M., U. Angst, and B. Elsener, Corrosion rate of carbon steel in carbonated concrete – A critical review. Cement and Concrete Research 103 (2018) 35-48.

[3] C. Alonso, C. Andrade, J.A. Gonzalez, Relation between resistivity and corrosion rate of reinforcements in carbonated mortar made with several cement types, Cement and Concrete Research 8 (1988) 687-698.

[4] A. Alonso, C. Andrade, Life time of rebars in carbonated concrete, in: J.M. Costa, A.D. Mercer (Eds.), Progress in understanding and prevention of corrosion, Institute of Materials, London, pp. 634-641.

[5] G.K. Glass, C.L. Page, N.R. Short, Factors affecting the corrosion rate of steel in carbonated mortars, Corrosion Science 32 (1991) 1283-1294.

[6] B. Elsener, C. Andrade, J. Gulikers, R. Polder, M. Raupach, Half-cell potential measurements – Potential mapping on reinforced concrete structures, Materials and Structures 36 (2003) 461-471.

[7] M. Messina, A.R. Belda, M. Gastaldi, M.R. Geiker, Measurement of electrical resistivity of cement-based material: effect of contact material between pre-existing material and post-embedded probe, In preparation.

[8] C. Andrade, J.A. Gonzalez, Quantitative measurements of corrosion rate of reinforcing steels embedded in concrete using polarization resistance measurements, Materials and Corrosion 29 (1978) 515-519.

[9] M. Stern, A.L. Geary, I. A theoretical analysis of the shape of polarization curves, Journal of the electrochemical society 104 (1957) 56-63.

[10] J.A. Gonzalez, A. Molina, M.L. Escudero, C. Andrade, Errors in the electrochemical evaluation of very small corrosion rates-I.Polarization resistance method applied to corrosion of steel in concrete, Corrosion Science 25 (1985) 917-930.

[11] A.B. Revert, K. Hornbostel, K. De Weerdt, M.R. Geiker, Determination of the polarization resistance of steel in carbonated fly-ash concrete – effect of measurement technique, Eurocorr 2017.

[12] L. Bertolini, M. Carsana, P. Pedeferri, Corrosion behavior of steel in concrete in the presence of stray current, Corrosion science 49 (2007) 1056-1068.

[13] M. Messina, M. Gastaldi, L. Bertolini, Estimation of corrosion propagation in carbonated reinforced concrete structures by monitoring of the electrical resistivity of concrete, Metallurgia italiana 109 (2017) 51-54.

[14] M. Messina, M. Gastaldi, L. Bertolini, Corrosion of steel reinforcement in carbonated concrete: estimation of corrosion propagation time by monitoring the concrete electrical resistivity at different concrete cover depths, In preparation.

Table 1. Mix proportions of each concrete.

	Portland cement	Blended cement with 18% Fly Ash	Blended cement with 30% Fly Ash
ID	OPC	18%FA	30%FA
Cement (kg/m^3)	371.4	369.8	369.5
Aggregate 1[a] (kg/m^3)	624.2	628.5	629.6
Aggregate 2[b] (kg/m^3)	1173.2	1166.9	1160.3
Water[c] (kg/m^3)	206.9	202.9	200.9
Superplasticiser[d] (kg/m^3)	3.78	3.69	3.68
Stabilizer[e] (kg/m^3)	0.56	0.55	0.54
Water/cement	0.557	0.548	0.543

[a] Ø=from 5 to 16 mm
[b] Ø=from 0 to 8 mm
[c] Tap water
[d] Dynamon XTend (Mapei)
[e] Viscostar 6K (Mapei)

Table 2. Chemical composition of each cement.

Designation	Percentage by mass[a]								
	SiO_2	Al_2O_3	Fe_2O_3	CaO	MgO	SO_3	P_2O_5	K_2O	Na_2O
O.P.C.	19.6	4.9	3.1	60.8	2.3	3.7	0.1	0.9	0.5
18%F.A.	25.5	7.6	4.2	50.7	2.1	3.3	0.2	1.1	0.6
30%F.A.	28.4	8.8	4.4	46.9	2.2	2.7	0.2	1.2	0.6

[a] Determined by X-Ray fluorescence spectroscopy

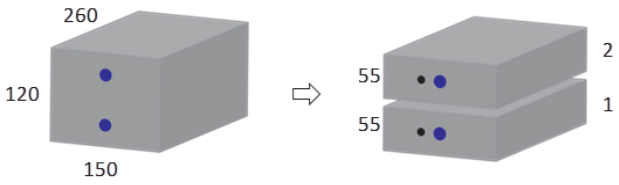

Figure 1. Schematic representation of the specimens (dimensions in millimetre).

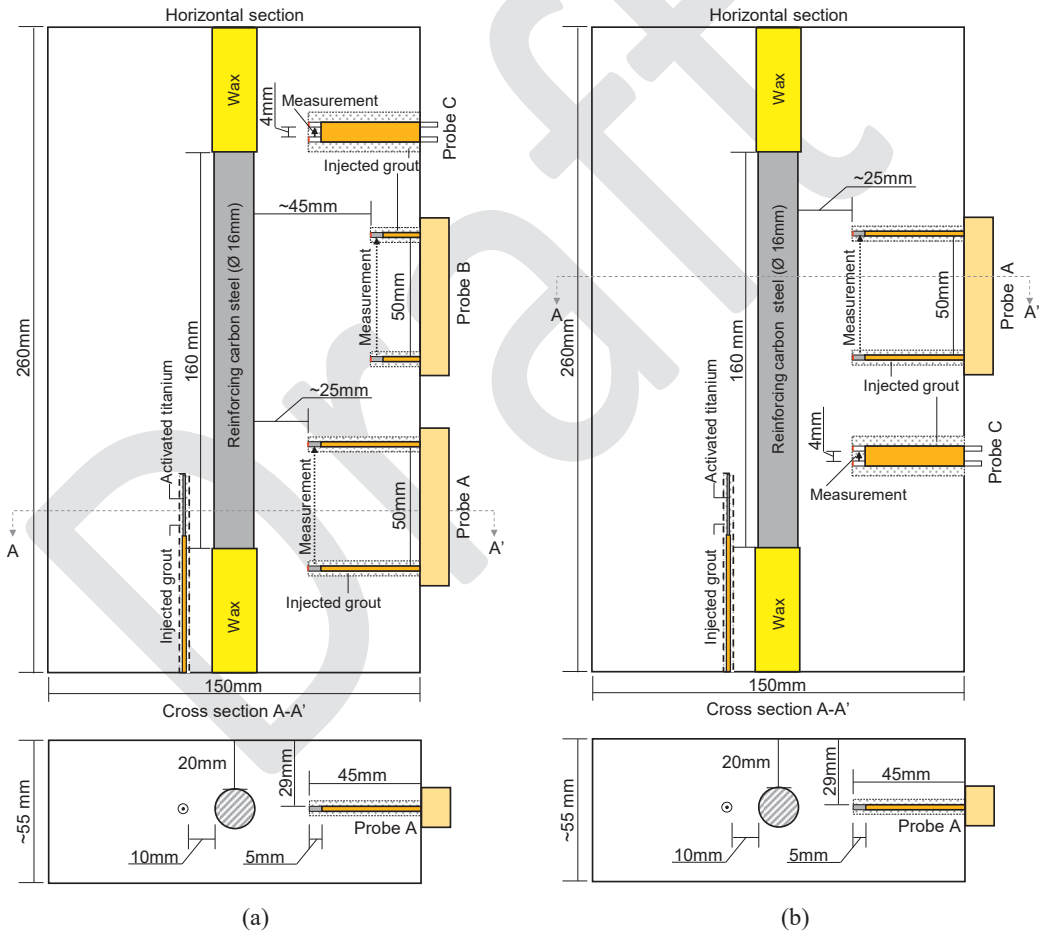

(a) (b)

Figure 2. Schematic representation of specimen 1 (a) and 2 (b) as well as post-embedded probes.

Table 3. Description of the post-embedded probes.

Designation	Geometry	Measuring parameter
Pseudo-reference electrode	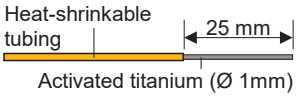	Corrosion potential at the same depth as the centre of the reinforcement
Probe A	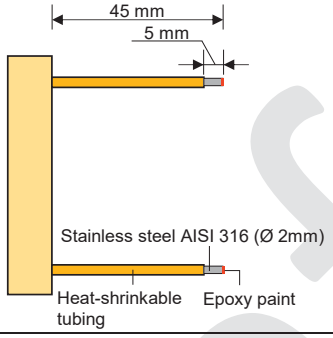	Electrical resistivity of injected grout plus carbonated concrete in the vicinity of reinforcing steel and at the same depth as the centre of the reinforcement.
Probe B	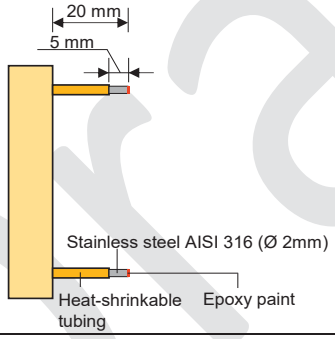	Electrical resistivity of injected grout plus carbonated concrete far from the reinforcing steel and at the same depth as the centre of the reinforcement.
Probe C	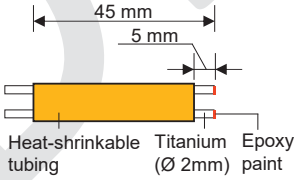	Electrical resistivity of injected grout at the same depth as the centre of the reinforcement.

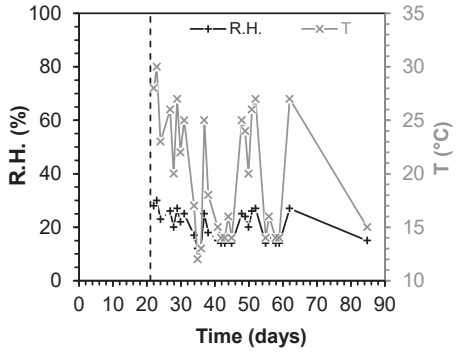

(a)

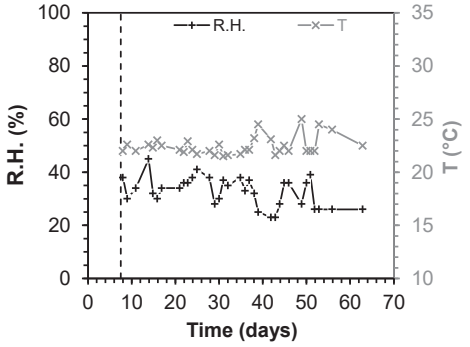

(b)

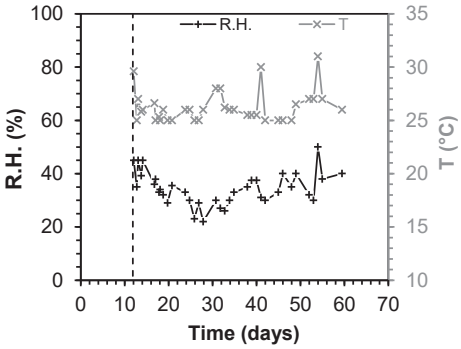

(c)

Figure 3. Relative humidity and temperature of laboratory in the course of the test on OPC specimens (a) 18%FA specimens (b) and 30%FA specimens (c). Before the dashed line the specimens were in submerged conditions.

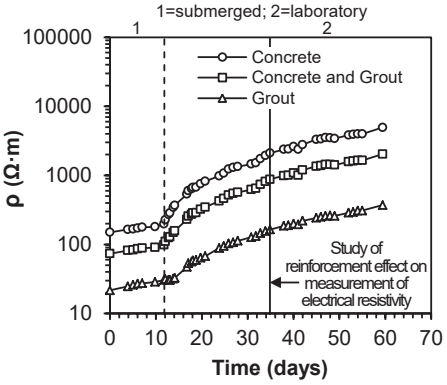

Figure 4. Electrical resistivity of the injected grout (contact material); concrete and grout (combined); concrete (compensated) against time in 30%FA specimen 1.

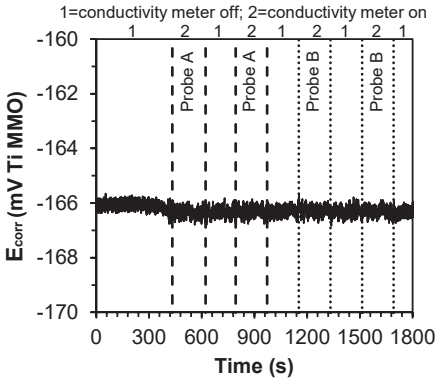

Figure 5. Corrosion potential of reinforcement in the course of time (condition 1) and in the course of the measurement of electrical resistivity carried out by the probe A and probe B (condition 2) in 30%FA specimen 1.

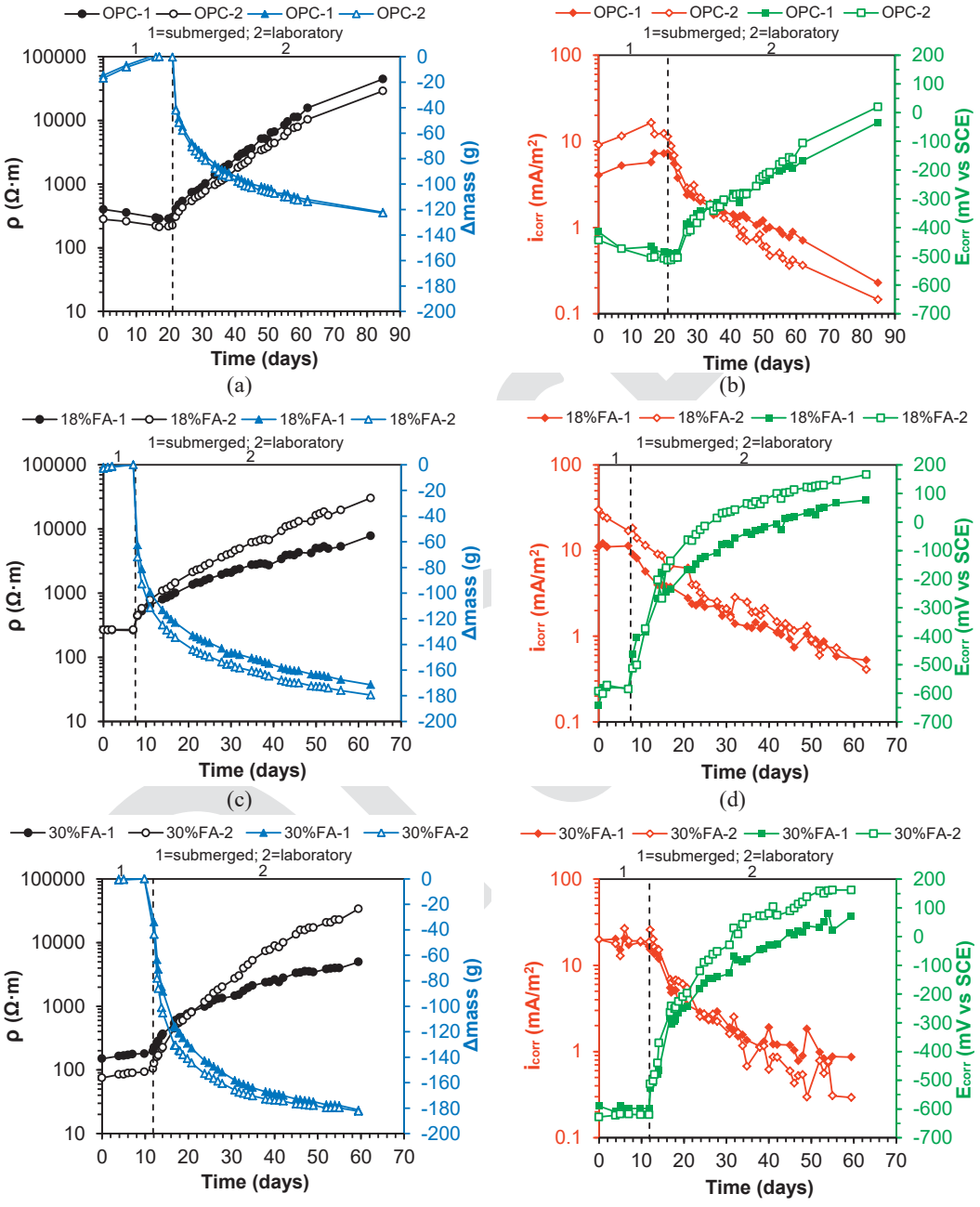

Figure 6. Electrical resistivity of concrete, mass change, corrosion current density and corrosion potential of reinforcement against time: (a-b) OPC specimens; (c-d) 18%FA specimens; (e-f) 30%FA specimens.

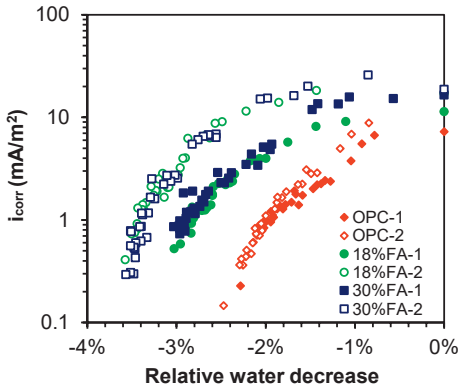

Figure 7. Corrosion current density as a function of relative water decrease.

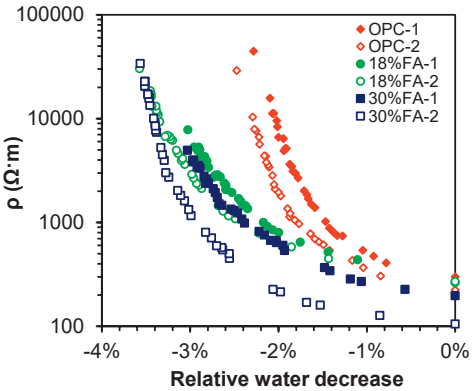

Figure 8. Electrical resistivity as a function of relative water decrease.

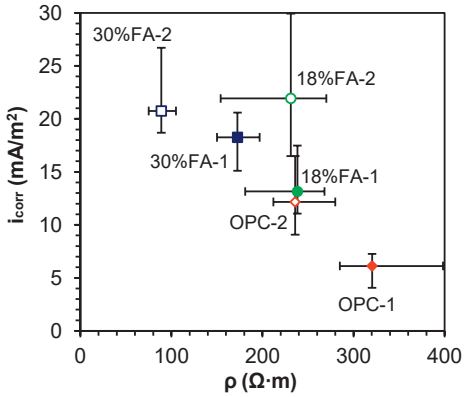

Figure 9. Corrosion current density as a function of electrical resistivity at capillary saturated condition.

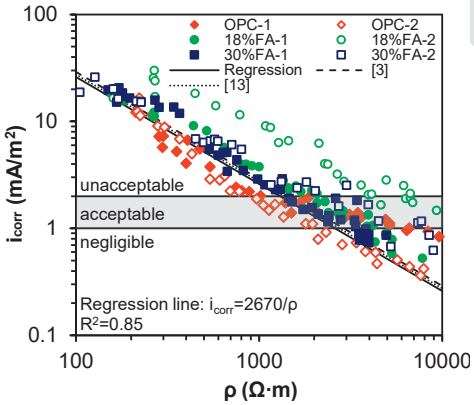

Figure 10. Corrosion current density as a function of electrical resistivity from capillary saturated conditions (left side) over drying in laboratory exposure (to the right).

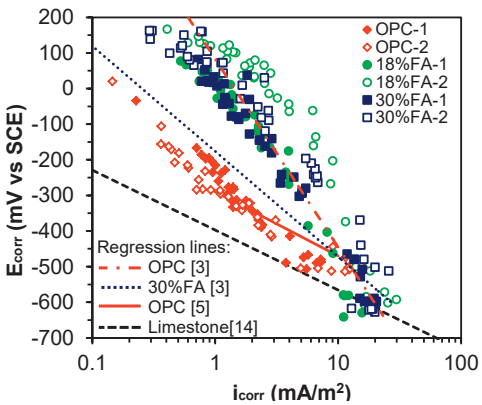

Figure 11. Corrosion potential as a function of corrosion current density from capillary saturated conditions (right side) over drying in laboratory exposure (to the left).

DEPARTMENT OF STRUCTURAL ENGINEERING
NORWEGIAN UNIVERSITY OF SCIENCE AND TECHNOLOGY

N–7491 TRONDHEIM, NORWAY
Telephone: +47 73 59 47 00 Telefax: +47 73 59 47 01

"Reliability Analysis of Structural Systems using Nonlinear Finite Element Methods",
C. A. Holm, 1990:23, ISBN 82-7119-178-0.

"Uniform Stratified Flow Interaction with a Submerged Horizontal Cylinder",
Ø. Arntsen, 1990:32, ISBN 82-7119-188-8.

"Large Displacement Analysis of Flexible and Rigid Systems Considering
Displacement-Dependent Loads and Nonlinear Constraints",
K. M. Mathisen, 1990:33, ISBN 82-7119-189-6.

"Solid Mechanics and Material Models including Large Deformations",
E. Levold, 1990:56, ISBN 82-7119-214-0, ISSN 0802-3271.

"Inelastic Deformation Capacity of Flexurally-Loaded Aluminium Alloy Structures",
T. Welo, 1990:62, ISBN 82-7119-220-5, ISSN 0802-3271.

"Visualization of Results from Mechanical Engineering Analysis",
K. Aamnes, 1990:63, ISBN 82-7119-221-3, ISSN 0802-3271.

"Object-Oriented Product Modeling for Structural Design",
S. I. Dale, 1991:6, ISBN 82-7119-258-2, ISSN 0802-3271.

"Parallel Techniques for Solving Finite Element Problems on Transputer Networks",
T. H. Hansen, 1991:19, ISBN 82-7119-273-6, ISSN 0802-3271.

"Statistical Description and Estimation of Ocean Drift Ice Environments",
R. Korsnes, 1991:24, ISBN 82-7119-278-7, ISSN 0802-3271.

“Properties of concrete related to fatigue damage: with emphasis on high strength concrete”,
G. Petkovic, 1991:35, ISBN 82-7119-290-6, ISSN 0802-3271.

"Turbidity Current Modelling",
B. Brørs, 1991:38, ISBN 82-7119-293-0, ISSN 0802-3271.

"Zero-Slump Concrete: Rheology, Degree of Compaction and Strength. Effects of Fillers as Part Cement-Replacement",
C. Sørensen, 1992:8, ISBN 82-7119-357-0, ISSN 0802-3271.

"Nonlinear Analysis of Reinforced Concrete Structures Exposed to Transient Loading",
K. V. Høiseth, 1992:15, ISBN 82-7119-364-3, ISSN 0802-3271.

"Finite Element Formulations and Solution Algorithms for Buckling and Collapse Analysis of Thin Shells",
R. O. Bjærum, 1992:30, ISBN 82-7119-380-5, ISSN 0802-3271.

"Response Statistics of Nonlinear Dynamic Systems",
J. M. Johnsen, 1992:42, ISBN 82-7119-393-7, ISSN 0802-3271.

"Digital Models in Engineering. A Study on why and how engineers build and operate digital models for decisison support",
J. Høyte, 1992:75, ISBN 82-7119-429-1, ISSN 0802-3271.

"Sparse Solution of Finite Element Equations",
A. C. Damhaug, 1992:76, ISBN 82-7119-430-5, ISSN 0802-3271.

"Some Aspects of Floating Ice Related to Sea Surface Operations in the Barents Sea",
S. Løset, 1992:95, ISBN 82-7119-452-6, ISSN 0802-3271.

"Modelling of Cyclic Plasticity with Application to Steel and Aluminium Structures",
O. S. Hopperstad, 1993:7, ISBN 82-7119-461-5, ISSN 0802-3271.

"The Free Formulation: Linear Theory and Extensions with Applications to Tetrahedral Elements
with Rotational Freedoms",
G. Skeie, 1993:17, ISBN 82-7119-472-0, ISSN 0802-3271.

"Høyfast betongs motstand mot piggdekkslitasje. Analyse av resultater fra prøving i Veisliter'n",
T. Tveter, 1993:62, ISBN 82-7119-522-0, ISSN 0802-3271.

"A Nonlinear Finite Element Based on Free Formulation Theory for Analysis of Sandwich Structures",
O. Aamlid, 1993:72, ISBN 82-7119-534-4, ISSN 0802-3271.

"The Effect of Curing Temperature and Silica Fume on Chloride Migration and Pore Structure of High Strength Concrete",
C. J. Hauck, 1993:90, ISBN 82-7119-553-0, ISSN 0802-3271.

"Failure of Concrete under Compressive Strain Gradients",
G. Markeset, 1993:110, ISBN 82-7119-575-1, ISSN 0802-3271.

"An experimental study of internal tidal amphidromes in Vestfjorden",
J. H. Nilsen, 1994:39, ISBN 82-7119-640-5, ISSN 0802-3271.

"Structural analysis of oil wells with emphasis on conductor design",
H. Larsen, 1994:46, ISBN 82-7119-648-0, ISSN 0802-3271.

"Adaptive methods for non-linear finite element analysis of shell structures",
K. M. Okstad, 1994:66, ISBN 82-7119-670-7, ISSN 0802-3271.

"On constitutive modelling in nonlinear analysis of concrete structures",
O. Fyrileiv, 1994:115, ISBN 82-7119-725-8, ISSN 0802-3271.

"Fluctuating wind load and response of a line-like engineering structure with emphasis on motion-induced wind forces",
J. Bogunovic Jakobsen, 1995:62, ISBN 82-7119-809-2, ISSN 0802-3271.

"An experimental study of beam-columns subjected to combined torsion, bending and axial actions",
A. Aalberg, 1995:66, ISBN 82-7119-813-0, ISSN 0802-3271.

"Scaling and cracking in unsealed freeze/thaw testing of Portland cement and silica fume concretes",
S. Jacobsen, 1995:101, ISBN 82-7119-851-3, ISSN 0802-3271.

"Damping of water waves by submerged vegetation. A case study of laminaria hyperborea",
A. M. Dubi, 1995:108, ISBN 82-7119-859-9, ISSN 0802-3271.

"The dynamics of a slope current in the Barents Sea",
Sheng Li, 1995:109, ISBN 82-7119-860-2, ISSN 0802-3271.

"Modellering av delmaterialenes betydning for betongens konsistens",
Ernst Mørtsell, 1996:12, ISBN 82-7119-894-7, ISSN 0802-3271.

"Bending of thin-walled aluminium extrusions",
Birgit Søvik Opheim, 1996:60, ISBN 82-7119-947-1, ISSN 0802-3271.

"Material modelling of aluminium for crashworthiness analysis",
Torodd Berstad, 1996:89, ISBN 82-7119-980-3, ISSN 0802-3271.

"Estimation of structural parameters from response measurements on submerged floating tunnels",
Rolf Magne Larssen, 1996:119, ISBN 82-471-0014-2, ISSN 0802-3271.

“Numerical modelling of plain and reinforced concrete by damage mechanics”,
Mario A. Polanco-Loria, 1997:20, ISBN 82-471-0049-5, ISSN 0802-3271.

“Nonlinear random vibrations - numerical analysis by path integration methods”,
Vibeke Moe, 1997:26, ISBN 82-471-0056-8, ISSN 0802-3271.

"Numerical prediction of vortex-induced vibration by the finite element method",
Joar Martin Dalheim, 1997:63, ISBN 82-471-0096-7, ISSN 0802-3271.

"Time domain calculations of buffeting response for wind sensitive structures",
Ketil Aas-Jakobsen, 1997:148, ISBN 82-471-0189-0, ISSN 0802-3271.

"A numerical study of flow about fixed and flexibly mounted circular cylinders",
Trond Stokka Meling, 1998:48, ISBN 82-471-0244-7, ISSN 0802-3271.

"Estimation of chloride penetration into concrete bridges in coastal areas",
Per Egil Steen, 1998:89, ISBN 82-471-0290-0, ISSN 0802-3271.

"Stress-resultant material models for reinforced concrete plates and shells",
Jan Arve Øverli, 1998:95, ISBN 82-471-0297-8, ISSN 0802-3271.

"Chloride binding in concrete. Effect of surrounding environment and concrete composition",
Claus Kenneth Larsen, 1998:101, ISBN 82-471-0337-0, ISSN 0802-3271.

"Rotational capacity of aluminium alloy beams",
Lars A. Moen, 1999:1, ISBN 82-471-0365-6, ISSN 0802-3271.

"Stretch Bending of Aluminium Extrusions",
Arild H. Clausen, 1999:29, ISBN 82-471-0396-6, ISSN 0802-3271.

"Aluminium and Steel Beams under Concentrated Loading",
Tore Tryland, 1999:30, ISBN 82-471-0397-4, ISSN 0802-3271.

"Engineering Models of Elastoplasticity and Fracture for Aluminium Alloys",
Odd-Geir Lademo, 1999:39, ISBN 82-471-0406-7, ISSN 0802-3271.

"Kapasitet og duktilitet av dybelforbindelser i trekonstruksjoner",
Jan Siem, 1999:46, ISBN 82-471-0414-8, ISSN 0802-3271.

"Etablering av distribuert ingeniørarbeid; Teknologiske og organisatoriske erfaringer fra en norsk ingeniørbedrift",
Lars Line, 1999:52, ISBN 82-471-0420-2, ISSN 0802-3271.

"Estimation of Earthquake-Induced Response",
Símon Ólafsson, 1999:73, ISBN 82-471-0443-1, ISSN 0802-3271.

"Coastal Concrete Bridges: Moisture State, Chloride Permeability and Aging Effects"
Ragnhild Holen Relling, 1999:74, ISBN 82-471-0445-8, ISSN 0802-3271.

"Capacity Assessment of Titanium Pipes Subjected to Bending and External Pressure",
Arve Bjørset, 1999:100, ISBN 82-471-0473-3, ISSN 0802-3271.

“Validation of Numerical Collapse Behaviour of Thin-Walled Corrugated Panels”,
Håvar Ilstad, 1999:101, ISBN 82-471-0474-1, ISSN 0802-3271.

“Strength and Ductility of Welded Structures in Aluminium Alloys”,
Miroslaw Matusiak, 1999:113, ISBN 82-471-0487-3, ISSN 0802-3271.

“Thermal Dilation and Autogenous Deformation as Driving Forces to Self-Induced Stresses in High Performance Concrete”,
Øyvind Bjøntegaard, 1999:121, ISBN 82-7984-002-8, ISSN 0802-3271.

“Some Aspects of Ski Base Sliding Friction and Ski Base Structure”,
Dag Anders Moldestad, 1999:137, ISBN 82-7984-019-2, ISSN 0802-3271.

"Electrode reactions and corrosion resistance for steel in mortar and concrete",
Roy Antonsen, 2000:10, ISBN 82-7984-030-3, ISSN 0802-3271.

"Hydro-Physical Conditions in Kelp Forests and the Effect on Wave Damping and Dune Erosion. A case study on Laminaria Hyperborea",
Stig Magnar Løvås, 2000:28, ISBN 82-7984-050-8, ISSN 0802-3271.

"Random Vibration and the Path Integral Method",
Christian Skaug, 2000:39, ISBN 82-7984-061-3, ISSN 0802-3271.

"Buckling and geometrical nonlinear beam-type analyses of timber structures",
Trond Even Eggen, 2000:56, ISBN 82-7984-081-8, ISSN 0802-3271.

”Structural Crashworthiness of Aluminium Foam-Based Components”,
Arve Grønsund Hanssen, 2000:76, ISBN 82-7984-102-4, ISSN 0809-103X.

“Measurements and simulations of the consolidation in first-year sea ice ridges, and some aspects of mechanical behaviour”,
Knut V. Høyland, 2000:94, ISBN 82-7984-121-0, ISSN 0809-103X.

”Kinematics in Regular and Irregular Waves based on a Lagrangian Formulation”,
Svein Helge Gjøsund, 2000-86, ISBN 82-7984-112-1, ISSN 0809-103X.

”Self-Induced Cracking Problems in Hardening Concrete Structures”,
Daniela Bosnjak, 2000-121, ISBN 82-7984-151-2, ISSN 0809-103X.

"Ballistic Penetration and Perforation of Steel Plates",
Tore Børvik, 2000:124, ISBN 82-7984-154-7, ISSN 0809-103X.

"Freeze-Thaw resistance of Concrete. Effect of: Curing Conditions, Moisture Exchange and Materials",
Terje Finnerup Rønning, 2001:14, ISBN 82-7984-165-2, ISSN 0809-103X

"Structural behaviour of post tensioned concrete structures. Flat slab. Slabs on ground",
Steinar Trygstad, 2001:52, ISBN 82-471-5314-9, ISSN 0809-103X.

"Slipforming of Vertical Concrete Structures. Friction between concrete and slipform panel",
Kjell Tore Fosså, 2001:61, ISBN 82-471-5325-4, ISSN 0809-103X.

"Some numerical methods for the simulation of laminar and turbulent incompressible flows",
Jens Holmen, 2002:6, ISBN 82-471-5396-3, ISSN 0809-103X.

“Improved Fatigue Performance of Threaded Drillstring Connections by Cold Rolling”,
Steinar Kristoffersen, 2002:11, ISBN: 82-421-5402-1, ISSN 0809-103X.

"Deformations in Concrete Cantilever Bridges: Observations and Theoretical Modelling",
Peter F. Takâcs, 2002:23, ISBN 82-471-5415-3, ISSN 0809-103X.

"Stiffened aluminium plates subjected to impact loading",
Hilde Giæver Hildrum, 2002:69, ISBN 82-471-5467-6, ISSN 0809-103X.

"Full- and model scale study of wind effects on a medium-rise building in a built up area",
Jónas Thór Snæbjørnsson, 2002:95, ISBN82-471-5495-1, ISSN 0809-103X.

“Evaluation of Concepts for Loading of Hydrocarbons in Ice-infested water”,
Arnor Jensen, 2002:114, ISBN 82-417-5506-0, ISSN 0809-103X.

”Numerical and Physical Modelling of Oil Spreading in Broken Ice”,
Janne K. Økland Gjøsteen, 2002:130, ISBN 82-471-5523-0, ISSN 0809-103X.

”Diagnosis and protection of corroding steel in concrete”,
Franz Pruckner, 20002:140, ISBN 82-471-5555-4, ISSN 0809-103X.

“Tensile and Compressive Creep of Young Concrete: Testing and Modelling”,
Dawood Atrushi, 2003:17, ISBN 82-471-5565-6, ISSN 0809-103X.

“Rheology of Particle Suspensions. Fresh Concrete, Mortar and Cement Paste with Various Types of Lignosulfonates”,
Jon Elvar Wallevik, 2003:18, ISBN 82-471-5566-4, ISSN 0809-103X.

“Oblique Loading of Aluminium Crash Components”,
Aase Reyes, 2003:15, ISBN 82-471-5562-1, ISSN 0809-103X.

“Utilization of Ethiopian Natural Pozzolans”,
Surafel Ketema Desta, 2003:26, ISSN 82-471-5574-5, ISSN:0809-103X.

“Behaviour and strength prediction of reinforced concrete structures with discontinuity regions”, Helge Brå, 2004:11, ISBN 82-471-6222-9, ISSN 1503-8181.

“High-strength steel plates subjected to projectile impact. An experimental and numerical study”, Sumita Dey, 2004:38, ISBN 82-471-6282-2 (printed version), ISBN 82-471-6281-4 (electronic version), ISSN 1503-8181.

“Alkali-reactive and inert fillers in concrete. Rheology of fresh mixtures and expansive reactions.”
Bård M. Pedersen, 2004:92, ISBN 82-471-6401-9 (printed version), ISBN 82-471-6400-0 (electronic version), ISSN 1503-8181.

“On the Shear Capacity of Steel Girders with Large Web Openings”.
Nils Christian Hagen, 2005:9 ISBN 82-471-6878-2 (printed version), ISBN 82-471-6877-4 (electronic version), ISSN 1503-8181.

”Behaviour of aluminium extrusions subjected to axial loading”.
Østen Jensen, 2005:7, ISBN 82-471-6873-1 (printed version), ISBN 82-471-6872-3 (electronic version), ISSN 1503-8181.

”Thermal Aspects of corrosion of Steel in Concrete”.
Jan-Magnus Østvik, 2005:5, ISBN 82-471-6869-3 (printed version), ISBN 82-471-6868 (electronic version), ISSN 1503-8181.

”Mechanical and adaptive behaviour of bone in relation to hip replacement.” A study of bone remodelling and bone grafting.
Sébastien Muller, 2005:34, ISBN 82-471-6933-9 (printed version), ISBN 82-471-6932-0 (electronic version), ISSN 1503-8181.

“Analysis of geometrical nonlinearities with applications to timber structures”.
Lars Wollebæk, 2005:74, ISBN 82-471-7050-5 (printed version), ISBN 82-471-7019-1 (electronic version), ISSN 1503-8181.

“Pedestrian induced lateral vibrations of slender footbridges”,
Anders Rönnquist, 2005:102, ISBN 82-471-7082-5 (printed version), ISBN 82-471-7081-7 (electronic version), ISSN 1503-8181.

“Initial Strength Development of Fly Ash and Limestone Blended Cements at Various Temperatures Predicted by Ultrasonic Pulse Velocity”,
Tom Ivar Fredvik, 2005:112, ISBN 82-471-7105-8 (printed version), ISBN 82-471-7103-1 (electronic version), ISSN 1503-8181.

“Behaviour and modelling of thin-walled cast components”,
Cato Dørum, 2005:128, ISBN 82-471-7140-6 (printed version), ISBN 82-471-7139-2 (electronic version), ISSN 1503-8181.

“Behaviour and modelling of selfpiercing riveted connections”,
Raffaele Porcaro, 2005:165, ISBN 82-471-7219-4 (printed version), ISBN 82-471-7218-6 (electronic version), ISSN 1503-8181.

”Behaviour and Modelling og Aluminium Plates subjected to Compressive Load”,
Lars Rønning, 2005:154, ISBN 82-471-7169-1 (printed version), ISBN 82-471-7195-3 (electronic version), ISSN 1503-8181.

”Bumper beam-longitudinal system subjected to offset impact loading”,
Satyanarayana Kokkula, 2005:193, ISBN 82-471-7280-1 (printed version), ISBN 82-471-7279-8 (electronic version), ISSN 1503-8181.

“Control of Chloride Penetration into Concrete Structures at Early Age”,
Guofei Liu, 2006:46, ISBN 82-471-7838-9 (printed version), ISBN 82-471-7837-0 (electronic version), ISSN 1503-8181.

“Modelling of Welded Thin-Walled Aluminium Structures”,
Ting Wang, 2006:78, ISBN 82-471-7907-5 (printed version), ISBN 82-471-7906-7 (electronic version), ISSN 1503-8181.

”Time-variant reliability of dynamic systems by importance sampling and probabilistic analysis of ice loads”,
Anna Ivanova Olsen, 2006:139, ISBN 82-471-8041-3 (printed version), ISBN 82-471-8040-5 (electronic version), ISSN 1503-8181.

“Fatigue life prediction of an aluminium alloy automotive component using finite element analysis of surface topography”.
Sigmund Kyrre Ås, 2006:25, ISBN 82-471-7791-9 (printed version), ISBN 82-471-7791-9 (electronic version), ISSN 1503-8181.

”Constitutive models of elastoplasticity and fracture for aluminium alloys under strain path change”,
Dasharatha Achani, 2006:76, ISBN 82-471-7903-2 (printed version), ISBN 82-471-7902-4 (electronic version), ISSN 1503-8181.

“Simulations of 2D dynamic brittle fracture by the Element-free Galerkin method and linear fracture mechanics”,
Tommy Karlsson, 2006:125, ISBN 82-471-8011-1 (printed version), ISBN 82-471-8010-3 (electronic version), ISSN 1503-8181.

“Penetration and Perforation of Granite Targets by Hard Projectiles”,
Chong Chiang Seah, 2006:188, ISBN 82-471-8150-9 (printed version), ISBN 82-471-8149-5 (electronic version), ISSN 1503-8181.

"Deformations, strain capacity and cracking of concrete in plastic and early hardening phases",
Tor Arne Hammer, 2007:234, ISBN 978-82-471-5191-4 (printed version), ISBN 978-82-471-5207-2 (electronic version), ISSN 1503-8181.

"Crashworthiness of dual-phase high-strength steel: Material and Component behaviour", Venkatapathi Tarigopula, 2007:230, ISBN 82-471-5076-4 (printed version), ISBN 82-471-5093-1 (electronic version), ISSN 1503-8181.

"Fibre reinforcement in load carrying concrete structures",
Åse Lyslo Døssland, 2008:50, ISBN 978-82-471-6910-0 (printed version), ISBN 978-82-471-6924-7 (electronic version), ISSN 1503-8181.

"Low-velocity penetration of aluminium plates",
Frode Grytten, 2008:46, ISBN 978-82-471-6826-4 (printed version), ISBN 978-82-471-6843-1 (electronic version), ISSN 1503-8181.

"Robustness studies of structures subjected to large deformations",
Ørjan Fyllingen, 2008:24, ISBN 978-82-471-6339-9 (printed version), ISBN 978-82-471-6342-9 (electronic version), ISSN 1503-8181.

"Constitutive modelling of morsellised bone",
Knut Birger Lunde, 2008:92, ISBN 978-82-471-7829-4 (printed version), ISBN 978-82-471-7832-4 (electronic version), ISSN 1503-8181.

"Experimental Investigations of Wind Loading on a Suspension Bridge Girder",
Bjørn Isaksen, 2008:131, ISBN 978-82-471-8656-5 (printed version), ISBN 978-82-471-8673-2 (electronic version), ISSN 1503-8181.

"Cracking Risk of Concrete Structures in The Hardening Phase",
Guomin Ji, 2008:198, ISBN 978-82-471-1079-9 (printed version), ISBN 978-82-471-1080-5 (electronic version), ISSN 1503-8181.

"Modelling and numerical analysis of the porcine and human mitral apparatus",
Victorien Emile Prot, 2008:249, ISBN 978-82-471-1192-5 (printed version), ISBN 978-82-471-1193-2 (electronic version), ISSN 1503-8181.

"Strength analysis of net structures",
Heidi Moe, 2009:48, ISBN 978-82-471-1468-1 (printed version), ISBN 978-82-471-1469-8 (electronic version), ISSN1503-8181.

"Numerical analysis of ductile fracture in surface cracked shells",
Espen Berg, 2009:80, ISBN 978-82-471-1537-4 (printed version), ISBN 978-82-471-1538-1 (electronic version), ISSN 1503-8181.

"Subject specific finite element analysis of bone – for evaluation of the healing of a leg lengthening and evaluation of femoral stem design",
Sune Hansborg Pettersen, 2009:99, ISBN 978-82-471-1579-4 (printed version), ISBN 978-82-471-1580-0 (electronic version), ISSN 1503-8181.

"Evaluation of fracture parameters for notched multi-layered structures",
Lingyun Shang, 2009:137, ISBN 978-82-471-1662-3 (printed version), ISBN 978-82-471-1663-0 (electronic version), ISSN 1503-8181.

"Modelling of Dynamic Material Behaviour and Fracture of Aluminium Alloys for Structural Applications"
Yan Chen, 2009:69, ISBN 978-82-471-1515-2 (printed version), ISBN 978-82 471-1516-9 (electronic version), ISSN 1503-8181.

"Nanomechanics of polymer and composite particles"
Jianying He 2009:213, ISBN 978-82-471-1828-3 (printed version), ISBN 978-82-471-1829-0 (electronic version), ISSN 1503-8181.

"Mechanical properties of clear wood from Norway spruce"
Kristian Berbom Dahl 2009:250, ISBN 978-82-471-1911-2 (printed version) ISBN 978-82-471-1912-9 (electronic version), ISSN 1503-8181.

"Modeling of the degradation of TiB_2 mechanical properties by residual stresses and liquid Al penetration along grain boundaries"
Micol Pezzotta 2009:254, ISBN 978-82-471-1923-5 (printed version) ISBN 978-82-471-1924-2 (electronic version) ISSN 1503-8181.

"Effect of welding residual stress on fracture"
Xiabo Ren 2010:77, ISBN 978-82-471-2115-3 (printed version) ISBN 978-82-471-2116-0 (electronic version), ISSN 1503-8181.

"Pan-based carbon fiber as anode material in cathodic protection system for concrete structures"
Mahdi Chini 2010:122, ISBN 978-82-471-2210-5 (printed version) ISBN 978-82-471-2213-6 (electronic version), ISSN 1503-8181.

"Structural Behaviour of deteriorated and retrofitted concrete structures"
Irina Vasililjeva Sæther 2010:171, ISBN 978-82-471-2315-7 (printed version) ISBN 978-82-471-2316-4 (electronic version) ISSN 1503-8181.

"Prediction of local snow loads on roofs"
Vivian Meløysund 2010:247, ISBN 978-82-471-2490-1 (printed version) ISBN 978-82-471-2491-8 (electronic version) ISSN 1503-8181.

"Behaviour and modelling of polymers for crash applications"
Virgile Delhaye 2010:251, ISBN 978-82-471-2501-4 (printed version) ISBN 978-82-471-2502-1 (electronic version) ISSN 1503-8181.

“Blended cement with reducted CO_2 emission – Utilizing the Fly Ash-Limestone Synergy”,
Klaartje De Weerdt 2011:32, ISBN 978-82-471-2584-7 (printed version) ISBN 978-82-471-2584-4 (electronic version) ISSN 1503-8181.

“Chloride induced reinforcement corrosion in concrete” Concept of critical chloride content – methods and mechanisms.
Ueli Angst 2011:113, ISBN 978-82-471-2769-9 (printed version) ISBN 978-82-471-2763-6 (electronic version) ISSN 1503-8181.

“A thermo-electric-Mechanical study of the carbon anode and contact interface for Energy savings in the production of aluminium”.
Dag Herman Andersen 2011:157, ISBN 978-82-471-2859-6 (printed version) ISBN 978-82-471-2860-2 (electronic version) ISSN 1503-8181.

“Structural Capacity of Anchorage Ties in Masonry Veneer Walls Subjected to Earthquake”. The implications of Eurocode 8 and Eurocode 6 on a typical Norwegain veneer wall.
Ahmed Mohamed Yousry Hamed 2011:181, ISBN 978-82-471-2911-1 (printed version) ISBN 978-82-471-2912-8 (electronic ver.) ISSN 1503-8181.

“Work-hardening behaviour in age-hardenable Al-Zn-Mg(-Cu) alloys”.
Ida Westermann , 2011:247, ISBN 978-82-471-3056-8 (printed ver.) ISBN 978-82-471-3057-5 (electronic ver.) ISSN 1503-8181.

“Behaviour and modelling of selfpiercing riveted connections using aluminium rivets”.
Nguyen-Hieu Hoang, 2011:266, ISBN 978-82-471-3097-1 (printed ver.) ISBN 978-82-471-3099-5 (electronic ver.) ISSN 1503-8181.

“Fibre reinforced concrete”.
Sindre Sandbakk, 2011:297, ISBN 978-82-471-3167-1 (printed ver.) ISBN 978-82-471-3168-8 (electronic ver) ISSN 1503:8181.

“Dynamic behaviour of cablesupported bridges subjected to strong natural wind”.
Ole Andre Øiseth, 2011:315, ISBN 978-82-471-3209-8 (printed ver.) ISBN 978-82-471-3210-4 (electronic ver.) ISSN 1503-8181.

“Constitutive modeling of solargrade silicon materials”
Julien Cochard, 2011:307, ISBN 978-82-471-3189-3 (printed ver). ISBN 978-82-471-3190-9 (electronic ver.) ISSN 1503-8181.

“Constitutive behavior and fracture of shape memory alloys”
Jim Stian Olsen, 2012:57, ISBN 978-82-471-3382-8 (printed ver.) ISBN 978-82-471-3383-5 (electronic ver.) ISSN 1503-8181.

“Field measurements in mechanical testing using close-range photogrammetry and digital image analysis”
Egil Fagerholt, 2012:95, ISBN 978-82-471-3466-5 (printed ver.) ISBN 978-82-471-3467-2 (electronic ver.) ISSN 1503-8181.

“Towards a better under standing of the ultimate behaviour of lightweight aggregate concrete in compression and bending”,
Håvard Nedrelid, 2012:123, ISBN 978-82-471-3527-3 (printed ver.) ISBN 978-82-471-3528-0 (electronic ver.) ISSN 1503-8181.

“Numerical simulations of blood flow in the left side of the heart”
Sigrid Kaarstad Dahl, 2012:135, ISBN 978-82-471-3553-2 (printed ver.) ISBN 978-82-471-3555-6 (electronic ver.) ISSN 1503-8181.

“Moisture induced stresses in glulam”
Vanessa Angst-Nicollier, 2012:139, ISBN 978-82-471-3562-4 (printed ver.) ISBN 978-82-471-3563-1 (electronic ver.) ISSN 1503-8181.

“Biomechanical aspects of distraction osteogensis”
Valentina La Russa, 2012:250, ISBN 978-82-471-3807-6 (printed ver.) ISBN 978-82-471-3808-3 (electronic ver.) ISSN 1503-8181.

“Ductile fracture in dual-phase steel. Theoretical, experimental and numerical study”
Gaute Gruben, 2012:257, ISBN 978-82-471-3822-9 (printed ver.) ISBN 978-82-471-3823-6 (electronic ver.) ISSN 1503-8181.

“Damping in Timber Structures”
Nathalie Labonnote, 2012:263, ISBN 978-82-471-3836-6 (printed ver.) ISBN 978-82-471-3837-3 (electronic ver.) ISSN 1503-8181.

“Biomechanical modeling of fetal veins: The umbilical vein and ductus venosus bifurcation”
Paul Roger Leinan, 2012:299, ISBN 978-82-471-3915-8 (printed ver.) ISBN 978-82-471-3916-5 (electronic ver.) ISSN 1503-8181.

“Large-Deformation behaviour of thermoplastics at various stress states”
Anne Serine Ognedal, 2012:298, ISBN 978-82-471-3913-4 (printed ver.) ISBN 978-82-471-3914-1 (electronic ver.) ISSN 1503-8181.

“Hardening accelerator for fly ash blended cement”
Kien Dinh Hoang, 2012:366, ISBN 978-82-471-4063-5 (printed ver.) ISBN 978-82-471-4064-2 (electronic ver.) ISSN 1503-8181.

“From molecular structure to mechanical properties”
Jianyang Wu, 2013:186, ISBN 978-82-471-4485-5 (printed ver.) ISBN 978-82-471-4486-2 (electronic ver.) ISSN 1503-8181.

“Experimental and numerical study of hybrid concrete structures”
Linn Grepstad Nes, 2013:259, ISBN 978-82-471-4644-6 (printed ver.) ISBN 978-82-471-4645-3 (electronic ver.) ISSN 1503-8181.

“Mechanics of ultra-thin multi crystalline silicon wafers”
Saber Saffar, 2013:199, ISBN 978-82-471-4511-1 (printed ver.) ISBN 978-82-471-4513-5 (electronic ver). ISSN 1503-8181.

“Through process modelling of welded aluminium structures”
Anizahyati Alisibramulisi, 2013:325, ISBN 978-82-471-4788-7 (printed ver.) ISBN 978-82-471-4789-4 (electronic ver.) ISSN 1503-8181.

“Combined blast and fragment loading on steel plates”
Knut Gaarder Rakvåg, 2013:361, ISBN978-82-471-4872-3 (printed ver.) ISBN 978-82-4873-0 (electronic ver.). ISSN 1503-8181.

“Characterization and modelling of the anisotropic behaviour of high-strength aluminium alloy”
Marion Fourmeau, 2014:37, ISBN 978-82-326-0008-3 (printed ver.) ISBN 978-82-326-0009-0 (electronic ver.) ISSN 1503-8181.

“Behaviour of threated steel fasteners at elevated deformation rates”
Henning Fransplass, 2014:65, ISBN 978-82-326-0054-0 (printed ver.) ISBN 978-82-326-0055-7 (electronic ver.) ISSN 1503-8181.

“Sedimentation and Bleeding”
Ya Peng, 2014:89, ISBN 978-82-326-0102-8 (printed ver.) ISBN 978-82-326-0103-5 (electric ver.) ISSN 1503-8181.

“Impact against X65 offshore pipelines”
Martin Kristoffersen, 2014:362, ISBN 978-82-326-0636-8 (printed ver.) ISBN 978-82-326-0637-5 (electronic ver.) ISSN 1503-8181.

“Formability of aluminium alloy subjected to prestrain by rolling”
Dmitry Vysochinskiy, 2014:363,, ISBN 978-82-326-0638-2 (printed ver.) ISBN 978-82-326-0639-9 (electronic ver.) ISSN 1503-8181.

“Experimental and numerical study of Yielding, Work-Hardening and anisotropy in textured AA6xxx alloys using crystal plasticity models”
Mikhail Khadyko, 2015:28, ISBN 978-82-326-0724-2 (printed ver.) ISBN 978-82-326-0725-9 (electronic ver.) ISSN 1503-8181.

“Behaviour and Modelling of AA6xxx Aluminium Alloys Under a Wide Range of Temperatures and Strain Rates”
Vincent Vilamosa, 2015:63, ISBN 978-82-326-0786-0 (printed ver.) ISBN 978-82-326-0787-7 (electronic ver.) ISSN 1503-8181.

“A Probabilistic Approach in Failure Modelling of Aluminium High Pressure Die-Castings”
Octavian Knoll, 2015:137, ISBN 978-82-326-0930-7 (printed ver.) ISBN 978-82-326-0931-4 (electronic ver.) ISSN 1503-8181.

“Ice Abrasion on Marine Concrete Structures”
Egil Møen, 2015:189, ISBN 978-82-326-1034-1 (printed ver.) ISBN 978-82-326-1035-8 (electronic ver.) ISSN 1503-8181.

“Fibre Orientation in Steel-Fibre-Reinforced Concrete”
Giedrius Zirgulis, 2015:229, ISBN 978-82-326-1114-0 (printed ver.) ISBN 978-82-326-1115-7 (electronic ver.) ISSN 1503-8181.

“Effect of spatial variation and possible interference of localised corrosion on the residual capacity of a reinforced concrete beam”
Mohammad Mahdi Kioumarsi, 2015:282, ISBN 978-82-326-1220-8 (printed ver.) ISBN 978-82-1221-5 (electronic ver.) ISSN 1503-8181.

“The role of concrete resistivity in chloride-induced macro-cell corrosion”
Karla Horbostel, 2015:324, ISBN 978-82-326-1304-5 (printed ver.) ISBN 978-82-326-1305-2 (electonic ver.) ISSN 1503-8181.

“Flowable fibre-reinforced concrete for structural applications”
Elena Vidal Sarmiento, 2015-335, ISBN 978-82-326-1324-3 (printed ver.) ISBN 978-82-326-1325-0 (electronic ver.) ISSN 1503-8181.

“Development of chushed sand for concrete production with microproportioning”
Rolands Cepuritis, 2016:19, ISBN 978-82-326-1382-3 (printed ver.) ISBN 978-82-326-1383-0 (electronic ver.) ISSN 1503-8181.

“Withdrawal properties of threaded rods embedded in glued-laminated timer elements”
Haris Stamatopoulos, 2016:48, ISBN 978-82-326-1436-3 (printed ver.) ISBN 978-82-326-1437-0 (electronic ver.) ISSN 1503-8181.

“An Experimental and numerical study of thermoplastics at large deformation”
Marius Andersen, 2016:191, ISBN 978-82-326-1720-3 (printed ver.) ISBN 978-82-326-1721-0 (electronic ver.) ISSN 1503-8181.

“Modeling and Simulation of Ballistic Impact”
Jens Kristian Holmen, 2016:240, ISBN 978-82-326-1818-7 (printed ver). ISBN 978-82-326-1819-4 (electronic ver.) ISSN 1503-8181.

“Early age crack assessment of concrete structures”
Anja B. Estensen Klausen, 2016:256, ISBN 978-82-326-1850-7 (printed ver). ISBN 978-82-326-1851-4 (electronic ver.) ISSN 1503-8181.

“Uncertainty quantification and sensitivity analysis for cardiovascular models”
Vinzenz Gregor Eck, 2016:234, ISBN 978-82-326-1806-4 (printed ver.) ISBN 978-82-326-1807-1 (electronic ver.) ISSN 1503-8181.

“Dynamic behaviour of existing and new railway catenary systems under Norwegain conditions”
Petter Røe Nåvik, 2016:298, ISBN 978-82-326-1935-1 (printed ver.) ISBN 978-82-326-1934-4 (electronic ver.) ISSN 1503-8181.

“Mechanical behaviour of particle-filled elastomers at various temperatures”
Arne Ilseng, 2016-295, ISBN978-82-326-1928-3 (printed ver.) ISBN 978-82-326-1929-0 (electronic ver.) ISSN 1503-8181.

“Nanotechnology for Anti-Icing Application”
Zhiwei He, 2016:348, ISBN 978-82-326-2038-8 (printed ver.) ISBN 978-82-326-2019-5 (electronic ver.) ISSN 1503-8181.

“Conduction Mechanisms in Conductive Adhesives with Metal-Coated Polyer Spheres”
Sigurd Rolland Pettersen, 2016:349, ISBN 978-326-2040-1 (printed ver,) ISBN 978-82-326-2041-8 (electronic ver.) ISSN 1503-8181.

“The interaction between calcium lignosulfonate and cement”
Alessia Colombo, 2017:20, ISBN 978-82-326-2122-4 (printed ver.) ISBN 978-82-326-2123-1 (electronic ver.) ISSN 1503-8181.

“Behaviour and Modelling of Flexible Structures Subjected to Blast Loading”
Vegard Aune, 2017:101, ISBN 978-82-326-2274-0 (printed ver.) ISBN 978-82-326-2275-7 (electronic ver.) ISSN 1503-8181.

“Behaviour of steel connections under quasi-static and impact loading”
Erik Løhre Grimsmo, 2017:159, ISBN 978-82-326-2390-7 (printed ver.) ISBN 978-82-326-2391-4 (electronic ver.) ISSN 1503-8181.

“An experimental and numerical study of cortical bone at he macro and Nano-scale”
Masoud Ramenzanzadehkoldeh,, 2017:208, ISBN 978-82-326-2488-1 (printed ver.) ISBN 978-82-326-2489-8 (electronic ver.) ISSN 1503-8181.

“Optoelectrical Properties of a Novel Organic Semiconductor: 6,13-Dichloropentacene”
Mao Wang, 2017:130, ISBN 978-82-326-2332-7 (printed ver.) ISBN 978-82-326-2333-4) (electronic ver.) ISSN 1503-8181.

“Core-shell structured microgels and their behavior at oil and water interface”
Yi Gong, 2017:182, ISBN 978-82-326-2436-2 (printed. ver.) ISBN 978-82-326-2437-9 (electronic ver.) ISSN 1503-8181.

“Aspects of design of reinforced concrete structures using nonliear finite element analyses”
Morten Engen, 2017:149, ISBN 978-82-326-2370-9 (printed ver.) ISBN 978-82-326-2371-6 (electronic ver.) ISSN 1503-8181.

“Numerical studies on ductile failure of aluminium alloys”
Lars Edvard Dæhli, 2017:284, ISBN 978-82-326-2636-6 (printed ver.) ISBN 978-82-326-2637-3 (electronic ver.) ISSN 1503-8181.

“Modelling and Assessment of Hydrogen Embrittlement in Steels and Nickel Alloys”
Haiyang Yu, 2017:278, ISBN 978-82-326-2624-3 (printed. ver.) ISBN 978-82-326-2625-0 (electronic ver.) ISSN 1503-8181.

“Network arch timber bridges with light timber deck on transverse crossbeams”
Anna Weronika Ostrycharczyk, 2017:318, ISBN 978-82-326-2704-2 (printed ver.) ISBN 978-82-326-2705-9 (electronic ver.) ISSN 1503-8181.

“Splicing of Large Glued Laminated Timber Elements by Use of Long Threated Rods”
Martin Cepelka, 2017:320, ISBN 978-82-326-2708-0 (printed ver.) ISBN 978-82-326-2709-7 (electronic ver.) ISSN 1503-8181.

“Thermomechanical behaviour of semi-crystalline polymers: experiments, modelling and simulation”
Joakim Johnsen, 2017-317, ISBN 978-82-326-2702-8 (printed ver.) ISBN 978-82-326-2703-5 (electronic ver.) ISSN 1503-8181.

“Small-Scale Plasiticity under Hydrogen Environment”
Kai Zhao, 2017:356, ISBN 978-82-326-2782-0 (printed ver.) ISBN 978-82-326-2783-7 (electronic er.) ISSN 1503-8181.

“Risk and Reliability Based Calibration of Structural Design Codes”
Michele Baravalle, 2017:342, ISBN 978-82-326-2752-3 (printed ver,) ISBN 978-82-326-2753-0 (electronic ver.) ISSN 1503-8181.

“Dynamic behaviour of floating bridges exposed to wave excitation”
Knut Andreas Kvåle, 2017:365, ISBN 978-82-326-2800-1 (printed ver.) ISBN 978-82-326-2801-8 (electronic ver.) ISSN 1503-8181.

“Dolomite calcined clay composite cement – hydration and durability”
Alisa Lydia Machner, 2018:39, ISBN 978-82-326-2872-8 (printed ver.). ISBN 978-82-326-2873-5 (electronic ver.) ISSN 1503-8181.

“Modelling of the self-excited forces for bridge decks subjected to random motions: an experimental study”
Bartosz Siedziako, 2018:52, ISBN 978-82-326-2896-4 (printed ver.). ISBN 978-82-326-2897-1 (electronic ver.) ISSN 1503-8181.

“A probabilistic-based methodology for evaluation of timber facade constructions”
Klodian Gradeci, 2018:69, ISBN 978-82-326-2928-2 (printed ver.) ISBN 978-82-326-2929-9 (electronic ver.) ISSN 1503-8181.

“Behaviour and modelling of flow-drill screw connections”
Johan Kolstø Sønstabø, 2018:73, ISBN 978-82-326-2936-7 (printed ver.) ISBN 978-82-326-2937-4 (electronic ver.) ISSN 1503-8181.

“Full-scale investigation of the effects of wind turbulence characteristics on dynamic behavior of long-span cable-supported bridges in complex terrain”
Aksel Fenerci, 2018 100, ISBN 9978-82-326-2990-9 (printed ver.) ISBN 978-82-326-2991-6 (electronic ver.) ISSN 1503-8181.

“Modeling and simulation of the soft palate for improved understanding of the obstructive sleep apnea syndrome”
Hongliang Liu, , 2018:101, ISBN 978-82-326-2992-3 (printed ver.) ISBN 978-82-326-2993-0 (electronic ver.) ISSN 1503-8181.

“Long-term extreme response analysis of cable-supported bridges with floating pylons subjected to wind and wave loads”.
Yuwang Xu, 2018:229, ISBN 978-82-326-3248-0 (printed ver.) ISBN 978-82-326-3249-7 (electronic ver.) ISSN 1503-8181.